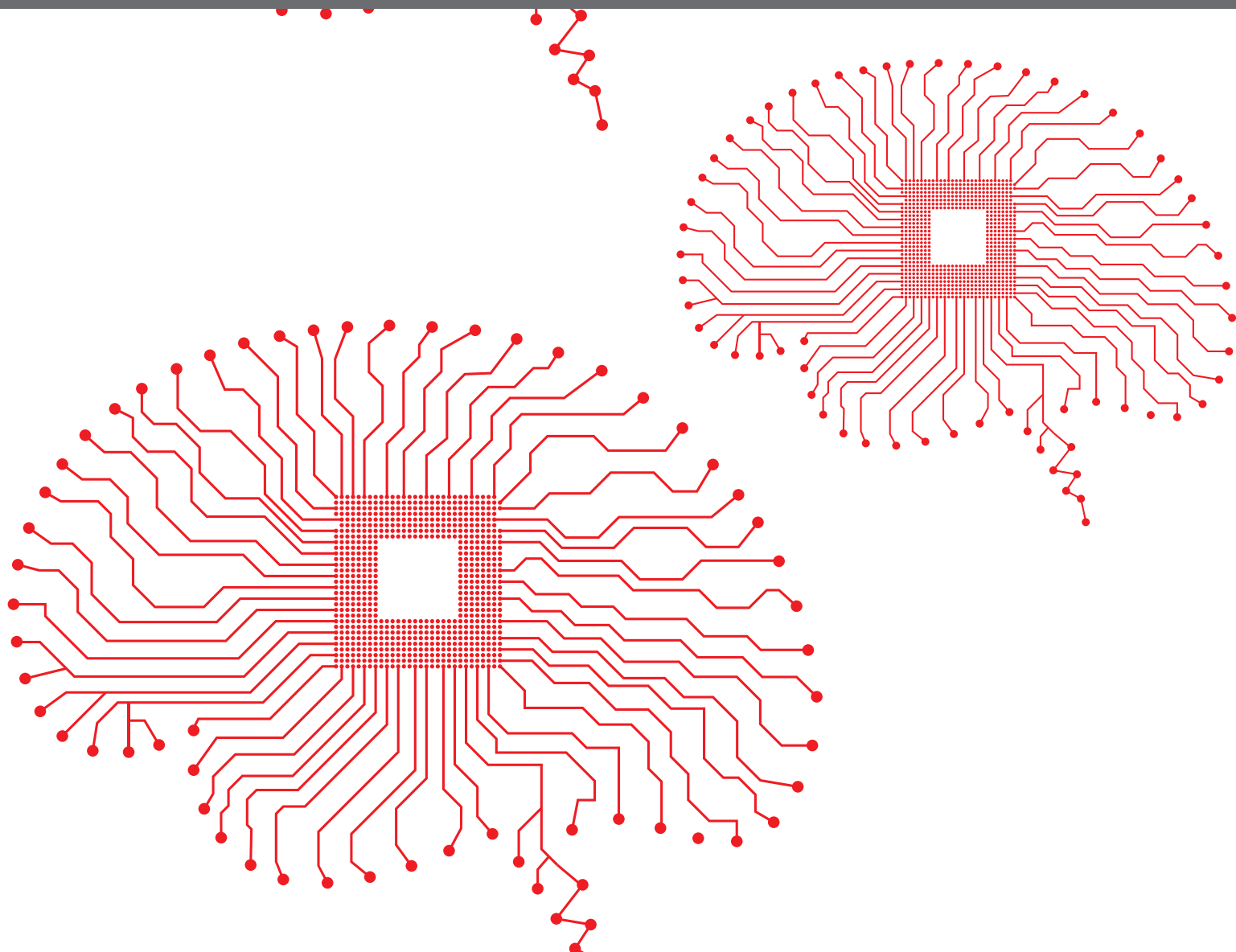


The background of the top half of the cover is a solid red color. Overlaid on this red background is a complex, white circuit board pattern. The pattern consists of numerous thin, white lines that branch out and connect to small white dots, resembling a network or a brain's neural pathways. The pattern is most dense in the upper left and right corners, with some lines extending towards the center.

COMPUTATIONAL METHODS FOR TRANSLATIONAL BRAIN-BEHAVIOR ANALYSIS

EDITED BY: Rong Chen, Tianyi Yan, Yiannis Ventikos and Jinghao Zhou
PUBLISHED IN: Frontiers in Neuroinformatics and
Frontiers in Computational Neuroscience





frontiers

Frontiers eBook Copyright Statement

The copyright in the text of individual articles in this eBook is the property of their respective authors or their respective institutions or funders. The copyright in graphics and images within each article may be subject to copyright of other parties. In both cases this is subject to a license granted to Frontiers.

The compilation of articles constituting this eBook is the property of Frontiers.

Each article within this eBook, and the eBook itself, are published under the most recent version of the Creative Commons CC-BY licence.

The version current at the date of publication of this eBook is CC-BY 4.0. If the CC-BY licence is updated, the licence granted by Frontiers is automatically updated to the new version.

When exercising any right under the CC-BY licence, Frontiers must be attributed as the original publisher of the article or eBook, as applicable.

Authors have the responsibility of ensuring that any graphics or other materials which are the property of others may be included in the CC-BY licence, but this should be checked before relying on the CC-BY licence to reproduce those materials. Any copyright notices relating to those materials must be complied with.

Copyright and source acknowledgement notices may not be removed and must be displayed in any copy, derivative work or partial copy which includes the elements in question.

All copyright, and all rights therein, are protected by national and international copyright laws. The above represents a summary only. For further information please read Frontiers' Conditions for Website Use and Copyright Statement, and the applicable CC-BY licence.

ISSN 1664-8714

ISBN 978-2-88966-897-7

DOI 10.3389/978-2-88966-897-7

About Frontiers

Frontiers is more than just an open-access publisher of scholarly articles: it is a pioneering approach to the world of academia, radically improving the way scholarly research is managed. The grand vision of Frontiers is a world where all people have an equal opportunity to seek, share and generate knowledge. Frontiers provides immediate and permanent online open access to all its publications, but this alone is not enough to realize our grand goals.

Frontiers Journal Series

The Frontiers Journal Series is a multi-tier and interdisciplinary set of open-access, online journals, promising a paradigm shift from the current review, selection and dissemination processes in academic publishing. All Frontiers journals are driven by researchers for researchers; therefore, they constitute a service to the scholarly community. At the same time, the Frontiers Journal Series operates on a revolutionary invention, the tiered publishing system, initially addressing specific communities of scholars, and gradually climbing up to broader public understanding, thus serving the interests of the lay society, too.

Dedication to Quality

Each Frontiers article is a landmark of the highest quality, thanks to genuinely collaborative interactions between authors and review editors, who include some of the world's best academicians. Research must be certified by peers before entering a stream of knowledge that may eventually reach the public - and shape society; therefore, Frontiers only applies the most rigorous and unbiased reviews.

Frontiers revolutionizes research publishing by freely delivering the most outstanding research, evaluated with no bias from both the academic and social point of view. By applying the most advanced information technologies, Frontiers is catapulting scholarly publishing into a new generation.

What are Frontiers Research Topics?

Frontiers Research Topics are very popular trademarks of the Frontiers Journals Series: they are collections of at least ten articles, all centered on a particular subject. With their unique mix of varied contributions from Original Research to Review Articles, Frontiers Research Topics unify the most influential researchers, the latest key findings and historical advances in a hot research area! Find out more on how to host your own Frontiers Research Topic or contribute to one as an author by contacting the Frontiers Editorial Office: frontiersin.org/about/contact

COMPUTATIONAL METHODS FOR TRANSLATIONAL BRAIN-BEHAVIOR ANALYSIS

Topic Editors:

Rong Chen, University of Maryland, Baltimore, United States

Tianyi Yan, Beijing Institute of Technology, China

Yiannis Ventikos, University College London, United Kingdom

Jinghao Zhou, University of Maryland, United States

Citation: Chen, R., Yan, T., Ventikos, Y., Zhou, J., eds. (2021). Computational Methods for Translational Brain-Behavior Analysis. Lausanne: Frontiers Media SA. doi: 10.3389/978-2-88966-897-7

Table of Contents

- 05** ***Aberrant Correlation Between the Default Mode and Salience Networks in Mild Traumatic Brain Injury***
Yongkang Liu, Wenzhong Wu, Xiao Chen, Minghua Wu, Gang Hu, Guoxing Zhou, Zhongqiu Wang and Rong Chen
- 16** ***Disrupted Rich Club Organization of Hemispheric White Matter Networks in Bipolar Disorder***
Dandan Li, Weichen Liu, Ting Yan, Xiaohong Cui, Zehua Zhang, Jing Wei, Yunxiao Ma, Nan Zhang, Jie Xiang and Bin Wang
- 30** ***Transition of Neural Activity From the Chaotic Bipolar-Disorder State to the Periodic Healthy State Using External Feedback Signals***
Hirotaka Doho, Sou Nobukawa, Haruhiko Nishimura, Nobuhiko Wagatsuma and Tetsuya Takahashi
- 45** ***Steering the Volume of Tissue Activated With a Directional Deep Brain Stimulation Lead in the Globus Pallidus Pars Interna: A Modeling Study With Heterogeneous Tissue Properties***
Simeng Zhang, Michele Tagliati, Nader Pouratian, Binith Cheeran, Erika Ross and Erlick Pereira
- 54** ***A Systemic Review of Available Low-Cost EEG Headsets Used for Drowsiness Detection***
John LaRocco, Minh Dong Le and Dong-Guk Paeng
- 68** ***Connectome-Based Model Predicts Deep Brain Stimulation Outcome in Parkinson's Disease***
Ruihong Shang, Le He, Xiaodong Ma, Yu Ma and Xuesong Li
- 76** ***Effects of Visual Attentional Load on the Tactile Sensory Memory Indexed by Somatosensory Mismatch Negativity***
Xin He, Jian Zhang, Zhilin Zhang, Ritsu Go, Jinglong Wu, Chunlin Li, Kai Gan and Duanduan Chen
- 88** ***A Spelling Paradigm With an Added Red Dot Improved the P300 Speller System Performance***
Yan Wu, Weiwei Zhou, Zhaohua Lu and Qi Li
- 97** ***Development of a Non-invasive Deep Brain Stimulator With Precise Positioning and Real-Time Monitoring of Bioimpedance***
Heng Wang, Zhongyan Shi, Weiqian Sun, Jianxu Zhang, Jing Wang, Yue Shi, Ruoshui Yang, Chunlin Li, Duanduan Chen, Jinglong Wu, Guo Gongyao and Yifei Xu
- 109** ***Biosignal-Based Attention Monitoring to Support Nuclear Operator Safety-Relevant Tasks***
Jung Hwan Kim, Chul Min Kim, Eun-Soo Jung and Man-Sung Yim
- 120** ***Alternation of Resting-State Functional Connectivity Between Visual Cortex and Hypothalamus in Guinea Pigs With Experimental Glucocorticoid Enhanced Myopia After the Treatment of Electroacupuncture***
Tao Zhang, Qian Jiang, Furu Xu, Ruixue Zhang, Dezheng Liu, Dadong Guo, Jianfeng Wu, Ying Wen, Xingrong Wang, Wenjun Jiang and Hongsheng Bi

- 132** *Stimulus Intervals Modulate the Balance of Brain Activity in the Human Primary Somatosensory Cortex: An ERP Study*
Yang Liu, Bo Dong, Jiajia Yang, Yoshimichi Ejima, Jinglong Wu, Qiong Wu and Ming Zhang
- 139** *Evaluation of Task fMRI Decoding With Deep Learning on a Small Sample Dataset*
Sunao Yotsutsuji, Miaomei Lei and Hiroyuki Akama



Aberrant Correlation Between the Default Mode and Salience Networks in Mild Traumatic Brain Injury

Yongkang Liu^{1†}, Wenzhong Wu^{2†}, Xiao Chen¹, Minghua Wu³, Gang Hu⁴, Guoxing Zhou⁵, Zhongqiu Wang^{1*} and Rong Chen^{6*}

¹ Department of Radiology, Affiliated Hospital of Nanjing University of Chinese Medicine, Nanjing, China, ² Department of Acupuncture & Rehabilitation, Affiliated Hospital of Nanjing University of Chinese Medicine, Nanjing, China, ³ Department of Brain Center, Affiliated Hospital of Nanjing University of Chinese Medicine, Nanjing, China, ⁴ School of Pharmacy, Nanjing University of Chinese Medicine, Nanjing, China, ⁵ Department of Radiology, Shanghai East Hospital, Tongji University School of Medicine, Shanghai, China, ⁶ Department of Diagnostic Radiology and Nuclear Medicine, University of Maryland School of Medicine, Baltimore, MD, United States

OPEN ACCESS

Edited by:

Petia D. Koprinkova-Hristova,
Institute of Information and
Communication Technologies
(BAS), Bulgaria

Reviewed by:

Afra Wohlschlaeger,
Technical University of
Munich, Germany
Qiang Luo,
Fudan University, China

*Correspondence:

Zhongqiu Wang
zhqwang001@126.com
Rong Chen
rong.chen.mail@gmail.com

[†]These authors have contributed
equally to this work

Received: 21 January 2020

Accepted: 12 June 2020

Published: 28 July 2020

Citation:

Liu Y, Wu W, Chen X, Wu M, Hu G,
Zhou G, Wang Z and Chen R (2020)
Aberrant Correlation Between the
Default Mode and Salience Networks
in Mild Traumatic Brain Injury.
Front. Comput. Neurosci. 14:68.
doi: 10.3389/fncom.2020.00068

Objectives: The specific intrinsic network coupling abnormalities in mild traumatic brain injury (mTBI) patients are poorly understood. Our objective is to compare the correlations among the default mode, salience, and central executive networks in patients with mTBI and healthy controls.

Methods: This 2-year prospective study included 32 acute mTBI patients and 37 healthy comparisons. We calculated the functional connectivity scores among the default mode, salience, and central executive networks. Then we conducted multilevel correlation analysis to investigate component correlations, global graph, and local functional connectivity changes.

Results: Patients with mTBI showed significant increased functional connectivity between the anterior part of the default mode network and the salience network compared with controls ($p = 0.013$, false discovery rate correction). Hyper-connectivity between the default mode and salience network was significantly positively correlated with the dimensional change card sort score in patients with mTBI ($r = 0.40$, $p = 0.037$). The average path length of mTBI patients was significantly higher than that of controls ($p = 0.028$).

Conclusions: Aberrant functional coupling between the default mode and salience networks were identified in acute mTBI patients. Our finding has great potential to improve our understanding of the network architecture of mTBI.

Keywords: mild traumatic brain injury, intrinsic network, multilevel analysis, default mode network, salience network, network coupling

KEY POINTS

- Aberrant correlation between the default mode and salience networks in acute mTBI.
- Hyper-connectivity significantly positively correlated with the dimensional change card sort score.
- Understanding of the network architecture of mTBI.

INTRODUCTION

Worldwide, traumatic brain injury affects about 10 million individuals annually (Hyder et al., 2007). Traumatic brain injury is associated with long-term disabilities including cognitive, psychological, motor, and sensory deficits. About 80% of traumatic brain injury patients are classified as mild traumatic brain injury (mTBI) (Kushner, 1998). Approximately 15% of mTBI patients have persistent neurological symptoms (Shenton et al., 2012).

fMRI is a non-invasive imaging technique for examining brain function. It uses changes in the BOLD signal to identify neuronal activity changes. Resting-state fMRI examines intrinsic functional connectivity in task-free conditions by mapping temporally synchronous, spatially distributed, spontaneous low-frequency BOLD signal fluctuation (Fox and Raichle, 2007). Resting-state fMRI provides a good signal to noise ratio and requires minimal patient compliance (Fox and Greicius, 2010). It has revealed a set of intrinsic connectivity networks. Voxels in an intrinsic connectivity network exhibit a coherent BOLD fluctuation pattern.

Many studies aimed at detecting changes in intrinsic connectivity networks in patients with traumatic brain injury (Sharp et al., 2014). Disruption of intrinsic connectivity networks could be a core mechanism of cognitive impairment in patients with traumatic brain injury. Resting-state fMRI studies have demonstrated complex patterns of intrinsic connectivity network abnormalities (Sharp et al., 2011; Shumskaya et al., 2012; Palacios et al., 2013; Pandit et al., 2013; Arenivas et al., 2014; Iraj et al., 2015). For example, Zhou et al. reported abnormal default mode network connectivity patterns in patients with mTBI which may provide insight into how neuronal communication and information integration are disrupted after mild head injury (Zhou et al., 2012).

The triple network model offers a theory for understanding cognitive dysfunction in brain disorders (Menon, 2011). The triple network model involves three intrinsic connectivity networks: the default mode network, the salience network, and the central executive network. The default mode network is anchored in the posterior cingulate cortex (PCC) and the medial prefrontal cortex (mPFC). It plays an important role in monitoring the internal mental landscape and is typically deactivated during most stimulus-driven tasks. The salience network is anchored in the dorsal anterior cingulate cortex (dACC) and frontoinsula cortex (FIC). It is involved in detecting, integrating, and filtering relevant interoceptive, autonomic, and emotional information. The central executive network is anchored in the dorsolateral prefrontal cortex (dlPFC) and posterior parietal cortex. It plays an important role in

higher-order cognitive function and attention control. The triple network model states that the couplings among the default mode, salience, and central executive networks are responsible for the cognitive impairment in many brain disorders. This model has been examined in autism, schizophrenia, and frontotemporal dementia (Uddin, 2014).

Although many studies examined intrinsic connectivity network abnormalities in mTBI, no studies focused on the triple network model and examined correlations among the default mode, salience, and central executive networks in acute mTBI patients. Our study investigates correlations among the default mode, salience, and central executive networks in acute mTBI patients. We use multilevel correlation analysis, which examines functional connectivity changes across different scales, to analyze resting-state fMRI data. Understanding correlations among intrinsic connectivity networks holds great potential to improve our knowledge of the neuropathology of mTBI. Identifying neuroimaging features may lead to more accurate diagnosis and effective treatments.

MATERIALS AND METHODS

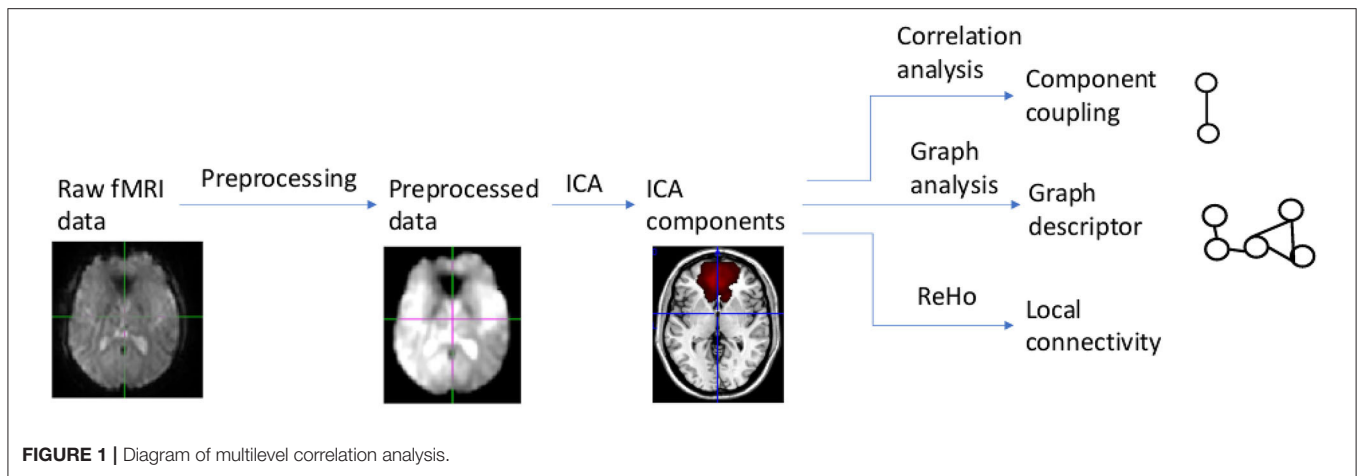
Participants

From August 2012 to July 2014, mTBI patients and healthy comparisons were recruited in Shanghai Dongfang Hospital. mTBI patients were enrolled in the emergency department. For a comparison group, healthy subjects were recruited from the nearby community through advertisements. The hospital's institutional review board approved this study. All individuals provided written informed consent.

The diagnosis of mTBI was established based on the criteria of the American Congress of Rehabilitative Medicine for mild brain injury (American Congress of Rehabilitation Medicine, 1993). A subject was considered to have mTBI if any one of the following symptoms was evident following external application of force to the brain: (1) any period of loss of consciousness, (2) loss of memory for events immediately before or after the accident, (3) alteration in mental state at the time of the accident, or (4) focal neurologic deficits that may or may not be transient. The inclusion criteria were: (1) loss of consciousness of 30 min or less, (2) Glasgow Coma Scale (GCS) score of 13–15 at 30 min post-injury, and (3) duration of post-traumatic amnesia no longer than 24 h. The exclusion criteria were: (1) penetrating head injury, (2) uremia, liver cirrhosis, heart failure, pulmonary edema, coagulopathy, or renal dysfunction, (3) pregnancy, (4) *in vivo* magnetic implants (such as iron, cochlear implants, vascular clips, etc.) or pacemaker, (5) patient either died or had already received cardiopulmonary resuscitation before arrival at the hospital, (6) positive CT findings, (7) history of other neurological diseases, (8) history of neuropsychological diseases.

The comparison group included healthy subjects who had no history of neurological, psychiatric, or central nervous system disease, and no prior TBI. All participants (mTBI and healthy subjects) were right-handed. Healthy subjects were matched to mTBI subjects by age, sex, education, and handedness at the group level.

Abbreviations: AUC, Area under the curve; BOLD, blood oxygen level-dependent; BSI-18, Brief Symptom Inventory-18; dACC, dorsal anterior cingulate cortex; dlPFC, dorsolateral prefrontal cortex; FA, fractional anisotropy; DTI, diffusion tensor imaging; FIC, frontoinsula cortex; fMRI, functional magnetic resonance imaging; GCS, Glasgow Coma Scale; mPFC, medial prefrontal cortex; mTBI, mild traumatic brain injury; PCC, posterior cingulate cortex; ReHo, regional homogeneity; ROI, region of interest; RPQ, Rivermead Post-Concussion Questionnaire; TBSS, tract-based spatial statistics.



Among 71 participants, two subjects with significant MRI motion problems were excluded. The final dataset included 32 acute stage mTBI patients and 37 healthy comparisons.

MRI Protocol

MR imaging was performed in mTBI patients within 7 days of the injury. MR data were acquired with a Philips Achieva 3.0T TX MRI scanner (Royal Philips, Amsterdam, Netherlands). The MR protocol included anatomical imaging (T1 and T2), resting-state fMRI, and DTI. High-resolution T1-weighted structural images were acquired with a MPRAGE sequence. The imaging parameters were TR/TE = 8.2/3.5 ms; flip angle = 8 degree; slice thickness = 1 mm, voxel size = 1×1 mm, FOV = 256×256 . The T1 acquisition time was 4.56 min. Resting-state fMRI data were acquired with a FE-EPI sequence. The sequence parameters were: TR/TE = 1,500/35 ms, flip angle = 90 degree, slice thickness = 5 mm, voxel size = 3.75×3.75 mm, FOV = 240×240 mm, acquired matrix = 64×64 , dyn = 210. Participants were asked to keep their eyes focused on cross-hairs projected onto a screen, and not think of anything during image acquisition. The total resting-state fMRI acquisition time was 5.35 min. Diffusion tensor images were acquired with a single-shot echo-planar sequence (TR/TE = 9,000/90 ms, slice thickness = 2 mm, voxel size = 2×2 mm, field of view = 256×256 mm). Diffusion gradients were set in 32 non-collinear directions by using two *b*-values (*b* = 0 and 1,000 s/mm²). The total DTI acquisition time was 5.5 min.

Neuropsychological Assessment

Neuropsychological tests were administrated within 24 h of MR imaging. We used the Dimensional Change Card Sort test (DCCS) to assess executive functioning (Zelazo, 2006). The DCCS is a standard procedure for measuring executive function, specifically tapping cognitive flexibility. In the DCCS, two target pictures are presented that vary along two dimensions (e.g., shape and color). Participants match a series of bivalent test pictures to the target pictures, first according to one dimension (e.g., color) and then, after several trials, sort the same cards a new way (e.g., shape). In “switch” trials, the participant must

change the dimension being matched. Scoring is based on a combination of accuracy and reaction time. This combination score is converted to a scale score with mean 100 and standard deviation (SD) 15. Higher scores indicate higher levels of executive functioning. DCCS was chosen because subjects with TBI often suffer impairments in their cognitive flexibility as a result of brain damage (Whiting et al., 2017).

Multilevel Correlation Analysis

Our data analysis and modeling method, called multilevel correlation analysis, is summarized in **Figure 1**. Multilevel correlation analysis centers on modeling correlations among the default mode, salience, and central executive networks. It includes the following modules: preprocessing, independent component analysis, component correlation analysis, graph analysis, and local connectivity analysis. Multilevel correlation analysis examines connectivity changes across different scales. Component correlation analysis focuses on localized changes in correlations among components. Graph analysis examines distributed, global level changes in information communication among components. Local connectivity analysis probes local functional connectivity changes.

Image Preprocessing

Our resting-state fMRI data preprocessing pipeline was based on FMRIB Software Library (FSL) (Jenkinson et al., 2012) and Analysis of Functional NeuroImages (AFNI) (Cox, 1996). This pipeline (Chen et al., 2016) included the following steps: skull stripping, slice-timing, and motion correction, Gaussian spatial smoothing, temporal filtering, regressing out nuisance parameters, and spatial normalization to the Montreal Neurological Institute (MNI) space.

We first dropped the first ten volumes to remove T1 equilibration effects. Then we performed slice-timing and motion correction followed by skull-stripping. Skull-stripping results were verified by visual inspection. We smoothed fMRI volumes using a Gaussian kernel with a full width at half maximum = 6 mm, and temporally filtered fMRI volumes with bandwidth = [0.005Hz 0.1Hz]. We extracted a base volume from the 4D fMRI

volume and registered this base volume to the subject's T1 volume using the mutual information-based registration in FSL. Based on the subject's T1 image segmentation results, we obtained white matter and CSF masks. We calculated the mean white matter and CSF signals. Then we regressed out the six motion parameters, the mean frame-wise displacement (FD), and the mean white matter and CSF signals. We registered the preprocessed 4D volume to the MNI space by applying the composite deformation field which combined the deformation field from the base volume to the subject's T1 volume, and that from the subject's T1 volume to the MNI space.

Excessive head motion is known to induce artifacts and false-positive correlations among brain structures in resting-state fMRI (Power et al., 2012). We employed relatively strict criteria to address the head motion problem. First, we excluded all subjects with mean FD of more than two standard deviations above the sample mean. Second, we regressed out head-motion parameters and mean FD from the BOLD signal.

Independent Component Analysis

We used Independent Component Analysis (ICA) to identify intrinsic networks. We performed probabilistic ICA (Beckmann and Smith, 2004) by applying MELODIC (Multivariate Exploratory Linear Optimized Decomposition into Independent Components) implemented in FSL to the preprocessed resting-state fMRI data from the comparison group. A multi-session temporal concatenation tool in MELODIC was used; variance normalization also was used. We detected component masks based on comparison group data for two reasons: first, applying ICA to data from both the mTBI and comparison groups is less sensitive in detecting differences in network changes (Rytty et al., 2013). Second, ICA results based on the comparison group are a more robust match with previous healthy subject group ICA templates (Rytty et al., 2013). The number of components used was 30 because previous studies found ICA with 30 components can reliably identify intrinsic networks (Shumskaya et al., 2012). MELODIC converted the estimated ICA maps to Z statistic images using a mixture model approach. The Z statistic images were thresholded with $Z = 4$ (Beckmann et al., 2009). Based on visual inspection of spatial maps and the related time courses and power spectrums, we identified components as ventricular, vascular, susceptibility, or motion-related artifacts (Kelly et al., 2010); these noise components were excluded from the analysis.

For an ICA component spatial map, we determined to which intrinsic network it belonged by using template matching. We used the Allen intrinsic network template (Allen et al., 2011) as the intrinsic network template because it is widely used to examine brain networks in health and disease. We calculated the cross-correlation between a component and a reference network and determined to which reference network the component belonged. We selected ICA components that were in the default mode, salience, and central executive networks. Subject-specific time courses relating to ICA component maps were extracted using dual regression. For each subject, the group-average set of spatial maps was regressed into the subject's 4D volumes. This resulted in a set of subject-specific time courses for ICA component spatial maps.

Component Correlation Analysis

Component correlation analysis centers on studying correlations among components. Each ICA component constituted a node. For each subject, we calculated the node time course; then calculated the Pearson correlation coefficient between a time course pair. We converted it to a Z score using Fisher's Z transformation. This Z score was referred to as a functional connectivity score. For a study with K components, we generated a $K \times K$ functional connectivity matrix for each subject.

For a functional connectivity score, we used the Wilcoxon rank-sum test to determine whether there was a significant difference between mTBI patients and healthy subjects. We used the False Discovery Rate (FDR) to address multiple comparisons. If the FDR corrected p -value was smaller than 0.05, there was a significant difference across groups. Such a score was a feature characterizing mTBI. Let F denote the detected feature set.

To assess the stability of our findings, we conducted a Jackknife resampling-based analysis. We removed one sample from the original dataset and then conducted the analysis based on the remaining samples. This resulted in a resampling based feature set. If our dataset has n samples, we will generate n resampling-based feature sets. We compared the original feature set with resampling based feature sets and calculated a stability metric λ . The stability metric was defined as $N_{[\text{original}=\text{resampling}]} / n$, where $N_{[\text{original}=\text{resampling}]}$ was the number of times that the original feature set was the same resampling based feature set, and n was the sample size. λ was between 0 and 1. Greater λ represented a more stable model.

Association With Executive Function

To investigate brain-behavior associations, we performed two association analyses. First, we conducted a correlation analysis between the detected feature and the DCCS score for mTBI subjects. Second, for all subjects (healthy and mTBI subjects), we conducted a regression analysis with the DCCS score as the dependent variable and the detected feature and the group-membership variables as predictors. This analysis detected group differences in the association between the DCCS score and the detected imaging feature. Normality was checked by the Shapiro-Wilk test.

Graph Analysis

Graph analysis uses graph theoretical methods to analyze functional connectivity matrices. Relative to component correlation analysis, it can generate global graph descriptors to characterize the topological or information-theoretical complexity of a graph. Graph analysis and component correlation analysis provide complementary information about couplings among the default mode, salience, and central executive networks.

An ICA component in the default mode, salience, and central executive networks was a node in a graph. We calculated the Pearson correlation coefficient between a component-time course pair; and converted it to a Z score. We generated a connectivity matrix for each subject. To generate a graph, we thresholded the connectivity matrix based on graph density. The density threshold was chosen as $0.35 < \text{graph density} < 0.4$

(step size was 0.02). The lower limit was chosen to prevent a disconnected graph; and the upper limit was chosen because brain networks in general are not densely connected and have a density <0.4 (Sporns, 2011). The thresholding step generated a weighted graph. Then we calculated two graph descriptors: the global clustering coefficient and average path length (Rubinov and Sporns, 2010). The clustering coefficient of a node was defined as the likelihood of the neighborhoods being connected with each other. The global clustering coefficient was the average of the clustering coefficient over all the nodes. The path length between the nodes was the sum of the edge length along the path. The average path length was the average of the shortest path length across node pairs. Both the global clustering coefficient and average path length were calculated based on the weighted graph. For each threshold, we calculated a graph descriptor. An aggregated graph descriptor was generated by calculating the area under the curve (AUC) across graph density thresholds (Bullmore and Bassett, 2011).

Stability Relative to ICA Component Mask Generation

We examined whether our findings were sensitive to the method generating ICA component masks. Let Mask(control) denote that ICA masks are generated based on controls. Let Mask(all) denote that ICA masks are generated based on all subjects (controls and mTBI). We rerun the whole ICA workflow using Mask(all). We used fsfcc (Jenkinson et al., 2012) to match Mask(control) and Mask(all). If a component in Mask(controls) matched multiple components in Mask(all), we merged these component masks in Mask(all). With this transformation, we can compare results in the Mask(control) and Mask(all) spaces.

Local Functional Connectivity Analysis

Local functional connectivity quantifies local functional couplings among spatially adjacent voxels. Regional homogeneity (ReHo) is widely used to examine local functional connectivity (Zang et al., 2004). In ReHo, Kendall's coefficient of concordance was used to measure regional homogeneity or similarity of the ranked time series of a given voxel with its nearest 26 neighbor voxels in a voxel-wise way. The intracranial voxels were extracted to generate a mask. Then 3D ReHo in AFNI was used to generate the ReHo map. Each subject's ReHo map was divided by its own mean ReHo within the brain mask for standardization purposes (Zang et al., 2004). Then voxel-wise t -test analysis was performed to detect voxels whose ReHo values were significantly different across groups. Monte Carlo simulation in AFNI was used for multiple comparison correction. Voxels with corrected p -value < 0.05 were significantly different across groups.

Anatomical Connectivity Analysis

To investigate anatomical connectivity underlying functional connectivity, we used Tract-Based Spatial Statistics (TBSS) implemented in FSL to detect changes in brain anatomical connectivity. We analyzed fractional anisotropy (FA) which quantifies local tract directionality and integrity. TBSS projects a subject's FA map to a common space, creates an FA skeleton, and projects each subject's FA onto the skeleton to generate

a skeletonized FA image for each subject. This skeletonized FA image represents brain anatomical connectivity. The white matter integrity differences were investigated by using the threshold-free cluster enhancement at p -value < 0.05 (5,000 permutations) fully corrected for multiple comparisons. If a voxel's corrected p -value was smaller than 0.05, we considered this voxel's FA changed across groups.

We also performed ROI based anatomical connectivity analysis. ROIs were defined using the Johns Hopkins University white matter tractography atlas. There was a total of 20 ROIs in our analysis representing major white matter fiber tracts. For each ROI, we calculated the average FA value in the skeletonized FA map. Then we used independent two-group Mann-Whitney U -test to identify ROIs whose FA values were different between the mTBI and comparison subjects. The FDR correction was used to correct for multiple testing.

RESULTS

Participant Characteristics

Participant characteristics are summarized in **Table 1**. Mean ages were 30 years (SD 6.0) and 31 years (SD 8.7) for mTBI patients and comparisons, respectively. There were no significant difference in age across groups (p -value = 0.37, two-sample t -test); no significant difference in the female:male ratio (p -value = 0.81, chi-square test); and no significant difference in education (p -value = 0.11, two-sample t -test). All subjects were right-handed.

For mTBI patients, the cause of injury included traffic accidents (Nine patients), falls (Two patients), sports-related accidents (Two patients), and objects striking the head (19 patients). The injury severity in mTBI patients was mild: 97% with GCS = 15. The RPQ measures severity of 16 post-concussion syndrome symptoms, as compared to the pre-morbid level. The mean RPQ was 16 (SD 13.2). The BSI-18 is a tool to assess the level of psychological distress after mTBI. It covers somatization, depression, and anxiety. The mean BSI-18 was 15 (SD 14.4).

TABLE 1 | Demographic (age, sex, education), neurocognition (DCCS), and disease severity (Rivermead post-concussion questionnaire and brief symptom inventory-18) of participants.

	mTBI ($n = 32$) Controls ($n = 37$)		P
	Mean (SD)	Mean (SD)	
Age (years)	30 (6.0)	31 (8.7)	0.37
Sex (female/male)	12/20	16/21	0.81
Education (years)	15 (2.2)	16 (2.2)	0.11
Dimensional change card sort test	98 (12.8)	103 (10.9)	0.01
Glasgow coma scale	15 (0.2)	—	—
Rivermead post-concussion questionnaire	16 (13.2)	—	—
Brief symptom inventory-18	15 (14.4)	—	—

SD, standard deviation.

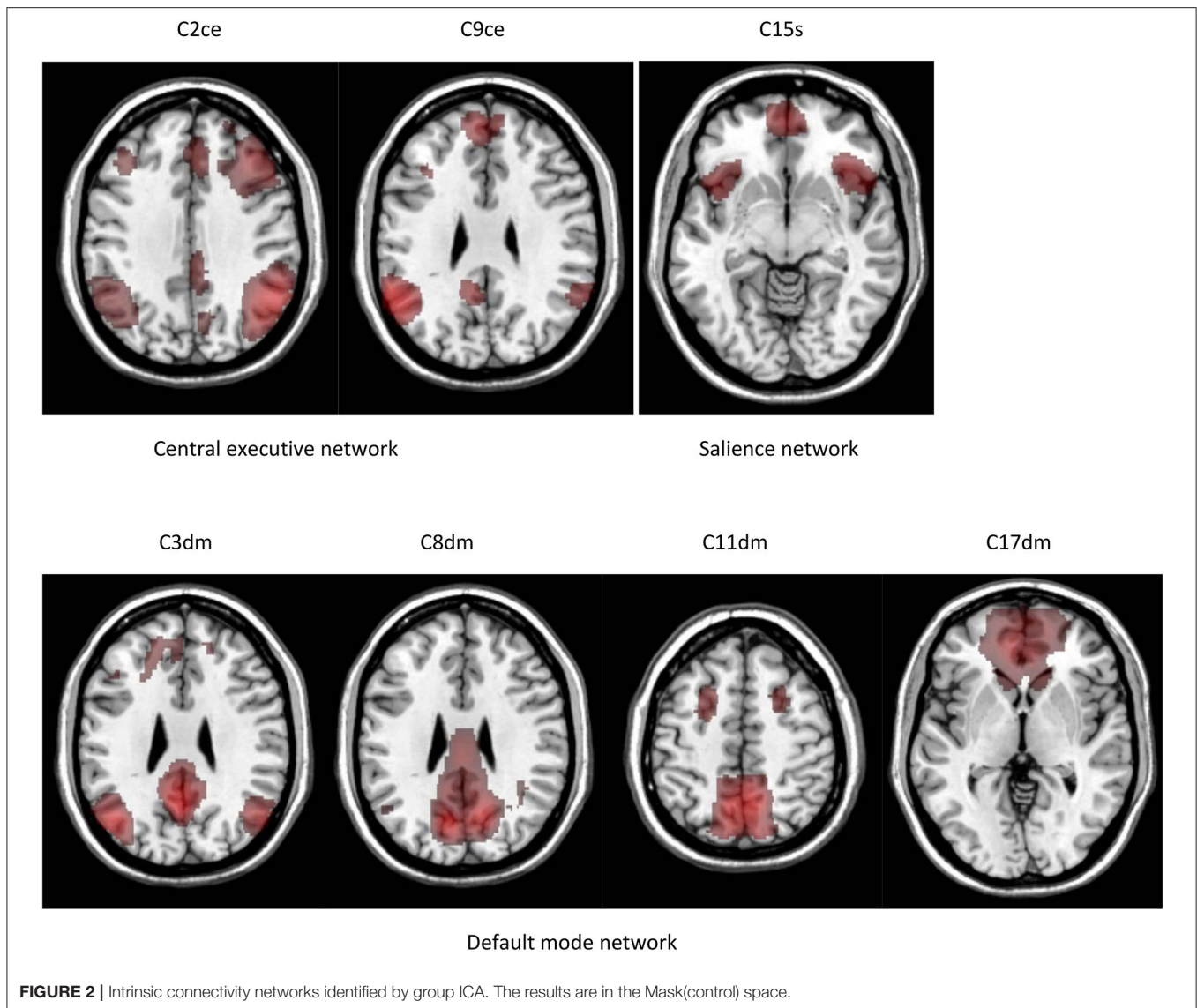


FIGURE 2 | Intrinsic connectivity networks identified by group ICA. The results are in the Mask(control) space.

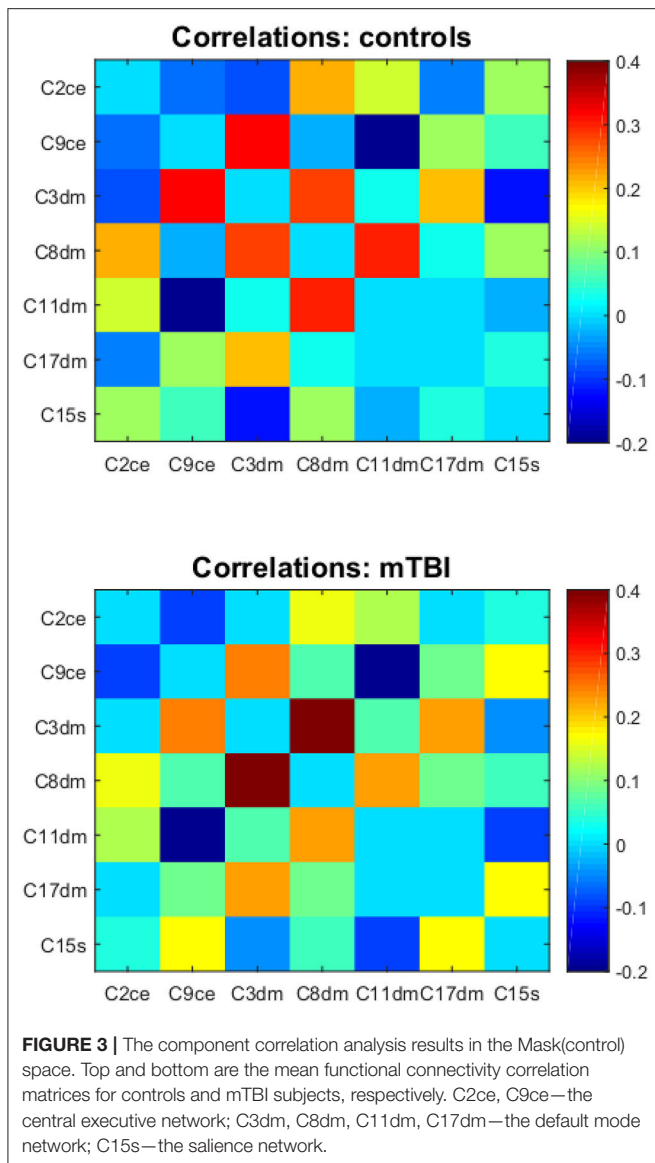
T1- and T2-weighted images were reviewed by an experienced neuroradiologist to identify structural abnormalities, including assessment for evidence of hemorrhage. The neuroradiologist was blinded to the group membership and clinical information. The images were found to be free of structural abnormalities for both mTBI patients and comparisons.

Component Correlations

We performed a 30-component group ICA using resting-state fMRI data from 37 comparison subjects. The component masks were in the Mask(control) space. Five components were identified as noise or artifact components. The remaining components were intrinsic connectivity networks. Our study centered on seven components in the default mode, salience, and central executive networks. These components are depicted in **Figure 2**. Components 2 and 9 are in the central executive network; components 3, 8, 11, 17 are in the default mode

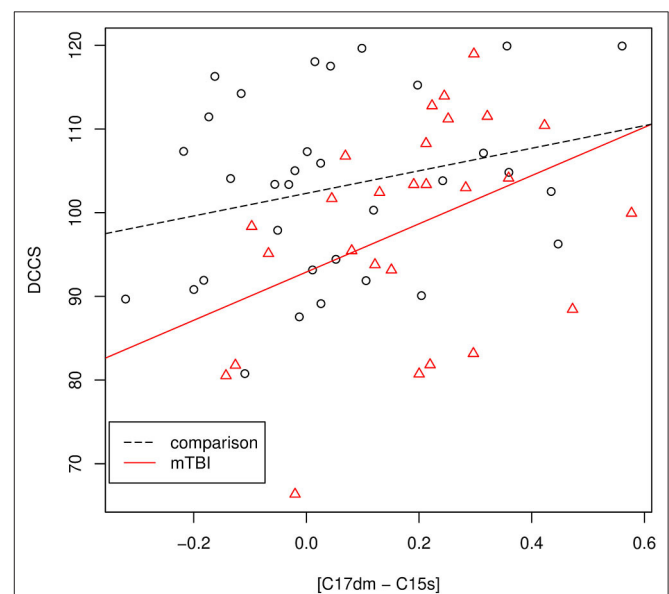
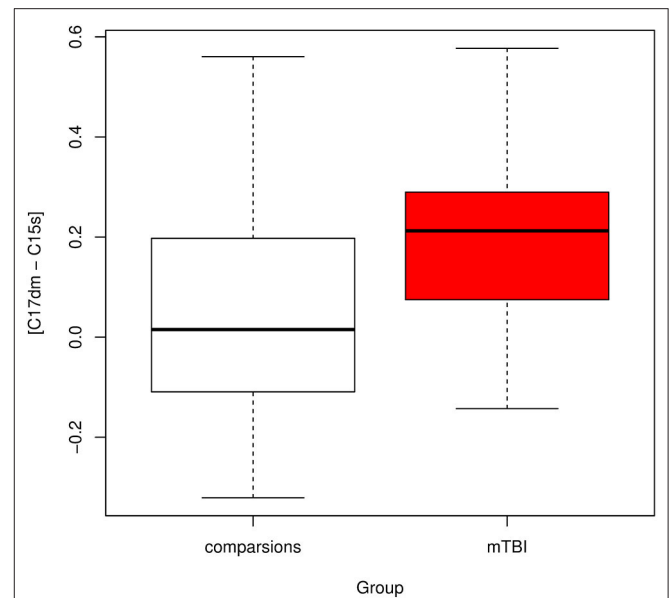
network; and component 15 is in the salience network. The central executive network includes two components. Component 2 is in the dlPFC and posterior parietal cortex, and component 9 is in the posterior parietal cortex. The default mode network includes four components. Components 3, 8, 11 are in the posterior part of the default mode network including the PCC and precuneus. Component 17 is in the anterior part of the default mode network anchored in the mPFC. The salience network is represented by component 15 which is primary in the dACC and the anterior insular.

Functional connectivity matrices for comparisons and mTBI patients are depicted in **Figure 3**. Correlations between component time courses revealed connectivity patterns consistent with known functional relationships. We observed a positive correlation between components in the same intrinsic network. We also found negative correlations between the default mode network components and components in the salience and central executive networks.



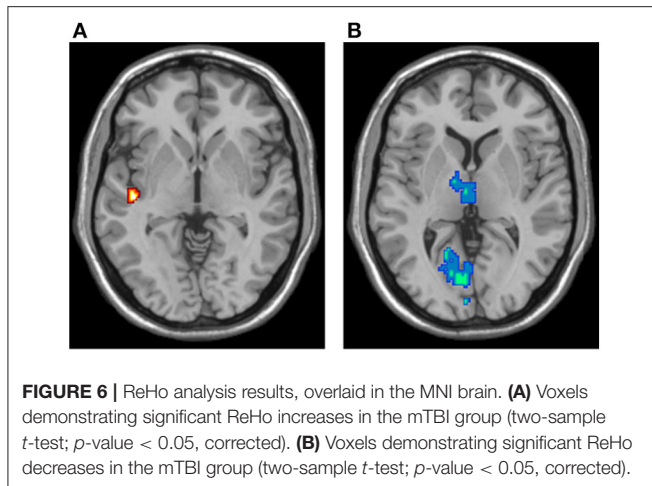
The correlation between a component in the default mode network (component 17) and a component in the salience network (component 15) was significantly different between mTBI and healthy subjects with corrected p -value = 0.013 (Figure 4). Let $[C17dm - C15s]$ denote the connection between component 17 (part of the default mode network) and 15 (part of the salience network). The mean functional connectivity scores of $[C17dm - C15s]$ were 0.037 (SD 0.22) and 0.201 (SD 0.18) for comparisons and mTBI patients, respectively.

We compared the resampling based feature sets to the original feature set and found that the original feature set was remarkably stable. For all 69 resampling based feature sets, we detected $[C17dm - C15s]$ were significantly higher in mTBI patients than comparison subjects (corrected p -value < 0.05).



Association With Executive Function

The results of the association analysis are depicted in Figure 5. For mTBI patients, we performed Pearson's correlation analysis between the DCCS score and $[C17dm - C15s]$. The DCCS score was positively associated with $[C17dm - C15s]$. The correlation coefficient was 0.40 (p -value = 0.037). To assess whether the association between DCCS and $[C17dm - C15s]$ was related to



mTBI severity, we built a regression model with DCCS as the dependent variable and [C17dm – C15s] and mTBI severity (Brief symptom inventory-18) as the independent variables. The mTBI severity term was not significant.

For mTBI patients and comparisons, we performed a regression analysis with the DCCS score as the dependent variable and [C17dm – C15s] and the group membership variable (comparisons and mTBI) as independent variables. The DCCS score was significantly associated with [C17dm – C15s] (*p*-value = 0.013) and the group membership variable (*p*-value = 0.0207). Then we added an interaction term ([C17dm – C15s] × group membership) to the regression model. This interaction term ([C17dm – C15s] × group membership) was not significant (*p*-value = 0.325).

DCCS is one task of the NIH Toolbox cognition measures which have seven tasks. All of them were administrated. The *p*-value of the association between DCCS and [C17dm – C15s] was not adjusted for multiple tasks (seven tasks in the NIH Toolbox cognition measures).

Graph Analysis

The nodes in our graph were components in the default mode, salience, and central executive networks. The average path length quantifies the ability for information to propagate in parallel. The AUC of the average path length of mTBI patients was significantly higher than that of controls. The mean AUCs were 2.02 (SD 0.50) and 2.29 (SD 0.64) for controls and mTBI patients, respectively. The two-sample *t*-test *p*-value was 0.028. The global clustering coefficient indicates the extent of the local interconnectivity or cliquishness in a graph. We found the AUC of the global clustering coefficient of mTBI patients was not significantly different from that of controls (*p*-value = 0.54).

Because there were two graph descriptors (the average path length and the global clustering coefficient), we conducted multiple comparisons correction using the false discovery rate. The average path length was marginally significant after correction (adjusted *p*-value = 0.056).

ReHo Analysis

ReHo results are shown in Figure 6. Compared to controls, mTBI patients showed significant ReHo decreases in the bilateral calcarine fissure and surrounding cortex, left cuneus, left lingual gyrus, and bilateral thalamus. These regions are in the visual and thalamus networks. Compared to controls, mTBI patients showed significant ReHo increases in the left rolandic operculum, left heschl gyrus, and left superior temporal gyrus. These regions are in the auditory network. No voxels in the default mode, salience, and central executive networks showed significant ReHo differences between controls and mTBI patients.

Anatomical Connectivity Analysis

Using DTI and TBSS, we found no significant anatomical connectivity differences in mTBI patients and comparisons. No voxels in the skeletonized FA space had a corrected *p*-value < 0.05. In ROI-based anatomical connectivity analysis, no ROIs had a corrected *p*-value < 0.05. We found no ROIs that demonstrated significant FA differences in mTBI patients and comparisons.

Stability Relative to ICA Component Masks

We examined whether our findings were sensitive to the method to generate ICA component masks. Let C2^{con} denote the component mask 2 in the Mask(control) space. We found that C2^{con} matched C2^{all}, C9^{con} matched C4^{all}, C3^{con} matched C17^{all}, C8^{con} matched C8^{all}, C11^{con} matched C9^{all} and C20^{all}, C17^{con} matched C19^{all}, C15^{con} matched C4^{all} and C10^{all}.

Our main finding was that [C17dm – C15s] was significantly higher in mTBI patients than controls in the Mask(control) space. We calculated the component coupling in the Mask(all) space which was correspondent to [C17dm – C15s] in the Mask(control) space. This component coupling was still significant (*p*-value = 0.032). The mean functional connectivity scores were 0.179 (SD 0.039) and 0.317 (SD 0.050) for controls and mTBI patients, respectively. The difference in the value of functional connectivity scores in the Mask(control) and Mask(all) spaces may reflect the component mask differences. The finding that [C17dm – C15s] in the Mask(control) space was significantly higher in mTBI patients than controls is not sensitive to the method to generate ICA component masks.

We assessed whether graph analysis results were sensitive to the method to generate ICA component masks [Mask(control) or Mask(all)]. In the Mask(all) space, we found that AUC of the average path length of mTBI patients was still higher than that of controls. The mean AUCs were 1.74 (SD 0.077) and 1.79 (SD 0.087) for controls and mTBI patients, respectively. This pattern was consistent with that in the Mask(control) space. However, the difference was not significant (*p*-value > 0.05). In the Mask(all) space, the AUC of the global clustering coefficient of mTBI patients was not significantly different from that of controls. This was consistent with the finding in the Mask(control) space.

DISCUSSION

In this study, we examined whether correlations among three intrinsic networks (the default mode, salience, and central

executive) were altered in acute mTBI patients. Using component correlation analysis [in the Mask(control) space], we found a pattern of hyper-connectivity between the anterior part of the default mode network and the salience network in acute mTBI patients. This finding was stable across data resampling. For all resampling datasets, we consistently detected this hyper-connectivity pattern; this was a localized pattern. Using graph analysis [in the Mask(control) space] to investigate a graph including nodes in the default mode, salience, and central executive networks, we found a global graph pattern change that indicated altered information propagation ability among nodes; this was a distributed pattern. Together, our study indicated altered couplings among the default mode, salience, and central executive networks in acute mTBI patients.

Our finding of hyper-connectivity between the anterior part of the default mode network and the salience network is consistent with other functional connectivity studies of TBI. In a meta-study of moderate and severe TBI (Hillary et al., 2015), 12 of 14 TBI studies reported hyper-connectivity in different brain regions such as structures in the default mode and salience networks. Shumskaya et al. (2012) analyzed resting-state fMRI data of 35 acute mTBI and 35 age-, gender-, and handedness-matched controls and found a cluster of increased functional connectivity in the right frontoparietal attention network in the mTBI group. In a study to investigate whether thalamic intrinsic connectivity networks are disrupted in patients with mTBI (Tang et al., 2011), Tang et al. analyzed resting-state fMRI data of 24 mTBI patients with mean 22 days post-injury and 17 controls, and found significantly increased thalamic intrinsic connectivity networks in mTBI patients. Hyper-connectivity is also observed in other neurological disorders such as Alzheimer's disease, mild cognitive impairment, and multiple sclerosis (Hillary et al., 2015).

The mechanism underlying hyper-connectivity between the anterior part of the default mode network and the salience network could be a compensatory or maladaptive response (Pievani et al., 2014). In the compensatory theory, hyper-connectivity in acute mTBI is a mechanism to meet cognitive demand. A maladaptive response might reflect an unsuccessful attempt to recruit brain regions to compensate for pathology, as well as a disrupted excitatory-inhibitory balance of damaged networks. We found that the hyper-connectivity in mTBI patients was positively correlated with the DCCS score which measures executive function (**Figure 5**). This hyper-connectivity predicted better performance in an executive functioning task. This finding suggests that hyper-connectivity between the anterior part of the default mode network and the salience network could be compensatory to meet cognitive demand.

The triple network model centers on the default mode, salience, and central executive networks. The default mode network shows decreased activation in stimulus-driven cognitive and affective information processing tasks, while the salience and central executive networks show increased activation in such tasks. In the triple network model, the salience network is an integral hub in mediating dynamic couplings between the default mode and central executive networks. Inappropriate

assignment of saliency to external stimuli or internal mental events is observed in many psychiatric and neurological disorders (Uddin, 2014). In this study, we found the salience network was excessively coupled to the default mode network. This hyper-connectivity may be a response to brain injury to meet cognitive demand.

In our graph analysis, we found that the average path length of mTBI patients was significantly higher than that of healthy subjects. The average path length quantifies the ability for information to propagate. Short path lengths ensure inter-node effective integrity and promote the transfer of information among nodes (Sporns, 2011). Thus, the mTBI-related increase in the average path length represents a distributed and global degeneration of functional connectivity among nodes in the default mode, salience, and central executive networks.

In our ReHo analysis, we found no significant ReHo differences in mTBI patients in voxels in the default mode, salience, and central executive networks. Therefore, the observed hyper-connectivity between the default mode and salience network may not reflect the local functional connectivity changes in the three intrinsic networks.

In our study, no significant anatomical connectivity differences were detected in mTBI patients. Acute mTBI was not associated with DTI-based anatomical connectivity abnormalities detectable with TBSS or ROI-based analysis. This suggests that the observed hyper-connectivity between the default mode and salience network may not reflect the anatomical connectivity changes in acute mTBI patients. Our finding is in accordance with (Ilvesmaki et al., 2014) which analyzed DTI data from 75 patients with acute mTBI and 40 age- and gender- matched controls. Using TBSS, they found no significant differences in FA between mTBI patients and controls. However, TBSS has limitations in that it is a univariate analysis method and cannot model tract couplings. It is possible that the effect of injury on a specific white matter tract is weak. Therefore, TBSS will detect no FA differences between mTBI patients and controls. Using multivariate analysis, the couplings among white matter tracts may provide complementary information about white matter integrity.

Our study used resting-state fMRI and ICA to examine correlations among the default mode, salience, and central executive networks. A related study Jilka et al. (2014) analyzed fMRI data of the Stop Signal Task (SST) of 44 moderate/severe and 13 mTBI and 25 controls. Jilka and colleagues found that for controls, functional connectivity between the salience network and the default mode network transiently increased during stopping; and this change in functional connectivity was not observed in traumatic brain injury patients with impaired cognitive control. Their study revealed abnormal coupling between the salience and default mode networks in traumatic brain injury. The major differences between Jilka's study and our study are: (1) Jilka's study examined the functional connectivity using task-based fMRI while our study used resting-state fMRI; (2) the patient population of Jilka's study was primarily moderate/severe traumatic brain injury while our study focused on mTBI.

This study has several limitations. First, our study is cross-sectional. Investigating brain functional and structural changes in acute mTBI patients is important for predicting prognosis and treatment optimization. Brain connectivity damages in the acute period can result in deterioration of cognitive function that may persist for years. Predicting outcomes based on baseline imaging features is an important problem (Chen and Herskovits, 2015). Future work using a longitudinal design and predictive modeling can address this problem. Second, our study is hypothesis-driven and examines correlations among the default mode, salience, and central executive networks in acute mTBI patients. We cannot exclude the possibility that other network correlations are also changed in mTBI. For example, we didn't examine correlations among the visual and thalamus networks and other networks, despite the visual and thalamus networks showed aberrant ReHo patterns. With the increasing number of intrinsic connectivity networks, we need a large sample size in order to achieve a statistical power to reveal changes in their correlations. We plan to conduct a large-scale network correlation analysis with a large sample size mTBI dataset.

In conclusion, we identified aberrant functional coupling between the default mode and salience networks in acute mTBI patients. Our finding has great potential to improve our understanding of the network architecture of mTBI, leading to accurate diagnosis and more effective treatments.

REFERENCES

- Allen, E., Erhardt, E., Damaraju, E., Gruner, W., Segall, J. M., Silva, R. F., et al. (2011). A baseline for the multivariate comparison of resting-state networks. *Front. Syst. Neurosci.* 5:2. doi: 10.3389/fnsys.2011.00002
- American Congress of Rehabilitation Medicine (1993). Definition of mild traumatic brain injury. *J. Head Trauma Rehabil.* 8, 86–87. doi: 10.1097/00001199-199309000-00010
- Arenivas, A., Diaz-Arrastia, R., Spence, J., Cullum, C. M., Krishnan, K., Bosworth, C., et al. (2014). Three approaches to investigating functional compromise to the default mode network after traumatic axonal injury. *Brain Imaging Behav.* 8, 407–419. doi: 10.1007/s11682-012-9191-2
- Beckmann, C., Mackay, C. E., Filippini, N., and Smith, S. M. (2009). Group comparison of resting-state fMRI data using multi-subject ICA and dual regression. *Neuroimage* 47:S148. doi: 10.1016/S1053-8119(09)71511-3
- Beckmann, C. F., and Smith, S. M. (2004). Probabilistic independent component analysis for functional magnetic resonance imaging. *IEEE Trans. Med. Imaging* 23, 137–152. doi: 10.1109/TMI.2003.822821
- Bullmore, E. T., and Bassett, D. S. (2011). Brain graphs: graphical models of the human brain connectome. *Annu. Rev. Clin. Psychol.* 7, 113–140. doi: 10.1146/annurev-clinpsy-040510-143934
- Chen, R., and Herskovits, E. H. (2015). Predictive structural dynamic network analysis. *J. Neurosci. Methods* 245, 58–63. doi: 10.1016/j.jneumeth.2015.02.011
- Chen, R., Nixon, E., and Herskovits, E. (2016). Advanced connectivity analysis (ACA): a large scale functional connectivity data mining environment. *Neuroinformatics* 14, 191–199. doi: 10.1007/s12021-015-9290-5
- Cox, R. W. (1996). AFNI: software for analysis and visualization of functional magnetic resonance neuroimages. *Comput. Biomed. Res.* 29, 162–173. doi: 10.1006/cbmr.1996.0014
- Fox, M. D., and Greicius, M. (2010). Clinical applications of resting state functional connectivity. *Front. Syst. Neurosci.* 4:19. doi: 10.3389/fnsys.2010.00019
- Fox, M. D., and Raichle, M. E. (2007). Spontaneous fluctuations in brain activity observed with functional magnetic resonance imaging. *Nat. Rev. Neurosci.* 8, 700–711. doi: 10.1038/nrn2201
- Hillary, F. G., Roman, C. A., Venkatesan, U., Rajtmajer, S. M., Bajo, R., and Castellanos, N. D. (2015). Hyperconnectivity is a fundamental response to neurological disruption. *Neuropsychology* 29, 59–75. doi: 10.1037/neu000110
- Hyder, A., Wunderlich, C. A., Puvanachandra, P., Gururaj, G., and Kobusingye, O. C. (2007). The impact of traumatic brain injuries: a global perspective. *NeuroRehabilitation* 22, 341–353. doi: 10.3233/NRE-2007-22502
- Ilvesmaki, T., Luoto, T. M., Hakulinen, U., Brander, A., Ryymin, P., Eskola, H., et al. (2014). Acute mild traumatic brain injury is not associated with white matter change on diffusion tensor imaging. *Brain* 137, 1876–1882. doi: 10.1093/brain/awu095
- Iraji, A., Benson, R. R., Welch, R. D., O'Neil, B. J., Woodard, J. L., Ayaz, S. I., et al. (2015). Resting state functional connectivity in mild traumatic brain injury at the acute stage: independent component and seed-based analyses. *J. Neurotrauma* 32, 1031–1045. doi: 10.1089/neu.2014.3610
- Jenkinson, M., Beckmann, C. F., Behrens, T. E. J., Woolrich, M. W., and Smith, S. M. (2012). FSL. *Neuroimage* 62, 782–790. doi: 10.1016/j.neuroimage.2011.09.015
- Jilka, S. R., Scott, G., Ham, T., Pickering, A., Bonnelle, V., Braga, R. M., et al. (2014). Damage to the salience network and interactions with the default mode network. *J. Neurosci.* 34, 10798–10807. doi: 10.1523/JNEUROSCI.0518-14.2014
- Kelly, R. E., Alexopoulos, G. S., Wang, Z., Gunning, F. M., Murphy, C. F., Morimoto, S. S., et al. (2010). Visual inspection of independent components: defining a procedure for artifact removal from fMRI data. *J. Neurosci. Methods* 189, 233–245. doi: 10.1016/j.jneumeth.2010.03.028
- Kushner, D. (1998). Mild traumatic brain injury: toward understanding manifestations and treatment. *Arch. Intern. Med.* 158, 1617–1624. doi: 10.1001/archinte.158.15.1617

DATA AVAILABILITY STATEMENT

The datasets generated are available from the corresponding author on reasonable request.

ETHICS STATEMENT

The studies involving human participants were reviewed and approved by the Institutional Review Board of Shanghai East Hospital. The patients/participants provided their written informed consent to participate in this study.

AUTHOR CONTRIBUTIONS

ZW and RC: design and conduct of the study. ZW, RC, YL, XC, WW, MW, GH, and GZ: collection, management, analysis and interpretation of the data, and preparation, review, or approval of the manuscript. All authors: contributed to the article and approved the submitted version.

FUNDING

This work was supported by the National Natural Science Foundation of China (No. 81771899), Peak Academic Talent Program of Jiangsu Province Hospital of Chinese Medicine (y2018rc04), and Jiangsu Provincial Key Research and Development Program (No. BE2017772).

- Menon, V. (2011). Large-scale brain networks and psychopathology: a unifying triple network model. *Trends Cogn. Sci.* 15, 483–506. doi: 10.1016/j.tics.2011.08.003
- Palacios, E. M., Sala-Llonch, R., Junque, C., Roig, T., Tormos, J. M., Bargallo, N., et al. (2013). Resting-state functional magnetic resonance imaging activity and connectivity and cognitive outcome in traumatic brain injury. *JAMA Neurol.* 70, 845–851. doi: 10.1001/jamaneurol.2013.38
- Pandit, A. S., Expert, P., Lambiotte, R., Bonnelle, V., Leech, R., Turkheimer, F. E., et al. (2013). Traumatic brain injury impairs small-world topology. *Neurology* 80, 1826–1833. doi: 10.1212/WNL.0b013e3182929f38
- Pievani, M., Filippini, N., van den Heuvel, M. P., Cappa, S. F., and Frisoni, G. B. (2014). Brain connectivity in neurodegenerative diseases—from phenotype to proteinopathy. *Nat. Rev. Neurol.* 10, 620–633. doi: 10.1038/nrneurol.2014.178
- Power, J. D., Barnes, K. A., Snyder, A. Z., Schlaggar, B. L., and Petersen, S. E. (2012). Spurious but systematic correlations in functional connectivity MRI networks arise from subject motion. *Neuroimage* 59, 2142–2154. doi: 10.1016/j.neuroimage.2011.10.018
- Rubinov, M., and Sporns, O. (2010). Complex network measures of brain connectivity: uses and interpretations. *Neuroimage* 52, 1059–1069. doi: 10.1016/j.neuroimage.2009.10.003
- Rytty, R., Nikkinen, J., Paavola, L., Abou Elseoud, A., Moilanen, V., Visuri, A., et al. (2013). GroupICA dual regression analysis of resting state networks in a behavioral variant of frontotemporal dementia. *Front. Hum. Neurosci.* 7:461. doi: 10.3389/fnhum.2013.00461
- Sharp, D. J., Beckmann, C. F., Greenwood, R., Kinnunen, K. M., Bonnelle, V., De Boissezon, X., et al. (2011). Default mode network functional and structural connectivity after traumatic brain injury. *Brain* 134, 2233–2247. doi: 10.1093/brain/awr175
- Sharp, D. J., Scott, G., and Leech, R. (2014). Network dysfunction after traumatic brain injury. *Nat. Rev. Neurol.* 10, 156–166. doi: 10.1038/nrneurol.2014.15
- Shenton, M. E., Hamoda, H. M., Schneiderman, J. S., Bouix, S., Pasternak, O., Rathi, Y., et al. (2012). A review of magnetic resonance imaging and diffusion tensor imaging findings in mild traumatic brain injury. *Brain Imaging Behav.* 6, 137–192. doi: 10.1007/s11682-012-9156-5
- Shumskaya, E., Andriessen, T. M., Norris, D. G., and Vos, P. E. (2012). Abnormal whole-brain functional networks in homogeneous acute mild traumatic brain injury. *Neurology* 79, 175–182. doi: 10.1212/WNL.0b013e31825f04fb
- Sporns, O. (2011). *Networks of the Brain*. Cambridge, MA: The MIT Press.
- Tang, L., Ge, Y., Sodickson, D. K., Miles, L., Zhou, Y., Reaume, J., et al. (2011). Thalamic resting-state functional networks: disruption in patients with mild traumatic brain injury. *Radiology* 260, 831–840. doi: 10.1148/radiol.11110014
- Uddin, L. Q. (2014). Salience processing and insular cortical function and dysfunction. *Nat. Rev. Neurosci.* 16, 55–61. doi: 10.1038/nrn3857
- Whiting, D. L., Deane, F. P., Simpson, G. K., McLeod, H. J., and Ciarrochi, J. (2017). Cognitive and psychological flexibility after a traumatic brain injury and the implications for treatment in acceptance-based therapies: a conceptual review. *Neuropsychol. Rehabil.* 27, 263–299. doi: 10.1080/09602011.2015.1062115
- Zang, Y., Jiang, T., Lu, Y., He, Y., and Tian, L. (2004). Regional homogeneity approach to fMRI data analysis. *Neuroimage* 22, 394–400. doi: 10.1016/j.neuroimage.2003.12.030
- Zelazo, P. D. (2006). The Dimensional Change Card Sort (DCCS): a method of assessing executive function in children. *Nat. Protoc.* 1, 297–301. doi: 10.1038/nprot.2006.46
- Zhou, Y., Milham, M. P., Lui, Y. W., Miles, L., Reaume, J., Sodickson, D. K., et al. (2012). Default-mode network disruption in mild traumatic brain injury. *Radiology* 265, 882–892. doi: 10.1148/radiol.12120748

Conflict of Interest: The authors declare that the research was conducted in the absence of any commercial or financial relationships that could be construed as a potential conflict of interest.

Copyright © 2020 Liu, Wu, Chen, Wu, Hu, Zhou, Wang and Chen. This is an open-access article distributed under the terms of the Creative Commons Attribution License (CC BY). The use, distribution or reproduction in other forums is permitted, provided the original author(s) and the copyright owner(s) are credited and that the original publication in this journal is cited, in accordance with accepted academic practice. No use, distribution or reproduction is permitted which does not comply with these terms.



Disrupted Rich Club Organization of Hemispheric White Matter Networks in Bipolar Disorder

Dandan Li¹, Weichen Liu¹, Ting Yan², Xiaohong Cui¹, Zehua Zhang¹, Jing Wei¹, Yunxiao Ma¹, Nan Zhang¹, Jie Xiang¹ and Bin Wang^{1*}

¹ College of Information and Computer, Taiyuan University of Technology, Taiyuan, China, ² Translational Medicine Research Center, Shanxi Medical University, Taiyuan, China

OPEN ACCESS

Edited by:

Tianyi Yan,
Beijing Institute of Technology, China

Reviewed by:

Stavros I. Dimitriadis,
Cardiff University, United Kingdom

Peng Xu,
University of Electronic Science
and Technology of China, China

*Correspondence:

Bin Wang
wangbin01@tyut.edu.cn

Received: 18 May 2020

Accepted: 22 July 2020

Published: 26 August 2020

Citation:

Li D, Liu W, Yan T, Cui X, Zhang Z, Wei J, Ma Y, Zhang N, Xiang J and Wang B (2020) Disrupted Rich Club Organization of Hemispheric White Matter Networks in Bipolar Disorder. *Front. Neuroinform.* 14:39. doi: 10.3389/fninf.2020.00039

Neuroimaging studies suggest disrupted connections of the brain white matter (WM) network in bipolar disorder (BD). A group of highly interconnected high-density structures, termed the ‘rich club,’ represents an important network for brain functioning. Recent works have revealed abnormal rich club organization in brain networks in BD. However, little is known regarding changes in the rich club organization of the hemispheric WM network in BD. Forty-nine BD patients and fifty-five age- and sex-matched normal controls (NCs) underwent diffusion tensor imaging (DTI). Graph theory approaches were applied to quantify group-specific rich club organization and nodal degree of hemispheric WM networks. We demonstrated that rich club organization of hemispheric WM networks in BD was disrupted, with disrupted feeder and local connections among hub and peripheral regions located in the default mode network (DMN) and the control execution network (CEN). In addition, BD patients showed abnormal asymmetry in the feeder and local connections, involving the hub and peripheral regions associated with emotion regulation and visuospatial functions. Moreover, the clinical symptoms of BD showed a significant correlation with the aberrant asymmetry in the regional degree of peripheral regions. These findings reveal that BD is closely associated with disrupted feeder and local connections but no alteration in rich-club connections in the rich club organization of hemispheric WM networks and provide novel insight into the changes of brain functions in BD.

Keywords: bipolar disorder, white matter connections, graph theory approach, hemispheric lateralization, rich club organization

INTRODUCTION

Hemispheric lateralization refers to the asymmetry of the two brain hemispheres in terms of their anatomy and function (Toga and Thompson, 2003; Parker et al., 2005; Yasser et al., 2011). This feature is thought to have originated from evolutionary, developmental, experiential and pathological factors (Toga and Thompson, 2003) and is a prominent characteristic of human brain development. Abnormal hemispheric lateralization has long been proposed to be a consequence of altered neurodevelopment in individuals with psychotic disorders (Ho et al., 2017). Studies on white matter (WM) have shown that aberrant brain region asymmetries are highly correlated with disturbed functions such as executive function (Yin et al., 2013), emotion (Schwartz et al., 1975;

Schulte et al., 2012), and language (O'Donoghue et al., 2017). Moreover, neuroimaging studies (Torgerson et al., 2013) have indicated that the WM structure in the brain is fundamental and crucial to brain function. Therefore, analyzing WM lateralization abnormalities might benefit the understanding of the underlying nature of brain function abnormalities in patients with psychiatric disorders and potentially help to elucidate disorder etiologies.

As one of the most distinct syndromes in psychiatry, bipolar disorder (BD) is mainly characterized as episodic elevations in emotion and disturbances in cognition function (Quraishi and Frangou, 2002; Saunders and Goodwin, 2010), affecting approximately 1% of the population (Belmaker, 2004; Collin et al., 2016). Accumulated structural studies (Bruno et al., 2008; Vivian et al., 2009; Mahon et al., 2013) have revealed abnormal asymmetries in the WM volume in BD patients. Moreover, lower fractional anisotropy (FA) in the right anterior cingulate gyrus [ACG] (Liu et al., 2010) and the right precuneus [PCUN] (Elisa et al., 2016) regions were observed in BD patients compared with normal controls (NCs). Notably, the ACG region is involved in cognitive and emotional processing (Bush et al., 2000), and the PCUN plays a role in regulating the memory function (Cavanna and Trimble, 2006). These studies may suggest that abnormal WM lateralization is a key factor in the manifestation of BD symptoms (Torgerson et al., 2013).

Complex network analysis combines diffusion tensor imaging (DTI) to model the brain as two hemispheric WM networks and examine the differences in WM organization between the left and right hemisphere networks (Yasser et al., 2011). Using graph theory approaches, accumulated evidence has revealed hemispheric asymmetries in the graph metrics of the brain WM network (Karen and Alexander, 2014; Zhong et al., 2016). Moreover, previous studies (Silk et al., 2016; Yang et al., 2017; Zhong et al., 2016; Li et al., 2018) have hypothesized that abnormal brain network asymmetry is linked to neuropsychiatric disorders. Accordingly, our prior study (Wang B. et al., 2018) using graph theory showed reduced hemispheric asymmetry in the topological organization of the brain WM networks of BD patients, such as global efficiency and small-worldness, suggesting the disrupted asymmetry of WM connections in BD.

The rich club organization, defined as a tendency for hub (high-degree) regions to be more densely connected among themselves than to peripheral (low-degree) regions (Power et al., 2013; Van den Heuvel and Sporns, 2013), is one of the key graph theory metrics that provides important information on the higher-level topology of brain networks (Van den Heuvel and Sporns, 2011; Collin et al., 2013). Recent studies on whole-brain WM networks (Collin et al., 2016; O'Donoghue et al., 2017; Wang Y. et al., 2018) have reported that the putamen [PUT], PCUN and insula [INS] are defined as hub regions and the rolandic operculum [ROL], inferior temporal gyrus [ITG], superior occipital gyrus [SOG], and lingual gyrus [LING] regions are defined as peripheral regions in BD patients. Notably, decreased asymmetry in the nodal efficiency of the ROL, ITG, SOG and LING has been revealed in BD patients (Wang B. et al., 2018). These findings may imply that abnormal hemispheric asymmetry in the rich club organization in BD occurs mainly

through reduced WM connectivity in peripheral brain regions. However, it is unknown whether there are changes in the rich club organization of the hemispheric WM networks in BD patients.

This work used DTI data from 49 BD patients and 55 age- and sex-matched NCs to construct hemispheric WM networks. Graph theory approaches were used to analyze the network topology. Two connectivity measures (density and strength) and the nodal degree were used to assess the property of rich club organization. We aimed to investigate how the patterns of rich club organization change in hemispheric WM networks in BD patients. This study may serve a functional role in clinical trials and interventions for BD.

MATERIALS AND METHODS

Subjects

All the subjects participating in the current study, including 49 BD patients and 55 age- and sex-matched NCs, were screened from the LA2K study. The detailed demographic and clinical characteristics for all the subjects are presented in **Table 1**. The Handedness described the handedness of subjects. It was obtained using a formula $(\text{Right} + \text{Left})/(\text{Right} - \text{Left})$. Patient symptoms were evaluated using the 17-item Hamilton Depression Rating Scale (HAM-D) (Hamilton, 1960) and the Young Mania Rating Scale (YMRS) (Young et al., 1978). The neuroimaging dataset was obtained via the publicly available OpenfMRI database¹. This study was approved by Institutional Review Board of the University of California, Los Angeles (UCLA).

Data Preprocessing and Network Construction

Structural MRI data were obtained using 3T Siemens Trio scanners located at the Ahmanson-Lovelace Brain Mapping Center and the Staglin Center for Cognitive Neuroscience at UCLA. High-resolution 3D echoplanar imaging was acquired with the following parameters: repetition time (TR) = 1.9 s, echo time (TE) = 2.26 ms, flip angle = 90°, field of view (FOV) = 250 × 250 mm², acquisition matrix = 256 × 256, sagittal plane, slice thickness = 1 mm, and 176 slices. Diffusion weighted imaging (DWI) data were collected using an echoplanar sequence with the following parameters: 64 directions, slice thickness = 2 mm, TR = 9 s, TE = 93 ms, 1 average, acquisition matrix = 96 × 96, flip angle = 90°, axial slices, and b = 1000 s/mm².

Data preprocessing and network construction were performed using the MATLAB toolbox named pipeline for analyzing brain diffusion images (PANDA_1.3.1, <http://www.nitrc.org/projects/panda>). The data preprocessing procedure includes corrections for simple head movements and eddy current distortions. The FA of each voxel was computed, with higher values indicating more directionally restricted diffusion of water molecules. Briefly, individual T1-weighted images were coregistered to the b0 images in the DTI space. The transformed T1 images were segmented into WM and then non-linearly transformed to the

¹<https://www.openfmri.org/>

TABLE 1 | Demographic and clinical characteristics of the samples.

Demographic characteristics	NC	BD	Statistics	
	<i>n</i> = 55	<i>n</i> = 49		
Age (years)	21–49 (33.7 ± 9.1)	22–50 (33.9 ± 9.0)	F = 0.209 ^a	<i>p</i> = 0.649
Male/Female	27/28	28/21	F = 0.674 ^b	<i>p</i> = 0.412
Duration of illness (months)	N/A	0–24 (2.1 ± 5.2)		
Medication dose (mg/day)	N/A	0–6210 (784.8 ± 1035.3)		
Handscore	0.80–1 (0.95 ± 0.09)	0.75–1 (0.93 ± 0.1)	F = 0.926 ^a	<i>p</i> = 0.338
YMRS	N/A	0–41 (11.9 ± 11.0)		
HAMD	N/A	0–32 (12.0 ± 8.4)		

^aStatistical comparison was performed using analysis of variance; ^bStatistical comparison was performed using a chi-square test.

International Consortium of Brain Mapping (ICBM) 152 T1 template in the Montreal Neurological Institute (MNI) space. The inverse transformations were used to warp the automated anatomical labeling (AAL) atlas from the MNI space to the DTI native space. Finally, for each individual DTI dataset, deterministic fiber tracking algorithms were used to reconstruct the WM pathways. In the brain mask, 7 seeds followed the main diffusion direction from voxel to voxel. The tractography was terminated when it reached a voxel with an FA value less than 0.1 or when the angle was greater than 35°. Based on the reconstructed fiber tracts, the WM connection between a pair of nodes was adopted if the fiber number (FN) was larger than 3 (Shu et al., 2011; Li et al., 2018; Wang et al., 2019). We selected the threshold value for the FN > 3 was to reduce pseudo-connections due to possible noise effects on the whole-brain WM tractography (Sun et al., 2015).

The whole-brain WM network was constructed for each subject based on AAL (Tzourio-Mazoyer et al., 2002) atlas. We normalized the AAL atlas to eliminate the hemispheric asymmetry effect of brain structure according to the methods proposed by Yan et al. (2009). Using the normalized AAL atlas, the whole-brain was divided into 90 regions (45 regions in each hemisphere). The node of structural network was defined as one region of the normalized AAL atlas. The weights of the structural network was defined the mean FA values of the connected fibers between 2 regions (Li et al., 2018; Yan et al., 2018; Wang et al., 2019). The reason for choosing FA is that it is an important indicator commonly used to examine the microstructure aspects of brain WM connections (Cui et al., 2013). Finally, a weighted 90 × 90 whole-brain anatomical network was constructed for each subject.

Graph Theory Analysis of the Hemispheric Network

Based on the weighted 90 × 90 whole-brain WM network, we discarded inter-hemispheric WM connections and separated the whole-brain network into two 45 × 45 hemispheric networks for each subject. The graph metrics including the rich club organization and nodal degree were computed to evaluate the topological structure of all hemispheric WM networks. The nodal degree measures the number of edges connected to the node.

This work used the GREYNA toolbox² (Wang et al., 2015) in MATLAB to analyze the network topology. The results of the network analyses were visualized using the BrainNet Viewer toolbox³ (Xia et al., 2013).

Description and Measurement of Rich Club Organization

Rich club organization describes the central backbone for global communication in the brain network (Van den Heuvel and Sporns, 2011, 2013), which refers to nodes with higher degrees within brain networks (Van den Heuvel and Sporns, 2011). The rich club organization was described based on the normalized rich club coefficients (RCs). The normalized RC was greater than 1 over a range of degrees, indicating the existence of a rich club organization in the brain connectome. The RC is computed as the sum of the weights of the subset of connections larger than *k* in the network divided by the sum of the set of the strongest connections in the total network. The normalized RC was computed by normalizing the RC relative to a set of 1000 comparable random networks for each subject. In order to preserve the same number of row and column as a real weighted structural network, this paper used the Maslovs wiring algorithm (Maslov and Sneppen, 2002) to generate a random network. In addition, the strength and the degree distribution of structural network was preserved in the random network.

The current study selected hub regions based on the group-average FA network. The top 7 high-degree regions corresponding to the highest-ranking 16% of nodes were identified as hub nodes for each individual subject. The remaining 38 regions were identified as peripheral nodes. Once the nodes were classified into hub nodes and peripheral nodes, the edges of the network were classified as rich-club connections between two hub nodes, feeder connections from one hub node to one peripheral node, or local connections between two peripheral nodes (Van den Heuvel and Sporns, 2011; Van den Heuvel et al., 2012). Notably, the present study used two connectivity measures, the connectivity density and connectivity strength, to distinguish three types of connections in the rich club organization of hemispheric WM networks. The connectivity density describes the proportion of connections out

²<http://www.nitrc.org/projects/gretna/>

³<http://www.nitrc.org/projects/bnv>

of the total number of possible edges in the hemispheric WM network. The connectivity strength is calculated as the total sum of the weighted FA values of all the connections in the hemispheric WM network.

Hemispheric Asymmetry in the Graph Metrics

This paper applied the formula $AS(X) = 100 \times [X(R) - X(L)] / [X(R) + X(L)]$ (Yasser et al., 2011; Wang et al., 2019) to estimate the hemispheric asymmetry of the network topology graph metrics, where $X(R)$ and $X(L)$ refer to the graph metric for the right and left hemispheric networks, respectively. A negative $AS(X)$ value indicates leftward asymmetry in the graph metric of X , while a positive $AS(X)$ value demonstrates a rightward advantage in the graph metric of X .

Statistical Analysis

All statistical analyses were performed using the Statistical Package for Social Science (SPSS, v19.0)⁴. For the group differences in the demographic characteristics, two-sample two-tailed t -tests were used for age and the hand score of subjects, and chi-square tests were used for sex. For both hemisphere and group differences in the graph metrics, repeated-measures analysis of variance (ANOVA) was employed with group as a between-subject factor and hemisphere (left and right) as the repeated-measures factor. Moreover, the hemisphere-by-group interaction was also considered. When the value of $p < 0.05$ (no correction for connectivity measures and Bonferroni-correction for nodal degree), the effect was statistically significant and *post hoc* tests (paired t -tests for hemisphere differences and independent t -tests for group differences) were performed. In this paper, the symbol * indicates the value of p is smaller than 0.05. The symbol ** indicates the value of p is smaller than 0.01. The symbol *** indicates the value of p is smaller than 0.001.

This work also examined the correlation between the graph metrics and the symptom severity of BD patients by calculating Spearman correlation coefficient. Relationships were considered significant for uncorrected values of $p < 0.05$ because these correlations were exploratory in nature. For all statistical analyses, age, sex and hand score were treated as covariates.

RESULTS

Rich Club Organization

We examined the hemisphere and group effects on the RCs and the normalized RCs, as shown in **Figure 1**. The **Figure 1** described the mean degree of per group after running RC procedure per subject. Notably, we reported the degree levels only for the two groups in which the rich club effects were detected across all subjects. As shown in **Figure 1A**, the values of the RC in the right hemisphere are significantly larger than those in the left hemisphere at the degree $k = 5-6$. The values of the RC in the NC group were higher than those in the BD group at degrees $k = 4-5$, as shown in **Figure 1B**. The normalized RCs increased with increasing nodal degrees k greater than 1

(**Figures 1C,D**), indicating that the rich-club organization existed in the hemispheric networks of both the NC and BD groups. Specially, we observed a specific k degree of 4 where normalized RC begin to be larger than 1. At degrees $k = 5-8$, significant group differences were observed in the normalized RCs as described in **Figure 1D**. However, we did not find any significant hemisphere differences in the normalized RCs, as presented in **Figure 1C**.

In this work, 16% of most consistently ranked nodes corresponding to the top 7 regions were defined as hub nodes across the two groups of subjects. In order of nodal degree, the seven regions were as follows: PUT, INS, PCUN, postcentral gyrus [PoCG], precentral gyrus [PreCG], temporal pole (superior) [TPOsup], middle occipital gyrus [MOG], illustrated in **Figure 2A**. The remaining 38 regions were classified as peripheral nodes. Based on the classification of the network nodes, the network edges were classified into three types of connections: rich-club connections linking two hub nodes, feeder connections linking hub and peripheral nodes, and local connections linking two peripheral nodes (**Figure 2B**).

Group and Hemisphere Effects on Rich Club Organization

Three Classifications of Connections

For connections in rich club organization, significant group and hemisphere effects on the connectivity density and strength are depicted in **Table 2** and **Figure 3**. As shown in **Table 2**, we found no significant group and hemisphere difference in the rich-club connections. Further analysis (**Figure 3**) showed smaller values for the connectivity measures in the BD patients than in the NCs, indicating disrupted feeder and local connections in BD. **Table 2** shows that feeder and local connections exhibited significant hemisphere-by-group interactions. The *post hoc* analysis revealed that the hemisphere-by-group interaction resulted from different patterns of hemispheric asymmetry in the feeder and local connections in the two groups of subjects. **Figures 3C,D** shows that BD patients exhibited a significant left hemisphere advantage in the two connectivity measures of feeder connections. However, the NC group exhibited significant rightward asymmetry in both the connectivity density and strength of local connections, as shown in **Figures 3E,F**.

The statistical analysis results of the asymmetry scores in the two connectivity measures of the rich club organization in the two groups are shown in **Table 3**. For the NCs, only the local connections exhibited a significant right hemisphere advantage (positive AS , $p < 0.001$) in the connectivity density and strength. For the BD patients, the rich-club connections and feeder connections showed significant a left hemisphere advantage in the connectivity density and strength. In addition, the feeder and local connections showed evident group differences in the asymmetry scores of the connectivity density and strength. This group-difference finding is in accordance with the significant group-by-hemisphere interaction observed in the connections of the rich club organization.

To examine whether connections is distributed among three classification of connections in the BD group compared to the NC group, and the left hemisphere compared to right hemisphere, an

⁴<http://www.spss.com/>

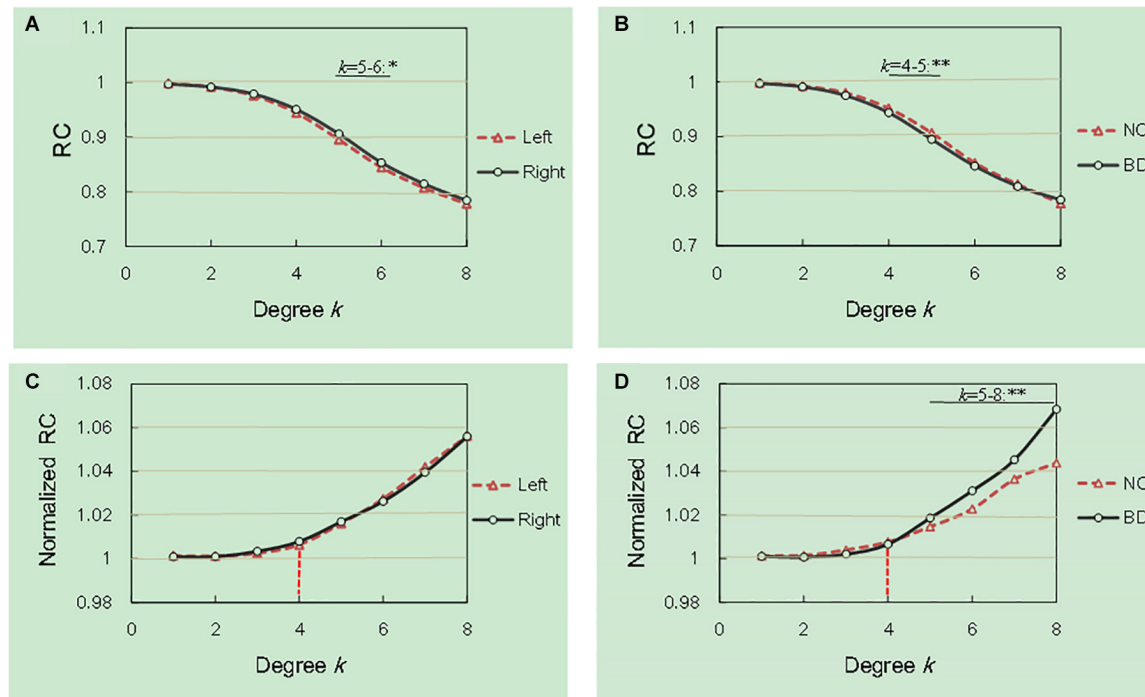


FIGURE 1 | Hemisphere and group differences in both the RCs and normalized RCs. **(A,B)** depicted significant hemisphere and group differences in RC, respectively. **(C,D)** depicted significant hemisphere and group differences in normalized RC, respectively. * $p < 0.05$; ** $p < 0.01$; *** $p < 0.001$.

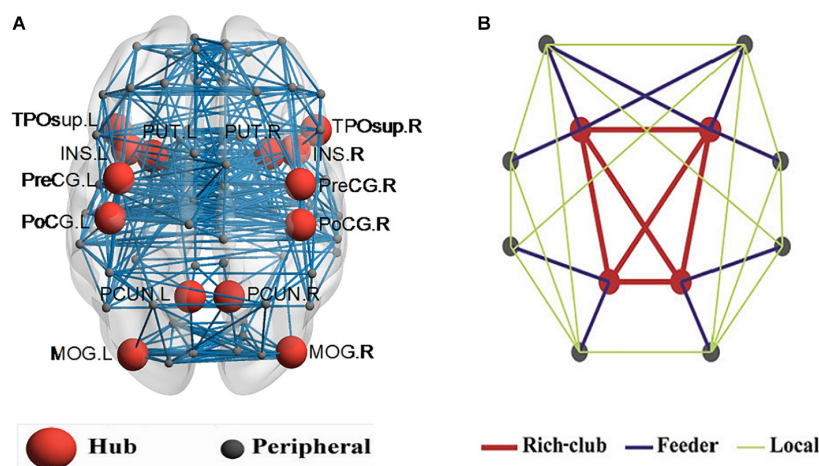


FIGURE 2 | Hub nodes and the three types of connections in the rich club organization. **(A)** depicted hub nodes (red nodes) across all NC and BD groups. **(B)** depicted a simplified example of the three types of connections.

additional analysis was performed. Abnormal WM connectivity was observed in the BD group relative to the NC group, with 161 connections (5 rich-club, 33 feeder, and 123 local connections; **Figure 4A**). Significant differences between the left and right hemisphere were observed in 58 connections (3 rich-club, 11 feeder, and 44 local connections; **Figure 4B**). A significant group difference between NC and BD group was observed in the hemispheric asymmetry of WM connectivity, with 32 connections (2 rich-club, 7 feeder, and 23 local connections;

Figure 4C). The proportion ($100\% \times \text{observed/total}$) of each classification of aberrant WM connections was illustrated in **Figure 4D**. These findings tend to suggest that the rich-club connections might be stable.

Nodal Degree of the Hub and Peripheral Regions

Figure 5 shows significant (Bonferroni-corrected, $p < 0.05$) group and hemisphere differences in the regional degree. Specifically, several regions including the PCUN hub region

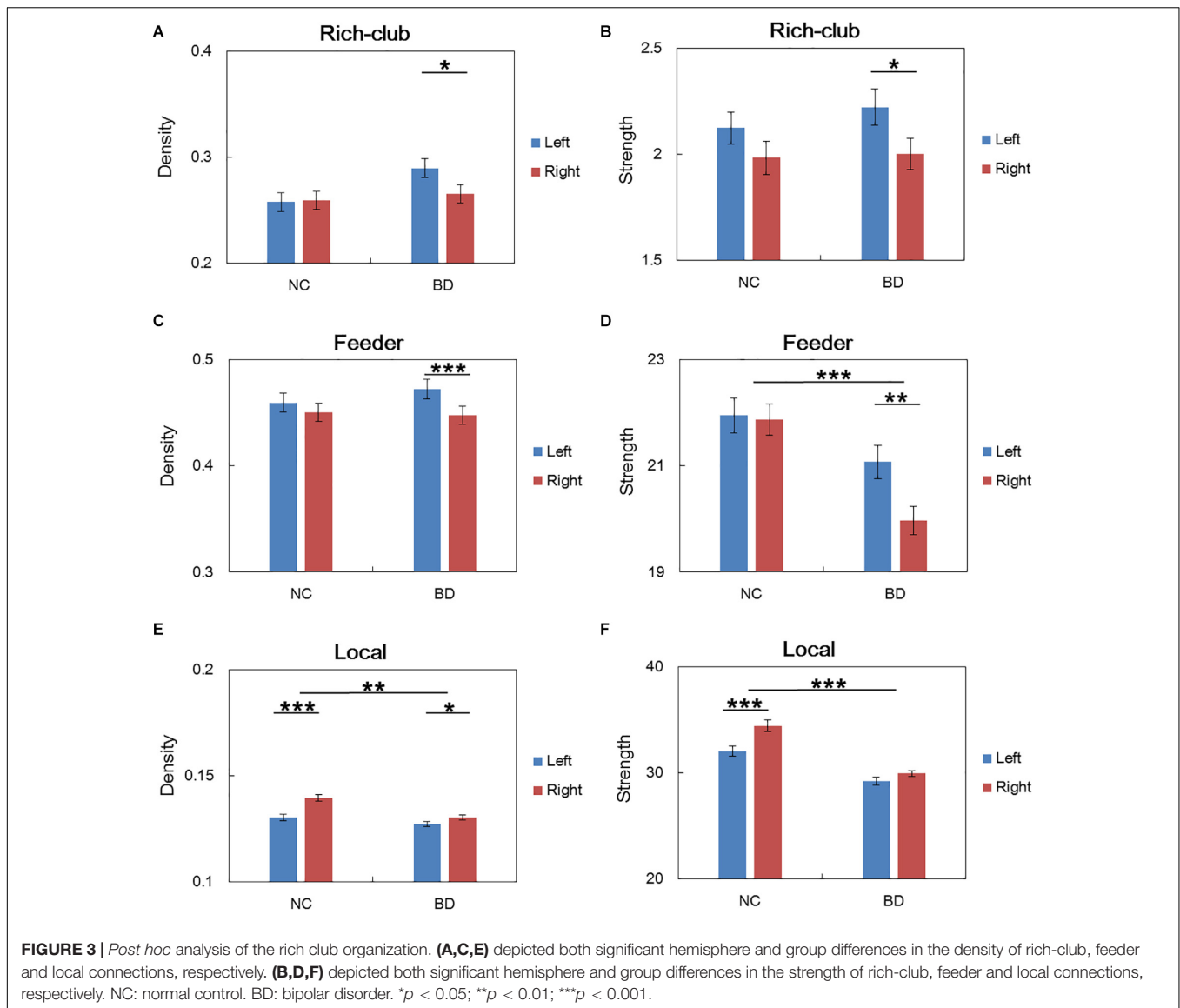


TABLE 2 | Differences in the connectivity measures of the rich club organization.

Connectivity measure	Rich club organization	Group difference $F_{1,99}$ (p -value)	Hemisphere difference $F_{1,99}$ (p -value)	Interaction $F_{1,99}$ (p -value)
Density	Rich-club	3.499 (0.064)	0.016 (0.901)	2.173 (0.144)
	Feeder	0.456 (0.501)	8.268 (0.005)	4.328 (0.040)
	Local	11.651 (0.001)	8.931 (0.004)	11.192 (0.001)
Strength	Rich-club	0.268 (0.606)	0.218 (0.642)	0.044 (0.835)
	Feeder	17.758 (< 0.001)	4.122 (0.045)	5.765 (0.018)
	Local	47.759 (< 0.001)	5.138 (0.026)	9.660 (0.002)

Significant differences ($p < 0.05$) were indicated by the bold text.

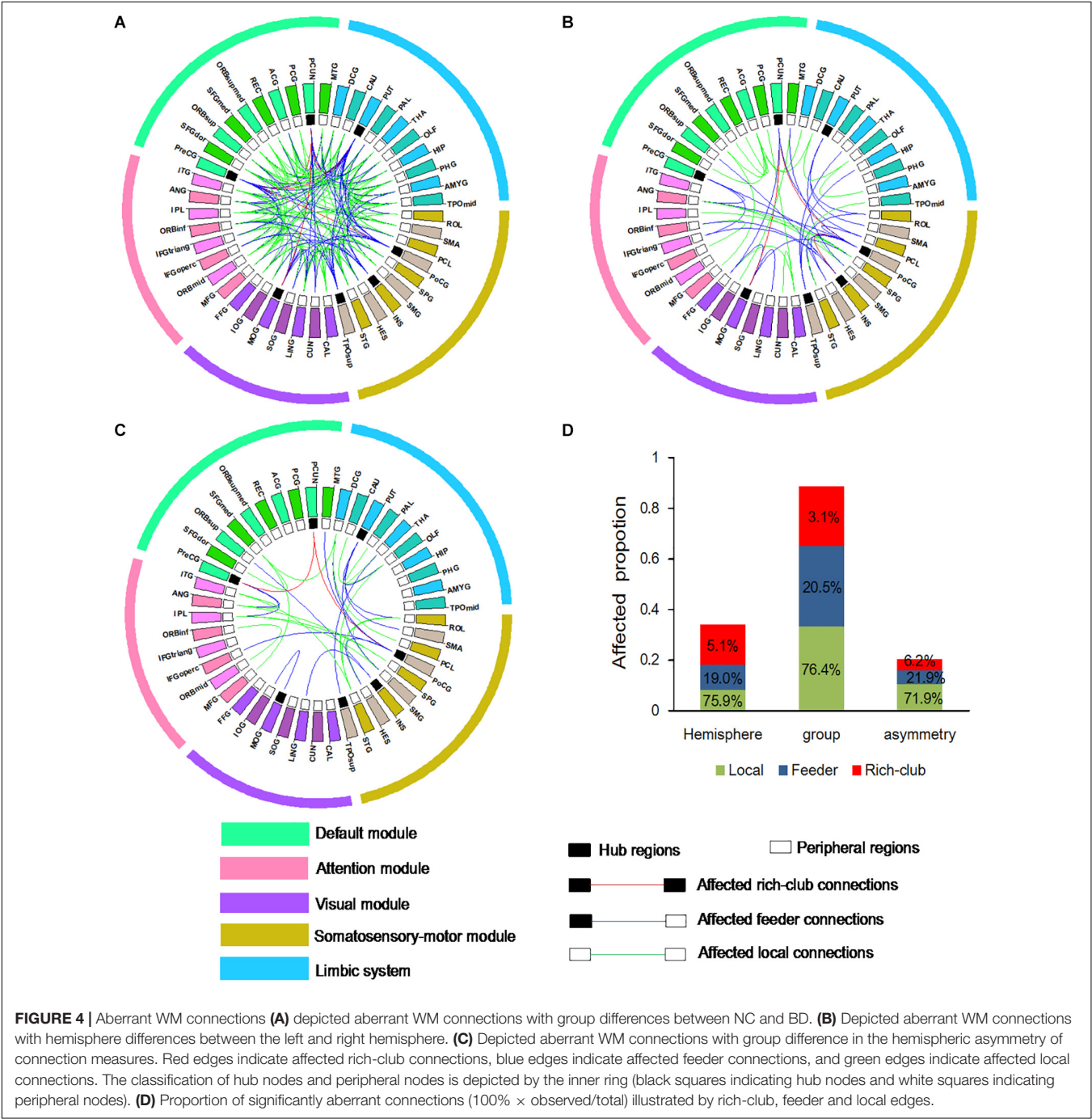
showed significant group differences in nodal degree, shown in **Figure 5A**. **Figure 5B** illustrated that eight regions including the MOG hub region exhibited prominent hemisphere differences in the nodal degree. Among these regions, the ACG, middle cingulate and paracingulate gyri [DCG], posterior cingulate gyrus

[PCG], MOG and inferior parietal lobule [IPL] showed evident left-greater-than-right asymmetries in the nodal degree, whereas the ROL, the supramarginal gyrus [SMG] and the angular gyrus [ANG] exhibited more advantageous nodal degrees in the right hemisphere than the left hemisphere. **Figure 5C** showed

TABLE 3 | Analysis of the asymmetry scores for the connectivity measures.

Connectivity measure	Rich club organization	NC group t_{54} (p -value)	BD Patients t_{48} (p -value)	BD versus NC $t_{1,102}$ (p -value)
Density	Rich-club	0.068 (0.946)	-2.687 (0.010)	1.710 (0.090)
	Feeder	-1.382 (0.173)	-4.096 (<0.001)	2.114 (0.037)
	Local	8.363 (<0.001)	2.064 (0.044)	2.972 (0.004)
Strength	Rich-club	-1.849 (0.070)	-2.638 (0.011)	0.101 (0.752)
	Feeder	0.019 (0.985)	-3.283 (0.002)	5.782 (0.018)
	Local	6.837 (<0.001)	1.695 (0.097)	7.220 (0.008)

Significant differences ($p < 0.05$) were indicated by the bold text.



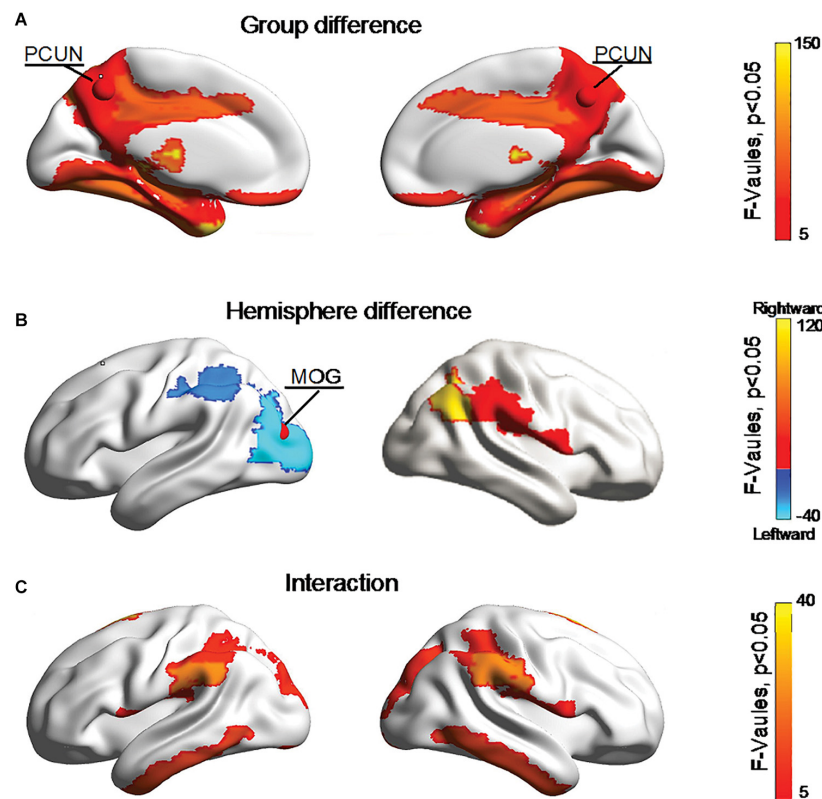


FIGURE 5 | Bonferroni-corrected group and hemisphere differences in the nodal degrees of the hub regions (red nodes) and peripheral regions. **(A)** Depicted regions with significant group differences in nodal degree. **(B)** Depicted regions with significant hemisphere differences in nodal degree. **(C)** Depicted regions with significant group-by-hemisphere interactions in nodal degree.

significant group-by-hemisphere interactions in nodal degree of eight peripheral regions. The *post hoc* analysis indicated that these interaction effects resulted from significant group differences in the asymmetry score of regional degree between the two groups, as shown in **Figure 6**.

Correlation With Symptoms of BD

This work investigated the relationship between the asymmetry score of abnormal nodal degrees of peripheral regions and the clinical symptoms of BD patients. Significant correlations are depicted in **Figure 7**. The ROL and SMG regions exhibited a positive relationship between the asymmetry score of the nodal degree and the YMRS score. Evident negative correlation was revealed between the asymmetry score of the LING regional degree and the HAMD score.

DISCUSSION

This work employed graph theory approaches to analyze abnormalities in the rich club organization of hemispheric WM brain networks in BD. Disrupted feeder and local connections were revealed in BD patients compared to NCs, which resulted in significantly leftward asymmetry in the feeder connections and decreased rightward asymmetry in the local connections in

BD patients. Moreover, we found that the asymmetry scores of the abnormal nodal degrees were significantly correlated with the symptoms of BD.

Rich Club Organization

The normalized RCs of the hemispheric WM networks increased and were greater than 1 over a range of degrees for the two groups of subjects, reflecting the existence of a rich club organization in the hemispheric WM networks (Yan et al., 2018; Wang et al., 2019). Moreover, the current work revealed a group of seven strongly interconnected hemispheric hub nodes comprising the PUT, INS, PCUN, PoCG, PreCG, TPOsup, and MOG regions for the two groups, largely consistent with previous studies on whole-brain networks (Collin et al., 2016; O'Donoghue et al., 2017; Wang Y. et al., 2018). Our findings suggested that the rich club organization existed in not only the whole-brain networks but also the hemispheric-brain networks (Wang et al., 2019).

Disrupted Connections in the Rich Club Organization in BD

Disruption of the Feeder and Local Connections

This work defined the FA as the weight of the network edge. We showed that feeder connections exhibited significantly reduced the connectivity strength but not the density in BD patients,

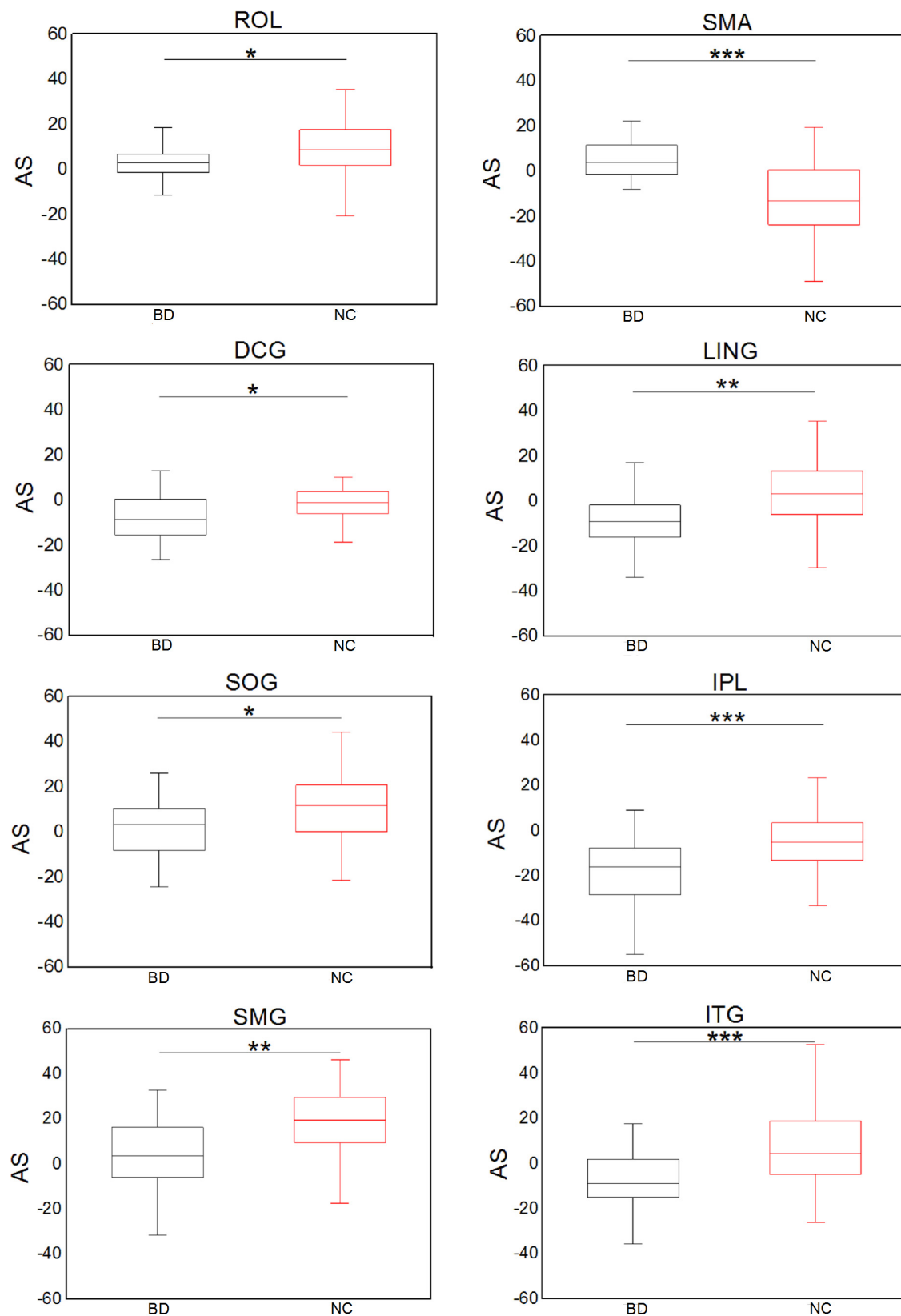


FIGURE 6 | Significant group differences in the asymmetry score of the nodal degree. * $p < 0.05$; ** $p < 0.01$; *** $p < 0.001$ (Bonferroni-corrected).

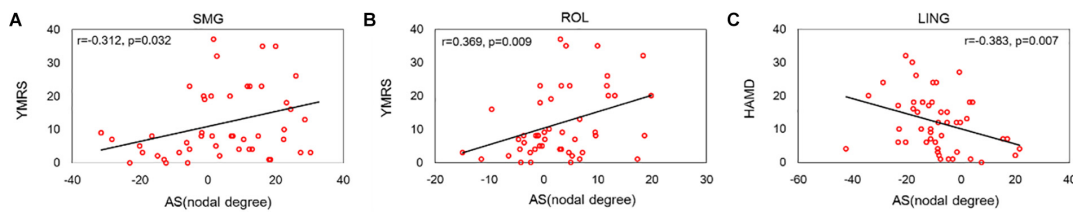


FIGURE 7 | Significant correlations between the asymmetry score of the nodal degree and the symptoms of BD patients. **(A)** Depicted a positive relationship between the nodal degree of SMG region and the score of YMRS symptom. **(B)** Depicted a positive relationship between the nodal degree of ROL region and the score of YMRS symptom. **(C)** Depicted a negative relationship between the nodal degree of LING region and the score of HAMD symptom.

suggesting significantly decreased FA in BD patients compared with the NC group. Our finding is consistent with previous work (Collin et al., 2016; Collin et al., 2017), showing no disruptions in the rich-club connections. Moreover, previous DTI studies (Serene et al., 2010; Collin et al., 2016) on BD have reported FA reductions in the brain WM related to the NC group, suggesting our results are reasonable. The FA value expresses the coherence of the organization of fibers within a voxel and provides an index of the structural integrity of WM (Keller et al., 2007; Pierpaoli and Basser, 1996). Hence, disrupted feeder connections may provide evidence of decreased WM integrity in BD patients. Prior studies (Sussmann et al., 2009; Benedetti et al., 2011) have revealed disruptions of the WM integrity is a possible structural marker of BD.

In addition, BD patients showed significantly decreased connectivity density of local connections compared with the NC group, reflecting disrupted WM connections. As one of the graph indexes, the clustering coefficient measures the existing number of connections between the node and its nearest neighbors out of all possible connections (Bullmore and Sporns, 2009). Previous studies on structural networks have reported disrupted, lower clustering coefficients (Leow et al., 2013; O'Donoghue et al., 2017) in BD patients than NCs, suggesting disrupted WM connections. Moreover, this work revealed decreased connectivity strength of local connections in BD patients, reflecting reduced WM integrity. The network efficiency measures the integration ability of connections in brain networks (Yasser et al., 2011). Lower values of the network efficiency were observed in the WM networks of BD patients (Wang Y. et al., 2018), demonstrating reduced WM integrity. In summary, this study divided all the WM connections into three classifications and found significant disruption in both the feeder and local connections in BD patients. Our findings reflect that disruptions of feeder and local connections may result in abnormal WM connectivity in BD patients.

Disconnections in Hub and Peripheral Regions

We found that the hub region PCUN and several peripheral regions showed decreased nodal degrees in BD patients, suggesting that disconnections linked these regions. Functional (Strakowski et al., 2000) and structural (O'Donoghue et al., 2015) studies have revealed disconnections in the PCUN region. Moreover, previous WM studies (Cui et al., 2011; Martinot et al., 2014) have revealed a significant reduction in the FA in the PCUN region in BD patients. Notably, the PCUN region

has an important role in the default mode network (DMN), which involved neurocognitive functions such as memory and attention (Delano-Wood et al., 2012). Combined with reduced nodal degree in the PCUN in BD, our findings may suggest that cognitive deficits may be more representative of BD (Maalouf et al., 2010).

This work revealed significant decrease in nodal degrees of several peripheral regions in BD patients. We observed that these abnormal regions (the ANG, middle temporal gyrus [MTG], inferior frontal gyrus (orbital part) [ORBinf], middle frontal gyrus (orbital part) [ORBmid], PCG, parahippocampal gyrus [PHG], rectus gyrus [REC], and middle temporal gyrus [TPOMid]) were predominantly located in the DMN. Consistently, studies (Forde et al., 2015; Wang et al., 2017) have reported aberrant connections in the DMN of BD patients. The DMN is believed to be involved in affective regulation (Kaiser et al., 2015). Aberrant connections in the DMN indicated impaired affective regulation function. Other abnormal regions, including inferior frontal gyrus (triangular) [IFGtriang], IPL, ITG and superior parietal gyrus [SPG] regions, are mainly located in control execution network (CEN). The CEN is responsible for high-level cognitive functions, such as attention and working memory (Menon, 2011). Our findings may reflect disrupted cognitive function in BD patients. Impairments in the function of the DMN and CEN in BD were revealed in previous structural (Wang Y. et al., 2018) and functional (Goya-Maldonado et al., 2016; Wang et al., 2016) studies. Hence, decreased nodal degrees of peripheral regions in the DMN and CEN may contribute to core deficits in cognitive and affective functioning in BD patients.

Abnormal Asymmetry of Feeder and Local Connections in BD

This work revealed significant group differences in the hemispheric asymmetry of the feeder and local connections. We observed that feeder connections showed evident leftward asymmetry in the two connectivity measures in BD patients but disappeared in the NCs, as shown in **Figure 3**. Consistently, our previous work (Wang et al., 2019) on NCs did not find hemispheric asymmetry in connectivity measures of feeder connections. Significantly decreased rightward asymmetry in the two connectivity measures of local connections was found in BD patients compared with NC, suggesting evident disruption of WM connections of the right hemisphere. The predominantly right hemispheric disconnections in BD patients were consistent with the abnormal right lateralization of WM in BD patients

(Vederine et al., 2011; Ho et al., 2017). It has been suggested that the right hemisphere is preferentially involved in emotions (Schwartz et al., 1975; Wheeler et al., 1993), visuospatial abilities (Cullen et al., 2016) and that disturbances of the right hemisphere underlie emotion dysregulation and visuospatial processing deficits (Caligiuri et al., 2004).

In addition, we found that several peripheral regions, including the IPL, ROL, LING, SOG, SMG and ITG, showed evident group differences in the asymmetry score of the nodal degree. Both feeder and local connections are linked to peripheral regions. Hence, asymmetry differences in these peripheral regions might contribute to abnormal hemispheric asymmetry in the feeder and local connections. Specifically, we found that the IPL, ITG and DCG regions showed evident leftward asymmetry of the nodal degree in BD patients. Accordingly, prior research (Liu et al., 2012) has shown left asymmetry in the regional homogeneity in the IPL region in BD. Structural researches (Hallahan et al., 2011; Lisy et al., 2011) have revealed left asymmetry of gray matter in the ITG region of BD patients. Functional research (Wang et al.) has showed increased functional connectivity in the left cingulate cortex and left temporal gyrus. These studies may provide support for our above-mentioned findings of leftward asymmetry in regional degree. Moreover, this work revealed that BD patients showed decreased rightward asymmetry in the nodal degree of the ROL, SOG, and SMG, suggesting that these regional degrees in the right hemisphere were disrupted. Notably, it has been demonstrated that the right ROL and SMG regions are involved in emotional regulation (Silani et al., 2013). A reduction in the nodal degree of these two regions may reflect impaired emotional regulation in BD. It was proven that alteration of emotional regulation is one of significant symptoms in BD patients (Pavuluri et al., 2006), demonstrating that our findings are reasonable. The SOG is associated with visuospatial processing (Green, 2006; Bearden et al., 2015). The reduced rightward asymmetry of the nodal degree in these regions might be associated with deficits in emotional and visuospatial functions (Bearden et al., 2015).

Clinical Correlation

We found that the asymmetry score of the ROL and SMG regional degree showed a positive relationship with the YMRS symptom score. Consistent with our findings, Gao et al. (2017) found that connectivity in the right ROL was positively associated with BD features. One research (Jie et al., 2015) reported that connections linking the ROL and SMG regions correlated with the BD feature. The LING region showed a negative relationship with the HAMD score of HAMD, suggesting that the number of LING-based connections decreases with increasing HAMD score. A previous research (Lv et al., 2016) revealed that the decreased connectivity strength linked to the right LING region showed a significant positive correlation with the scores on the HAMD. These studies show that our findings are reasonable and correct. Specially, these three regions are defined as peripheral regions in this work. Hence, our correlation results may provide support for our findings of no disruption in rich-club connections and abnormal hemispheric asymmetries as a marker of BD.

CONCLUSION

This work examined changes in the rich club organization of the hemispheric WM networks in BD. We revealed no disruption in the rich-club connections but significantly disrupted feeder and local connections in BD patients. Moreover, these abnormal connections involving regions in DMN and CEN supported impaired attention, working memory and affective functioning in BD patients. In addition, aberrant asymmetry in the feeder and local connections was found in BD patients, which might be related to emotional regulation and visuospatial functions. The correlation results showed that the abnormal asymmetry of peripheral regional degree was related to clinical symptoms in BD patients. These findings highlight the potential for stable rich-club connections but not feeder and local connections in the rich club organization of hemispheric WM networks in BD patients. This work provides another perspective for understanding the pathological mechanisms of BD.

DATA AVAILABILITY STATEMENT

Publicly available datasets were analyzed in this study. This data can be found here: <https://www.openfmri.org/>.

ETHICS STATEMENT

The studies involving human participants were reviewed and approved by Institutional Review Board of the University of California, Los Angeles (UCLA). The patients/participants provided their written informed consent to participate in this study. Written informed consent was obtained from the individual(s) for the publication of any potentially identifiable images or data included in this article.

AUTHOR CONTRIBUTIONS

DL completed the entire study of the experiment and writing. WL, JW, YM, and NZ revised the manuscript. TY, XC, ZZ, and JX provided advice and guidance. BW provided the research ideas. ZZ completed the interpretation data, revision of the manuscript and provided critical suggestions for our manuscript proof. All authors contributed to the article and approved the submitted version.

FUNDING

This work was supported by the National Natural Science Foundation of China (61906130 and 61503273).

SUPPLEMENTARY MATERIAL

The Supplementary Material for this article can be found online at: <https://www.frontiersin.org/articles/10.3389/fninf.2020.00039/full#supplementary-material>

REFERENCES

- Bearden, C. E., Hoffman, K. M., and Cannon, T. D. (2015). The neuropsychology and neuroanatomy of bipolar affective disorder : a critical review. *Bipolar Disord.* 3, 106–150. doi: 10.1034/j.1399-5618.2001.030302.x
- Belmaker, R. H. (2004). Bipolar disorder. *N. Engl. J. Med.* 351, 476–486.
- Benedetti, F., Yeh, P. H., Bellani, M., Radaelli, D., Nicoletti, M. A., Poletti, S., et al. (2011). Disruption of white matter integrity in bipolar depression as a possible structural marker of illness. *Biol. Psychiatry* 69, 309–317. doi: 10.1016/j.biopsych.2010.07.028
- Bruno, S., Cercignani, M., and Ron, M. A. (2008). White matter abnormalities in bipolar disorder: a voxel-based diffusion tensor imaging study. *Bipolar Disord.* 10, 460–468. doi: 10.1111/j.1399-5618.2007.00552.x
- Bullmore, E., and Sporns, O. (2009). Complex brain networks: graph theoretical analysis of structural and functional systems. *Nat. Rev. Neurosci.* 10, 186–198. doi: 10.1038/nrn2575
- Bush, G., Luu, P., and Posner, M. I. (2000). Cognitive and emotional influences in anterior cingulate cortex. *Trends Cogn. Sci.* 4, 215–222. doi: 10.1016/s1364-6613(00)01483-2
- Caligiuri, M. P., Brown, G. G., Meloy, M. J., Eyler, L. T., Kindermann, S. S., Ebersson, S., et al. (2004). A functional magnetic resonance imaging study of cortical asymmetry in bipolar disorder. *Bipolar Disord.* 6, 183–196. doi: 10.1111/j.1399-5618.2004.00116.x
- Cavanna, A. E., and Trimble, M. R. (2006). The precuneus: a review of its functional anatomy and behavioural correlates. *Brain* 129, 564–583. doi: 10.1093/brain/awl004
- Collin, G., Kahn, R. S., De Reus, M. A., Cahn, W., and Mp, V. D. H. (2013). Structural and functional aspects relating to cost and benefit of rich club organization in the human cerebral cortex. *Cereb. Cortex* 24, 2258–2267. doi: 10.1093/cercor/bht064
- Collin, G., Mp, V. D. H., Abramovic, L., Vreeker, A., de Reus, M. A., van Haren, N. E., et al. (2016). Brain network analysis reveals affected connectome structure in bipolar I disorder. *Hum. Brain Mapp.* 37, 122–134. doi: 10.1002/hbm.23017
- Collin, G., Scholtens, L. H., Kahn, R. S., Mh, H., and Mp, V. D. H. (2017). Affected anatomical rich club and structural-functional coupling in young offspring of schizophrenia and bipolar disorder patients. *Biol. Psychiatry* 82, 746–755. doi: 10.1016/j.biopsych.2017.06.013
- Cui, L., Chen, Z., Deng, W., Huang, X., Lia, M., Ma, X., et al. (2011). Assessment of white matter abnormalities in paranoid schizophrenia and bipolar mania patients. *Psychiatry Res. Neuroimaging* 194, 347–353. doi: 10.1016/j.pscychresns.2011.03.010
- Cui, Z., Zhong, S., Xu, P., He, Y., and Gong, G. (2013). PANDA: a pipeline toolbox for analyzing brain diffusion images. *Front. Hum. Neurosci.* 7:42. doi: 10.3389/fnins.2018.00042
- Cullen, B., Ward, J., Graham, N. A., Deary, I. J., and Evans, J. J. (2016). Prevalence and correlates of cognitive impairment in euthymic adults with bipolar disorder: a systematic review. *J. Affect. Disord.* 205, 165–181. doi: 10.1016/j.jad.2016.06.063
- Delano-Wood, L., Stricker, N. H., Sorg, S. F., Nation, D. A., Jak, A. J., Woods, S. P., et al. (2012). Posterior cingulum white matter disruption and its associations with verbal memory and stroke risk in mild cognitive impairment. *J. Alzheimers Dis. JAD* 29, 589–603. doi: 10.3233/jad-2012-102103
- Elisa, A., Chiara, C., Gabriele, S., Giovanni, M., Fabrizio, P., Carlo, C., et al. (2016). White matter microstructural characteristics in Bipolar I and Bipolar II disorder: a diffusion tensor imaging study. *J. Affect. Disord.* 189, 176–183. doi: 10.1016/j.jad.2015.09.035
- Forde, N. J., O'Donoghue, S., Scanlon, C., Emsell, L., Chaddock, C., Leemans, A., et al. (2015). Structural brain network analysis in families multiply affected with bipolar I disorder. *Psychiatry Res. Neuroimaging* 234, 44–51. doi: 10.1016/j.pscychresns.2015.08.004
- Gao, S., Osuch, E. A., Wammes, M., Theberge, J., Jiang, T., Calhoun, V. D., et al. (2017). “Discriminating bipolar disorder from major depression based on kernel SVM using functional independent components,” in *Proceedings of the Twenty Seventh International Conference on Machine Learning for Signal Processing*, Japan.
- Goya-Maldonado, R., Brodmann, K., Keil, M., Trost, S., Dechent, P., and Gruber, O. (2016). Differentiating unipolar and bipolar depression by alterations in large-scale brain networks. *Hum. Brain Mapp.* 37, 808–818. doi: 10.1002/hbm.23070
- Green, M. F. (2006). Cognitive impairment and functional outcome in schizophrenia and bipolar disorder. *J. Clin. Psychiatry* 67:e12. doi: 10.4088/jcp.1006e12
- Hallahan, B., Newell, J., Soares, J. C., Brambilla, P., Strakowski, S. M., Fleck, D. E., et al. (2011). Structural MRI in bipolar disorder: an international collaborative mega-analysis of individual patient data. *J. Sci.* 26, 10–11.
- Hamilton, M. A. X. (1960). A rating scale for depression. *J. Neurol. Neurosurg. Psychiatry* 23, 56–62.
- Ho, N. F., Li, Z., Ji, F., Wang, M., Kuswanto, C. N., Sum, M. Y., et al. (2017). Hemispheric lateralization abnormalities of the white matter microstructure in patients with schizophrenia and bipolar disorder. *J. Psychiatry Neurosci.* 42:160090.
- Jie, N. F., Osuch, E. A., Zhu, M. H., Ma, X. Y., and Calhoun, V. D. (2015). “Discriminating bipolar disorder from major depression using whole brain functional connectivity: a feature selection analysis With SVM-Foba algorithm,” in *Proceedings of the 2015 IEEE International Workshop On Machine Learning For Signal Processing*, Boston, MA.
- Kaiser, R. H., Andrews-Hanna, J. R., Wager, T. D., and Pizzagalli, D. A. (2015). Large-Scale network dysfunction in major depressive disorder: a meta-analysis of resting-state functional connectivity. *JAMA Psychiatry* 72:603. doi: 10.1001/jamapsychiatry.2015.0071
- Karen, C., and Alexander, L. (2014). Hemispheric lateralization of topological organization in structural brain networks. *Hum. Brain Mapp.* 35, 4944–4957. doi: 10.1002/hbm.22524
- Keller, T. A., Kana, R. K., and Just, M. A. (2007). A developmental study of the structural integrity of white matter in autism. *Neuroreport* 18, 23–27. doi: 10.1097/01.wnr.0000239965.21685.99
- Leow, A., Ajilore, O., Zhan, L., Arienzo, D., Gadelkarim, J., Zhang, A., et al. (2013). Impaired inter-hemispheric integration in bipolar disorder revealed with brain network analyses. *Biol. Psychiatry* 73, 183–193. doi: 10.1016/j.biopsych.2012.09.014
- Li, D., Li, T., Niu, Y., Xiang, J., Cao, R., Liu, B., et al. (2018). Reduced hemispheric asymmetry of brain anatomical networks in attention deficit hyperactivity disorder. *Brain Imaging Behav.* 13, 1–16.
- Lisy, M. E., Jarvis, K. B., DelBello, M. P., Mills, N. P., Weber, W. A., Fleck, D., et al. (2011). Progressive neurostructural changes in adolescent and adult patients with bipolar disorder. *Bipolar Disord.* 13, 396–405. doi: 10.1111/j.1399-5618.2011.00927.x
- Liu, C.-H., Ma, X., Li, F., Wang, Y.-J., Tie, C.-L., Li, S.-F., et al. (2012). Regional homogeneity within the default mode network in bipolar depression: a resting-state functional magnetic resonance imaging study. *PLoS One* 7:e48181. doi: 10.1371/journal.pone.0048181
- Liu, J. X., Chen, Y. S., Hsieh, J. C., Su, T. P., Yeh, T. C., and Chen, L. F. (2010). Differences in white matter abnormalities between bipolar I and II disorders. *J. Affect. Disord.* 127, 309–315. doi: 10.1016/j.jad.2010.05.026
- Lv, D., Lin, W., Xue, Z., Pu, W., Yang, Q., Huang, X., et al. (2016). Decreased functional connectivity in the language regions in bipolar patients during depressive episodes but not remission. *J. Affect. Disord.* 2016, 116–124. doi: 10.1016/j.jad.2016.03.026
- Maalouf, F. T., Klein, C., Clark, L., Sahakian, B. J., Labarbara, E. J., Versace, A., et al. (2010). Impaired sustained attention and executive dysfunction: bipolar disorder versus depression-specific markers of affective disorders ?. *Neuropsychologia* 48, 1862–1868. doi: 10.1016/j.neuropsychologia.2010.02.015
- Mahon, K., Burdick, K. E., Ikuta, T., and Braga, R. J. (2013). Abnormal temporal lobe white matter as a biomarker for genetic risk of bipolar disorder. *Biol. Psychiatry* 73, 177–182. doi: 10.1016/j.biopsych.2012.07.033
- Martinot, M. P., Lemaitre, H., Artiges, E., Miranda, R., Goodman, R., Penttilä, J., et al. (2014). White-matter microstructure and gray-matter volumes in adolescents with subthreshold bipolar symptoms. *Mol. Psychiatry* 19:462. doi: 10.1038/mp.2013.44
- Maslov, S., and Sneppen, K. (2002). Specificity and stability in topology of protein networks. *Science* 296, 910–913. doi: 10.1126/science.1065103

- Menon, V. (2011). Large-scale brain networks and psychopathology: a unifying triple network model. *Trends Cogn. Sci.* 15, 483–506. doi: 10.1016/j.tics.2011.08.003
- O'Donoghue, S., Cannon, D. M., Perlini, C., and Brambilla, P. (2015). Applying neuroimaging to detect neuroanatomical dysconnectivity in psychosis. *Epidemiol. Psychiatr. Sci.* 24, 298–302. doi: 10.1017/s2045796015000074
- O'Donoghue, S., Kilmartin, L., O'Hara, D., Emsell, L., Langan, C., Mcinerney, S., et al. (2017). Anatomical integration and rich-club connectivity in euthymic bipolar disorder. *Psychol. Med.* 47, 1609–1623. doi: 10.1017/s0033291717000058
- Parker, G. J. M., Luzzi, S., Alexander, D. C., Wheeler-Kingshott, C. A. M., Ciccarelli, O., and Ralph, M. A. L. (2005). Lateralization of ventral and dorsal auditory-language pathways in the human brain. *Neuroimage* 24, 656–666. doi: 10.1016/j.neuroimage.2004.08.047
- Pavuluri, M. N., Schenkel, L. S., Subhash, A., Harral, E. M., Kristian, S. H., Herbener, E. S., et al. (2006). Neurocognitive function in unmedicated manic and medicated euthymic pediatric bipolar patients. *Am. J. Psychiatry* 163, 286–293. doi: 10.1176/appi.ajp.163.2.286
- Pierpaoli, C., and Basser, P. J. (1996). Toward a quantitative assessment of diffusion anisotropy. *Magnet. Resonan. Med.* 36, 893–906. doi: 10.1002/mrm.1910360612
- Power, J. D., Schlaggar, B. L., Lessovschlaggar, C. N., and Petersen, S. E. (2013). Evidence for hubs in human functional brain networks. *Neuron* 79, 798–813. doi: 10.1016/j.neuron.2013.07.035
- Quraishi, S., and Frangou, S. (2002). Neuropsychology of bipolar disorder: a review. *J. Affect. Disord.* 72, 209–226. doi: 10.1016/s0165-0327(02)00091-5
- Saunders, K. E. A., and Goodwin, G. M. (2010). The course of bipolar disorder. *Adv. Psychiatr. Treat.* 16, 318–328.
- Schulte, T., Müller-Oehring, E. M., Sullivan, E. V., and Pfefferbaum, A. (2012). White matter fiber compromise contributes differentially to attention and emotion processing impairment in alcoholism, HIV-infection, and their comorbidity. *Neuropsychologia* 50, 2812–2822. doi: 10.1016/j.neuropsychologia.2012.07.042
- Schwartz, G. E., Davidson, R. J., and Maer, F. (1975). Right hemisphere lateralization for emotion in the human brain: interactions with cognition. *Science* 190, 286–288. doi: 10.1126/science.1179210
- Serene, H., Song, A. W., and Kang, S. (2010). White matter abnormalities in bipolar disorder: insights from diffusion tensor imaging studies. *J. Neural Transm.* 117, 639–654. doi: 10.1007/s00702-010-0368-9
- Shu, N., Liu, Y., Li, K., Duan, Y., Wang, J., Yu, C., et al. (2011). Diffusion tensor tractography reveals disrupted topological efficiency in white matter structural networks in multiple sclerosis. *Cereb. Cortex* 21, 2565–2577. doi: 10.1093/cercor/bhr039
- Silani, G., Lamm, C., Ruff, C. C., and Singer, T. (2013). Right supramarginal gyrus is crucial to overcome emotional egocentricity bias in social judgments. *J. Neurosci.* 33, 15466–15476. doi: 10.1523/jneurosci.1488-13.2013
- Silk, T. J., Vilgis, V., Adamson, C., Chen, J., Smit, L., Vance, A., et al. (2016). Abnormal asymmetry in frontostriatal white matter in children with attention deficit hyperactivity disorder. *Brain Imaging Behav.* 10, 1080–1089. doi: 10.1007/s11682-015-9470-9
- Strakowski, S. M., Delbello, M. P., Adler, C., Cecil, D. M., and Sax, K. W. (2000). Neuroimaging in bipolar disorder. *Bipolar Disord.* 2, 148–164.
- Sun, Y., Chen, Y., Collinson, S. L., Bezerianos, A., and Sim, K. (2015). Reduced hemispheric asymmetry of brain anatomical networks is linked to schizophrenia: a connectome study. *Cereb. Cortex* 27, 602–615.
- Sussmann, J. E., Lymer, G. K. S., Mckirdy, J., Moorhead, T. W. J., Maniega, S. M., Job, D., et al. (2009). White matter abnormalities in bipolar disorder and schizophrenia detected using diffusion tensor magnetic resonance imaging. *Biopolar Disord.* 11, 11–18. doi: 10.1111/j.1399-5618.2008.00646.x
- Toga, A. W., and Thompson, P. M. (2003). Mapping brain asymmetry. *Nat. Rev. Neurosci.* 4, 37–48. doi: 10.1038/nrn1009
- Torgerson, C. M., Irimia, A., Leow, A. D., Bartzokis, G., Moody, T. D., Jennings, R. G., et al. (2013). DTI tractography and white matter fiber tract characteristics in euthymic bipolar I patients and healthy control subjects. *Brain Imaging Behav.* 7:129. doi: 10.1007/s11682-012-9202-3
- Tzourio-Mazoyer, N., Landeau, B., Papathanassiou, D., Crivello, F., Etard, O., Delcroix, N., et al. (2002). Automated anatomical labeling of activations in SPM using a macroscopic anatomical parcellation of the MNI MRI single-subject brain. *Neuroimage* 15, 273–289. doi: 10.1006/nimg.2001.0978
- Van den Heuvel, M. P., and Sporns, O. (2011). Rich-club organization of the human connectome. *J. Neurosci.* 31, 15775–15786. doi: 10.1523/jneurosci.3539-11.2011
- Van den Heuvel, M. P., and Sporns, O. (2013). Network hubs in the human brain. *Trends Cogn. Sci.* 17, 683–696. doi: 10.1016/j.tics.2013.09.012
- Van den Heuvel, M. P., Kahn, R. S., Goni, J., and Sporns, O. (2012). High-cost, high-capacity backbone for global brain communication. *Proc. Natl. Acad. Sci. U.S.A.* 109, 11372–11377. doi: 10.1073/pnas.1203593109
- Vederine, F., Wessa, M., Leboyer, M., and Houenou, J. (2011). A meta-analysis of whole-brain diffusion tensor imaging studies in bipolar disorder. *Prog. Neuro Psychopharmacol. Biol. Psychiatry* 35, 1820–1826. doi: 10.1016/j.pnpbp.2011.05.009
- Vivian, K., Peter, K., Babak, A., Ema, S., Todd, L., Kelvin, L., et al. (2009). Lower orbital frontal white matter integrity in adolescents with bipolar I disorder. *J. Am. Acad. Child Adolesc. Psychiatry* 48, 79–86. doi: 10.1097/chi.0b013e3181900421
- Wang, B., Li, T., Zhou, M., Zhao, S., Niu, Y., Wang, X., et al. (2018). The abnormality of topological asymmetry in hemispheric brain anatomical networks in bipolar disorder. *Front. Neurosci.* 12:618. doi: 10.3389/fnins.2018.00618
- Wang, Y., Deng, F., Jia, Y., Wang, J., and Huang, R. (2018). Disrupted rich club organization and structural brain connectome in unmedicated bipolar disorder. *Psychol. Med.* 49, 510–518. doi: 10.1017/s0033291718001150
- Wang, B., Zhan, Q., Yan, T., Imtiaz, S., and Li, D. (2019). Hemisphere and gender differences in the rich-club organization of structural networks. *Cereb. Cortex* 29, 4889–4901. doi: 10.1093/cercor/bhz027
- Wang, J., Wang, X., Xia, M., Liao, X., and He, Y. (2015). GREYNA: a graph theoretical network analysis toolbox for imaging connectomics. *Front. Hum. Neurosci.* 9:386. doi: 10.3389/fnhum.2015.00386
- Wang, Y., Wang, J., Jia, Y., Zhong, S., Zhong, M., Sun, Y., et al. (2017). Topologically convergent and divergent functional connectivity patterns in unmedicated unipolar depression and bipolar disorder. *Transl. Psychiatry* 7:e1165. doi: 10.1038/tp.2017.117
- Wang, Y., Zhong, S., Jia, Y., Sun, Y., Wang, B., Liu, T., et al. (2016). Disrupted resting-state functional connectivity in nonmedicated bipolar disorder. *Radiology* 280:151641.
- Wheeler, R. E., Davidson, R. J., and Tomarken, A. J. (1993). Frontal brain asymmetry and emotional reactivity: a biological substrate of affective style. *Psychophysiology* 30, 82–89. doi: 10.1111/j.1469-8986.1993.tb03207.x
- Xia, M., Wang, J., and He, Y. (2013). BrainNet viewer: a network visualization tool for human brain connectomics. *PLoS One* 8:e68910. doi: 10.1371/journal.pone.0068910
- Yan, H., Zuo, X. N., Wang, D., Wang, J., Zhu, C., Milham, M. P., et al. (2009). Hemispheric asymmetry in cognitive division of anterior cingulate cortex: a resting-state functional connectivity study. *Neuroimage* 47, 1579–1589. doi: 10.1016/j.neuroimage.2009.05.080
- Yan, T., Wang, W., Liu, Y., Chen, K., and Han, Y. (2018). Rich club disturbances of the human connectome from subjective cognitive decline to Alzheimer's disease. *Theranostics* 8, 3237–3255. doi: 10.7150/thno.23772
- Yang, C., Zhong, S., Zhou, X., Wei, L., Wang, L., and Nie, S. (2017). The abnormality of topological asymmetry between hemispheric brain white matter networks in Alzheimer's disease and mild cognitive impairment. *Front. Aging Neurosci.* 9, 261–273. doi: 10.3389/fnagi.2017.00261
- Yasser, I. M., Alejandro, P. F., Morris, D. M., Canales-Rodríguez, E. J., Haroon, H. A., Lorna, G. P., et al. (2011). Brain hemispheric structural efficiency and interconnectivity rightward asymmetry in human and nonhuman primates. *Cereb. Cortex* 21:56. doi: 10.1093/cercor/bhq058

- Yin, X., Han, Y., Ge, H., Xu, W., Huang, R., Zhang, D., et al. (2013). Inferior frontal white matter asymmetry correlates with executive control of attention. *Hum. Brain Mapp.* 34, 796–813. doi: 10.1002/hbm.21477
- Young, R. C., Biggs, J. T., Ziegler, V. E., and Meyer, D. A. (1978). A rating scale for mania: reliability, validity and sensitivity. *Br. J. Psychiatry* 133, 429–435. doi: 10.1192/bjp.133.5.429
- Zhong, S., He, Y., Shu, H., and Gong, G. (2016). Developmental changes in topological asymmetry between hemispheric brain white matter networks from adolescence to young adulthood. *Cereb. Cortex* 27:bhw109. doi: 10.1093/cercor/bhw109

Conflict of Interest: The authors declare that the research was conducted in the absence of any commercial or financial relationships that could be construed as a potential conflict of interest.

Copyright © 2020 Li, Liu, Yan, Cui, Zhang, Wei, Ma, Zhang, Xiang and Wang. This is an open-access article distributed under the terms of the Creative Commons Attribution License (CC BY). The use, distribution or reproduction in other forums is permitted, provided the original author(s) and the copyright owner(s) are credited and that the original publication in this journal is cited, in accordance with accepted academic practice. No use, distribution or reproduction is permitted which does not comply with these terms.



Transition of Neural Activity From the Chaotic Bipolar-Disorder State to the Periodic Healthy State Using External Feedback Signals

Hirota Doho^{1,2†}, Sou Nobukawa^{3*†}, Haruhiko Nishimura², Nobuhiko Wagatsuma⁴ and Tetsuya Takahashi^{5,6}

¹ Faculty of Education, Teacher Training Division, Kochi University, Kochi, Japan, ² Graduate School of Applied Informatics, University of Hyogo, Kobe, Japan, ³ Department of Computer Science, Chiba Institute of Technology, Narashino, Japan, ⁴ Department of Information Science, Faculty of Science, Toho University, Funabashi, Japan, ⁵ Research Center for Child Mental Development, Kanazawa University, Kanazawa, Japan, ⁶ Department of Neuropsychiatry, University of Fukui, Yoshida, Japan

OPEN ACCESS

Edited by:

Tianyi Yan,
Beijing Institute of Technology, China

Reviewed by:

Ergin Yilmaz,
Bulent Ecevit University, Turkey
Adam Ponzi,
Okinawa Institute of Science and
Technology Graduate University,
Japan

*Correspondence:

Sou Nobukawa
nobukawa@cs.it-chiba.ac.jp

[†]These authors have contributed
equally to this work

Received: 16 May 2020

Accepted: 20 July 2020

Published: 28 August 2020

Citation:

Doho H, Nobukawa S, Nishimura H,
Wagatsuma N and Takahashi T (2020)
Transition of Neural Activity From the
Chaotic Bipolar-Disorder State to the
Periodic Healthy State Using External
Feedback Signals.
Front. Comput. Neurosci. 14:76.
doi: 10.3389/fncom.2020.00076

Chronotherapy is a treatment for mood disorders, including major depressive disorder, mania, and bipolar disorder (BD). Neurotransmitters associated with the pathology of mood disorders exhibit circadian rhythms. A functional deficit in the neural circuits related to mood disorders disturbs the circadian rhythm; chronotherapy is an intervention that helps resynchronize the patient's biological clock with the periodic daily cycle, leading to amelioration of symptoms. In previous reports, Hadaeghi et al. proposed a non-linear dynamic model composed of the frontal and sensory cortical neural networks and the hypothalamus to explain the relationship between deficits in neural function in the frontal cortex and the disturbed circadian rhythm/mood transitions in BD (hereinafter referred to as the Hadaeghi model). In this model, neural activity in the frontal and sensory lobes exhibits periodic behavior in the healthy state; while in BD, this neural activity is in a state of chaos-chaos intermittency; this temporal departure from the healthy periodic state disturbs the circadian pacemaker in the hypothalamus. In this study, we propose an intervention based on a feedback method called the "reduced region of orbit" (RRO) method to facilitate the transition of the disturbed frontal cortical neural activity underlying BD to healthy periodic activity. Our simulation was based on the Hadaeghi model. We used an RRO feedback signal based on the return-map structure of the simulated frontal and sensory lobes to induce synchronization with a relatively weak periodic signal corresponding to the healthy condition by applying feedback of appropriate strength. The RRO feedback signal induces chaotic resonance, which facilitates the transition to healthy, periodic frontal neural activity, although this synchronization is restricted to a relatively low frequency of the periodic input signal. Additionally, applying an appropriate strength of the RRO feedback signal lowered the amplitude of the periodic input signal required to induce a synchronous state compared with the periodic signal applied alone. In conclusion, through a chaotic-resonance effect induced by the RRO feedback method,

the state of the disturbed frontal neural activity characteristic of BD was transformed into a state close to healthy periodic activity by relatively weak periodic perturbations. Thus, RRO feedback-modulated chronotherapy might be an innovative new type of minimally invasive chronotherapy.

Keywords: bipolar disorder, neural network, chaotic resonance, feedback control, chaos-chaos intermittency, chronotherapy

1. INTRODUCTION

Mood disorders, including major depressive disorder, mania, and bipolar disorder (BD), exhibit high morbidity, high suicide rates, and multiple relapses during long-term treatment; effective treatments and diagnostic methods are long-standing unmet needs (reviewed in Drevets, 2000; Kessler et al., 2003; The Wellcome Trust Case Control Consortium, 2007; Price and Drevets, 2010). Accumulating neuroimaging evidence reveals the multiple and complex pathologies of mood disorders (reviewed in Baskaran et al., 2012; Vargas et al., 2013; Chiapponi et al., 2016; Arnone, 2019). Particularly, functional magnetic resonance imaging (fMRI) and electroencephalography (EEG) have revealed region-specific enhancements and depressions in neural activity in regions such as the amygdala, hippocampus, and prefrontal cortex associated with major depressive disorder (reviewed in Baskaran et al., 2012; Arnone, 2019) and BD (Vargas et al., 2013). Furthermore, deficits in the excitatory and inhibitory neural pathways, typified as employing the neurotransmitters glutamic acid and gamma-aminobutyric acid (GABA), respectively, and abnormal cortical neural networks are reportedly also associated with mood disorders (Brambilla et al., 2003; Hasler et al., 2007; Sanacora et al., 2012; Schloesser et al., 2012; reviewed in Chiapponi et al., 2016). For the treatment of mood disorders, antidepressants (e.g., selective serotonin reuptake inhibitors, serotonin, and norepinephrine reuptake inhibitors) and mood stabilizers (e.g., lithium carbonate and clozapine) are widely used (Hirschfeld et al., 2003; López-Muñoz et al., 2006; Tobe et al., 2017). However, in the treatment of BD, mood stabilizers in particular exhibit troublesome side effects, such as progressive renal failure and a narrow therapeutic index (Hirschfeld et al., 2003; López-Muñoz et al., 2006). Therefore, alternative treatments are needed, either to relieve symptoms directly or to enhance the effects of conventional pharmacological therapy, allowing dosages to be minimized.

As an alternative treatment, chronotherapy has been garnering research attention (reviewed in Abreu and Bragança, 2015). The release of neurotransmitters associated with the pathology of mood disorders, such as serotonin, noradrenaline, glutamic acid, GABA, and dopamine, exhibits circadian rhythms (Weiner et al., 1992; Castaneda et al., 2004; Weber et al., 2004; Hampp et al., 2008; Cain et al., 2017). In mood disorders, dysregulated neural circuits disturb these circadian rhythms (Yeragani et al., 2003; Glenn et al., 2006; Bonsall et al., 2011; Moore et al., 2014; reviewed in Albrecht, 2013). Chronotherapy promotes the transition of the disturbed circadian rhythms to periodic ones, consequently leading to the improvement of

symptoms (Abreu and Bragança, 2015). Chronotherapies include light therapy and combination therapy (light therapy with drugs; Leibenluft et al., 1995; Terman and Terman, 2005). However, light therapy must be individualized, and customization of the luminance and wavelength of the light for each patient is difficult. Moreover, the use of inappropriate parameters in light therapy carries a risk of inducing mixed states, hypomania, and autonomic hyperactivation in cases of BD (Terman and Terman, 2005; Sit et al., 2007; Abreu and Bragança, 2015).

Circadian rhythms are a phenomenon in which biological signals exhibiting oscillations synchronize with the daily cycle; to describe these temporal behaviors at multiple hierarchical levels, from the molecular to the synaptic network, non-linear dynamic models have been proposed (Pavlidis, 1969; Goldbeter, 1995; Kurosawa et al., 2006; reviewed in Pikovsky et al., 2003; Herzog, 2007; Pavlidis, 2012). In addition to circadian rhythms, non-linear dynamic modeling has been considered key for understanding the pathology of the transition of mood between mania and depression with a view to treatment (Daugherty et al., 2009; reviewed in Hadaeghi et al., 2013a,b). Daugherty et al. and Hadaeghi et al. have demonstrated that the mood transition is caused by the phenomenon of chaos-chaos intermittency, in which the orbit of an oscillator in the phase plane hops between separated chaotic attractor regions. Hadaeghi et al. demonstrated the effect using the forced Duffing oscillator and the Liénard oscillator (Daugherty et al., 2009; Hadaeghi et al., 2013a). Furthermore, to explain the relationships between deficits in neural networks in the frontal cortex and disturbances of circadian rhythm/mood transitions in BD, Hadaeghi et al. and Bayani et al. proposed a non-linear dynamic model (referred to as the Hadaeghi model in this study) composed of frontal and sensory cortical neural networks interacting with the hypothalamus (Hadaeghi et al., 2016; Bayani et al., 2017). In this model, activity in the neural networks of the frontal and sensory cortices exhibits periodicity in the healthy state but is transferred to a state of chaos-chaos intermittency in patients with BD. The temporal fluctuation based on the healthy periodic state reflects the controlling parameter of the circadian pacemaker in the hypothalamus (Hadaeghi et al., 2016). Consequently, disturbances in the circadian rhythm, which are observed in BD because of mood transitions, appear (Hadaeghi et al., 2016; Bayani et al., 2017). The circadian rhythms reproduced by the model are highly congruent with actual clinically observed disturbances of circadian rhythms (Hadaeghi et al., 2016).

Accumulating research on the effect of fluctuations on synchronization phenomena in non-linear systems reveals that fluctuations induce many types of synchronization, such as chaos

synchronization, coherence resonance, stochastic resonance, and chaotic resonance (reviewed in Pikovsky et al., 2003; Anishchenko et al., 2007; Rajasekar and Sanjuán, 2016). The mechanism of stochastic resonance in particular, in which synchronization to a weak input signal is enhanced by additive noise, has biomedical applications, such as the development of devices and methods for enhancing human tactile sensory performance (Enders et al., 2013; Kurita et al., 2013, 2016; Seo et al., 2014). Similar to the synchronization phenomenon of stochastic resonance, in chaotic resonance, the synchronization to a weak input signal is enhanced by the internal chaotic dynamics instead of additive noise (reviewed in Anishchenko et al., 2007; Rajasekar and Sanjuán, 2016). Chaotic resonance has been widely studied in many types of systems, including neural systems (Nishimura et al., 2000; Nobukawa and Nishimura, 2016; Nobukawa et al., 2016, 2017; Baysal et al., 2019; reviewed in Nobukawa and Nishimura, 2020). In these fluctuation-enhanced synchronization phenomena, the strength of the external perturbation required for the development of a periodic state is weaker than that required for forced oscillations (Sinha, 1999; reviewed in Pikovsky et al., 2003; Anishchenko et al., 2007; Rajasekar and Sanjuán, 2016). Therefore, using these synchronization phenomena may be a strategy for administering minimally invasive chronotherapy.

According to the Hadaeghi model, in patients with BD, the presence of chaos-chaos intermittency in the neural activity of the frontal cortex disturbs the circadian rhythm (Hadaeghi et al., 2016; Bayani et al., 2017). Therefore, methods that promote the transition from chaos-chaos intermittency to periodic behavior may stabilize the disturbed circadian rhythm. As the best candidate, we proposed a chaos controlling method known as the “reduced region of orbit” (RRO) method, in which chaos-chaos intermittency is synchronized to an external, weak periodic signal using a feedback principle (Nobukawa et al., 2018b). The RRO feedback signals reduce the absolute values of local maximum and minimum values of the return-map functions, causing a bifurcation called attractor merging, which underlies the chaos-chaos intermittency (Nobukawa et al., 2018b). Because the synchronization of chaos-chaos intermittency is maximally facilitated around the attractor-merging bifurcation (review in Anishchenko et al., 2007; Rajasekar and Sanjuán, 2016), an appropriate strength of the RRO feedback signal can induce synchronization, i.e., RRO feedback signals induce chaotic resonance (Nobukawa et al., 2018b). Initially, the RRO feedback signal was applied to simple cubic map systems to induce chaotic resonance (Nobukawa et al., 2018b). Subsequently, the use of an RRO feedback signal has been applied to several types of systems, such as coupled cubic maps (Nobukawa et al., 2019a) and Chua’s circuit (Nobukawa et al., 2020). These studies revealed that chaotic resonance induced by RRO feedback possesses advantages over other forms of synchronization induced by fluctuations (Nobukawa et al., 2019b, 2020). Particularly, the chaotic resonance induced by the RRO feedback method exhibits higher sensitivity than stochastic resonances induced by additive noise and are more adaptable to various types of attractor conditions (Nobukawa et al., 2019b). Studies on chaotic resonance induced by the RRO feedback method have

been applied to neural systems (Nobukawa and Shibata, 2019; Nobukawa et al., 2019b). Therefore, in addition to stochastic resonance controlled by additive noise in neural systems (Enders et al., 2013; Kurita et al., 2013, 2016; Seo et al., 2014), chaotic resonance controlled by RRO feedback is at the stage where biomedical applications can be considered.

In this context, we hypothesized that the chaotic resonance induced by RRO feedback will facilitate chronotherapy by adapting to the daily neural activity of each patient, allowing for minimally invasive treatments. To verify this hypothesis, we applied chaotic resonance induced by RRO feedback signals to a model of a patient with BD based on the Hadaeghi model and evaluated the transition to periodic behavior of the disturbed frontal cortical neural activity. In detail, we first developed the RRO feedback method using the Hadaeghi model from the return-map structure of the frontal and sensory cortical neural system. Second, the chaotic resonance induced by an RRO feedback signal in combination with a weak periodic signal was evaluated. Third, the amounts of perturbation required for entrainment were compared between chaotic resonance induced by RRO feedback and synchronization induced by the application of a periodic signal alone, i.e., a forced oscillation.

2. MATERIALS AND METHODS

2.1. Neural System Composed of the Frontal and Sensory Cortices

The pathology of BD involves multiple complex neural pathways (Sanacora et al., 2012; Schloesser et al., 2012; Tobe et al., 2017). Hadaeghi et al. (2016) focused on the pathological consequences of competition between excitatory (glutamatergic) and inhibitory (GABAergic) neurons in the frontal cortex (Tretter et al., 2011; Montague et al., 2012) as major etiological factors in BD. They constructed a neural system composed of the frontal and sensory cortices to reproduce healthy and disturbed BD-associated neural activities on a diurnal timescale (Hadaeghi et al., 2016; Bayani et al., 2017). **Figure 1** shows an overview of this system. This neural system has two neural pathways, excitatory and inhibitory, from the sensory cortex to the frontal cortex; the neural activity produced by the interaction between these pathways is fed back to the sensory cortex (Hadaeghi et al., 2016).

The daily neural activity of the frontal cortex $x(n)$ ($n = 1, 2, \dots$ days), which represents the long-term firing rate dynamics, is controlled by the competition of the excitatory and inhibitory neural populations (Hadaeghi et al., 2016):

$$x(n+1) = F(x(n)), \quad (1)$$

$$F(x) = B \tanh(w_2 x) - A \tanh(w_1 x), \quad (2)$$

where w_1 and w_2 are the synaptic weights of inputs to the inhibitory and excitatory neural populations, respectively. A and B correspond to the synaptic weights of the outputs of the inhibitory and excitatory neural populations, respectively, as overall neurotransmitter levels. The parameters used in this study were determined by previous research (Hadaeghi et al., 2016; Bayani et al., 2017) as follows: $w_1 = 0.2223$, $w_2 = 1.487$, and $B = 5.82$. In this study, as well as in the previous research, A

is the main bifurcation parameter (Hadaeghi et al., 2016; Bayani et al., 2017).

2.2. Controlling Frontal Cortical Neural Activity by RRO Feedback

Hadaeghi et al. demonstrated that healthy circadian rhythms and the disturbed circadian rhythms associated with BD are produced by a period- p state in the periodic window and a chaos-chaos intermittency state in the frontal cortical neural activity, respectively (Hadaeghi et al., 2016). The concrete behaviors of frontal neurons $x(n)$ given by Equations (1) and

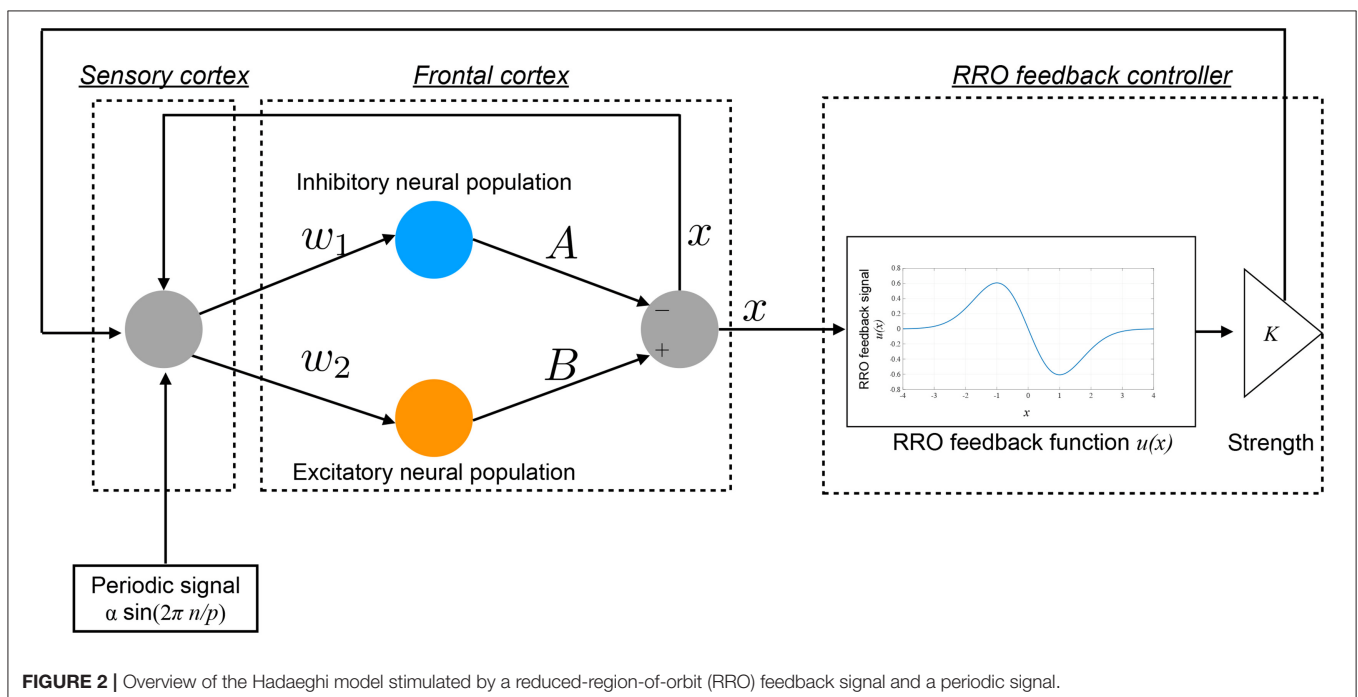
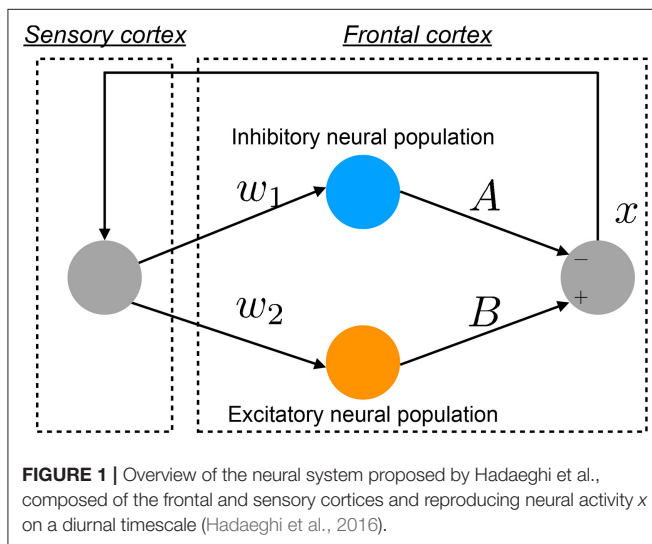
(2) corresponding to healthy and BD states are demonstrated in section 3.1. In this study, we developed a feedback signal to facilitate the transition of the chaos-chaos intermittency of $x(n)$ to the period- p state using an RRO-type chaotic resonance. An overview of the system for this control method is presented in **Figure 2**. The daily neural activity of the frontal cortex $x(n)$ is controlled by RRO feedback signals $Ku(x)$ and a periodic input signal $S(n) = \alpha \sin(2\pi n/p)$, as follows:

$$x(n+1) = F(x(n)) + Ku(x(n)) + S(n), \quad (3)$$

$$u(x) = -(x - x_d) \exp(-(x - x_d)^2 / (2\sigma^2)). \quad (4)$$

Here, K , x_d , and σ represent the RRO feedback strength, the merging point of two chaotic attractors, and a parameter to determine the region of the RRO feedback effect, respectively. In this study, $x_d = 0$ and $\sigma = 1.0$ were used, because the return-map structure has a point symmetry at around $x = 0$ with local maximum and minimum values of the map function located within the region $-\sigma < x < \sigma$ ($\sigma = 1.0$) (Nobukawa et al., 2018b). We used four values, 4, 8, 16, and 32, for the period p .

To explain the effect of the RRO feedback signal $Ku(x)$ in the absence of the periodic input signal ($\alpha = 0$), **Figure 3A** shows the map function of $F(x) + Ku(x)$ and the orbit $x(n)$ in the presence/absence of RRO feedback signals. Attractor merging (chaos-chaos intermittency) occurs if $F(f_{\max}) + Ku(f_{\max}) < 0$ and $F(f_{\min}) + Ku(f_{\min}) > 0$, where f_{\max} and f_{\min} are the local maximum and minimum of the map function, respectively. For an inhibitory synaptic weight $A = 9.8, 12.0$ in the absence of feedback ($K = 0$), the attractor merging conditions are satisfied (left graph in **Figure 3A**). The orbit $x(n)$ hops between



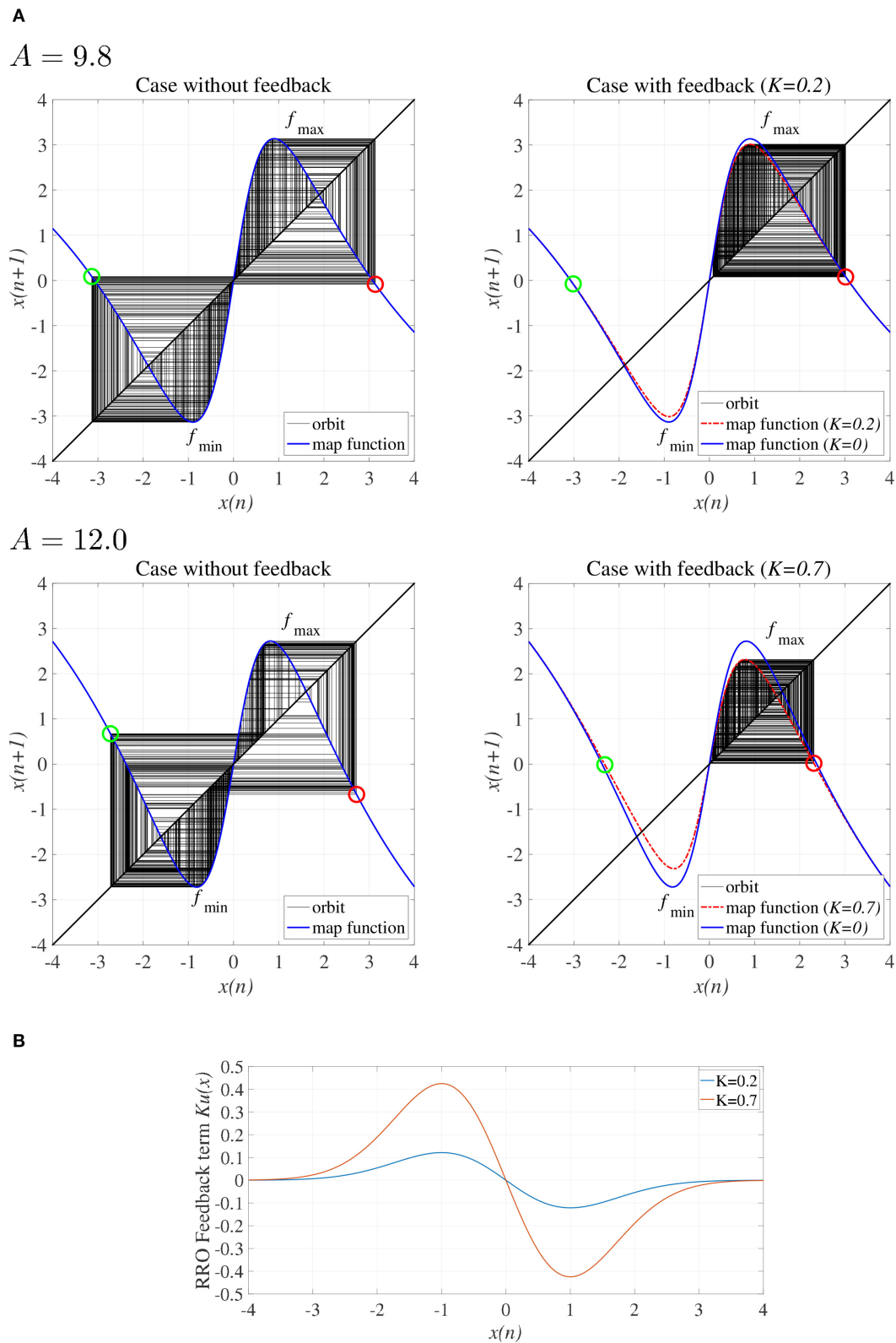


FIGURE 3 | (A) Map function $F(x) + Ku(x)$ for $A = 9.8, 12.0$ with and without external feedback signals in the return map between $x(n)$ and $x(n + 1)$. The left and right graphs indicate, respectively, map functions satisfying attractor merging conditions with $K = 0.0$ and not satisfying attractor merging conditions with $K = 0.2$ in the
(Continued)

FIGURE 3 | $A = 9.8$ case and $K = 0.7$ in the $A = 12.0$ case. Red and green circles indicate $F(f_{\max}) + Ku(f_{\max})$ and $F(f_{\min}) + Ku(f_{\min})$, respectively. RRO feedback separates the merged attractors by decreasing the absolute values of f_{\max} and f_{\min} . **(B)** RRO feedback signal $K(u(x))$ for $K = 0.2, 0.7$. The local maximum and minimum of $K(u(x))$ are located at the local minimum and maximum of the F map function, respectively.

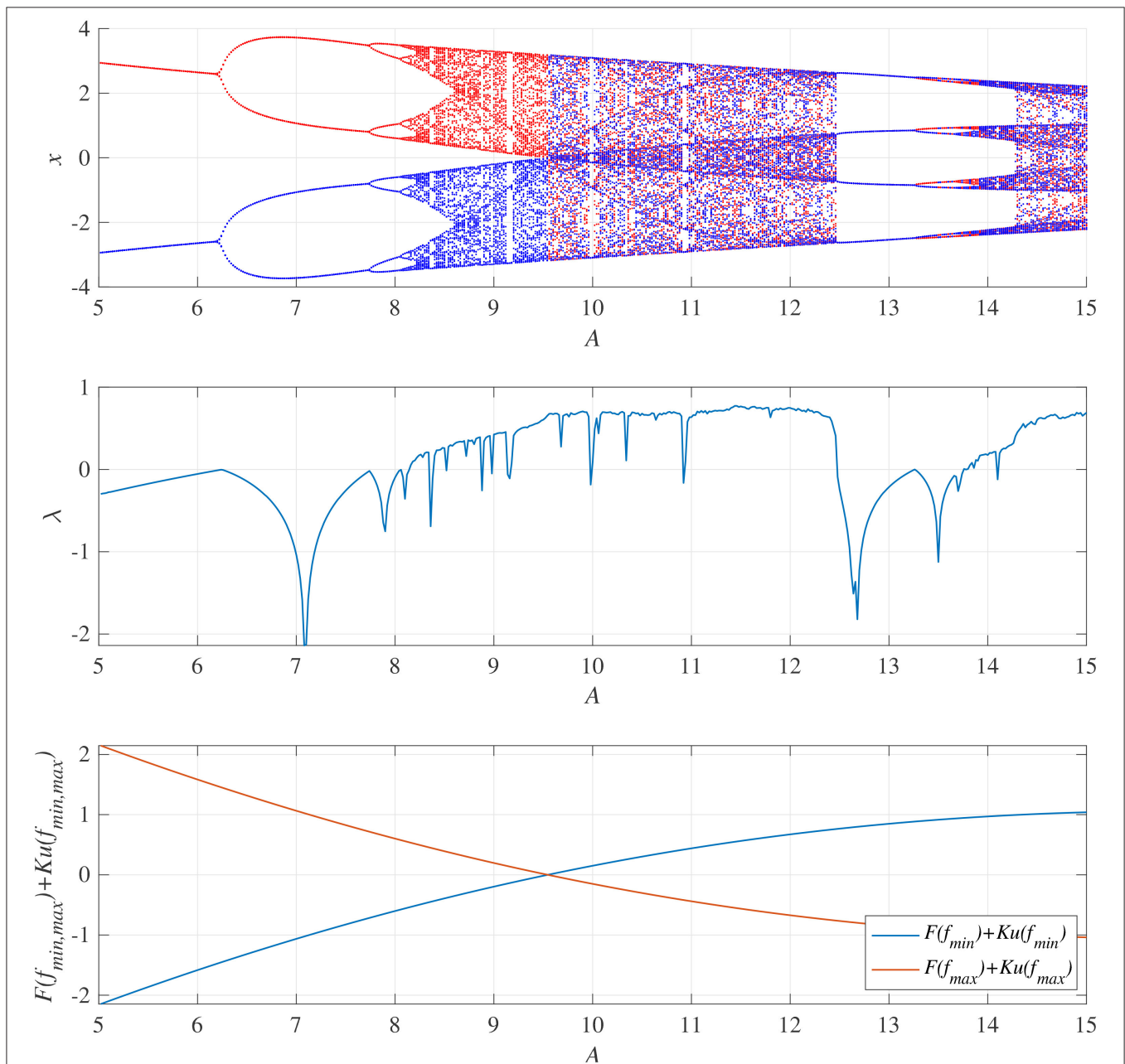
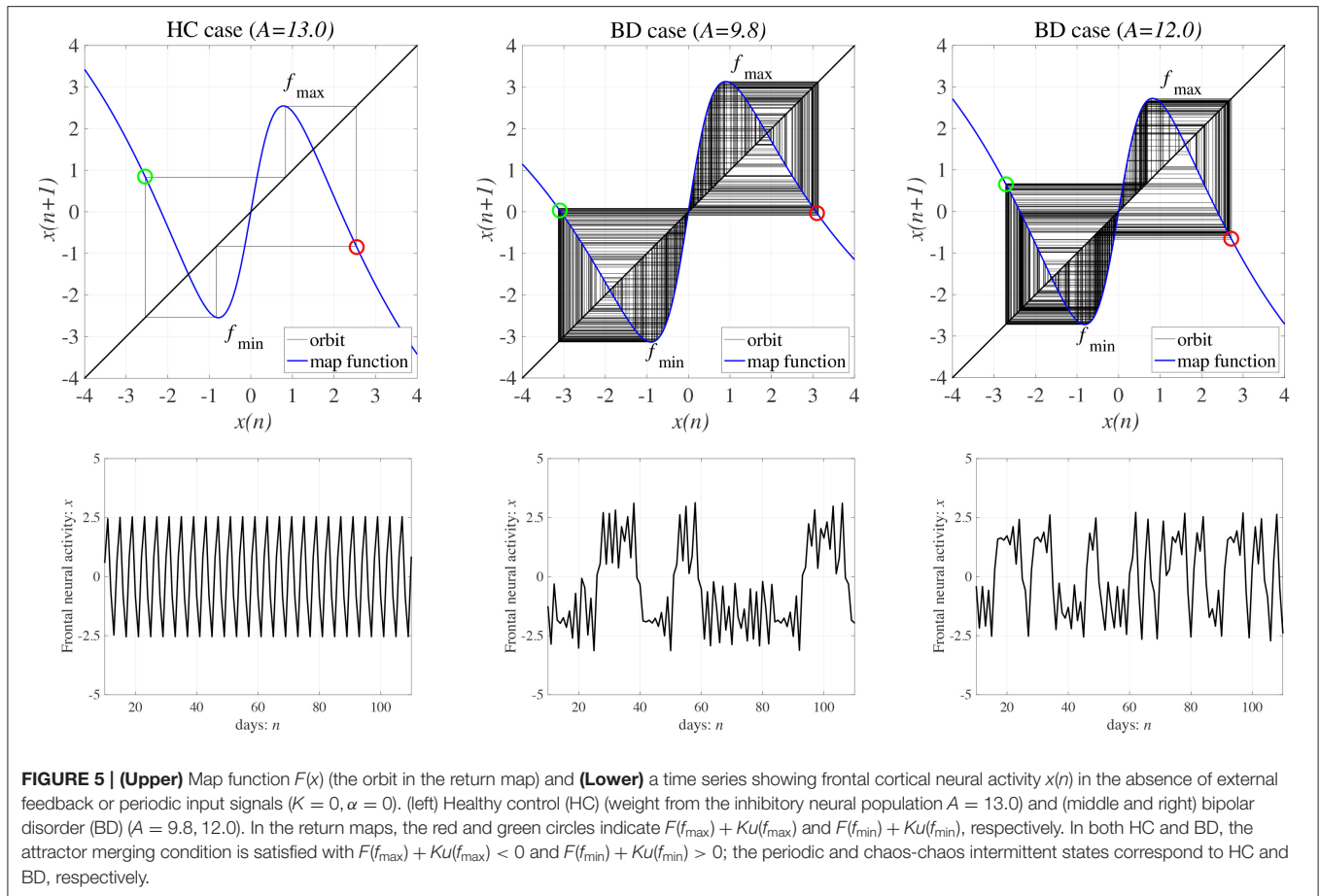


FIGURE 4 | System behaviors in the neural network comprised the frontal and sensory cortices as a function of the synaptic weight from the inhibitory neural population, A , in the absence of feedback and periodic signals ($K = 0, \alpha = 0$). **(Top)** Bifurcation diagram of the frontal neural activity $x(n)$ represented by Equation (1) as a function of A . Blue and red dots indicate positive and negative initial values of $x(0)$, respectively. **(Middle)** Lyapunov exponent λ as a function of A . **(Bottom)** $F(f_{\min,max}) + Ku(f_{\min,max})$ as a function of A . The frontal neural behavior in the periodic window $12.5 \lesssim A \lesssim 13.5$ corresponds to that of healthy controls (HC), while the chaos-chaos intermittent behavior in $9.8 \lesssim A \lesssim 12.5$ and $A \gtrsim 13.5$ corresponds to that of patients with BD (Hadaeghi et al., 2016).

positive and negative x regions, i.e., chaos-chaos intermittency arises. With positive feedback ($K = 0.2$ in the $A = 9.8$ case and $K = 0.7$ in the $A = 12.0$ case, **Figure 3B**), the absolute

values of f_{\max} and f_{\min} are reduced, and the attractor merging conditions are not satisfied; the orbit $x(n)$ is constrained to lie within either the positive or negative x region, depending



on the initial value of $x(0)$, as shown in the right graph of **Figure 3A**.

2.3. Evaluation Indices

For the evaluation of the attractor-merging bifurcation, the conditions $F(f_{\max}) + Ku(f_{\max})$ and $F(f_{\min}) + Ku(f_{\min})$ were utilized. $F(f_{\max, \min}) + Ku(f_{\max, \min}) = 0$ corresponds to the attractor-merging bifurcation point. To judge the chaotic state of frontal cortical neural activity $x(n)$, the Lyapunov exponent was calculated as (Parker and Chua, 2012):

$$\lambda = \frac{1}{\tau M} \sum_{k=1}^M \ln \left(\frac{d^k(t_l = \tau)}{d^k(t_l = 0)} \right). \quad (5)$$

Here, $d^k(t_l = 0) = d_0$ ($k = 1, 2, \dots, M$) denotes M perturbed initial conditions to $x(n)$ applied at $n = n_0 + (k - 1)\tau$. Their time evolution for $t_l \in [0: \tau]$ is $d^k(t_l = \tau) = (x(n) - x'(n))|_{n=n_0+k\tau}$. Furthermore, $x'(n)$ is a perturbation applied to the orbit. $\lambda > 0$ and $\lambda < 0$ correspond to the chaotic and periodic states, respectively.

The synchronization between $x(n)$ and $S(n)$ was evaluated using their correlation coefficient at time delay τ as follows:

$$C(\tau) = \frac{C_{sx}(\tau)}{\sqrt{C_{ss}C_{xx}}}, \quad (6)$$

$$C_{sx}(\tau) = \langle (S(n + \tau) - \langle S \rangle)(x(n) - \langle x \rangle) \rangle, \quad (7)$$

$$C_{ss} = \langle (S(n) - \langle S \rangle)^2 \rangle, \quad (8)$$

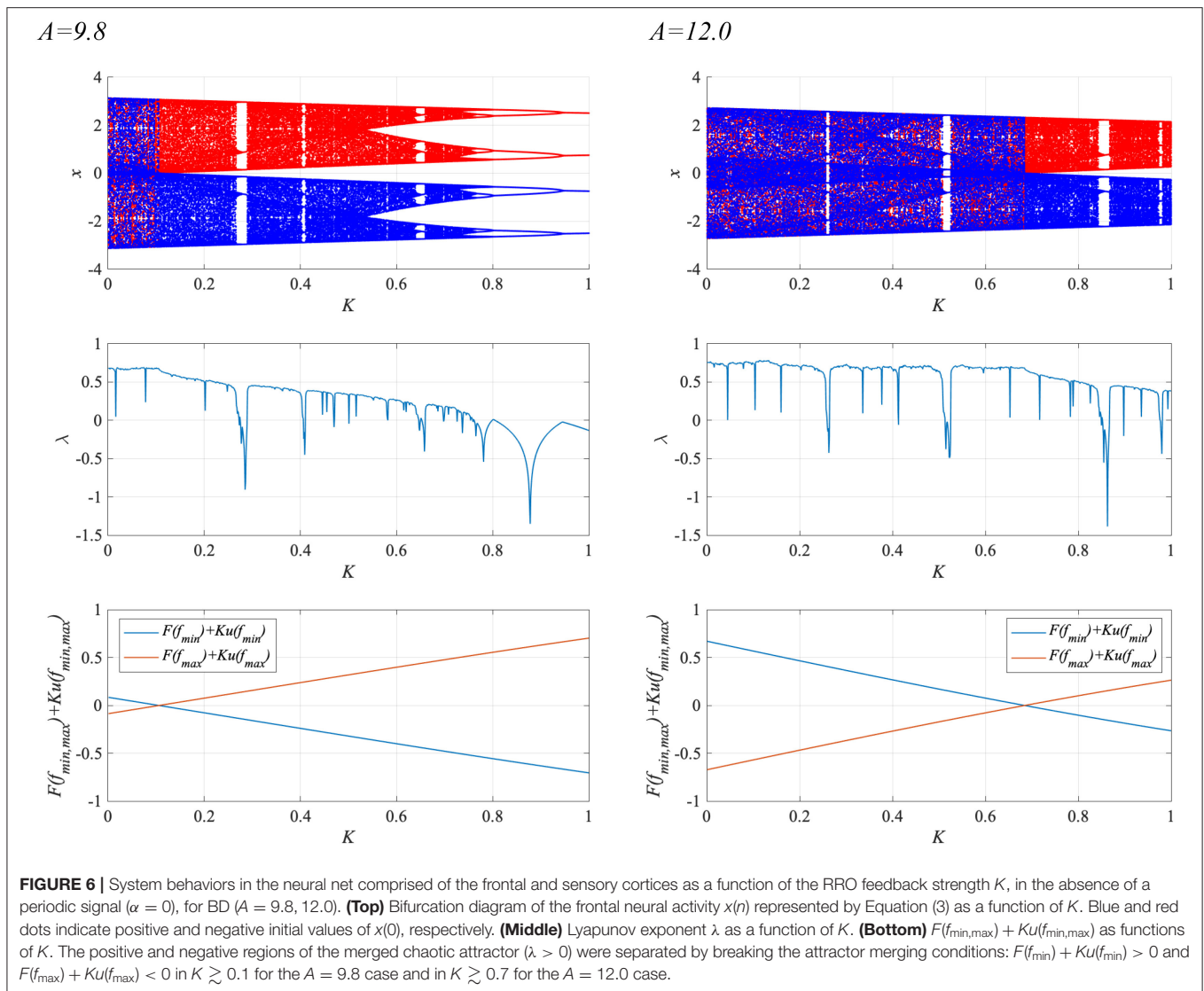
$$C_{xx} = \langle (x(n) - \langle x \rangle)^2 \rangle, \quad (9)$$

where $\langle \cdot \rangle$ denotes the average in n . In this study, τ is set to the value for $\max_{\tau} C(\tau)$ in each time series of $x(n)$. The values for $\max_{\tau} C(\tau)$ are measured against ten trials with different initial values of $x(0)$.

To evaluate the amount of the perturbation due to the RRO feedback signal $Ku(x)$ plus the periodic input signal $S(n)$, we used the temporal mean value of the squared perturbations:

$$\Xi = \langle (Ku(x(n)))^2 + (S(n))^2 \rangle, \quad (10)$$

where $\langle \cdot \rangle$ denotes the average in n . The values for Ξ are measured against ten trials with different initial values of $x(0)$.



3. RESULTS

3.1. Frontal Cortical Neural Activity on a Diurnal Timescale

We demonstrated activity in a neural system composed of the frontal and sensory cortices. **Figure 4** shows the bifurcation diagram of the frontal neural activity $x(n)$, Lyapunov exponent λ , and $F(f_{\min,\max}) + Ku(f_{\min,\max})$ as functions of synaptic weights from the inhibitory neural population A in the absence of a feedback or periodic signal ($K = 0, \alpha = 0$). With an increase in the A value, $x(n)$ exhibits a period-doubling bifurcation and enters a chaotic state $A \gtrsim 8.1$ ($\lambda > 0$). In $8.1 \lesssim A \lesssim 9.8$, $x(n)$ is trapped in either the negative or the positive region, depending on the initial values of $x(0)$, $F(f_{\min}) + Ku(f_{\min}) < 0$, and $F(f_{\max}) + Ku(f_{\max}) > 0$. The attractor merging conditions $F(f_{\min}) + Ku(f_{\min}) > 0$ and $F(f_{\max}) + Ku(f_{\max}) < 0$ are satisfied in $A \gtrsim 9.8$; consequently, $x(n)$ hops back and forth between negative and positive regions, which is known as chaos-chaos intermittency.

This effect corresponds with the merger of attractors in the negative and positive regions of the bifurcation diagram. The window of periodicity is $12.5 \lesssim A \lesssim 13.5$. Hadaeghi et al. considered that frontal neural activity in the periodic window corresponds to that of healthy subjects (healthy control [HC]), whereas chaos-chaos intermittent activity corresponds to that of patients with BD (Hadaeghi et al., 2016). **Figure 5** shows typical examples of the frontal neural activity $x(n)$ governed by Equation (1) in HCs and in patients with BD. At $A = 13.0$, corresponding with typical HC behavior, $x(n)$ exhibits the periodic-4 state, where the parameter set is located in the periodic window in the top part of **Figure 4**. In this periodic window, various period- p states exist through period-doubling bifurcation; therefore, as healthy period- p states, we used $p = 4, 8, 16, 32$ in this study. At $A = 9.8, 12.0$, corresponding to BD behavior, $x(n)$ exhibits chaos-chaos intermittency. In both HC and BD cases, the attractor merging condition is satisfied with $F(f_{\max}) + Ku(f_{\max}) < 0$ and $F(f_{\min}) + Ku(f_{\min}) > 0$.

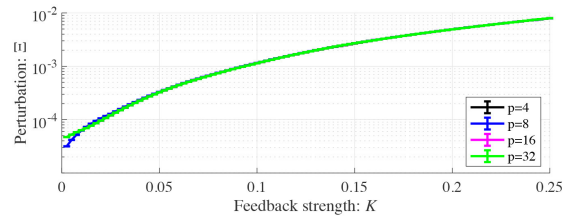
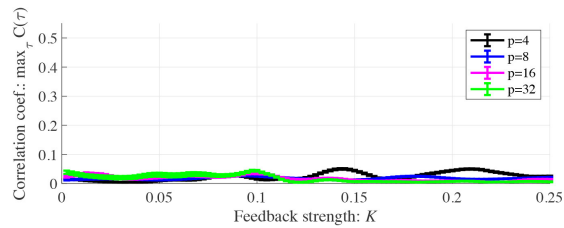
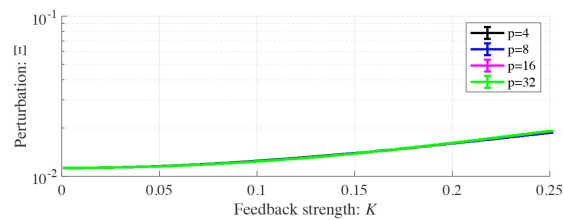
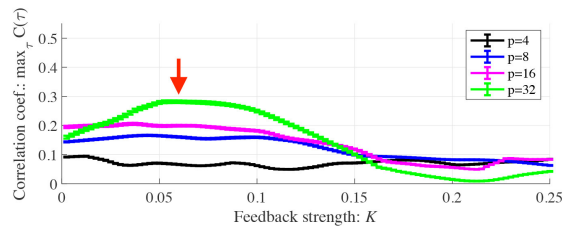
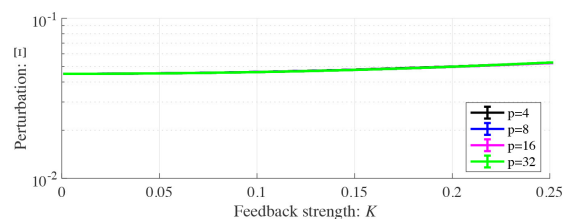
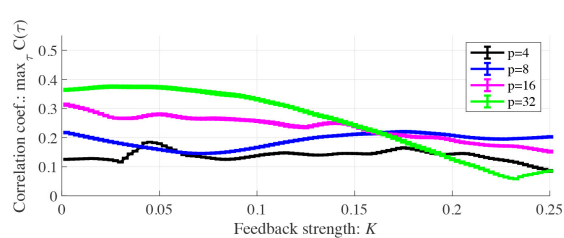
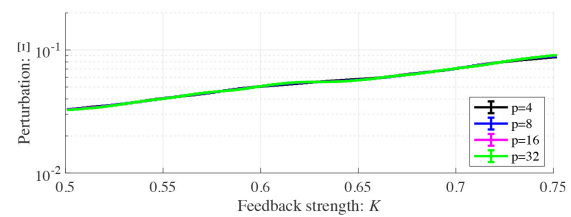
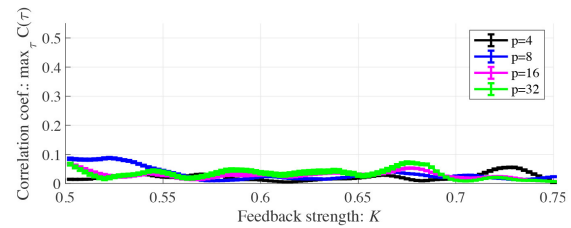
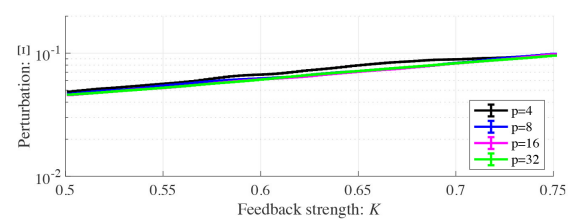
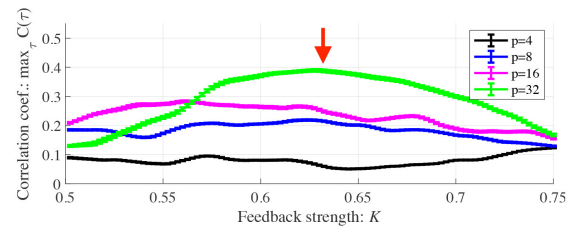
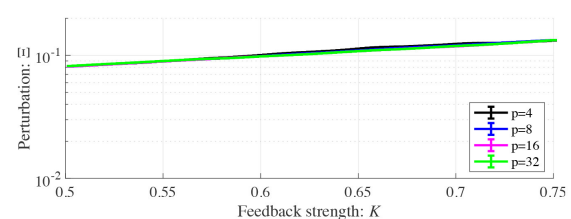
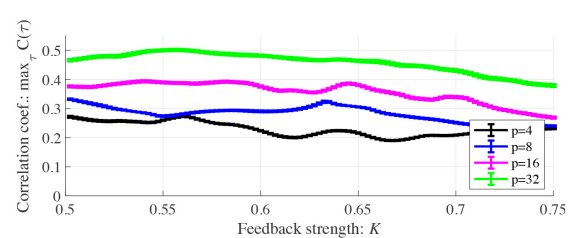
$A=9.8$ $\alpha = 0.01$  $\alpha = 0.15$  $\alpha = 0.30$  $A=12.0$ $\alpha = 0.01$  $\alpha = 0.15$  $\alpha = 0.30$ 

FIGURE 7 | Synchronization of neural activity $x(n)$ to a weak periodic input signal $S(n)$ ($\alpha = 0.01, 0.15, 0.3$ and $p = 4, 8, 16, 32$) and perturbations of the RRO feedback signal and the periodic input signal in BD cases ($A = 9.8, 12.0$). Here, the period p values are chosen based on the healthy periodic- p states locating in the (Continued)

FIGURE 7 | periodic window in $12.5 \lesssim A \lesssim 13.5$ in **Figure 4**. Dependence of **(Upper)** $\max_{\tau} C(\tau)$ and **(Lower)** Ξ on the RRO feedback strength K . Solid black lines and error bars show the mean and standard deviation across ten trials. In the lower panels, the scales of the vertical axes differ. In the case with $\alpha = 0.15$ and $p = 32$ (represented by red arrows), $\max_{\tau} C(\tau)$ exhibits a unimodal maximum ($\max_{\tau} C(\tau) \approx 0.3$ in $A = 9.8$ and $\max_{\tau} C(\tau) \approx 0.4$ in $A = 12.0$) at around the attractor-merging bifurcation at $K \approx 0.06$ in $A = 9.8$, and $K \approx 0.63$ in $A = 12.0$. At this K condition, the perturbation amounts Ξ are 0.012, 0.049 in the $A = 9.8, 12.0$ cases, respectively.

3.2. Transition From Disturbed Neural Activity to a Periodic State by RRO Feedback Plus Periodic Input Signal

To enhance synchronization to weak input signals, the system parameters must be adjusted to those of the attractor-merging bifurcation (Nobukawa et al., 2018b). **Figure 6** shows the behavior of the neural system composed of the frontal and sensory cortices as a function of RRO feedback strength K , in the absence of a periodic signal ($\alpha = 0$), for BD ($A = 9.8, 12.0$). Shown are the bifurcation diagram of the frontal neural activity $x(n)$ given by Equation (3), the Lyapunov exponent λ , and $F(f_{\min, \max}) + Ku(f_{\min, \max})$. The separation of merged chaotic attractors ($\lambda > 0$) into positive and negative regions arises at the region for $F(f_{\min}) + Ku(f_{\min}) < 0$, $F(f_{\max}) + Ku(f_{\max}) > 0$ in $K \gtrsim 0.1$ for the $A = 9.8$ case and in $K \gtrsim 0.7$ for the $A = 12.0$ case.

Subsequently, synchronization of $x(n)$ to a weak periodic input signal $S(n)$ ($\alpha = 0.01, 0.15, 0.3$ and $p = 4, 8, 16, 32$) and the evaluated perturbations of the RRO feedback and periodic signals are shown. Here, the p values are chosen based on the healthy periodic- p states locating at the periodic window in $12.5 \lesssim A \lesssim 13.5$. **Figure 7** shows the dependence of $\max_{\tau} C(\tau)$ and Ξ on the RRO feedback strength K . In the case with $\alpha = 0.15$ and $p = 32$, $\max_{\tau} C(\tau)$ exhibits a unimodal maximum ($\max_{\tau} C(\tau) \approx 0.3$ in $A = 9.8$ and $\max_{\tau} C(\tau) \approx 0.4$ in $A = 12.0$) at around the attractor-merging bifurcation defined as $F(f_{\min, \max}) + Ku(f_{\min, \max}) = 0$ at $K \approx 0.06$ in $A = 9.8$ and $K \approx 0.63$ in $A = 12.0$ (see **Figure 6**), i.e., chaotic resonance is induced by the RRO feedback signal. Therefore, applying the RRO feedback signal together with a weak periodic signal brings the neural activity $x(n)$ of BD close to the healthy periodic state. This chaotic resonance is induced when the perturbation $\Xi = 0.012, 0.049$, at $A = 9.8, 12.0$, respectively. This perturbation is relatively small in comparison to the variation range: $-2.5 \lesssim x(n) \lesssim 2.5$, as shown in the bifurcation diagram of **Figure 6**. Under conditions of higher input frequency ($p = 2, 4, 8, 16$) or weaker signal strength ($\alpha = 0.01$), the values of $\max_{\tau} C(\tau)$ are significantly reduced. At stronger signal strength ($\alpha = 0.3$), the values of $\max_{\tau} C(\tau)$ exhibit a tendency to decrease monotonically with increasing K . Thus, chaotic resonance can be induced by RRO feedback signals at an appropriate signal strength and frequency. **Figure 8** shows a typical time series of frontal neural activity $x(n)$ in synchronization with a weak periodic input signal $S(n)$ under conditions that induce chaotic resonance in **Figure 7**, i.e., $p = 32, \alpha = 0.15$, and $K = 0.06$ in the $A = 9.8$ case; and $K = 0.63$ in the $A = 12.0$ case. The result shows synchronization between the chaos-chaos intermittency of $x(n)$ and the periodic input signal $S(n)$, with hopping between positive and negative $x(n)$ regions. Additionally, **Figure 9** shows the bifurcation diagram of $x(n)$ represented by Equation (3) as a function of K under a weak

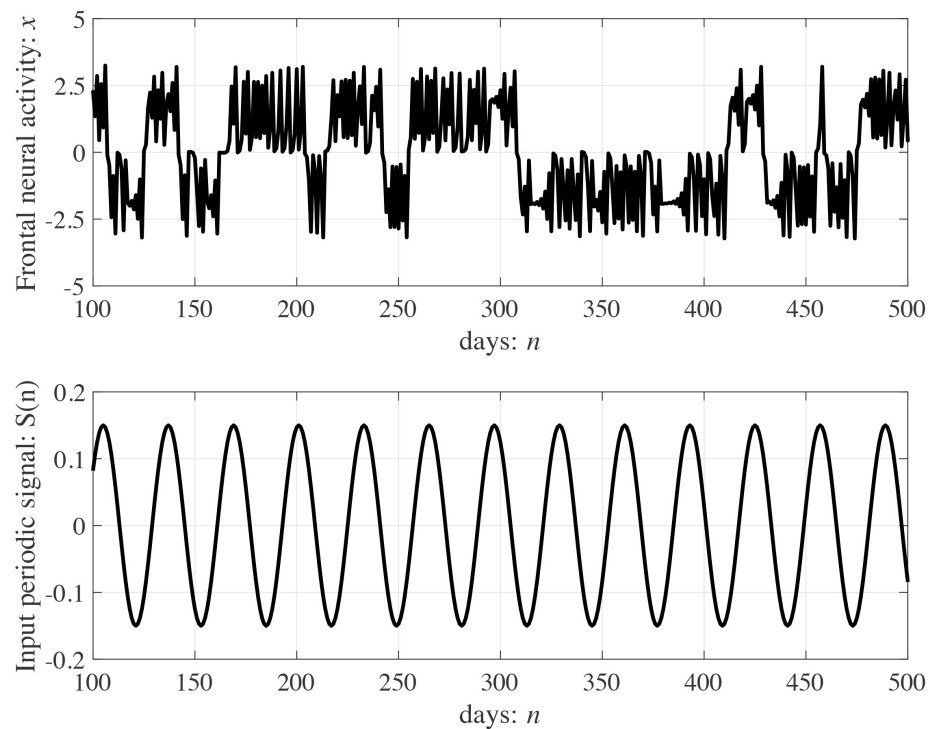
periodic input signal $S(n)$ ($p = 32, \alpha = 0.15$) in BD, in ($A = 9.8, 12.0$) cases. The chaos-chaos intermittency between positive and negative $x(n)$ regions is maintained until around the peak of $\max_{\tau} C(\tau)$ (represented in **Figure 7**) in $K \lesssim 0.18$ for the $A = 9.8$ case and in $K \lesssim 0.79$ for the $A = 12.0$ case. Therefore, the chaotic resonance confirmed in **Figure 7** produces synchronization of the chaos-chaos intermittency with the periodic input signal $S(n)$.

To evaluate the effect of the RRO feedback signal on synchronization, we compared the synchronization induced by RRO feedback with that in its absence ($K = 0$). **Figure 10** shows the dependence of $\max_{\tau} C(\tau)$ and Ξ on the signal strength α in the case of no RRO feedback under the condition where chaotic resonance is induced by the RRO feedback signal at $p = 32$ in **Figure 7**. In the $A = 9.8$ case with $\alpha \gtrsim 0.22$, $\max_{\tau} C(\tau)$ exceeds 0.3, which corresponds to the maximum value of $\max_{\tau} C(\tau)$ under RRO feedback presented in **Figure 7**. Moreover, the perturbation amount Ξ at $\alpha \approx 0.22$ required for accomplishing $\max_{\tau} C(\tau) \approx 0.3$ is approximately 0.025; however, under RRO feedback, it is $\Xi \approx 0.012$ at $K \approx 0.06$ for a peak correlation of $\max_{\tau} C(\tau) \approx 0.3$. Therefore, the RRO feedback signal reduces the amount of perturbation needed for the transition to the periodic state. In the $A = 12.0$ case, the same tendency seen in the $A = 9.8$ case is confirmed. That is, the perturbation amount Ξ at $\alpha \approx 0.95$ required for accomplishing $\max_{\tau} C(\tau) \approx 0.4$ is approximately 0.41; however, under RRO feedback, it is $\Xi \approx 0.049$ at $K \approx 0.63$ for a peak correlation of $\max_{\tau} C(\tau) \approx 0.4$.

4. DISCUSSION AND CONCLUSIONS

In this study, we verified our hypothesis that chaotic resonance induced by RRO feedback signals can enable the delivery of chronotherapy by minimally invasive treatments. In a simulation based on the Hadaeghi model, we evaluated the transition of the disturbed frontal cortical neural activity corresponding to BD to the periodic behavior found in the HCs that was induced by RRO feedback signals. We found that the RRO feedback signal, which is based on the return-map structure of the modeled frontal and sensory cortical neural system, induced synchronization to weak, periodic signals corresponding to the healthy condition at appropriate feedback strength, although this synchronization was restricted to a relatively low frequency of the input signal. Thus, the chaotic resonance induced by the RRO feedback signal facilitates the transition to a state that is close to healthy, periodic frontal neural activity in the case where this activity has a relatively low frequency. Additionally, the combined amount of perturbation due to the RRO feedback signal and the periodic input signal was significantly smaller than that required for inducing a synchronous state by applying only the periodic signal.

$A=9.8$ case ($K=0.06$, $\alpha=0.15$, $p=32$)



$A=12.0$ case ($K=0.63$, $\alpha=0.15$, $p=32$)

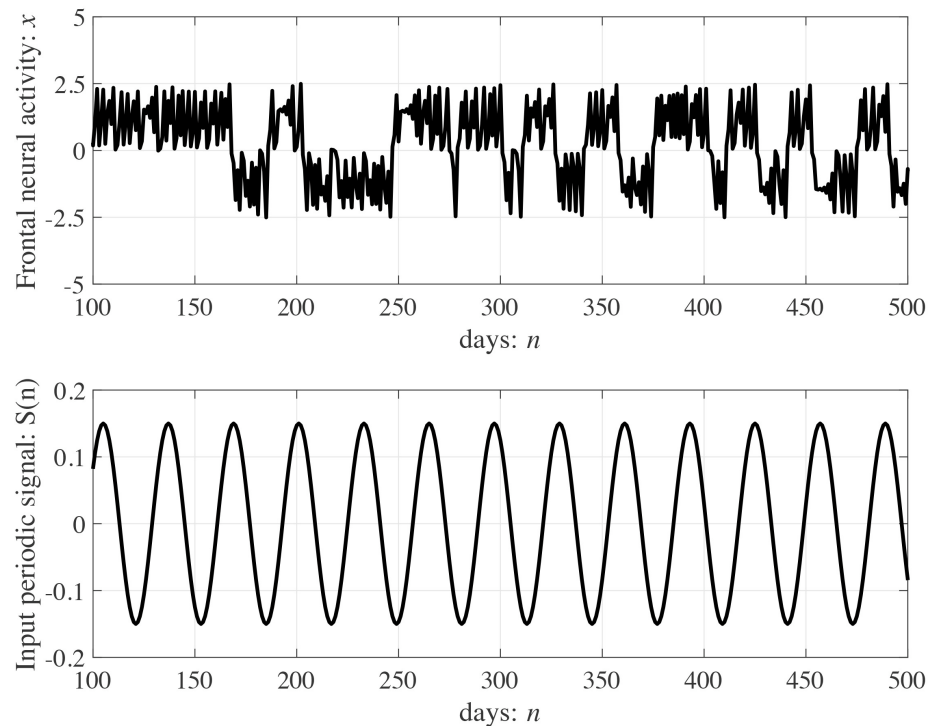
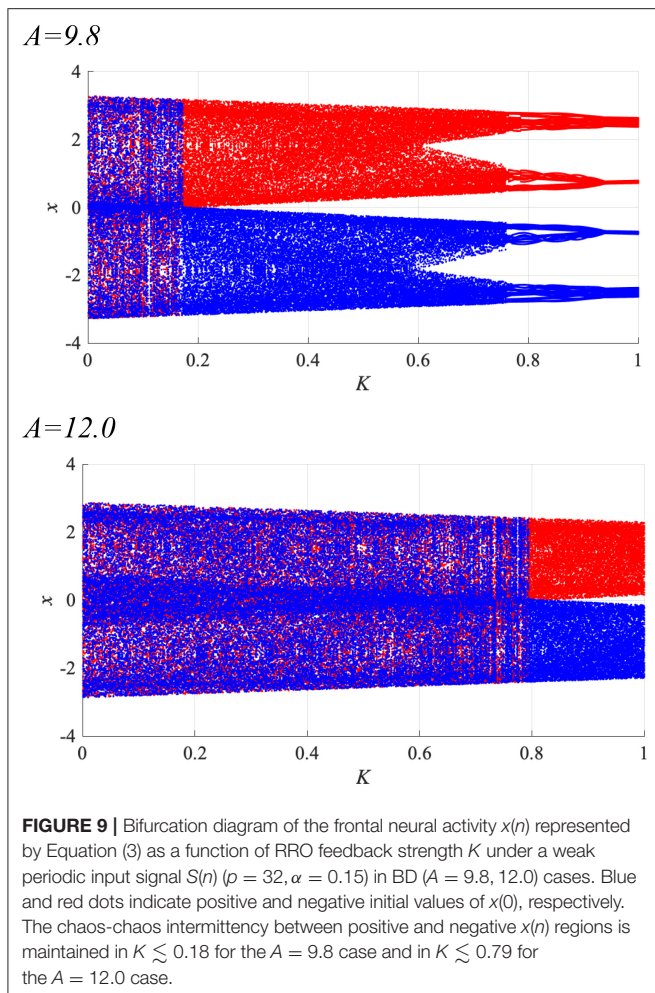


FIGURE 8 | Typical time series of frontal neural activity $x(n)$ in synchronization with a weak periodic input signal $S(n)$ under the conditions for inducing chaotic resonance shown in **Figure 7**. Synchronization between the chaos-chaos intermittency of $x(n)$ and the periodic input signal $S(n)$ is shown, which features hopping between positive and negative $x(n)$ regions ($\max_{\tau} C(\tau) \approx 0.3, 0.4$ in $A = 9.8, 12.0$ cases, respectively).

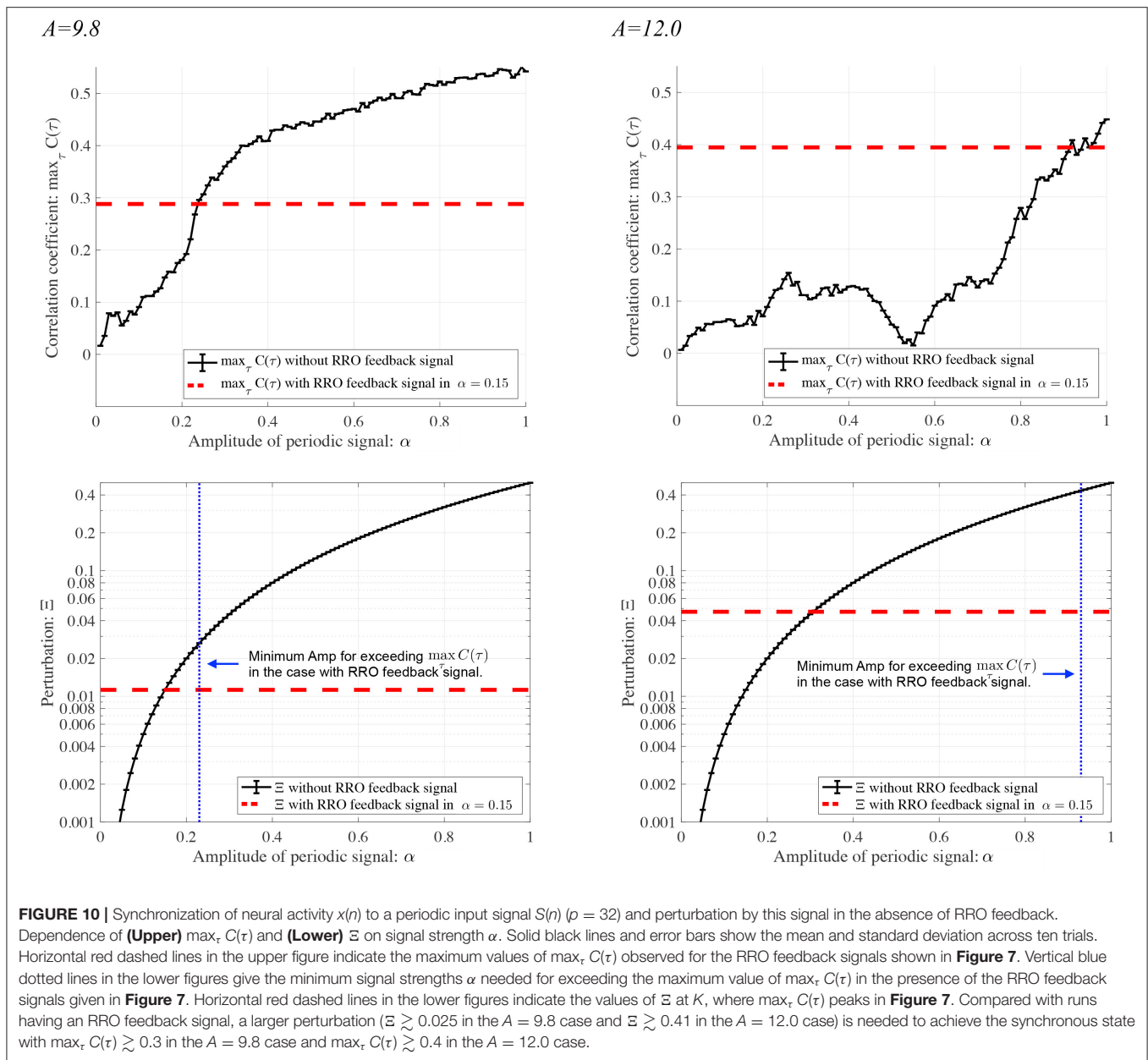


First, we must consider the reason the RRO feedback signal facilitates synchronization by small perturbations. Over the past few decades, studies of non-linear control aimed at stabilizing chaotic activity have proposed many methods such as the Ott-Grebogi-Yorke method, the delay feedback method, and the H_∞ method (Ott et al., 1990; Pyragas, 1992; Nakajima, 1997; Jiang et al., 2005; reviewed in Schöll and Schuster, 2008). These conventional chaos control methods stabilize the chaotic orbit to equilibrium points and periodic orbits. In contrast, the RRO feedback method does not eliminate chaotic behavior but adjusts local maximum and minimum values of the map function; consequently, the feedback strength at which chaotic behavior is maintained in RRO is smaller than that of conventional chaos control methods, in which chaotic behavior is completely suppressed (Nobukawa et al., 2018b). Moreover, by virtue of chaotic resonance at around the attractor-merging bifurcation induced by the RRO feedback signal, chaos-chaos intermittency synchronizes with input signals even at low input-signal strength (Sinha, 1999; Nishimura et al., 2000; reviewed in Anishchenko et al., 2007; Rajasekar and Sanjuán, 2016). Utilizing these advantages of the RRO feedback method and of chaotic resonance should facilitate the

transition of the disturbed neural activity of BD to a healthy periodic state.

Furthermore, the application of RRO feedback signals with periodic input signals shows great promise for actual chronotherapy practice. In current chronotherapy, the administration of the light stimulus and the medication occurs at a fixed time each day to enable the transition of neural activity to a periodic state with a circadian period (Yeragani et al., 2003; Glenn et al., 2006; Bonsall et al., 2011; Moore et al., 2014; reviewed in Albrecht, 2013). This treatment may correspond to the case we consider here, in which neural activity is stabilized by applying only a periodic input signal (see Figure 10). The application of the light stimulus and medication on a schedule modulated by the daily frontal neural activity of each patient would correspond to the application of RRO feedback signals in combination with the periodic input signal, in which the amount of perturbation needed for the transition to the periodic state is expected to be significantly reduced. That is, this strategy may lead to a reduction in the amounts of stimulus and medication necessary to transition from a disturbed frontal neural activity to a healthy periodic state. Furthermore, this effect might also contribute to a reduction in mixed states, hypomania, and autonomic hyperactivations that can occur in BD chronotherapy due to overapplication of light stimuli and medication. Additionally, methods for measuring the daily variation of frontal neural activity are now under development, with a focus on EEG approaches (Croce et al., 2018; González et al., 2019). These methods might contribute to the realization of a form of chronotherapy modulated by RRO feedback.

The following limitations of this study must be considered. First, only the neural system composed of frontal and sensory cortices was considered. However, the circadian rhythms targeted in chronotherapy are produced not only by the frontal and sensory cortices but also by the hypothalamus (Hadaeghi et al., 2016; Bayani et al., 2017). Therefore, the evaluation of chaotic resonance induced by the RRO feedback method in a neural system comprising both the frontal/sensory cortex and the hypothalamus is important for evaluating its applicability to chronotherapy. Second, we used competition between excitatory and inhibitory neurons in this study to describe long-term neural dynamics in the frontal cortex. However, the questions of what reflects the long-term dynamics of brain activity and what mechanism produces it are currently controversial (Croce et al., 2018; González et al., 2019). Therefore, it is important that our proposed method be verified with models based on other neural mechanisms for producing long-term neural dynamics in the frontal cortex. In such evaluations, the use of spiking neuron models, which exhibit highly realistic neurodynamics (Nobukawa et al., 2017, 2018a, reviewed in Ma and Tang, 2017), would enhance the pathological validity of the neural network used to simulate BD (Brambilla et al., 2003; Hasler et al., 2007; Sanacora et al., 2012; Schloesser et al., 2012; reviewed in Chiapponi et al., 2016). Third, from the viewpoint of chaotic resonance, the disturbed neural activity described as chaotic dynamics in this study was close to the healthy periodic state. However, to stabilize more challenging forms of chaotic behavior, other candidate chaos control methods must be considered; we



plan to research these points in the future. In addition to model-based studies, the methods of measuring the daily-timescale variation in the frontal neural activity that have recently been proposed (Croce et al., 2018; González et al., 2019) will be crucial for applications and will aid in the estimation of the controlling parameters required by RRO feedback methods.

In conclusion, in this simulation study, chaotic resonance induced by the RRO feedback method enabled the disturbed frontal neural activity characteristic of BD to be transitioned close to a healthy periodic state by relatively weak perturbations. Despite its limitations, this study demonstrated that chronotherapy modulated by the RRO feedback method might be a new type of minimally invasive therapy for BD.

DATA AVAILABILITY STATEMENT

The raw data supporting the conclusions of this article will be made available by the authors, without undue reservation.

AUTHOR CONTRIBUTIONS

SN, HN, and TT conceived the methods. SN and NW analyzed the results, wrote the main text, and prepared all figures. SN and HD conducted the experiments. All authors have reviewed the manuscript.

FUNDING

This work was supported by JSPS KAKENHI for Scientific Research (C) [grant number 20K11976] to HN. It was partially supported by JST CREST [grant number JPMJCR17A4].

REFERENCES

- Abreu, T., and Bragança, M. (2015). The bipolarity of light and dark: a review on bipolar disorder and circadian cycles. *J. Affect. Disord.* 185, 219–229. doi: 10.1016/j.jad.2015.07.017
- Albrecht, U. (2013). “Circadian clocks and mood-related behaviors,” in *Circadian Clocks*, eds A. Kramer and M. Mrosovsky (Berlin; Heidelberg: Springer), 227–239. doi: 10.1007/978-3-642-25950-0_9
- Anishchenko, V. S., Astakhov, V., Neiman, A., Vadivasova, T., and Schimansky-Geier, L. (2007). *Nonlinear Dynamics of Chaotic and Stochastic Systems: Tutorial and Modern Developments*. Berlin; Heidelberg: Springer Science & Business Media.
- Arnone, D. (2019). Functional MRI findings, pharmacological treatment in major depression and clinical response. *Prog. Neuro Psychopharmacol. Biol. Psychiatry* 91, 28–37. doi: 10.1016/j.pnpbp.2018.08.004
- Baskaran, A., Milev, R., and McIntyre, R. S. (2012). The neurobiology of the eeg biomarker as a predictor of treatment response in depression. *Neuropharmacology* 63, 507–513. doi: 10.1016/j.neuropharm.2012.04.021
- Bayani, A., Hadaeghi, F., Jafari, S., and Murray, G. (2017). Critical slowing down as an early warning of transitions in episodes of bipolar disorder: a simulation study based on a computational model of circadian activity rhythms. *Chronobiol. Int.* 34, 235–245. doi: 10.1080/07420528.2016.1272608
- Baysal, V., Saraç, Z., and Yilmaz, E. (2019). Chaotic resonance in Hodgkin–Huxley neuron. *Nonlinear Dyn.* 97, 1275–1285. doi: 10.1007/s11071-019-05047-w
- Bonsall, M. B., Wallace-Hadrill, S. M., Geddes, J. R., Goodwin, G. M., and Holmes, E. A. (2011). Nonlinear time-series approaches in characterizing mood stability and mood instability in bipolar disorder. *Proc. R. Soc. B Biol. Sci.* 279, 916–924. doi: 10.1098/rspb.2011.1246
- Brambilla, P., Perez, J., Barale, F., Schettini, G., and Soares, J. (2003). Gabaergic dysfunction in mood disorders. *Mol. Psychiatry* 8, 721–737. doi: 10.1038/sj.mp.4001362
- Cain, S. W., Rawashdeh, O. A., Siu, M., Kim, S. C., and Ralph, M. R. (2017). Dopamine dependent setting of a circadian oscillator underlying the memory for time of day. *Neurobiol. Learn. Memory* 141, 78–83. doi: 10.1016/j.nlm.2017.03.015
- Castaneda, T. R., de Prado, B. M., Prieto, D., and Mora, F. (2004). Circadian rhythms of dopamine, glutamate and GABA in the striatum and nucleus accumbens of the awake rat: modulation by light. *J. Pineal Res.* 36, 177–185. doi: 10.1046/j.1600-079X.2003.00114.x
- Chiapponi, C., Piras, F., Piras, F., Caltagirone, C., and Spalletta, G. (2016). Gaba system in schizophrenia and mood disorders: a mini review on third-generation imaging studies. *Front. Psychiatry* 7:61. doi: 10.3389/fpsy.2016.00061
- Croce, P., Quercia, A., Costa, S., and Zappasodi, F. (2018). Circadian rhythms in fractal features of EEG signals. *Front. Physiol.* 9:1567. doi: 10.3389/fphys.2018.01567
- Daugherty, D., Roque-Urrea, T., Urrea-Roque, J., Troyer, J., Wirkus, S., and Porter, M. A. (2009). Mathematical models of bipolar disorder. *Commun. Nonlinear Sci. Num. Simul.* 14, 2897–2908. doi: 10.1016/j.cnsns.2008.10.027
- Drevets, W. C. (2000). Neuroimaging studies of mood disorders. *Biol. Psychiatry* 48, 813–829. doi: 10.1016/S0006-3223(00)01020-9
- Enders, L. R., Hur, P., Johnson, M. J., and Seo, N. J. (2013). Remote vibrotactile noise improves light touch sensation in stroke survivors' fingertips via stochastic resonance. *J. Neuroeng. Rehabil.* 10:105. doi: 10.1186/1743-0003-10-105
- Glenn, T., Whybrow, P. C., Rasgon, N., Grof, P., Alda, M., Baethge, C., et al. (2006). Approximate entropy of self-reported mood prior to episodes in bipolar disorder. *Bipolar Disord.* 8, 424–429. doi: 10.1111/j.1399-5618.2006.00373.x
- Goldbeter, A. (1995). A model for circadian oscillations in the drosophila period protein (per). *Proc. R. Soc. Lond. Ser. B Biol. Sci.* 261, 319–324. doi: 10.1098/rspb.1995.0153
- González, J., Cavelli, M., Mondino, A., Pascovich, C., Castro-Zaballa, S., Tortorolo, P., et al. (2019). Decreased electrocortical temporal complexity distinguishes sleep from wakefulness. *Sci. Rep.* 9, 1–9. doi: 10.1038/s41598-019-54788-6
- Hadaeghi, F., Hashemi Golpayegani, M. R., and Gharibzadeh, S. (2013a). What is the mathematical description of the treated mood pattern in bipolar disorder? *Front. Comput. Neurosci.* 7:106. doi: 10.3389/fncom.2013.00106
- Hadaeghi, F., Hashemi Golpayegani, M. R., Jafari, S., and Murray, G. (2016). Toward a complex system understanding of bipolar disorder: a chaotic model of abnormal circadian activity rhythms in euthymic bipolar disorder. *Austral. N. Z. J. Psychiatry* 50, 783–792. doi: 10.1177/0004867416642022
- Hadaeghi, F., Hashemi Golpayegani, M. R., and Moradi, K. (2013b). Does “crisis-induced intermittency” explain bipolar disorder dynamics? *Front. Comput. Neurosci.* 7:116. doi: 10.3389/fncom.2013.00116
- Hampp, G., Ripberger, J. A., Houben, T., Schmutz, I., Blex, C., Perreau-Lenz, S., et al. (2008). Regulation of monoamine oxidase a by circadian-clock components implies clock influence on mood. *Curr. Biol.* 18, 678–683. doi: 10.1016/j.cub.2008.04.012
- Hasler, G., van der Veen, J. W., Tuminis, T., Meyers, N., Shen, J., and Drevets, W. C. (2007). Reduced prefrontal glutamate/glutamine and γ -aminobutyric acid levels in major depression determined using proton magnetic resonance spectroscopy. *Arch. Gen. Psychiatry* 64, 193–200. doi: 10.1001/archpsyc.64.2.193
- Herzog, E. D. (2007). Neurons and networks in daily rhythms. *Nat. Rev. Neurosci.* 8, 790–802. doi: 10.1038/nrn2215
- Hirschfeld, R., Calabrese, J. R., Weissman, M. M., Reed, M., Davies, M. A., Frye, M. A., et al. (2003). Screening for bipolar disorder in the community. *J. Clin. Psychiatry* 64, 53–59. doi: 10.4088/jcp.v64n0111
- Jiang, W., Guo-Dong, Q., and Bin, D. (2005). H8 variable universe adaptive fuzzy control for chaotic system. *Chaos Solitons Fractals* 24, 1075–1086. doi: 10.1016/j.chaos.2004.09.056
- Kessler, R. C., Berglund, P., Demler, O., Jin, R., Koretz, D., Merikangas, K. R., et al. (2003). The epidemiology of major depressive disorder: results from the national comorbidity survey replication (NCS-R). *JAMA* 289, 3095–3105. doi: 10.1001/jama.289.23.3095
- Kurita, Y., Shinohara, M., and Ueda, J. (2013). Wearable sensorimotor enhancer for fingertip based on stochastic resonance effect. *IEEE Trans. Hum. Mach. Syst.* 43, 333–337. doi: 10.1109/TSMC.2013.2242886
- Kurita, Y., Sueda, Y., Ishikawa, T., Hattori, M., Sawada, H., Egi, H., et al. (2016). Surgical grasping forceps with enhanced sensorimotor capability via the stochastic resonance effect. *IEEE/ASME Trans. Mechatron.* 21, 2624–2634. doi: 10.1109/TMECH.2016.2591591
- Kurosawa, G., Aihara, K., and Iwasa, Y. (2006). A model for the circadian rhythm of cyanobacteria that maintains oscillation without gene expression. *Biophys. J.* 91, 2015–2023. doi: 10.1529/biophysj.105.076554
- Leibenluft, E., Turner, E. H., Feldman-Naim, S., Schwartz, P. J., Wehr, T. A., and Rosenthal, N. E. (1995). Light therapy in patients with rapid cycling bipolar disorder: preliminary results. *Psychopharmacol. Bull.* 31, 705–710.
- López-Muñoz, F., Vieta, E., Rubio, G., García-García, P., and Alamo, C. (2006). Bipolar disorder as an emerging pathology in the scientific literature: a bibliometric approach. *J. Affect. Disord.* 92, 161–170. doi: 10.1016/j.jad.2006.02.006
- Ma, J., and Tang, J. (2017). A review for dynamics in neuron and neuronal network. *Nonlinear Dyn.* 89, 1569–1578. doi: 10.1007/s11071-017-3565-3
- Montague, P. R., Dolan, R. J., Friston, K. J., and Dayan, P. (2012). Computational psychiatry. *Trends Cogn. Sci.* 16, 72–80. doi: 10.1016/j.tics.2011.11.018

ACKNOWLEDGMENTS

The authors would like to thank Dr. Fatemeh Hadaeghi for useful discussion of the numerical simulations.

- Moore, P. J., Little, M. A., McSharry, P. E., Goodwin, G. M., and Geddes, J. R. (2014). Mood dynamics in bipolar disorder. *Int. J. Bipolar Disord.* 2:11. doi: 10.1186/s40345-014-0011-z
- Nakajima, H. (1997). On analytical properties of delayed feedback control of chaos. *Phys. Lett. A* 232, 207–210. doi: 10.1016/S0375-9601(97)00362-9
- Nishimura, H., Katada, N., and Aihara, K. (2000). Coherent response in a chaotic neural network. *Neural Process. Lett.* 12, 49–58. doi: 10.1023/A:1009626028831
- Nobukawa, S., Doho, H., Shibata, N., Nishimura, H., and Yamanishi, T. (2020). Chaos-chaos intermittency synchronization controlled by external feedback signals in Chua's circuits. *IEICE Trans. Fundamentals Electron. Commun. Comput. Sci.* (Cham), 103, 303–312. doi: 10.1587/transfun.2019EAP1081
- Nobukawa, S., and Nishimura, H. (2016). Chaotic resonance in coupled inferior olive neurons with the Llinás approach neuron model. *Neural Comput.* 28, 2505–2532. doi: 10.1162/NECO_a_00894
- Nobukawa, S., and Nishimura, H. (2020). Synchronization of chaos in neural systems. *Front. Appl. Math. Stat.* 6:19. doi: 10.3389/fams.2020.00019
- Nobukawa, S., Nishimura, H., and Yamanishi, T. (2016). "Evaluation of chaotic resonance by Lyapunov exponent in attractor-merging type systems," in *International Conference on Neural Information Processing* (Springer), 430–437.
- Nobukawa, S., Nishimura, H., and Yamanishi, T. (2017). Chaotic resonance in typical routes to chaos in the Izhikevich neuron model. *Sci. Rep.* 7, 1–9. doi: 10.1038/s41598-017-01511-y
- Nobukawa, S., Nishimura, H., and Yamanishi, T. (2018a). Routes to chaos induced by a discontinuous resetting process in a hybrid spiking neuron model. *Sci. Rep.* 8, 1–11. doi: 10.1038/s41598-017-18783-z
- Nobukawa, S., Nishimura, H., Yamanishi, T., and Doho, H. (2018b). Controlling chaotic resonance in systems with chaos-chaos intermittency using external feedback. *IEICE Trans. Fundamentals Electron. Commun. Comput. Sci.* 101, 1900–1906. doi: 10.1587/transfun.E101.A.1900
- Nobukawa, S., Nishimura, H., Yamanishi, T., and Doho, H. (2019a). Induced synchronization of chaos-chaos intermittency maintaining asynchronous state of chaotic orbits by external feedback signals. *IEICE Trans. Fundamentals Electron. Commun. Comput. Sci.* 102, 524–531. doi: 10.1587/transfun.E102.A.524
- Nobukawa, S., and Shibata, N. (2019). Controlling chaotic resonance using external feedback signals in neural systems. *Sci. Rep.* 9:4990. doi: 10.1038/s41598-019-41535-0
- Nobukawa, S., Shibata, N., Nishimura, H., Doho, H., Wagatsuma, N., and Yamanishi, T. (2019b). Resonance phenomena controlled by external feedback signals and additive noise in neural systems. *Sci. Rep.* 9, 1–15. doi: 10.1038/s41598-019-48950-3
- Ott, E., Grebogi, C., and Yorke, J. A. (1990). Controlling chaos. *Phys. Rev. Lett.* 64:1196. doi: 10.1103/PhysRevLett.64.1196
- Parker, T. S., and Chua, L. (2012). *Practical Numerical Algorithms for Chaotic Systems*. New York, NY: Springer Science & Business Media.
- Pavlidis, T. (1969). Populations of interacting oscillators and circadian rhythms. *J. Theoret. Biol.* 22, 418–436. doi: 10.1016/0022-5193(69)90014-9
- Pavlidis, T. (2012). *Biological Oscillators: Their Mathematical Analysis*. Amsterdam: Elsevier.
- Pikovsky, A., Rosenblum, M., and Kurths, J. (2003). *Synchronization: A Universal Concept in Nonlinear Sciences*, Vol. 12. Cambridge: Cambridge University Press.
- Price, J. L., and Drevets, W. C. (2010). Neurocircuitry of mood disorders. *Neuropsychopharmacology* 35, 192–216. doi: 10.1038/npp.2009.104
- Pyragas, K. (1992). Continuous control of chaos by self-controlling feedback. *Phys. Lett. A* 170, 421–428. doi: 10.1016/0375-9601(92)90745-8
- Rajasekar, S., and Sanjuán, M. A. F. (2016). *Nonlinear Resonances*. Cham: Springer.
- Sanacora, G., Treccani, G., and Popoli, M. (2012). Towards a glutamate hypothesis of depression: an emerging frontier of neuropsychopharmacology for mood disorders. *Neuropharmacology* 62, 63–77. doi: 10.1016/j.neuropharm.2011.07.036
- Schloesser, R. J., Martinowich, K., and Manji, H. K. (2012). Mood-stabilizing drugs: mechanisms of action. *Trends Neurosci.* 35, 36–46. doi: 10.1016/j.tins.2011.11.009
- Schöll, E., and Schuster, H. G. (2008). *Handbook of Chaos Control*. Vol. 2. Weinheim: Wiley Online Library.
- Seo, N. J., Kosmopoulos, M. L., Enders, L. R., and Hur, P. (2014). Effect of remote sensory noise on hand function post stroke. *Front. Hum. Neurosci.* 8:934. doi: 10.3389/fnhum.2014.00934
- Sinha, S. (1999). Noise-free stochastic resonance in simple chaotic systems. *Phys. A Stat. Mech. Appl.* 270, 204–214. doi: 10.1016/S0378-4371(99)00136-3
- Sit, D., Wisner, K. L., Hanusa, B. H., Stull, S., and Terman, M. (2007). Light therapy for bipolar disorder: a case series in women. *Bipolar Disord.* 9, 918–927. doi: 10.1111/j.1399-5618.2007.00451.x
- Terman, M., and Terman, J. S. (2005). Light therapy for seasonal and nonseasonal depression: efficacy, protocol, safety, and side effects. *CNS Spectrums* 10, 647–663. doi: 10.1017/S1092852900019611
- The Wellcome Trust Case Control Consortium (2007). Genome-wide association study of 14,000 cases of seven common diseases and 3,000 shared controls. *Nature* 447:661. doi: 10.1038/nature05911
- Tobe, B. T., Crain, A. M., Winquist, A. M., Calabrese, B., Makiyama, H., Zhao, W.-N., et al. (2017). Probing the lithium-response pathway in hiPSCs implicates the phosphoregulatory set-point for a cytoskeletal modulator in bipolar pathogenesis. *Proc. Natl. Acad. Sci. U.S.A.* 114, E4462–E4471. doi: 10.1073/pnas.1700111114
- Tretter, F., Gebicke-Haerter, P., An der Heiden, U., Rujescu, D., Mewes, H., and Turck, C. (2011). Affective disorders as complex dynamic diseases—a perspective from systems biology. *Pharmacopsychiatry* 44, S2–S8. doi: 10.1055/s-0031-1275278
- Vargas, C., López-Jaramillo, C., and Vieta, E. (2013). A systematic literature review of resting state network-functional MRI in bipolar disorder. *J. Affect. Disord.* 150, 727–735. doi: 10.1016/j.jad.2013.05.083
- Weber, M., Lauterburg, T., Tobler, I., and Burgunder, J.-M. (2004). Circadian patterns of neurotransmitter related gene expression in motor regions of the rat brain. *Neurosci. Lett.* 358, 17–20. doi: 10.1016/j.neulet.2003.12.053
- Weiner, N., Clement, H.-W., Gamsa, D., and Wesemann, W. (1992). Circadian and seasonal rhythms of 5-HT receptor subtypes, membrane anisotropy and 5-HT release in hippocampus and cortex of the rat. *Neurochem. Int.* 21, 7–14. doi: 10.1016/0197-0186(92)90062-V
- Yeragani, V. K., Pohl, R., Mallavarapu, M., and Balon, R. (2003). Approximate entropy of symptoms of mood: an effective technique to quantify regularity of mood. *Bipolar Disord.* 5, 279–286. doi: 10.1034/j.1399-5618.2003.00012.x

Conflict of Interest: The authors declare that the research was conducted in the absence of any commercial or financial relationships that could be construed as a potential conflict of interest.

Copyright © 2020 Doho, Nobukawa, Nishimura, Wagatsuma and Takahashi. This is an open-access article distributed under the terms of the Creative Commons Attribution License (CC BY). The use, distribution or reproduction in other forums is permitted, provided the original author(s) and the copyright owner(s) are credited and that the original publication in this journal is cited, in accordance with accepted academic practice. No use, distribution or reproduction is permitted which does not comply with these terms.



Steering the Volume of Tissue Activated With a Directional Deep Brain Stimulation Lead in the Globus Pallidus Pars Interna: A Modeling Study With Heterogeneous Tissue Properties

Simeng Zhang^{1*}, Michele Tagliati², Nader Pouratian³, Binith Cheeran¹, Erika Ross¹ and Erick Pereira⁴

¹ Neuromodulation Division, Abbott, Plano, TX, United States, ² Cedars Sinai Medical Center, Los Angeles, CA, United States, ³ Department of Neurosurgery, University of California, Los Angeles, Los Angeles, CA, United States, ⁴ Research Institute of Molecular and Clinical Sciences, St. George's University of London, London, United Kingdom

OPEN ACCESS

Edited by:

Yiannis Ventikos,
University College London,
United Kingdom

Reviewed by:

Jiang Wang,
Tianjin University, China
Da-Hui Wang,
Beijing Normal University, China

*Correspondence:

Simeng Zhang
david.zhang@abbott.com

Received: 11 May 2020

Accepted: 20 August 2020

Published: 25 September 2020

Citation:

Zhang S, Tagliati M, Pouratian N, Cheeran B, Ross E and Pereira E (2020) Steering the Volume of Tissue Activated With a Directional Deep Brain Stimulation Lead in the Globus Pallidus Pars Interna: A Modeling Study With Heterogeneous Tissue Properties. *Front. Comput. Neurosci.* 14:561180. doi: 10.3389/fncom.2020.561180

Objective: To study the effect of directional deep brain stimulation (DBS) electrode configuration and vertical electrode spacing on the volume of tissue activated (VTA) in the globus pallidus, pars interna (GPi).

Background: Directional DBS leads may allow clinicians to precisely direct current fields to different functional networks within traditionally targeted brain areas. Modeling the shape and size of the VTA for various monopolar or bipolar configurations can inform clinical programming strategies for GPi DBS. However, many computational models of VTA are limited by assuming tissue homogeneity.

Methods: We generated a multimodal image-based detailed anatomical (MIDA) computational model with a directional DBS lead (1.5 mm or 0.5 mm vertical electrode spacing) placed with segmented contact 2 at the ventral posterolateral “sensorimotor” region of the GPi. The effect of tissue heterogeneity was examined by replacing the MIDA tissues with a homogeneous tissue of conductance 0.3 S/m. DBS pulses (amplitude: 1 mA, pulse width: 60 μ s, frequency: 130 Hz) were used to produce VTAs. The following DBS contact configurations were tested: single-segment monopole (2B-/Case+), two-segment monopole (2A-/2B-/Case+ and 2B-/3B-/Case+), ring monopole (2A-/2B-/2C-/Case+), one-cathode three-anode bipole (2B-/3A+/3B+/3C+), three-cathode three-anode bipole (2A-/2B-/2C-/3A+/3B+/3C+). Additionally, certain vertical configurations were repeated with 2 mA current amplitude.

Results: Using a heterogeneous tissue model affected both the size and shape of the VTA in GPi. Electrodes with both 0.5 mm and 1.5 mm vertical spacing (1 mA) modeling showed that the single segment monopolar VTA was entirely contained within the GPi when the active electrode is placed at the posterolateral “sensorimotor” GPi. Two segments in a same ring and ring settings, however, produced VTAs outside of the GPi

border that spread into adjacent white matter pathways, e.g., optic tract and internal capsule. Both stacked monopolar settings and vertical bipolar settings allowed activation of structures dorsal to the GPi in addition to the GPi. Modeling of the stacked monopolar settings with the DBS lead with 0.5 mm vertical electrode spacing further restricted VTAs within the GPi, but the VTA volumes were smaller compared to the equivalent settings of 1.5 mm spacing.

Keywords: VTA, DBS, GPi, heterogeneous, Parkinson's disease, directional, segmented, current steering

INTRODUCTION

Deep brain stimulation (DBS) is an established therapy for treatment of advanced movement disorders including Parkinson's disease, tremor, and dystonia. In Parkinson's disease, in addition to the subthalamic nucleus (STN), the posterolateral "sensorimotor" region of the globus pallidus pars interna (GPi) is also targeted due to its larger size and demonstrated efficacy to improve tremor, bradykinesia, rigidity, and drug-induced dyskinesia (Bejjani et al., 1998; Williams et al., 2014; Mirza et al., 2017; Wong et al., 2019). While several studies have reported similar motor benefits when comparing GPi to STN DBS, others have reported less improvement in rigidity and bradykinesia with GPi DBS compared to STN DBS (Krack et al., 1998; Houeto et al., 2000; Okun et al., 2009; Volkmann et al., 2009). In dystonia, GPi is the DBS target of choice with demonstrated long-term efficacy and cost-benefit (Volkmann et al., 2012).

More recently, studies showing significant improvement in bradykinesia with GPi DBS examined the location of the DBS lead within the pallidum and noted that superior outcomes were associated with active contacts located in the dorsal portion of the GPi near the medial medullary lamina (Bejjani et al., 1998; Krack et al., 1998; Yelnik et al., 2000). In addition, stimulation of the external segment of the globus pallidus (GPe) has also been demonstrated to improve bradykinesia and rigidity symptoms (Vitek et al., 2004; Johnson and McIntyre, 2008; Johnson et al., 2012). Therefore, stimulating at the level of medial medullary lamina between GPi and GPe is an emerging concept in GPi programming. The exact mechanisms of GPi DBS-induced symptom relief are still under active investigation. It is likely that, similar to STN DBS where stimulation appears to activate axons leaving and adjacent to the STN (Hashimoto et al., 2003; Xu et al., 2008), a similar mechanism exists for GPi DBS (Johnson et al., 2012; Zhang et al., 2012; Muralidharan et al., 2017). Thus it is likely that stimulation of this region near the medial medullary lamina activates not only GPi motor efferents, but also axons passing through or adjacent to GPi (Parent et al., 1995; Sato et al., 2000).

Computational modeling of the volume of tissue activated (VTA) in DBS is a widely accepted technique that facilitates visualization of the affected or activated tissue areas surrounding the DBS electrode. Though it is a simplified method that does not differentiate between the activation of different neural components (i.e., cell body vs. fiber), or account for the different cell types and orientations, the VTA is generally considered to represent an "averaged" response that can be correlated with

programming settings and clinical results (Dembek et al., 2017; Johnson et al., 2019; Reich et al., 2019).

Traditional VTA studies have focused on monopolar settings with ring electrodes, where a sphere-shaped activation profile is generated (Butson and McIntyre, 2008). The segmented DBS lead, which has multiple electrode segments around the lead circumference, was recently approved by the FDA for targeting STN, GPi, and the ventral intermediate nucleus of the thalamus (VIM). Recent modeling studies have now extended the VTA calculation to segmented DBS leads. Activation of a single electrode segment of these leads resulted in a shift in laterality of the VTA, sometimes known as directional DBS (Buhlmann et al., 2011; Zhang et al., 2019). However, there have been very few studies where bipolar settings have been used to model the VTA (Buhlmann et al., 2011; Duffley et al., 2019), and among those that have, homogeneous tissue models were used. Additionally, to date there has been a lack of computational modeling studies that incorporate both heterogeneous tissue properties and bipolar settings in this space.

Incorporating tissue heterogeneity and anisotropy plays an important role in shaping the VTA (Butson et al., 2007; Gunalan et al., 2017, 2018; Howell and McIntyre, 2017; Ineichen et al., 2018). When incorporating tissue heterogeneity, the electric field changes from spherical to irregular shapes that are stimulation target-dependent (Ineichen et al., 2018). Additionally, according to vector analyses of electric field isolevels, compared to other DBS targets, the GPi has the greatest angles of deviation as a result of tissue heterogeneity and anisotropy (Aström et al., 2012). Taken together these findings provide compelling evidence to suggest that the actual VTA is not spherical, and more physiologically and anatomically accurate models are necessary to more precisely model tissue activation.

By leveraging our previous work calculating VTAs in the STN (Zhang et al., 2019), we hereby report a computational model for VTAs in the globus pallidus (GP) using directional leads. Here, we demonstrate the utility and potential advantages of using two vertical electrode spacing options (0.5 mm and 1.5 mm) with various monopolar and bipolar settings, and their effects on the size and shape of the resultant VTA in a heterogeneous tissue model. This study provides a simple framework to guide the selection of lead segments/contacts and programming parameters to sculpt the VTA in order to target two example regions of the pallidum: the posterolateral "sensorimotor" GPi, or GPi and GPe at the level of medial medullary lamina.

METHODS

Finite Element Models

A finite element model (FEM) of the human head was implemented in Sim4Life v4.0 with the multimodal image-based detailed anatomical (MIDA) model following the methodology described in our previous publication (Zhang et al., 2019). Since in the original MIDA model, the GP was not segmented into the internal and external segments, we performed a manual segmentation by overlaying the MNI atlas onto the MIDA GP (performed with FSL), and then segmenting the region into 3 sub-regions: GPi, GPe, and medial medullary lamina (area between GPe and GPi). A segmented DBS lead (Infinity, Abbott) with 0.5 mm or 1.5 mm vertical inter-electrode spacing was placed in the globus pallidus (23 degrees toward anterior direction in sagittal plane and 11 degrees toward lateral direction in coronal plane with segmented electrode 2A facing anterior), with segmented contact 2 in the ventral posterolateral portion of the left GPi. The surface of contact 2 was ~2.25 mm away from the lateral boarder and 2.3 mm from the posterior boarder of the GPi (**Supplementary Figure 1**). A 0.5 mm thick encapsulation layer was added around the lead (Anderson et al., 2019). The electrical conductivity of the brain tissues, platinum-iridium contacts on the DBS lead, and polyurethane insulation on the lead were determined from the IT'IS database 3.1.1 (DATABASE >> IT'IS Foundation)¹. To demonstrate the effect of tissue heterogeneity on the FEM, as an example, a homogeneous tissue model was also used to calculate VTAs for configuration 4 (see next section) by replacing the entire internal structures of the head with homogeneous tissue with a 0.3 S/m conductance (Geddes and Baker, 1967).

Electrical potentials were calculated using various contact configurations by setting the boundaries of the active contacts to a voltage-controlled condition (Dirichlet boundary condition). The return electrode (anode) of the monopolar stimulation was represented using the boundaries of the epidermis layer in the MIDA head model. A bounding box of size 175.2 x 227.5 x 251.5 mm that encompassed all other model structures was modeled with zero normal current density (Neumann boundary condition). To determine the equivalent current delivered, the total current flux was calculated over the boundary of the cathode(s). Given the input voltage and the current flux on the cathode(s), an impedance of the electrode-tissue interface (ETI) was calculated and the equivalent current delivered was computed.

A rectilinear, volumetric mesh grid was generated from the model geometries with 0.04 mm maximum edge size for the electrodes, 0.1 mm max edge size for structures near the electrode (in a region of interest of 27 x 20 x 23 mm³), and 5 mm maximum step size elsewhere (over 98 million elements total). Convergence was set to a relative value of 1e-8 and an absolute value of 1e-10. Finally, an electromagnetic ohmic quasi-static solver was used to solve the following equation at the mesh nodes at the given

current amplitude and frequency:

$$\nabla \cdot \bar{\epsilon} \nabla \varphi = 0 \quad (1)$$

where $\bar{\epsilon}$ is the complex electric permittivity, φ is the electric potential, and:

$$\bar{\epsilon} = \epsilon_R \epsilon_0 + \frac{\sigma}{j\omega} \quad (2)$$

where ϵ_R is the relative permittivity, ϵ_0 is the relative permittivity of perfect vacuum, and σ is the electrical conductivity.

Multi-compartment axons that were 20 mm in length and 5.7 μ m diameter were distributed on axonal planes that were perpendicular to the lead and 0.5 mm apart from one another. Within each plane, the axons were arranged parallel to one another with 0.25 mm spacing and rotated 5 times by 30 degrees per rotation. The electrical potentials from the FEM were interpolated along each neuron and delivered as extracellular stimulation to determine which axons were activated for a given contact configuration and stimulation set. All neuronal activations were computed in Sim4Life.

DBS Parameters and Configurations

DBS pulses of 1 mA with 60 μ s pulse width (biphasic with passive discharge) and 130 Hz were used when modeling VTAs. Since electrode 2A was facing anterior, electrode 2B was determined to be the most optimal electrode for activation of posterolateral GPi. Therefore, the following common DBS contact **configurations** were tested (**Figure 1**):

1. single-segment monopole (2B-/Case+)
2. two-segment monopole
 - a. row (2A-/2B-/Case+)
 - b. vertically stacked (2B-/3B-/Case+)
3. ring monopole (2A-/2B-/2C-/Case+)
4. one-cathode-ring-anode bipole (2B-/3A+/3B+/3C+)
5. ring-cathode-ring-anode bipole (2A-/2B-/2C-/3A+/3B+/3C+).

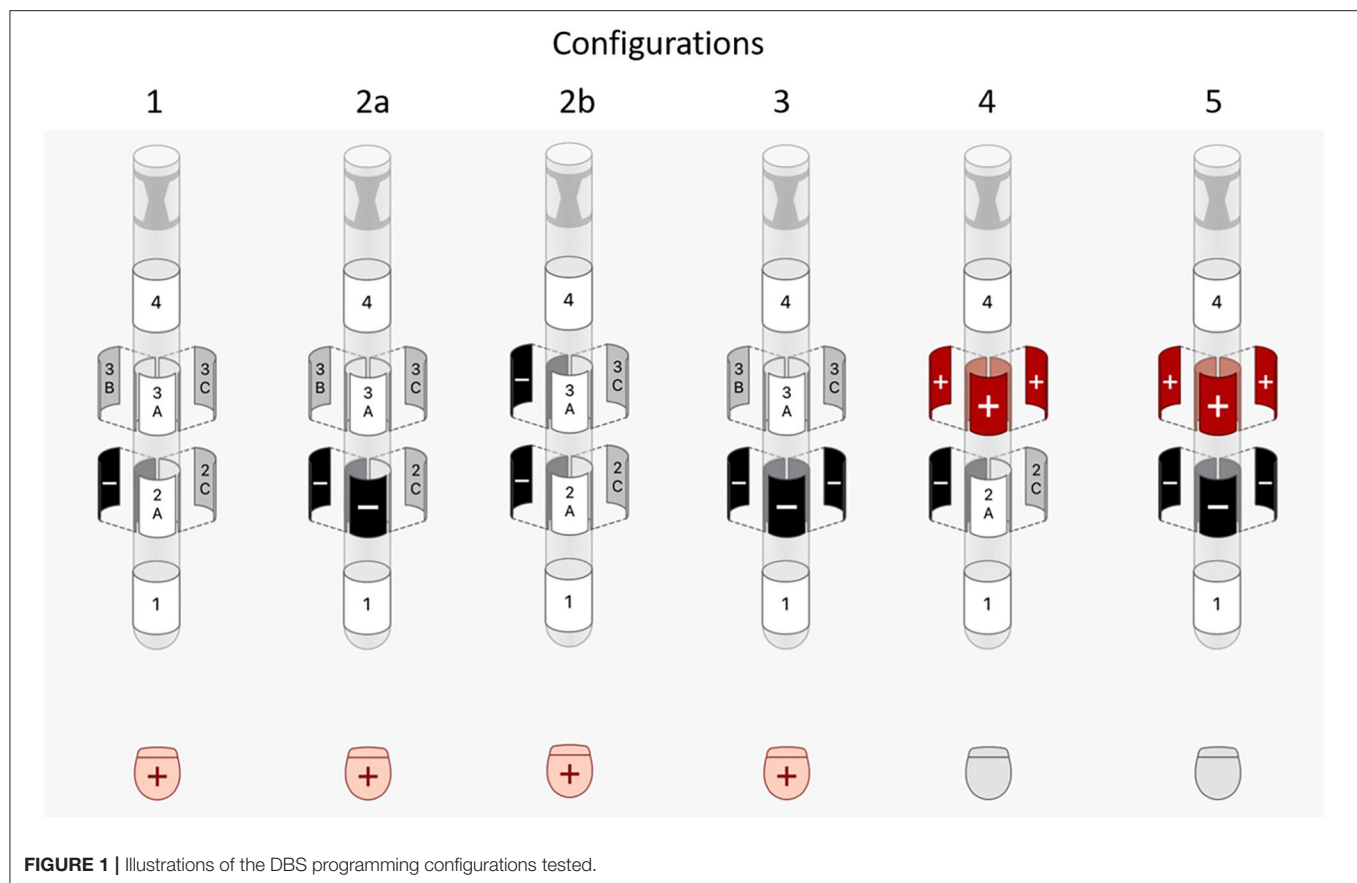
Configuration 2b, 4, and 5, which contain vertically activated segments, were repeated for a directional DBS lead with 0.5 mm vertical electrode spacing. In addition, all configurations were repeated using an amplitude of 2 mA.

All configurations that contained two or more segments were simulated as if the electrodes were connected via hardware parallel connections. This is sometimes referred to as “co-activation” and is a common method of activation when the DBS system only has a single current source.

Volume of Tissue Activated Generation

The volumes of tissue activated (VTA) were calculated in Matlab R2017b according to previously described methods by bounding the action potential initiation (API) sites in space to form a 3D volume (Zhang et al., 2019). The 3D volume was then sub-divided into four volumes: (1) inside GPi, (2) between GPi and GPe, (3) inside GPe, and (4) outside GP, by partitioning the VTA into voxels in each region.

¹DATABASE. IT'IS Foundation. Available online at: <https://itis.swiss/virtual-population/tissue-properties/database/> (accessed August 31, 2018).



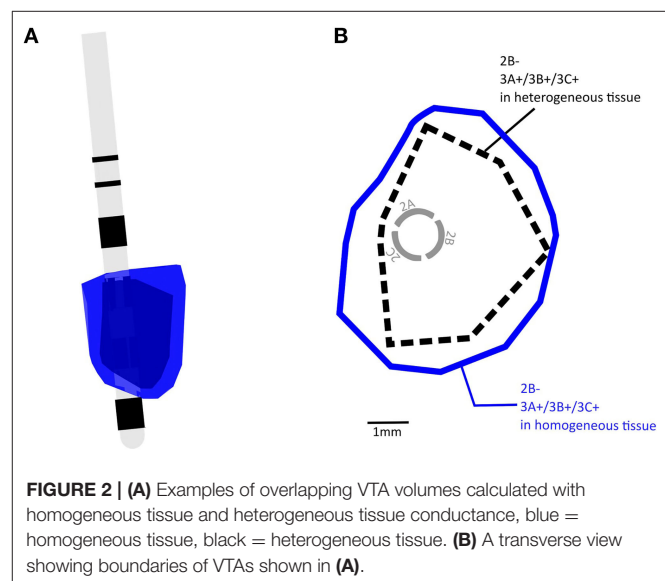
RESULTS

Effect of Tissue Heterogeneity

Consistent with previous findings, replacing the heterogeneous MIDA model with a homogeneous model for configuration 4 resulted in VTAs that were 42.9% larger in size and more regular in shape at the cross sections (Butson et al., 2007; Gunalan et al., 2017, 2018; Howell and McIntyre, 2017; Ineichen et al., 2018). The VTA for configuration 4 in a homogeneous and heterogeneous model is shown in **Figure 2** and the transverse cross-sectional outline in 2B. We used the heterogeneous tissue model to calculate all remaining VTAs in this study.

VTA Volume

When the active electrode was placed near the ventral posterolateral “sensorimotor” GPi, and at low current settings such as 1 mA current, the VTAs produced by configurations 1, 2a, and 3 (**Figure 1**) were entirely within the GPi (**Figure 3A**). However, as the current increases from 1 to 2 mA, VTAs enlarged and exceeded the GPi boundary from the ventral side (and sometimes medial side) into undesired side effect regions such as the optic tract or the internal capsule (**Figure 3C**, blue). Consistent with previous findings, the VTAs with the single-segment monopole (configuration 1) generated the most axially asymmetric and largest VTA at the cathodic contact (Zhang et al., 2019).



For the vertically stacked two-segment monopole configuration (configuration 2b), at 1 mA current amplitude, the VTA elongated dorsally along the lead and activates more structures dorsal to the GPi such as the medial medullary lamina

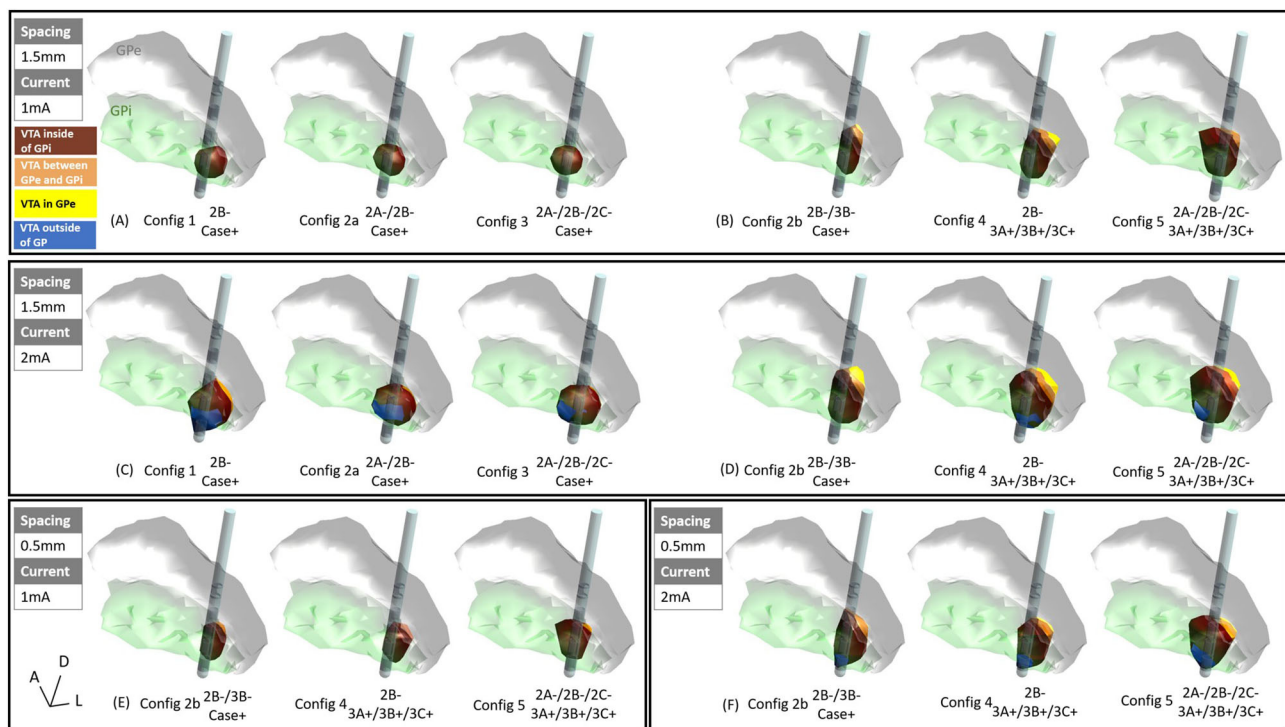


FIGURE 3 | VTAs for various configurations: **(A)** 1.5 mm vertical spacing with 1 mA current, settings 1, 2a, and 3 (see methods), **(B)** 1.5 mm vertical spacing with 1 mA current, settings 2b, 4, and 5, **(C)** 1.5 mm vertical spacing with 2 mA current, settings 1, 2a, and 3, **(D)** 1.5 mm vertical spacing with 2 mA current, settings 2b, 4, and 5, **(E)** 0.5 mm vertical spacing with 1 mA current, settings 2b, 4, and 5, **(F)** 0.5 mm vertical spacing with 2 mA current, settings 2b, 4, and 5, marron = VTA inside of GPi, orange = VTA between GPe and GPi (medial medullary lamina), yellow = VTA inside of GPe, blue = VTA outside of GP.

(Figure 3B, orange) and GPe (Figure 3B, yellow). Note that because the vertical electrode segments are stacked facing the same direction, the directionality of the VTA was the same for stacked two-segment configuration 2b as the single segment configuration 1. A similar activation profile was also observed for vertical bipolar settings (configurations 4 and 5), where VTAs extended to dorsal structures to the GPi (for 1.5 mm spacing: Figure 3B, and for 0.5 mm spacing: Figure 3E). At 2 mA, the VTA volume expanded, also exceeding the ventral border involving regions associated with the development of side effects (blue regions in Figures 3D,F). However, the VTAs of regions associated with side effects were on average 86.6% smaller in configurations 2b, 4, and 5 (Figures 3D,F) than those in configurations 1, 2a, and 3 (Figure 3C).

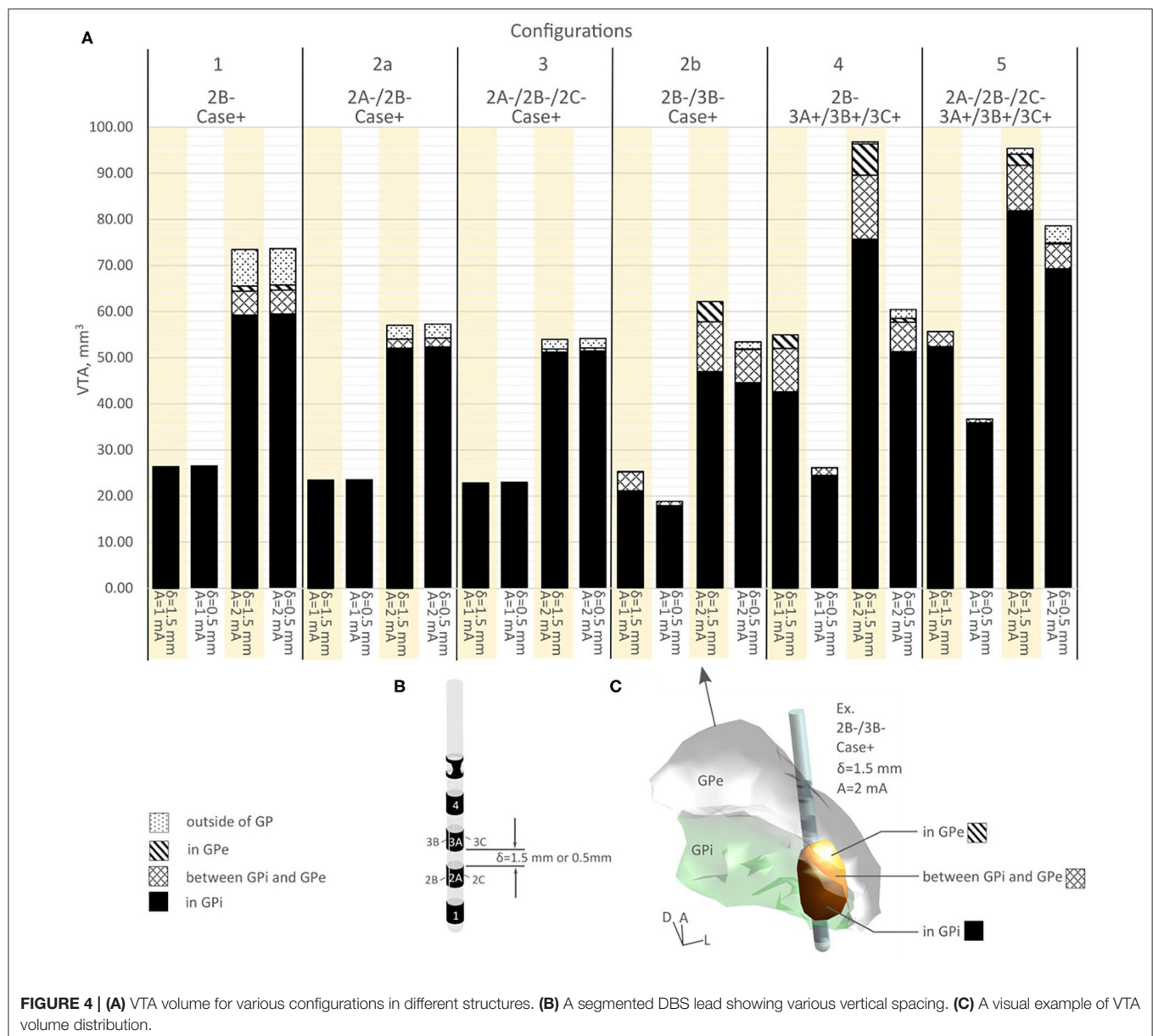
A detailed volume break-down of the VTAs in each of the sub-regions is summarized in Figure 4 (Supplementary Table 1). Because configurations 1, 2a, and 3 did not engage any vertical electrode combinations, these three configurations produced the same VTA distribution between the 1.5 mm DBS electrode and the 0.5 mm DBS electrode (Figure 4A, Supplementary Table 1). In configurations 2b, 4, and 5, compared to the 1.5 mm lead, the 0.5 mm DBS lead produced smaller VTAs with the same current amplitude. The resulting VTA was much more concentrated in GPi. At 1 mA, configurations 2b, 4, and 5 with 0.5 mm vertical electrode spacing produced a VTA that was on average 95.39%

within the GPi, while 1.5 mm vertical spacing produced a VTA that was on average 85.01% in GPi. Similarly, at 2 mA current amplitude, configurations 2b, 4, and 5 with 0.5 mm vertical electrode spacing produced a VTA that was on average 85.45% in the GPi, while a 1.5 mm vertical spacing produced VTA that was on average 79.86% in GPi.

In the bipolar configurations, switching from configuration 4 to 5, the 1.5 mm vertical spacing DBS lead produced similar VTAs (1.31% increase in volume for 1 mA current, −1.48% decrease in volume for 2 mA current, see Figure 4A and Supplementary Table 1). However, the composition of volumes activated changed switching from configuration 4 to 5, as the % volume in GPi increased from 77.47 to 94.15% for 1 mA, and from 78.17 to 85.83% for 2 mA (Figure 4A, Supplementary Table 1). For the 0.5 mm DBS lead, both the volume and the % volume within GPi increased when switching from configurations 4 to 5. The % volume in GPi increased from 93.53 to 97.71% for 1 mA current amplitude, and from 84.79 to 88.16% for 2 mA. The VTA volumes increased an average of 35.31% switching from configuration 4 to 5.

DISCUSSION

This study explored the effect of tissue heterogeneity and various electrode montages on the VTA to help inform



directional programming of the GPi. In particular, the effects of vertical electrode spacing in combination with commonly used monopolar and bipolar settings on VTAs in both GPi and structures dorsal to the GPi were examined.

Strategies of Programming GPi DBS Based on VTAs

To maximize therapeutic response when targeting the posterolateral GPi, the goal is to maximize the VTA within the GPi while minimizing VTA extension to off target regions that are associated with side effects, such as the internal capsule or optic tract. In this study, we found that if a DBS electrode is placed well within the sensorimotor territory of the GPi, using a single segment of the DBS electrode (configuration 1), two active segments (configuration 2a), or ring mode (configuration 3) can

all produce VTAs that are entirely within the GPi at low current amplitudes (1 mA in this study). Among the three configurations, single segment activation (configuration 1) produced the largest VTA. We also observed that if the electrode was placed closer to regions that could cause side effects we could restrict the VTA by use a single segment (configuration 1) to steer the VTA toward the desired region of interest since single segment activation produced a VTA with maximum axial asymmetry (Zhang et al., 2019).

Another way to maximize GPi activation without extension into neighboring structures such as GPe, optic tract or internal capsule, while offering more flexible selections of configurations may be to use a DBS lead with 0.5 mm vertical spacing. At low current amplitudes, in addition to the 3 above mentioned configurations, users can also use vertical stacked

monopolar settings (configuration 2b) and vertical bipolar settings (configurations 4, 5).

Vertical configurations (configurations 2b, 4, 5) are generally helpful to stretch the VTA and involve a greater dorsal-to-ventral extent of the target that could include the dorsal pallidum structures such as the medial medullary lamina and/or ventral portions of GPe. Additionally, one can opt to use a 1.5 mm vertically spaced DBS lead to further elongate and enlarge the VTA to reach the dorsal pallidum structures. Correspondingly, if the user wants to increase volume of VTA inside of GPi compared to dorsal structures, one can switch to the 0.5 mm vertical spacing DBS electrode, or switch from using a monopole as cathode in a bipolar setting (configuration 4) to using a ring as cathode in a bipolar setting (configuration 5), as doing so will increase the VTA volume at the level of the cathode located inside of GPi. **Table 1** summarized these findings.

Note that the electrode with 1.5 mm vertical spacing consistently resulted in larger VTA volume than the one with 0.5 mm vertical spacing for the parameters tested. This can potentially mean that using a DBS lead with 1.5 mm vertical spacing can activate a given volume of GPi and dorsal pallidal structures with less current amplitude compared to the lead with 0.5 mm vertical spacing.

Limitations of Bipolar VTA

The VTA method used in this paper was a direct bounding method, which bounded the API of axons of various orientations. This is different from the “center node remapping” method, where the APIs were remapped to the center node of the activated axons. The two methods did not differ significantly for cathodal stimulation, as the API tend to be the node that is closest to the cathode (Anderson et al., 2019), but because of the virtual cathode effect, the axons near the anode tend to initiate APIs that are further toward the distal ends, rather than the node that is closest to the anode (Slopesma et al., 2018; Anderson et al., 2019). The direct bounding VTA method used here therefore resulted in VTAs that were larger at the anode than previously reported. There was evidence that previously reported method likely underestimated the activations near the anode (Slopesma et al., 2018; Anderson et al., 2019; Duffley et al., 2019), therefore, the method used here that incorporates multiple orientations orthogonal to the lead offered a more directly interpretable VTA activation profile, especially for a larger target such as the globus pallidus, and especially with a lead with larger vertical spacing (1.5 mm). However, a bigger VTA produced by bipolar stimulations does not directly translate to better therapy or equate with lower side effect threshold—the shape of the VTA matters more in terms of overlapping with therapy regions and side effect pathway activations.

Axonal fiber orientation also matters for bipolar stim (Slopesma et al., 2018; Anderson et al., 2019). The axonal grid used in this study contained axons that were perpendicular to the DBS lead, but in the GP, there are fibers that run parallel to the lead, and future simulations should certainly include parallel fibers in the model. This resulted in an under-estimation of the axonal activation. However, this effect could be compensated by the choice of using 4.7 μ m axon fibers, where most of the fibers in GP have smaller fiber diameter. Overall, The effects of using

TABLE 1 | Summary of strategies of programming GPi DBS based on VTAs.

Desired activation target	Additional criteria	Recommended vertical spacing	Recommended configurations
Posterolateral “sensorimotor” GPi only	-	0.5 mm or 1.5 mm	1, 2a, 3
	-	0.5 mm	2b, 4, 5
GPi, medial medullary lamina and/or GPe	less GPi activation	1.5 mm	2b, 4
	more GPi activation	0.5 mm	2b, 5

the direct bounding VTA method, not including parallel fibers, and using 4.7 μ m axons should counter-balance each other and produce a reasonable VTA estimation.

Other Limitations and Future Directions

In this study, we examined commonly used electrode activation configurations for DBS in the GP. We did not examine many other possible activation configurations such as multipolar stimulation or using one segment as the anode, as those configurations are not commonly practiced in the clinic. Future studies might include those configurations for a complete assessment of the VTAs in GPi DBS. Additionally, this current study only used 1 mA and 2 mA as stimulation current amplitudes as examples to offer guidance on the VTA size and inform programming. The clinician will still need to increase and titrate the current levels to obtain the best therapeutic effects, and the end results will be highly dependent on the location and orientation of the electrode. Additionally, the parameters simulated here alone were not enough for visually aided programming—since VTA is not linearly correlated to the input current amplitude, further subdivision of current is needed to produce the finer VTAs that can be used for visual programming.

One other limitation of this study is that only tissue heterogeneity was reflected with different conductance values. Tissue anisotropy was not incorporated, which might play an even bigger role than tissue conductance alone (Aström et al., 2012). In future studies we plan to introduce tissue anisotropy into the MIDA model. Additionally, we plan to implement a patient-specific version of the MIDA model that is extracted based on the patient’s imaging data. The electrode location and orientation will be detected by postoperative CTs and co-registered to the MRIs to produce a more accurate representation of the VTA in individual patients.

CONCLUSION

We demonstrated for the first time using a heterogeneous tissue conductance computational model that if the traditional posterolateral “sensorimotor” GPi is the target, depending on lead placement, using one or more electrode segments of the same ring with the optimal current level can achieve a VTA the incorporates a significant region of the sensorimotor GPi without current spread into adjacent areas. Using a single segment also produced a VTA with the largest volume. Using stacked vertical

two-cathode settings produced a VTA that expanded the VTA in the dorsal-to-ventral direction and could be used to include regions dorsal to the GPI. Alternatively, vertical bipolar settings can also effectively enlarge the VTA at the anode without activating areas ventral to the cathode. We also showed that with these settings and a lead well placed within the sensorimotor territory of the GPI, using a DBS electrode with 0.5 mm vertical electrode spacing would be beneficial for restricting a greater percentage of the VTA to the GPI, while a 1.5 mm vertical electrode spacing could be used to expand the VTA volume and extend the VTA to more dorsal regions.

DATA AVAILABILITY STATEMENT

The datasets presented in this article are not readily available because only computational models were used. Requests to access the datasets should be directed to david.zhang@abbott.com.

REFERENCES

- Anderson, D. N., Duffley, G., Vorwerk, J., Dorval, A. D., and Butson, C. R. (2019). Anodic stimulation misunderstood: Preferential activation of fiber orientations with anodic waveforms in deep brain stimulation. *J. Neural Eng.* 16:590. doi: 10.1088/1741-2552/aae590
- Aström, M., Lemaire, J. J., and Wardell, K. (2012). Influence of heterogeneous and anisotropic tissue conductivity on electric field distribution in deep brain stimulation. *Med. Biol. Eng. Comput.* 50, 23–32. doi: 10.1007/s11517-011-0842-z
- Bejjani, B., Damier, P., Arnulf, I., Papadopoulos, S., Bonnet, A., Vidailhet, M., et al. (1998). Deep brain stimulation in Parkinson's disease: Opposite effects of stimulation in the pallidum. *Mov. Disord.* 13, 969–970. doi: 10.1002/mds.870130618
- Buhlmann, J., Hofmann, L., Tass, P. A., and Hauptmann, C. (2011). Modeling of a segmented electrode for desynchronizing deep brain stimulation. *Front. Neuroeng.* 4:15. doi: 10.3389/fneng.2011.00015
- Butson, C. R., Cooper, S. E., Henderson, J. M., and McIntyre, C. C. (2007). Patient-specific analysis of the volume of tissue activated during deep brain stimulation. *Neuroimage* 34, 661–670. doi: 10.1016/j.neuroimage.2006.09.034
- Butson, C. R., and McIntyre, C. C. (2008). Current steering to control the volume of tissue activated during deep brain stimulation. *Brain Stimul.* 1, 7–15. doi: 10.1016/j.brs.2007.08.004
- Dembek, T. A., Reker, P., Visser-Vandewalle, V., Wirths, J., Treuer, H., Klehr, M., et al. (2017). Directional DBS increases side-effect thresholds-A prospective, double-blind trial. *Mov. Disord.* 32, 1380–1388. doi: 10.1002/mds.27093
- Duffley, G., Anderson, D. N., Vorwerk, J., Dorval, A. D., and Butson, C. R. (2019). Evaluation of methodologies for computing the deep brain stimulation volume of tissue activated. *J. Neural Eng.* 16:066024. doi: 10.1088/1741-2552/ab3c95
- Geddes, L. A., and Baker, L. E. (1967). The specific resistance of biological material-A compendium of data for the biomedical engineer and physiologist. *Med. Biol. Eng.* 5, 271–293. doi: 10.1007/BF02474537
- Gunalan, K., Chaturvedi, A., Howell, B., Duchin, Y., Lempka, S. F., Patriat, R., et al. (2017). Creating and parameterizing patient-specific deep brain stimulation pathway-activation models using the hyperdirect pathway as an example. *PLoS ONE* 12:e0176132. doi: 10.1371/journal.pone.0176132
- Gunalan, K., Howell, B., and McIntyre, C. C. (2018). Quantifying axonal responses in patient-specific models of subthalamic deep brain stimulation. *Neuroimage* 172, 263–277. doi: 10.1016/j.neuroimage.2018.01.015
- Hashimoto, T., Elder, C. M., Okun, M. S., Patrick, S. K., and Vitek, J. L. (2003). Stimulation of the subthalamic nucleus changes the firing pattern of pallidal neurons. *J. Neurosci.* 23, 1916–1923. doi: 10.1523/jneurosci.23-05-01916.2003

AUTHOR CONTRIBUTIONS

SZ, BC, and EP: conception and design of study. SZ: acquisition of data and drafting the manuscript. All authors: analysis and/or interpretation of data, revising the manuscript critically for important intellectual content, and approval of the version of the manuscript to be published.

FUNDING

This study is funded by Abbott.

SUPPLEMENTARY MATERIAL

The Supplementary Material for this article can be found online at: <https://www.frontiersin.org/articles/10.3389/fncom.2020.561180/full#supplementary-material>

- Houeto, J. L., Bejjani, P. B., Damier, P., Stedler, C., Bonnet, A. M., Pidoux, B., et al. (2000). Failure of long-term pallidal stimulation corrected by subthalamic stimulation in PD. *Neurology* 55, 728–730. doi: 10.1212/WNL.55.5.728
- Howell, B., and McIntyre, C. C. (2017). Role of soft-tissue heterogeneity in computational models of deep brain stimulation. *Brain Stimul.* 10, 46–50. doi: 10.1016/j.brs.2016.09.001
- Ineichen, C., Shepherd, N. R., and Sürücü, O. (2018). Understanding the effects and adverse reactions of deep brain stimulation: is it time for a paradigm shift toward a focus on heterogeneous biophysical tissue properties instead of electrode design only? *Front. Hum. Neurosci.* 12:468. doi: 10.3389/fnhum.2018.00468
- Johnson, K. A., Fletcher, P. T., Servello, D., Bona, A., Porta, M., Ostrem, J. L., et al. (2019). Image-based analysis and long-term clinical outcomes of deep brain stimulation for Tourette syndrome: A multisite study. *J. Neurol. Neurosurg. Psychiatry*. doi: 10.1136/jnnp-2019-320379
- Johnson, M. D., and McIntyre, C. C. (2008). Quantifying the neural elements activated and inhibited by globus pallidus deep brain stimulation. *J. Neurophysiol.* 100, 2549–2563. doi: 10.1152/jn.90372.2008
- Johnson, M. D., Zhang, J., Ghosh, D., McIntyre, C. C., and Vitek, J. L. (2012). Neural targets for relieving parkinsonian rigidity and bradykinesia with pallidal deep brain stimulation. *J. Neurophysiol.* 108, 567–577. doi: 10.1152/jn.00039.2012
- Krack, P., Pollak, P., Limousin, P., Hoffmann, D., Xie, J., Benazzouz, A., et al. (1998). Subthalamic nucleus or internal pallidal stimulation in young onset Parkinson's disease. *Brain* 121, 451–457. doi: 10.1093/brain/121.3.451
- Mirza, S., Yazdani, U., Dewey, R., Patel, N., Dewey, R. B., Miocinovic, S., et al. (2017). Comparison of Globus Pallidus Interna and Subthalamic Nucleus in Deep Brain Stimulation for Parkinson Disease: An Institutional Experience and Review. *Parkinsons. Dis.* 2017:20. doi: 10.1155/2017/3410820
- Muralidharan, A., Zhang, J., Ghosh, D., Johnson, M. D., Baker, K. B., and Vitek, J. L. (2017). Modulation of Neuronal Activity in the Motor Thalamus during GPI-DBS in the MPTP Nonhuman Primate Model of Parkinson's Disease. *Brain Stimul.* 10, 126–138. doi: 10.1016/j.brs.2016.10.005
- Okun, M. S., Fernandez, H. H., Wu, S. S., Kirsch-Darrow, L., Bowers, D., Bova, F., et al. (2009). Cognition and mood in Parkinson's disease in subthalamic nucleus versus globus pallidus interna deep brain stimulation: The COMPARE trial. *Ann. Neurol.* 65, 586–595. doi: 10.1002/ana.21596
- Parent, A., Charara, A., and Pinault, D. (1995). Single striatofugal axons arborizing in both pallidal segments and in the substantia nigra in primates. *Brain Res.* 698, 280–284. doi: 10.1016/0006-8993(95)01017-p
- Reich, M. M., Horn, A., Lange, F., Roothans, J., Paschen, S., Runge, J., et al. (2019). Probabilistic mapping of the antidystonic effect of pallidal neurostimulation: a multicentre imaging study. *Brain* 142, 1386–1398. doi: 10.1093/brain/awz046

- Sato, F., Parent, M., Levesque, M., and Parent, A. (2000). Axonal branching pattern of neurons of the subthalamic nucleus in primates. *J. Comp. Neurol.* 424, 142–152. doi: 10.1002/1096-9861(20000814)424:1<142::aid-cne10>3.0.co;2-8
- Slopesma, J. P., Peña, E., Patriat, R., Lehto, L. J., Gröhn, O., Mangia, S., et al. (2018). Clinical deep brain stimulation strategies for orientation-selective pathway activation. *J. Neural Eng.* 15:978. doi: 10.1088/1741-2552/aad978
- Vitek, J. L., Hashimoto, T., Peoples, J., DeLong, M. R., and Bakay, R. A. E. (2004). Acute stimulation in the external segment of the globus pallidus improves parkinsonian motor signs. *Mov. Disord.* 19, 907–915. doi: 10.1002/mds.20137
- Volkman, J., Albanese, A., Kulisevsky, J., Tornqvist, A.-L., Houeto, J.-L., Pidoux, B., et al. (2009). Long-term effects of pallidal or subthalamic deep brain stimulation on quality of life in Parkinson's disease. *Mov. Disord.* 24, 1154–1161. doi: 10.1002/mds.22496
- Volkman, J., Wolters, A., Kupsch, A., Müller, J., Kühn, A. A., Schneider, G. H., et al. (2012). Pallidal deep brain stimulation in patients with primary generalised or segmental dystonia: 5-year follow-up of a randomised trial. *Lancet Neurol.* 11, 1029–1038. doi: 10.1016/S1474-4422(12)70257-0
- Williams, N. R., Foote, K. D., and Okun, M. S. (2014). Subthalamic nucleus versus globus pallidus internus deep brain stimulation: translating the rematch into clinical practice. *Mov. Disord. Clin. Pract.* 1, 24–35. doi: 10.1002/mdc3.12004
- Wong, J. K., Cauraugh, J. H., Ho, K. W. D., Broderick, M., Ramirez-Zamora, A., Almeida, L., et al. (2019). STN vs. GPi deep brain stimulation for tremor suppression in Parkinson disease: a systematic review and meta-analysis. *Park. Relat. Disord.* 58, 56–62. doi: 10.1016/j.parkreldis.2018.08.017
- Xu, W., Russo, G. S., Hashimoto, T., Zhang, J., and Vitek, J. L. (2008). Subthalamic nucleus stimulation modulates thalamic neuronal activity. *J. Neurosci.* 28, 11916–11924. doi: 10.1523/JNEUROSCI.2027-08.2008
- Yelnik, J., Damier, P., Bejjani, B. P., Francois, C., Gervais, D., Dormont, D., et al. (2000). Functional mapping of the human globus pallidus: contrasting effect of stimulation in the internal and external pallidum in Parkinson's disease. *Neuroscience* 101, 77–87. doi: 10.1016/s0306-4522(00)00364-x
- Zhang, J., Wang, Z. I., Baker, K. B., and Vitek, J. L. (2012). Effect of globus pallidus internus stimulation on neuronal activity in the pedunculo-pontine tegmental nucleus in the primate model of Parkinson's disease. *Exp. Neurol.* 233, 575–580. doi: 10.1016/j.expneurol.2011.07.007
- Zhang, S., Silburn, P., Pouratian, N., Cheeran, B., Venkatesan, L., Kent, A., et al. (2019). Comparing current steering technologies for directional deep brain stimulation using a computational model that incorporates heterogeneous tissue properties. *Neuromodulation Technol. Neural Interface.* 2019:13031. doi: 10.1111/ner.13031

Conflict of Interest: SZ, BC, and ER are employees and receive salary from Abbott. MT, NP, and EP consult for Abbott and receives compensation for their time. NP also serves as a consultant for Medtronic, Boston Scientific, Second Sight Medical Products and receives grand support from Second Sight Medical Products and BrainLab. MT also serves as a consultant for Medtronic, Boston Scientific and Revance. The authors declare that this study received funding from Abbott. The funder was not involved in the study design, collection, analysis, interpretation of data, the writing of this article or the decision to submit it for publication.

Copyright © 2020 Zhang, Tagliati, Pouratian, Cheeran, Ross and Pereira. This is an open-access article distributed under the terms of the Creative Commons Attribution License (CC BY). The use, distribution or reproduction in other forums is permitted, provided the original author(s) and the copyright owner(s) are credited and that the original publication in this journal is cited, in accordance with accepted academic practice. No use, distribution or reproduction is permitted which does not comply with these terms.



A Systemic Review of Available Low-Cost EEG Headsets Used for Drowsiness Detection

John LaRocco[†], Minh Dong Le[†] and Dong-Guk Paeng^{*}

Ocean Systems Engineering, Jeju National University, Jeju City, South Korea

OPEN ACCESS

Edited by:

Tianyi Yan,
Beijing Institute of Technology, China

Reviewed by:

Aleksandra Dagmara Kawala-Sterniuk,
Opole University of
Technology, Poland
Theerawit Wilaiprasitporn,
Vidyasirimedhi Institute of Science
and Technology, Thailand

*Correspondence:

Dong-Guk Paeng
paeng@jejunu.ac.kr

[†]These authors have contributed
equally to this work

Received: 18 April 2020

Accepted: 24 August 2020

Published: 15 October 2020

Citation:

LaRocco J, Le MD and Paeng D-G
(2020) A Systemic Review of Available
Low-Cost EEG Headsets Used for
Drowsiness Detection.
Front. Neuroinform. 14:553352.
doi: 10.3389/fninf.2020.553352

Drowsiness is a leading cause of traffic and industrial accidents, costing lives and productivity. Electroencephalography (EEG) signals can reflect awareness and attentiveness, and low-cost consumer EEG headsets are available on the market. The use of these devices as drowsiness detectors could increase the accessibility of safety and productivity-enhancing devices for small businesses and developing countries. We conducted a systemic review of currently available, low-cost, consumer EEG-based drowsiness detection systems. We sought to determine whether consumer EEG headsets could be reliably utilized as rudimentary drowsiness detection systems. We included documented cases describing successful drowsiness detection using consumer EEG-based devices, including the Neurosky MindWave, InteraXon Muse, Emotiv Epoc, Emotiv Insight, and OpenBCI. Of 46 relevant studies, ~27 reported an accuracy score. The lowest of these was the Neurosky Mindwave, with a minimum of 31%. The second lowest accuracy reported was 79.4% with an OpenBCI study. In many cases, algorithmic optimization remains necessary. Different methods for accuracy calculation, system calibration, and different definitions of drowsiness made direct comparisons problematic. However, even basic features, such as the power spectra of EEG bands, were able to consistently detect drowsiness. Each specific device has its own capabilities, tradeoffs, and limitations. Widely used spectral features can achieve successful drowsiness detection, even with low-cost consumer devices; however, reliability issues must still be addressed in an occupational context.

Keywords: electroencephalography (EEG), drowsiness detection, low-cost, consumer EEG, fatigue detection, device portability

INTRODUCTION

Drowsiness is defined as the transition between the states of responsiveness and sleep, during which reaction times are reduced (US Dot National Highway Traffic Safety Administration, 2018). Drowsiness or fatigue is a major cause of road accidents and has significant implications for road safety, due to clear declines in attention, the recognition of dangerous drivers, and the diminished vehicle-handling abilities associated with drowsiness (Wang, 2011; Solaz et al., 2016). In addition, drowsiness-related accidents cost billions of US dollars and result in the loss of lives in industry, including transportation, manufacturing, mining, maritime, and aerospace sectors. Thus, developing a reliable, non-invasive method for drowsiness detection can save both money and lives (US Dot National Highway Traffic Safety Administration, 2018).

Key economic sectors, such as transportation, construction, security, and manufacturing, reported loss of productivity and lives due to drowsiness (Wang, 2011; Solaz et al., 2016). In the transportation sector, drowsiness-influenced road accidents represent social and economic problems worldwide. In the European Union (EU), 25% of road accidents have been associated with fatigue and drowsiness, compared with 40% of fatal accidents in the United States (US) (Solaz et al., 2016; Wei et al., 2018). According to a National Highway Traffic Safety Administration (NHTSA) report, ~83,000 road accidents reported annually in the US are caused by driver fatigue. Their analysis showed that ~416,000 crashes were caused by drowsy driving during the 5-year period from 2005 to 2009 (Wang et al., 2017; US Dot National Highway Traffic Safety Administration, 2018). In 2017, the NHTSA report reported that 3,166 fatalities resulted from distraction-affected crashes (US Dot National Highway Traffic Safety Administration, 2018). The factors that contributed to drowsiness included long working hours, the use of medication, lack of sleep, and continuous driving (Zhang et al., 2017). However, the exact definition of drowsiness is highly variable.

The term drowsiness is sometimes used interchangeably with the term fatigue in the literature. Although physiological state detection has been used to detect either (or both) states, researchers have defined certain differences between drowsiness and fatigue. Fatigue was defined as the decrease in physical and mental performance resulting from exhaustion (Vuckovic et al., 2002; Cabral et al., 2016). Drowsiness can be a symptom of fatigue, which can occur without drowsiness (Vuckovic et al., 2002). Other concepts, such as microsleep, can be used to describe a similar lack of responsiveness but have mechanisms distinct from those associated with fatigue and drowsiness (Davidson et al., 2007; Izquierdo-Reyes et al., 2016). Electroencephalography (EEG) has been used to identify these mechanisms, but the body of such work examining these other concepts is less well-defined than the total body of work associated with drowsiness research (Bryan Van Hal and Bossemeyer, 2014; Cabral et al., 2016; Wang et al., 2017; Rundo et al., 2019).

The prediction of drowsiness using EEG is a well-defined research topic. Approaches that utilize conventional EEG systems have advantages for the quantitative assessment of alertness levels, which requires expensive computational signal processing (Mard et al., 2011; Correa et al., 2014; Shabani et al., 2016; Zhang et al., 2017). Observing changes in the power spectra or spatio-temporal features of EEG frequency bands have commonly been used to detect subject drowsiness, but other methods have been investigated (Ayala Meza, 2017; Min et al., 2017; Majkowski et al., 2018). EEG-based drowsiness detection systems could be easily integrated into protective or occupational headgear for use in occupations that require such equipment (Wilaiprasitporn and Yagi, 2016).

Research- and medical-grade EEG systems rely on the use of dozens of channels, rendering such systems impractical for real-world occupational use (Ries et al., 2014). In contrast, low-cost EEG systems offer potential solutions for drowsiness prediction. These systems typically include fewer electrodes than medical

and research headsets, but their low prices make them accessible to hobbyists, small businesses, and developing countries. The use of consumer EEG headsets as drowsiness detectors has been previously investigated (Rodríguez et al., 2013; Van Hal et al., 2014; Salehi et al., 2015). A review of consumer EEG headsets as research tools was investigated, but it did not include occupational contexts (Sawangjai et al., 2019).

This review was conducted to evaluate the feasibility, complexity, and difficulty of using low-cost EEG systems for occupational drowsiness detection, such as drivers and security guards. PRISMA standards for systematic reviews were considered (Moher et al., 2009). The initial problem was the cost of drowsiness on economic productivity and safety. The implementation of low-cost, EEG-based detection could make the technology more accessible. Drowsiness detection systems implemented with low-cost EEG devices were compared. The successful outcomes were low-cost, robust implementations. A validation required study designs replicating occupational conditions with multiple subjects. A systematic search was conducted investigate prior implementations of low-cost EEG-based drowsiness detection systems.

SEARCH METHODOLOGY

Summary

In recent years, the number of portable, low-cost EEG-based systems available on the market has increased (Wei et al., 2018). Research examining the use of low-cost EEG systems has focused on the continuous recording of EEG data and/or the replication of larger EEG analytical systems using portable devices. In this review, we surveyed research papers that described the use of low-cost EEG devices, focusing on the devices where the headset was below \$1,000 USD in price, independent of licensing fees: the InteraXon Muse, the Neurosky MindWave, the Emotiv Epoc, the Emotiv Insight, and the OpenBCI. These devices represent a sample of widely-used commercial models. Although other devices and suppliers have been used (Li and Chung, 2015), the search was focused on those non-invasive EEG devices that were below \$1000, not marketed as medical devices, accessible to consumers, prominent in the hobbyist community, and have provided tools or options for brain-computer interface (BCI) applications. **Table 1** presents a comparison of these commercial, low-cost EEG headsets. Most low-cost headsets use dry electrodes, which are more convenient for casual users. Similarly, most headsets come bundled with software that includes research tools, open-source software, and additional hardware (Lin et al., 2014; Farnsworth, 2017).

Headset Information

The primary investigated headsets were the InteraXon Muse, the Neurosky MindWave, OpenBCI, and the Emotiv Epoc and Insight.

InterAxon Muse

The InteraXon Muse is a compact EEG system that measures brain activity via 4 EEG sensors (Muse, InteraXon) and can utilize Bluetooth to send data to nearby devices. Muse claimed that

TABLE 1 | Comparison of consumer EEG headsets.

Device	Electrodes	Sampling Rate	External Information	References
InteraXon	-Rigid electrode placement	- 256 Hz	- Research Tools for Windows, Mac, and Linux	Doudou et al., 2018
Muse v1, v2	- 4 channels: AF7, AF8, TP9, TP10	- 12 bits	- Source Developer Kit (SDK) for Android, IOS, Windows - Cost: \$200 USD	
Neurosky MindWave	- Rigid electrode placement - 1 channel: AFz	- 512 Hz - 12 bits	-SDK Available - Cost: \$99.99 USD	Doudou et al., 2018
OpenBCI	- Up to 16 channels - Flexible electrode placement at 35 locations	- 256 Hz - 24 bits	-Open-source software, firmware, and hardware -Cost: \$500 USD for 8 channels, \$949 USD for 16	Doudou et al., 2018
Emotiv Epoc, Flex, and Insight	- Rigid electrode placement - Epoc: 14 channels (AF3, F7, F3, FC5, T7, P7, O1, O2, P8, T8, FC6, F4, F8, AF4) -Insight: 5 channels (AF3, AF4, T7, T8, Pz)	- 128 Hz - 14 bits	-Research Tools for Windows, Mac, and Linux -Cost: \$799 USD (Epoc), \$299 USD (Insight)	Doudou et al., 2018

the headband could assist the user to achieve a state of deep relaxation. Based on the 10–20 International electrode placement convention, the dry electrodes were located at FPz, AF7, AF8, TP9, and TP10 (Krigolson et al., 2017). Electrode FPz was utilized as the reference electrode. The specifications detailed correspond to the original Muse device.

Neurosky Mindwave

Neurosky developed the single-channel MindWave as a low-cost, single-channel, dry EEG headset that is able to wirelessly transmit EEG via Bluetooth Low Energy or classic Bluetooth (Doudou et al., 2018). The MindWave device consists of a headset, with a T-shaped headband, a wider ear clip, and a flexible arm. The device's reference and ground electrodes are placed on the ear, while the EEG electrode is positioned on the forehead above the eye. Neurosky EEG headsets come with training software, educational apps, and software developer information. Free developer tools are also available for researchers. While Neurosky makes other models, the MindWave was the most frequently used model in the relevant studies (Lin et al., 2014; Doudou et al., 2018).

OpenBCI

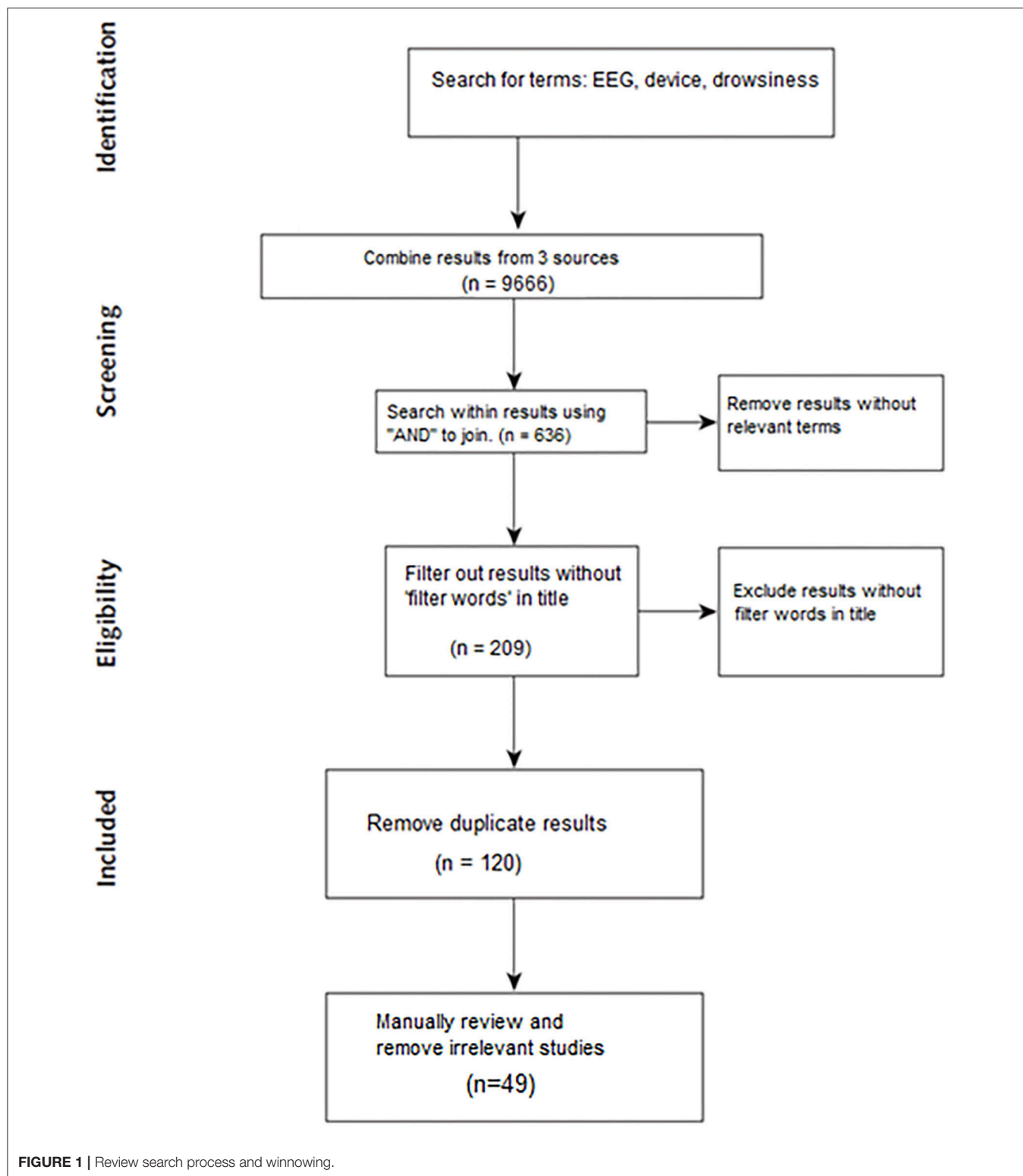
The OpenBCI Ultracortex Mark IV is an open-source, 3D-printable headset intended to work with any OpenBCI board. It is capable of recording research-grade brain activity EEG. The Ultracortex Mark IV headset is capable of sampling up to 16 channels of EEG from up to 35 different locations, based on the 10–20 International System (Mohamed et al., 2018b). The OpenBCI boards include options for 4 channels, 8 channels, and 16 channels. The OpenBCI is an open-source assemblage of parts, requiring assembly prior to use (Murphy and Russomanno, 2016). Therefore, it is not as widely used as readily-purchased consumer devices, but it theoretically allows greater customization. It has previously been used for drowsiness detection in a driving simulator.

Emotiv Insight and Epoc

Emotiv offers both the smaller, cheaper Insight and the larger, more expensive Epoc (and its upgraded counterpart, the Epoc+). The Emotiv Epoc is the most expensive of the investigated EEG headsets, containing more electrodes than the others (de Lissa et al., 2015). It has two electrode arms, each containing sensor electrodes and two reference electrodes. The locations provide coverage of the temporal, parietal, and occipital lobes. Emotiv provides a free companion app for users to monitor their emotions. They also offer pay-to-download games, such as Arena, which allows users to experience mental commands. Emotiv provides a two-tiered SDK for the Epoc. The headset has been used in research, from BCI to brain state detection (Badcock et al., 2013, 2015; Manolova et al., 2016). However, the Epoc and Epoc+ were the most common models found. Results returned using “Insight” as a keyword instead yielded results referencing the Epoc and Epoc+.

Scope

The purpose of this review is to identify examples and reports that described the successful use of specific, low-cost, consumer EEG headsets for drowsiness detection. These headsets will be referred to as “low-cost” for simplicity for the remainder of this paper. The scope and aims of the review process were not designed to comment on the algorithms and approaches used for drowsiness detection. Even single-channel EEG headsets, including custom-made headsets, have been successfully used for drowsiness detection in a research context (Ogino, 2018). For this review, a successful study was defined as a system that achieved greater than random accuracy in detecting drowsiness using EEG. Simple, robust algorithms for both drowsiness detection and general EEG processing were preferred, as these are likely to be more easily implemented by resource-constrained small businesses, individuals in developing countries, and others who are



unable to afford more complex EEG headsets or purpose-built systems. To facilitate comparisons and ensure search replicability, the PRISMA convention on systematic reviews and meta-analyses was followed (Moher et al., 2009). The

PRISMA conventional facilitates the process and replication of research reviews. A prior review focused on the broader viability of low-cost EEG as research tools, but not narrower occupational contexts (Sawangjai et al., 2019). Thus, the primary

aim of this review was to determine whether commercial, low-cost EEG headsets can easily be used for occupational drowsiness detection.

Eligibility Criteria

This review focused primarily studies related to low-cost EEG headsets that those non-invasive EEG devices that were below \$1,000 USD, not marketed as medical devices, accessible to consumers, prominent in the hobbyist community, and have provided tools or options for brain-computer interface (BCI) applications. Because commercial EEG systems have been publicly available for approximately one decade prior to the current date, only papers published within this period were included, starting from 2009. This year was shortly before the commercial release of the Emotiv, the earliest of the listed systems. Similarly, the total body of relevant results was thought to represent only a fraction of the total work on drowsiness detection; therefore, conference papers, completed dissertations, and validation studies were included. However, conference papers were excluded if they were published within 1 year of a journal paper on the same topic and by the same authors.

Data Combination

Two independent searchers, co-authors M. and J., gathered their findings in a reference document. Redundant results were eliminated, and information on each study was gathered. Data items included the authorship and publication of each work, the study design, experimental implementation, reported results, and concluding analysis. Specific preprocessing, feature extraction, and classification techniques were recorded, as was any statistical analysis performed on the results. Information on the computing platform used was also recorded. The primary information sought by each searcher included the work's criteria of "success," "accuracy," and other performance metrics. Numerical values, such as the confusion matrix, were used to calculate statistical measures, if provided by the work in question.

Search Strategy and Parameters

Google Scholar, IEEE Xplore, and PubMed were used as primary sources, due to the large databases available using these sources and their prior use in other reviews. All three search resources have been used in prior literature reviews in the field of biomedical engineering; however, many of the results could be accessed by multiple search engines. The resulting papers were grouped according to the model of EEG headset used. Duplicate results were removed by software.

The use of low-cost EEG headsets for drowsiness detection was described by only a limited number of studies, as the relevant results were those that utilized a low-cost EEG headset as the primary EEG recording system. The search included three phases. The first was the search for keywords, which included the terms: electroencephalography (EEG), drowsiness, and the device name. Second, the three keywords were joined by "AND." During the third phase of the search, specific words were sought in the title: (encephalography OR EEG) AND (drowsiness OR fatigue OR tired) AND ([*device name*]). The filter words included: drowsiness, fatigue, and tired.

Results from each source were combined, and duplicates were removed. These "filter words" were selected based on their use in prior papers and literature reviews (Vuckovic et al., 2002; Cabrall et al., 2016; Guo et al., 2017; Min et al., 2017). Similarly, any paper that did not include any of the filter words in the title was eliminated.

The remaining papers were included in the review. The removal of papers through the search process is depicted in **Figure 1**.

Table 2 summarizes the final results, according to the specific brand of EEG device used.

The final papers are further detailed in search results. However, potential bias and limitations had to be accounted for.

Bias and Error Sources

Possible sources of error included the ranking algorithms used by the search and indexing processes of Google Scholar, PubMed, and IEEE Xplore. The ranking processes of each search engine potentially missed relevant material. The primary purpose of this review was to identify examples describing the use of each consumer EEG headset for drowsiness detection, rather than performing a model-specific critique of each and every device. Similarly, the primary biases in published works would be toward positive results, potentially limiting insights from less successful studies.

A less clear topic was managing potentially relevant studies in affective computing and emotion recognition. Drowsiness has a range of definitions in the research literature, and a range of nearly synonymous terms used interchangeably in different contexts. There was the potential of drowsiness being one of several discrete states detected in an emotion recognition study, rather than an exclusively binary classification (Tan, 2012). Similarly, other studies integrated other signals than EEG (Polosky et al., 2017). In such cases, each study's structure was evaluated to determine if the system, as reported, could be used as to estimate drowsiness. If not, it was excluded from the final review (Alchalabi et al., 2018).

Data Management

Each search result would be evaluated for relevant data items. These include system parameters and study parameters. System parameters are those relevant to the drowsiness detection system, including the algorithms used for feature extraction and classification. Study parameters include those relevant to the entire study, including experimental design, cohort size, and performance results. The reported classifier accuracy,

TABLE 2 | Relevant results after search process.

Brand	Papers
InterAxon	11
Neurosky	16
OpenBCI	5
Emotiv	17

how reliably a device rates drowsiness, was the primary performance result.

RESULTS

Overview

The use of low-cost EEG headsets represents a logical progression based on the accomplishments reported using clinical and research-grade systems. These tasks range from brain-computer interfaces (BCIs) to brain-state rating to drowsiness detection. Much of the reported work has been context-specific, necessitating a thorough look at each study, and some works listed multiple headsets or lacked an experimental component, requiring that they be listed separately. The experimental use of each headset is described.

Crowley et al. (2010) performed psychological tests to induce stress and correlated the results with measured attention and meditation signals, using a Neurosky Mindset. They were able to detect when a subject's emotions changed using the Stroop and Towers of Hanoi tests. Both tests used in this study resulted in clear indications of subject stress and alertness changes, based on the attention and meditation parameters measured by the headset. However, this study would be cited as the basis for others.

Wei (2017) wrote a doctoral dissertation on drowsiness detection based on the detection of neural activity. The document largely described the real-life challenges faced by drowsiness detection in the context of BCI. In addition, experimental work on calibration was performed. Despite the research relevancy, a research 32-channel Quik-Cap Neuroscan EEG headset was used.

Wei et al. (2018) described the potential advantages of smaller, non-hair bearing (NHB) dry electrode headsets relative to larger ones. Smaller headsets that did not offer full coverage of the head were less affected by hair than larger ones. Specific devices named included the Neurosky and InterAxon devices. Potential advantages, including cost and ease of occupational use, were discussed.

Doudou et al. (2018) listed a number of consumer and portable EEG headsets (including all of the headsets reviewed here) and rated them using a number of parameters. Their particular focus was driver-based drowsiness detection. However, the authors did not perform any direct, experimental comparisons. The complete omission of any results was explicitly mentioned in their future work sections, however.

Lakhan et al. (2019) used consumer headsets in affective computing. With a study of 200 healthy subjects, they claimed predictive accuracies approximating those on costlier EEG systems. They used an OpenBCI EEG system for their work. The separate tasks included affective video selection and emotion recognition. No other low-cost headsets were investigated for the study, although they were mentioned in the article. The article lacked extensive discussion of potential context-specific advantages or limitations.

Majumder et al. (2019) performed a review of drowsiness detection. The review covered both consumer EEG devices and more purpose-built devices. It was found that power spectral densities of EEG bands were the most commonly utilized features across studies. The final conclusion was that identifying the specific EEG bands and brain sites would limit the need for EEG electrodes, reduce processing requirements, and improve accuracy.

Wexler and Thibault (2019) took a critical view of consumer EEG headsets and many of the claims made regarding their use. In particular, the authors reported that such consumer devices could serve as drowsiness detectors, despite a lack of reliability with regards to the identification of other brain states. They also discussed the legal and ethical complexities of such devices. Many issues were raised, but not all fully addressed.

InterAxon Muse

Bashivan et al. (2015) collected EEG data from 16 individuals. The authors used support vector machines (SVMs), sparse logistic regression, and deep belief networks (DBN) to discriminate among states of mind induced by different video inputs. The results demonstrated the significant potential for wearable, consumer EEG devices to differentiate among different cognitive states in different situations.

Krigolson et al. (2017) used a Muse for their BCI research. The authors used *t*-tests to observe and quantify statistically significant differences in event-related potentials in 60 subjects, including the N200 and the P300, during both a visual oddball task and a reward-learning task. Statistical tests were conducted for each case.

Rohit et al. (2017) used a Muse for real-time drowsiness detection. Spectral features were used with an SVM classifier on a total of 23 subjects. The study also investigated a blink-based method of drowsiness detection but found this method to be less accurate than the spectral power-based method.

Almogbel et al. (2018) investigated a single subject in a simulated driving task. Temporal feature vectors, from each of the Muse headset's 4 channels, were fed into a convolutional neural network (CNN). Various cognitive workloads were compared in both urban and rural driving scenarios. The CNN was used to estimate the workload based on EEG. The highest accuracy across scenarios was 95.3%. However, no field testing was conducted.

Bakshi (2018) detailed a system to detect cognitive workload through EEG. A Muse headband was used to collect EEG from 28 subjects, and spectral features were calculated for each band. For classification, a linear SVM, a radial basis SVM, a logistic regression model, and a shallow artificial network were used. The linear SVM was easily able to achieve an average accuracy of 99.1%. However, the system was not validated in live trials.

Teo and Chia (2018) proposed using EEG to detect interest and monotony while subjects were immersed in a virtual reality (VR) simulation. Users were exposed to a VR roller-coaster experience while wearing an EEG headset. Using a deep learning approach, accuracy rates of 78–96% were achieved. While “detecting interest” was a novel concept, more supporting research could have been cited.

TABLE 3 | InterAxon Muse Studies.

Paper	Year	Features	Classification	Accuracy	Size
Bashivan et al.	2015	Spectral Features	SVM, Regression, DBN	N/A	16
Krigolson et al.	2017	Amplitude	<i>t</i> -test	N/A	60
Rohit et al.	2017	Spectral Features	SVM	87%	23
Almogbel et al.,	2018	Raw EEG	CNN	95.30%	1
Bakshi	2018	Spectral Features	SVM, Regression, NN	99.10%	28
Teo and Chia	2018	Spectral Features	Deep NN	96%	24
Araújo	2019	Spectral Features	NN	81.10%	3
Foong et al.	2019	Spectral Features	NU (RBF+SVM)	93.80%	29
Mehreen et al.	2019	Spectral Features, Gyro	Linear SVM	92%	50
Dunbar et al.	2020	Spectral Features	N/A	N/A	25
Hoffman	2020	Spectral Features	ANOVA	N/A	19

Araújo (2019) used a second version Muse for drowsy driver detection in a thesis. A scaled artifact rejection was implemented based on the measured spectral power, prior to bandpass filtering. The features used were the power spectral density of different EEG bands. An artificial neural network was used for classification. Three subjects were used for model generation, training, and testing. Final testing accuracies included 70.8, 75.8, and 96.7% for a total average of 81.1% on testing data. In addition to the small sample size, the age of subjects was not addressed.

Foong et al. (2019) used EEG band-based power spectra to identify drowsiness in 29 subjects. Decreases in alpha and beta band power and increases in the theta band power were cited as signature features of drowsiness detection. The final reported accuracy was $93.8 \pm 8.2\%$. A negative-unlearned (NU) algorithm, consisting of a combination of SVM and radial basis function (RBF) was positively reported on. However, the offline implementation precluded assessments for real-time performance.

Mehreen et al. (2019) used multimodal signals from a Muse headset for drowsiness detection. In addition to EEG power spectral features and blink detection, they used accelerometer and gyroscope data to detect head movements, with head nodding corresponding to drowsiness periods. They reported a 92% accuracy, using leave-one-out cross-validation with 50 subjects.

Dunbar et al. (2020) simulated a driving task with 25 subjects. A Muse was used in a driving task. Spectral band power was used for the automated classification. Unlike algorithm-based papers, the purpose was to investigate if self-reported measures were consistent with documented electrophysiological changes. The electrophysiological changes and self-reported measures were consistent across subjects. However, a larger population subject size would be required for decisive confirmation.

Hoffmann (2020) combined gamification with EEG-based drowsiness detection. The dissertation consisted of an evaluation of a Muse headset, a companion app, and a larger study. Alpha and beta band power were the main feature used, calculated after filtering. A total of 19 subjects were used in validating the EEG headset. A combination of the EEG headset and app using self-reported measures were used in the larger studies. Analysis of variance (ANOVA) was used for a comparison of EEG across

different states. A limitation was studying the app's effect on stress outside of the evaluated metrics, as well as the relatively low size.

Of the entries reporting accuracy, the minimum was 83.3%, and the maximum was 99.1%. As shown in **Table 3**, these results suggested that the InterAxon Muse could be sufficiently reliable for use as a drowsiness detection system, due to both its convenience and its successful use during physiological state detection.

Neurosky MindWave

Jones and Schwartz (2010) wrote a short article reviewing several low-cost EEG devices, including a Neurosky device, and their abilities to detect drowsiness. The signal frequency content was divided into the following clinically relevant frequency bands: alpha (8–13 Hz), beta (14–30 Hz), and theta (4–7 Hz) waves. When comparing the power spectra, the alpha and beta waves decreased when drowsy, while the theta waves remained constant.

AlZu'bi et al. (2013) reported on three feature extraction methods using EEG: power spectral density, log variance, and statistical features. These features were fused into a single fatigue index; however, no accuracy scores were reported.

Shin et al. (2013) used EEG signals combined with an SVM classifier. A total of 5 subjects wore the MindWave for 3 h each night, to capture the onset of sleep and drowsiness. Analysis of variance (ANOVA) was performed on the extracted features, identifying statistically significant ($p < 0.001$) differences between the alert and the drowsiness states. The results reported an accuracy of 88.9% from a single subject, preventing larger validation of the system.

Lim et al. (2014) examined changes in the low alpha EEG band during eye closure. A total of 50 subjects were rated, with periods denoted by the Karolinska scale. The system had a lower accuracy rate than comparable systems, with an accuracy of 31% per second. However, the reported false alarm rate was 0.5%. Comparable MindWave-based systems reported accuracy higher than the reported rate, such as Supriyadi and Karyono (accuracy of 68.11%).

Supriyadi and Karyono (2014) used a MindWave device as a drowsiness detection system. An alarm was triggered when the

classifier detected a drowsy state, based on low alpha, high alpha, and theta spectral features. They reported an accuracy of 68.11%.

Abdel-Rahman et al. (2015) designed a mobile app to work with the MindWave EEG headset. They reported a 98% accuracy rate, using a spectral feature-based detection method during a simulated driving task. However, they used a binary state to determine whether the subject was in Stage 1 sleep, rather than other drowsiness markers used in other work.

Dunne et al. (2015) investigated a real-time, Stage 1 sleep detection system. The EEG signal was filtered into low alpha, high alpha, high beta, and low beta bands and then used to predict potential sleep onset. The results suggested that even single-channel systems, such as the Neurosky MindWave, may be sufficient for real-time drowsiness detection schemes.

Joshi et al. (2015) performed a limited literature review describing EEG-based drowsiness and fatigue detection. Their review covered specific examples of the MindWave being used, due to its low cost. The low-cost EEG examples described in this review are also described here. However, they did not detail their search methodologies, nor did they include any EEG devices beside the MindWave.

Lin et al. (2015) used a Neurosky device as a real-time, EEG-based drowsiness detection device. The paper detailed a combined approach to drowsiness detection, integrating drowsiness detectors with other automobile safety features. However, no quantifiable results, such as accuracy, were summarized.

Putra et al. (2016) reported the development of an EEG-based microsleep detector for driving. The device used features from the different EEG spectral bands. However, no experimental results were reported in the paper.

Sadeghi et al. (2016) detailed the use of EEG-based drowsiness detection by passing data to wearable devices for processing. To scale the proposed SafeDrive app, the authors propose the HumaNet framework, which integrates both model-related and context-related information. The system was intended to work with both the Neurosky MindWave and the Emotiv Epov. The average performance values reported included an accuracy of 91%, a sensitivity of 83%, and a specificity of 99%.

Patel et al. (2017) evaluated the Neurosky MindWave specifically as a drowsiness detector. Using a driving simulator, a total of 7 subjects had EEG recorded. These 10 s sessions were divided into attentive driving and drowsy driving, and a paired *t*-test was performed on them. No statistically significant differences ($p > 0.05$) were found between averaged epochs for each category.

Anwar et al. (2018) used a Neurosky MindWave to record a meditating subject's EEG output and compared this with that of a 19-channel conventional EEG setup. Similar spectral changes were observed using both devices, although the measured amplitudes were different. Spectral data from different phases of meditation, such as the beginning and end, were also compared. Changes in the alpha and delta bands were noted.

Sethi et al. (2018) used a Mindwave device for assessing e-learning outcomes. EEG data was gathered from each subject (out of 42), without feedback. Following this, the subject was exposed to feedback for subsequent EEG recording sessions.

Spectral features and proprietary parameters of attentiveness and meditation were compared for the same person, and then compared to the subject's EEG afterwards.

Aboalayon and Faezipour (2019) investigated a wireless EEG sleep stage detection system with a single channel Mindwave device. The system evaluated a real-time simulated driving task. However, the study was limited by its scope and length, precluding a definitive result on the device's performance.

Nissimagoudar and Nandi (2020) detailed an EEG detection system using alpha power, and using SVM for classification. The study used 10 subjects. The work detailed the expansion of a driver assistant, aimed at improving performance and safety behind the wheel. A range of classification results were reported from 74 to 89%, although highly dependent upon spatio-temporal features corresponding to drowsiness states.

Of those entries reporting accuracy, the performance ranges from 31 to 97.6%. As shown in **Table 4**, these results suggested that the Neurosky MindWave may be used for an EEG-based drowsiness detection system, although additional processing and feature extraction may be required.

OpenBCI Ultracortex

Karuppusamy and Kang (2017) used a 14-channel custom EEG headset with an OpenBCI board. They manually rated drowsiness periods using manually tagged videos of eye closure. The highest performing classifier reported was an SVM with a Gaussian kernel, with an accuracy of 81.2%.

Shen et al. (2017) reported a method of drowsiness detection beyond a binary state classifier. They did not report a specific accuracy, but they described a testing method that returned results that were independent of a subject's age and were based on the channels C4 and P3. They used a hybrid OpenBCI and Emotiv-based system to quantify spectral power across 50 test cases. According to the authors, the "depth of drowsiness" method described in this study was the first implementation of a non-binary drowsiness detector using a low-cost EEG system. They reported an accuracy of 82%, over a prior reported accuracy of 70% (Yin et al., 2011).

Mohamed et al. (2018a,b) used the Mark IV headset to analyze EEG output during driver behavior, based on spectral features. The input signal was divided into standard bands (delta, theta, alpha, and beta). To estimate the alertness level, the following feature extraction techniques were evaluated: the periodogram, Lomb-Scargle, multi-taper, and Welch's method. A multilayer neural network was used to evaluate the performance across all extracted features, with 10-fold cross-validation. The highest average classification accuracy was obtained using Welch's method, with 85.0% for testing accuracy. As the averaged sum of multiple periodograms, Welch's method was robust and not computationally intensive.

As shown in **Table 5**, these results suggested that the OpenBCI may be utilized for drowsiness detection, but the entire system must be assembled from component parts. Of the reported accuracies, the minimum was 79.4%, and the maximum was 96.4%. The additional complexity may decrease the accessibility relative to other systems.

TABLE 4 | Neurosky MindWave Studies.

Paper	Year	Features	Classification	Accuracy	Size
Jones and Schwartz	2010	Spectral Features	N/A	N/A	5
AlZu'bi et al.	2013	PSD, log variance, stats	Fatigue index	N/A	1
Shin et al.	2013	Spectral Features	SVM	88.90%	1
Lim et al.	2014	Alpha band power	Triggering window	31%	50
Suprihadi and Karyono	2014	Spectral Features	Spectral threshold	68.11%	1
Abdel-Rahman et al.	2015	Periodogram	Neural network	97.60%	60
Dunne et al.	2015	Alpha and Beta Features	Threshold	81%	3
Joshi et al.	2015	Spectral Features	Threshold	N/A	1
Lin et al.	2015	Spectral Features	Threshold	N/A	1
Putra et al.	2016	Spectral Features	Threshold	N/A	0
Sadeghi et al.	2016	Alpha, Beta, Theta Power	Markov Chain Model	91%	1
Patel et al.	2017	Spectral Features	Paired <i>t</i> -test	N/A	7
Anwar et al.	2018	Spectral Features	Averaged threshold	75%	20
Sethi et al.	2018	Spectral Features, eSense	N/A	N/A	42
Aboalayon and Faezipour	2019	Spectral Features	N/A	N/A	1
Nissimagoudar and Nandi	2020	Spectral Features	SVM	74-89%	10

TABLE 5 | OpenBCI Studies.

Paper	Year	Features	Classification	Accuracy	Size
Karuppusamy and Kang	2017	PCA	Gaussian SVM	81.20%	N/A
Polosky et al.	2017	Spectral Features	Neural Network	N/A	1
Shen et al.	2017	Spectral Features	Threshold	82%	10
Mistry et al.	2018	Spectral Features	Threshold	79.40%	4
Mohamed et al.	2018	Spectral Features	Multilayer NN	96.40%	25

Emotiv Insight and Epoc

Li and Chung (2014, 2015) used a combination of EEG and eyelid closure degree (ECD) to detect drowsiness. A smartphone was used as a processor, in conjunction with an Emotiv headset, resulting in a multimodal drowsiness detector. The phone's camera was used to detect ECD. The combined EEG-ECD detection system achieved an accuracy rate of up to 87.5%. They noted that the combination of the two measurements was able to overcome the shortcomings of each individual measurement.

Pomer-Escher et al. (2014) used spectral features from the alpha and theta bands of EEG. No real time classification was performed, but an ANOVA was conducted across features, channels, and conditions. In particular, the alpha power and ratio of theta to alpha were found to be measurements of fatigue.

Wang et al. (2015) proposed the use of sample entropy and rhythm energies for EEG-based mental fatigue estimation. A wavelet transform was used to find non-linear features in the EEG segment. Wavelet features and a backpropagation neural network (BPNN) were combined for classification. However, no accuracy was reported.

Dkhil et al. (2015, 2017) used an Epoc to validate a Fast Fourier Transform (FFT)-based method. A fuzzy logic system was used to assess drowsiness. This technique was also tested on Physionet sleep samples, but no accuracy value was reported.

Chen et al. (2016) compared four devices for drowsy driver detection: an Emotiv Epoc, a Neurosky MindWave, a camera, and a gyroscope. A total of three subjects were investigated. EEG spectral features were combined with regression for classification. The MindWave had an accuracy of 71%, but a high rate of misclassifications. The Emotiv Epoc had a reported accuracy of 92%, attributed to the greater number of electrodes. Compared with the other devices, EEG was found to be the most cost-effective means of driver detection.

Nugraha et al. (2016) and Sarno et al. (2016) used an Emotiv headset for drowsiness detection. Data from 30 volunteers were collected during driving simulator sessions that ranged from 33 to 60 min in length. A cross-channel correlation between spectral features was calculated for each subject. Both k-nearest neighbor (KNN) and SVM classifiers were used to detect drowsiness. The KNN system achieved a mean accuracy of 96%, whereas the SVM classifier achieved a mean accuracy of 81%.

Sawicki et al. (2016) examined a new measure for drowsiness detection, based on the maximum differences between the alpha band and the theta band, and a combined alpha-theta spectral power. An ANOVA was used to find significant differences between the feature under different lighting conditions. However, no accuracy value was reported.

Damit et al. (2017) developed a multi-modal fatigue estimation system for soldiers. The EEG of 10 subjects was

gathered. Features extracted included spectral power and the discrete wavelet transform (DWT). In particular, the peak alpha frequency (PAF) was the primary EEG feature. No classification was performed, but a paired *t*-test was performed.

Alchalcabi et al. (2017) investigated the use of the Epoc+ as a tool for treating attention deficit hyperactivity disorder (ADHD) and attention deficit disorder (ADD). A virtual reality game was controlled using the headset. Instead of detecting drowsiness, the system was used to increase focus, and the authors reported an increase of 10% in healthy subjects that used the EEG-based controls.

Pham et al. (2018) directly examined real-time drowsiness detection using an Emotiv Epoc. The primary features extracted were spectral features, and classification was performed with SVM. The reported accuracy was 70%, with a single subject.

Poorna et al. (2018) investigated drowsiness detection in a driving simulation. Two feature sets were collected, spectral band powers and temporal characteristics. Principal component analysis (PCA) was used to reduce the number of features. Two algorithms were used for classification: k-nearest neighbor (KNN) and an artificial neural network (ANN). Reported classification accuracies were 80% for KNN and 85% for ANN.

Bajwa et al. (2019) tested a distracted driver detection system. A total of 13 subjects were investigated. Features include time-domain features and frequency-domain features, including spectral band power and wavelets. A multilayer perceptron (MLP) and Bayesian network were used for classification. Testing was performed while driving in a controlled environment, an isolated parking lot. The reported accuracies include 91.54% for distraction detection, and 76.99% in identifying the cause of distraction.

Chen et al. (2019) explored the EEG of fatigue affecting drivers. Fourteen participants provided data for the study. EEG data was decomposed into band-based features using the wavelet

packet transform (WPT). A parameter called phase-lag index (PLI) was proposed for network activity rating. Classification was performed with an SVM, and resulted in a reported accuracy of 94.4%.

Li et al. (2019) proposed four methods to identify fatigue. Most were derived from spectral features, which were used to establish a mental fatigue level (MFL). A simulated excavator task was used to validate the experiment with 15 participants. However, no classification was performed. However, an MF-based threshold was established from experimental data.

Rahma and Rahmatillah (2019) used an Epoc+ device for drowsiness data acquisition. EEG features were converted to discrete wavelet transforms (DWTs) and then subjected to common spatial patterns (CSP). The authors reported an average accuracy ranging from 91.67 to 93.75%, whereas the exclusion of CSP processing reduced the accuracy to no more than 87%.

Saichoo and Boonbrahm (2019) detailed a real-time driver drowsiness detection system used EEG band based spectral features, using the Emotiv Epoc+. Spectral band power was calculated using wavelets, Fourier transforms, and autoregressive estimates. Spatial filtering techniques, such as principal component analysis, were used for signal enhancement. Five volunteers were used. The system was able to correctly identify drowsiness at a rate of up to 83.33%, but had an overall accuracy of 70%. However, the system had difficulties with correct identification of non-drowsy states.

Tan et al. (2020) used data from a 40-min simulated driving task with 18 subjects, gathered with an Emotiv Epoc. Feature extraction involved band-based spectral power with a 2 s window. A time series classification (TSC) model was used, which assigned a label to each time segment. A Long-term Recurrent Convolutional Network (LCRN) was used for classification. As

TABLE 6 | Emotiv Insight, Flex, and Epoc Studies.

Paper	Year	Features	Classification	Accuracy	Size
Li and Chung	2014–2015	Spectral, Eye Closure	SVM	82.71%	6
Pomer-Esche et al.	2014	Spectral Features	ANOVA	N/A	N/A
Dkhil et al.	2015–2017	Spectral Features	Fuzzy Logic Controller	N/A	1
Wang et al.	2015	Spectral, Wavelets, Entropy	BPNN	N/A	3
Chen et al.	2016	Spectral Features	Regression	92%	3
Nugraha et al.	2016	Spectral Features, Gyro	KNN, SVM	81–90%	6
Sawicki et al.	2016	Spectral Features	ANOVA	N/A	50
Alchalcabi et al.	2017	Spectral Features	State-based BCI	N/A	4
Damit et al.	2017	Wavelets, Spectral Features	Paired <i>t</i> -test	N/A	10
Pham et al.	2018	Spectral Features	SVM	70%	1
Poorna et al.	2018	Spectral Features	KNN, ANN	80–85%	18
Bajwa et al.	2019	Wavelets, Spectral Features	MLP, Bayesian Net	91.54%	13
Chen et al.	2019	PLI, Wavelet Transform	SVM	94.40%	14
Li et al.	2019	Spectral Features	MF Threshold	N/A	15
Rahma and Rahmatillah	2019	DWT	CSP	91.67–93.75%	1
Saichoo and Boonbrahm	2019	DWT, FT, AR	Thresholding	70%	5
Tan et al.	2020	Spectral Features	LCRN	83.33%	18

a preprint, the work still awaited peer review when discussed by the authors.

As shown in **Table 6**, the results suggest that the Emotiv Epoc and Epoc+ may be used for drowsiness detection, but proprietary firmware and software represent a potential issue. All entries reporting accuracy have a minimum of at least 80%. Support for Emotiv devices is difficult without the appropriate license.

DISCUSSION

Findings

Examples of EEG-based drowsiness detection were found for each examined brand, including the Emotiv Epoc, the Neurosky MindWave, the OpenBCI, and the InteraXon Muse, and all examined EEG systems were utilized in at least one successful example of real-time drowsiness detection (Abdel-Rahman et al., 2015; Nugraha et al., 2016; Mohamed et al., 2018b; Teo and Chia, 2018). A total of 27 surveyed studies reported an accuracy score. In terms of evaluated average accurate performance, the least consistent of these was the Neurosky MindWave, but the minimum of reported from the others was an OpenBCI study with 79.4% (Mistry et al., 2018). Although these systems may not be as accurate as research- or medical-grade systems, they may be sufficient for deployment in certain occupational contexts. For example, these systems could be deployed by smaller businesses in developing countries or by professions with the urgent need for easily available drowsiness detection systems. However, the different experimental designs utilized by each study make direct comparisons among these systems challenging.

Furthermore, several successful studies utilized relatively simple algorithms and spectral features, including FFT, EEG band powers, and linear classifiers (Abdel-Rahman et al., 2015; Nugraha et al., 2016; Mohamed et al., 2018b; Teo and Chia, 2018). The use of “complex” algorithms requiring more processing power, such as SVM, convolution neural networks, and deep learning systems, may constrain the ability to implement these systems (Nugraha et al., 2016). Even these more “complex” algorithms can easily run on an external device, such as a smartphone. Thus, even a single-electrode Neurosky Mindwave, when providing data to a properly trained classifier in controlled conditions, can achieve high accuracy in certain cases (Abdel-Rahman et al., 2015).

The usage of proven classification techniques and features demonstrates the relative ease of designing a drowsiness detection system, although low levels of accuracy, sensitivity, and specificity and the necessity of training are likely issues that may be encountered. However, the “best” headset depends on the user-specific trade-offs among algorithm complexity, performance, and price (AlZu'bi et al., 2013; Abdel-Rahman et al., 2015; Chen et al., 2016).

Limitations

The current review had several limitations. First, the scope of the investigation was constrained by the small sample size. Second, the implementations and evaluation criteria greatly differed across the investigated papers, often using similar terminology

for different concepts. For example, “drowsiness” was defined differently across studies, which included fatigue, microsleeps, and sleep stages (Vuckovic et al., 2002; Cabrall et al., 2016). In addition, the review included validation studies, conference results, and graduate dissertations, in addition to peer-reviewed journal articles. Future work would likely require alterations to the search and inclusion criteria.

Future Work

Further steps are necessary to further examine the viability of using low-cost consumer EEG headsets as drowsiness detectors. First, the eligibility and search criteria should be further refined to more thoroughly cover the published literature. In addition, common performance metrics and definitions would ideally be described and consistently maintained. Comparisons of the data acquisition systems, feature extraction methods, and classification algorithms would be required. Finally, several additional brands and models of EEG headsets would need to be examined. Combining all of these steps would allow a more thorough meta-analysis to be performed.

CONCLUSIONS

Traditional medical- and research-grade EEG systems have been successfully used for drowsiness and brain state estimation but are less versatile outside of a controlled laboratory environment. Between medical and consumer systems, innate limitations include a reduced number of electrodes, computation complexity, and noise removal capabilities. Low-cost EEG headsets show greater design convenience for “real world” occupational use. Several of these devices, including the Emotiv Epoc, Neurosky Mindwave, InterAxon Muse, and OpenBCI, have been utilized as drowsiness detectors, to varying degrees of success. However, open-source software and occupational refinement may boost the capabilities of these systems over time. This flexibility is advantageous to developing countries, small businesses, and hobbyist users; however, the final selection of optimal models and algorithms will be highly context-specific.

DATA AVAILABILITY STATEMENT

All datasets generated for this study are included in the article/supplementary material.

AUTHOR CONTRIBUTIONS

JL and ML performed the literature search. D-GP provided facilities and support. All authors contributed to the article and approved the submitted version.

FUNDING

This work was supported by the National Research Foundation of Korea (NRF) grant 2018R1A2B2007997, funded by the Korean government Ministry of Science, ICT, and Future Planning (MSIP) and the Focused Ultrasound Foundation.

REFERENCES

- Abdel-Rahman, A. S., Seddik, A. F., and Shawky, D. M. (2015). "An affordable approach for detecting drivers' drowsiness using EEG signal analysis," in *Proceedings of the International Conference on Advances in Computing, Communications, and Informatics* (Kochi), 1326–1332.
- Aboalayon, K., and Faezipour, M. (2019). "Single channel EEG for near real-time sleep stage detection," in *Proceedings of the International Conference on Computational Science and Computational Intelligence* (Yogyakarta), 641–645.
- Alchalabi, A. E., Shirmohammadi, S., Eddin, A. N., and Elsharnouby, M. (2018). Focus: detecting ADHD patients by an EEG-based serious game. *IEEE Trans. Instrum. Meas.* 67, 1512–1520. doi: 10.1109/TIM.2018.2838158
- Alchalcabi, A. E., Eddin, A. N., and Shirmohammadi, S. (2017). "More attention, less deficit: wearable EEG-based serious game for focus improvement," in *Proceedings of the IEEE International Conference on Serious Games and Applications for Health* (Perth, WA), 1–8.
- Almogbel, M. A., Dang, A. H., and Kameyama, W. (2018). "EEG-signals based cognitive workload detection of vehicle driver using deep learning," in *Proceedings from the International Conference on Advanced Communication Technology* (Chuncheon), 256–259.
- AlZu'bi, H. S., Al-Nuaimy, W., and Al-Zubi, N. S. (2013). "EEG-based driver fatigue detection," in *Proceedings of the International Conference on Developments in eSystems Engineering* (Abu Dhabi), 111–114.
- Anwar, D., Garg, P., Naik, V., Gupta, A., and Kumar, A. (2018). "Use of portable EEG sensors to detect meditation," in *Proceedings of the International Conference on Communication Systems & Networks* (Bangalore), 705–710.
- Araújo, B. C. (2019). *Drowsiness Detection Using a Headband and Artificial Neural Networks*. Coimbra: University of Coimbra. Available online at: <https://estudogeral.sib.uc.pt/bitstream/10316/88133/1/Beatriz%20Campos%20Rapos%20Medeiros%20Araujo.pdf> (accessed June 27, 2020).
- Ayala Meza, R. B. (2017). *EEG Biometrics During Sleep and Wakefulness: Performance Optimization and Security Implications*. Montreal, QC: École Polytechnique de Montréal.
- Badcock, N., Mousikou, P., Mahajan, Y., De Lissa, P., Thie, J., and McArthur, G. (2013). Validation of the Emotiv EPOC EEG gaming system for measuring research quality auditory ERPs. *PeerJ* 1:e38. doi: 10.7717/peerj.38
- Badcock, N., Preece, K., de Wit, B., Glenn, K., Fieder, N., Thie, J., et al. (2015). Validation of the Emotiv EPOC EEG system for research quality auditory event-related potentials in children. *PeerJ* 3:e907. doi: 10.7717/peerj.907
- Bajwa, G., Fazeen, M., and Dantu, R. (2019). Detecting driver distraction using stimuli-response EEG analysis. *arXiv* 1904:09100.
- Bakshi, V. (2018). *Towards Practical Driver Cognitive Workload Monitoring via Electroencephalography*. Toronto, ON: University of Toronto.
- Bashivan, P., Rish, I., and Heisig, S. (2015). Mental state recognition via wearable EEG. *arXiv preprint arXiv* 1602.00985.
- Bryan Van Hal, S. R., and Bossemeyer, R. (2014). Low-cost EEG-based sleep detection. *Conf. Proc. IEEE Eng. Med. Biol. Soc.* 2014, 4571–4574. doi: 10.1109/EMBC.2014.6944641
- Cabrall, C. D., Happee, R., and De Winter, J. C. (2016). From Mackworth's clock to the open road: a literature review on driver vigilance task operationalization. *Transp. Res. F* 40, 169–189. doi: 10.1016/j.trf.2016.04.001
- Chen, E., Durairaj, D., Hew, B., Hoppel, M., and Huang, P. (2016). *Quantitative and Qualitative Trade-Off Analysis of Drowsy Driver Detection Methods: Single Electrode Wearable EEG Device, Multi-Electrode Wearable EEG Device, and Head-Mounted Gyroscope*. College Park, MD: University of Maryland.
- Chen, J., Wang, H., Wang, Q., and Hua, C. (2019). Exploring the fatigue affecting electroencephalography based functional brain networks during real driving in young males. *Neuropsychologia* 129, 200–211. doi: 10.1016/j.neuropsychologia.2019.04.004
- Correa, A. G., Orosco, L., and Laciari, E. (2014). Automatic detection of drowsiness in EEG records based on multimodal analysis. *Med. Eng. Phys.* 244–249. doi: 10.1016/j.medengphy.2013.07.011
- Crowley, K., Sliney, A., Pitt, I., and Murphy, D. (2010). "Evaluating a brain-computer interface to categorise human emotional response," in *Proceedings of the IEEE International Conference on Advanced Learning Technologies* (Sousse), 276–278.
- Damit, D. F., Senanayake, S. A., Malik, O. A., and Tuah, N. J. (2017). "Neuromuscular fatigue analysis of soldiers using DWT based EMG and EEG data fusion during load carriage," in *Proceedings of the Asian Conference on Intelligent Information and Database Systems* (Kanazawa), 602–612.
- Davidson, P. R., Jones, R. D., and Peiris, M. T. (2007). EEG-based lapse detection with high temporal resolution. *IEEE Trans. Biomed. Eng.* 54, 832–839. doi: 10.1109/TBME.2007.893452
- de Lissa, P., Sörensen, S., Badcock, N., Thie, J., and McArthur, G. (2015). Measuring the face-sensitive N170 with a gaming EEG system: a validation study. *J. Neurosci. Methods* 253, 47–54. doi: 10.1016/j.jneumeth.2015.05.025
- Dkhil, M. B., Chawech, N., Wali, A., and Alimi, A. M. (2017). "Towards an automatic drowsiness detection system by evaluating the alpha band of EEG signals," in *Proceedings from International Symposium on Applied Machine Intelligence and Informatics* (Marrakesh), 000371–000376.
- Dkhil, M. B., Wali, A., and Alimi, A. M. (2015). "Drowsy driver detection by EEG analysis using fast fourier transform," in *Proceedings of the International Conference on Intelligent Systems Design and Applications*, 313–318.
- Doudou, M., Bouabdallah, A., and Cherfaoui, V. (2018). A light on physiological sensors for efficient driver drowsiness detection system. *Sens. Transducers* 224, 39–50. doi: 10.5220/0006607800990106
- Dunbar, J., Gilbert, J. E., and Lewis, B. (2020). Exploring differences between self-report and electrophysiological indices of drowsy driving: a usability examination of a personal brain-computer interface device. *J. Safety Res.* 74, 27–34. doi: 10.1016/j.jsr.2020.04.006
- Dunne, B., van Hal, B., Rhodes, S., and Bossemeyer, R. (2015). Low-cost EEG-based sleep detection. *Conf. Proc. IEEE Eng. Med. Biol. Soc.* 2014, 4571–4574.
- Farnsworth, B. (2017). *EEG Headset Comparison – A Technical Overview of 10 Headsets*. iMotions. Copenhagen.
- Foong, R., Ang, K. K., Zhang, Z., and Quek, C. (2019). An iterative cross-subject negative-unlabeled learning algorithm for quantifying passive fatigue. *J. Neural Eng.* 16:056013. doi: 10.1088/1741-2552/ab255d
- Guo, Z., Pan, Y., Zhao, G., Cao, S., and Zhang, J. (2017). Detection of driver vigilance level using EEG signals and driving contexts. *IEEE Trans. Reliab.* 67, 370–380. doi: 10.1109/TR.2017.2778754
- Hoffmann, A. (2020). *The Iterative Development and Evaluation of the Gamified Stress Management App "Stress-Mentor"*. Kaiserslautern: Technical University of Kaiserslautern.
- Izquierdo-Reyes, J., Mendoza-Ramirez, R. A., Bustamante-Bello, M. R., and Alonso-Valerdi, L. M. (2016). "Review of passive BCI framework for advanced driver assistance systems in intelligent transportation," in *Proceedings of the International Virtual Concept Workshop on Intelligent Transport Systems and Data Science* (Guadalajara), 1–4.
- Jones, A., and Schwartz, G. (2010). *Using Brain-Computer Interfaces to Analyze EEG Data for Safety Improvement*. Team for Research in Ubiquitous Secure Technology.
- Joshi, D. H., Jaliya, U. K., and Thakore, D. (2015). *Raw EEG-Based Fatigue and Drowsiness Detection: A Review*. 1–5.
- Karuppusamy, N. S., and Kang, B. Y. (2017). Driver fatigue prediction using eeg for autonomous vehicle. *Adv. Sci. Lett.* 23, 9561–9564. doi: 10.1166/asl.2017.9747
- Krigolson, O. E., Williams, C. C., Norton, A., Hassall, C. D., and Colino, F. L. (2017). Choosing MUSE: validation of a low-cost, portable EEG system for ERP research. *Front. Neurosci.* 11:109. doi: 10.3389/fnins.2017.00109
- Lakhan, P., Banluesombatkul, N., Changniam, V., Dhithijaiyarn, R., Leelaarporn, P., Boonchieng, E., et al. (2019). Consumer grade brain sensing for emotion recognition. *IEEE Sens. J.* 19, 9896–9907. doi: 10.1109/JSEN.2019.2928781
- Li, G., and Chung, W. Y. (2014). Estimation of eye closure degree using EEG sensors and its application in driver drowsiness detection. *Sensors* 14, 17491–17515. doi: 10.3390/s140917491
- Li, G., and Chung, W. Y. (2015). A context-aware EEG headset system for early detection of driver drowsiness. *Sensors* 15, 20873–20893. doi: 10.3390/s150820873
- Li, H., Wang, D., Chen, J., Luo, X., Li, J., and Xing, X. (2019). Pre-service fatigue screening for construction workers through wearable EEG-based signal spectral analysis. *Automation Construct.* 106:102851. doi: 10.1016/j.autcon.2019.102851
- Lim, C. K., Chia, W. C., and Chin, S. W. (2014). "A mobile driver safety system: analysis of single-channel EEG on drowsiness detection," in *Proceedings of the International Conference on Computational Science and Technology* (Kuala Lumpur).
- Lin, C. J., Ding, C. H., Liu, C. C., and Liu, Y. L. (2015). "Development of a real-time drowsiness warning system based on an embedded system,"

- in *Proceedings of the International Conference on Advanced Robotics and Intelligent Systems* (Taipei).
- Lin, C. T., Chuang, C. H., Huang, C. S., Tsai, S. F., Lu, S. W., Chen, Y. H., et al. (2014). Wireless and wearable EEG system for evaluating driver vigilance. *IEEE Trans. Biomed. Circuits Syst.* 8, 165–176. doi: 10.1109/TBCAS.2014.2316224
- Majkowski, A., Kolodziej, M., Rak, R. J., Tarnowski, P., and Szczepanek, K. (2018). “Detecting symptoms of driver fatigue using video analysis,” in *Proceedings of the International Conference Computational Problems of Electrical Engineering* (Banska Stiavnica).
- Majumder, S., Guragain, B., Wang, C., and Wilson, N. (2019). “On-board drowsiness detection using EEG: current status and future prospects,” in *Proceedings on the IEEE International Conference on Electro Information Technology* (Brookings, SD), 483–490.
- Manolova, A., Tsenov, G., Lazarova, V., and Neshov, N. (2016). “Combined EEG and EMG fatigue measurement framework with application to hybrid brain-computer interface,” in *Proceedings from the IEEE International Black Sea Conference on Communications and Networking* (Varna), 1–5.
- Mard, Z., Ashtiani, S., and Mohammad Mikaili, M. (2011). EEG-based drowsiness detection for safe driving using chaotic features and statistical tests. *J. Med. Signals Sens.* 130–137. doi: 10.4103/2228-7477.95297
- Mehreen, A., Anwar, S. M., Haseeb, M., Majid, M., and Ullah, M. O. (2019). A hybrid scheme for drowsiness detection using wearable sensors. *IEEE Sens. J.* 19, 5119–5126. doi: 10.1109/JSEN.2019.2904222
- Min, J., Wang, P., and Hu, J. (2017). Driver fatigue detection through multiple entropy fusion analysis in an EEG-based system. *PLoS ONE* 12:e0188756. doi: 10.1371/journal.pone.0188756
- Mistry, K. S., Pelayo, P., Anil, D. G., and Ge, K. (2018). “Brain-computer interface (BCI) based systems can be used to control external devices by translating a certain set of patterns in the brain signals into actions,” in *Proceedings of the International Instrumentation and Measurement Technology Conference* (Houston, TX).
- Mohamed, F., Ahmed, S., Ibrahim, Z., and Yaacob, S. (2018a). “Comparison of features based on spectral estimation for the analysis of EEG signals in driver behavior,” in *Proceedings from the International Conference on Computational Approach in Smart Systems Design and Applications* (Kuching), 1–7.
- Mohamed, F., Nataraj, S. K., Ahmed, S. F., and Yaacob, S. (2018b). An approach in determining fatiguedness and drowsiness. *Res. Inventy Int. J. Eng. Sci.* 8, 2278–4721.
- Moher, D., Liberati, A., Tetzlaff, J., and Altman, D. (2009). Preferred reporting items for systematic reviews and meta-analyses: the PRISMA statement. *Ann. Intern. Med.* 151, 264–269. doi: 10.7326/0003-4819-151-4-200908180-00135
- Murphy, J., and Russomanno, C. (2016). *OpenBCI: Biosensing for Everybody*. Kickstarter. Available online at: www.kickstarter.com/projects/openbci/openbci-biosensing-for-everybody
- Nissimagoudar, P. C., and Nandi, A. V. (2020). “Precision enhancement of driver assistant system using EEG based driver consciousness analysis & classification,” in *Computational Network Application Tools for Performance Management*, eds M. Pant, T. K. Sharma, S. Basterrech, and C. Banerjee (Singapore: Springer), 247–257.
- Nugraha, B. T., Sarno, R., Asfani, D. A., Igasaki, T., and Munawar, M. N. (2016). Classification of driver fatigue state based on eeg using Emotiv EPOC+. *J. Theoretic. Appl. Inform. Technol.* 86:1.
- Ogino, M. (2018). Portable drowsiness detection through use of a prefrontal single-channel electroencephalogram. *Sensor* 18:4477. doi: 10.3390/s18124477
- Patel, K., Shah, H., Dcosta, M., and Shastri, D. (2017). “Evaluating neurosky’s single-channel EEG sensor for drowsiness detection,” in *Proceedings of the International Conference on Human-Computer Interaction* (Vancouver, BC), 243–250.
- Pham, T. T., Nguyen, T. D., Le, Q. K., and Huynh, Q. L. (2018). “Application of portable EEG device in detection and classification drowsiness by support vector machine,” in *Proceedings of the International Conference on the Development of Biomedical Engineering in Vietnam* (Ho Chi Minh City), 521–526.
- Polosky, N., Jagannath, J., O’Connor, D., Saarinen, H., and Foulke, S. (2017). “Artificial neural network with electroencephalogram sensors for brainwave interpretation: brain-observer-indicator development challenges,” in *Proceedings of the International Conference and Expo on Emerging Technologies for a Smarter World* (Stony Brook, NY), 1–6.
- Pomer-Escher, A., Tello, R., Castillo, J., and Bastos-Filho, T. (2014). “Analysis of mental fatigue in motor imagery and emotional stimulation based on EEG,” in *Proceedings from the Congresso Brasileiro de Engenharia Biomedica* (Vitoria).
- Poorna, S. S., Arsha, V. V., Aparna, P. T. A., Gopal, P., and Nair, G. J. (2018). “Drowsiness detection for safe driving using PCA EEG signals,” in *Progress in Computing, Analytics and Networking. Advances in Intelligent Systems and Computing*, Vol. 710, eds P. Pattnaik, S. Rautaray, H. Das and J. Nayak (Singapore: Springer). doi: 10.1007/978-981-10-7871-2_40
- Putra, A. E., Atmaji, C., and Utami, T. G. (2016). “EEG-based microsleep detector using microcontroller,” in *Proceedings of the International Conference on Information Technology and Electrical Engineering* (Chiang Mai), 1–4.
- Rahma, O. N., and Rahmatillah, A. (2019). Drowsiness analysis using common spatial pattern and extreme learning machine based on electroencephalogram signal. *J. Med. Signals Sens.* 9:130. doi: 10.4103/jmss.JMSS_54_18
- Ries, A. J., Touryan, J., Vettel, J., McDowell, K., and Hairston, W. D. (2014). A comparison of electroencephalography signals acquired from conventional and mobile systems. *J. Neurosci. Neuroeng.* 3, 10–20. doi: 10.1166/jnsne.2014.1092
- Rodríguez, A., Rey, B., and Alcañiz, M. (2013). Validation of a low-cost EEG device for mood induction studies. *Ann. Rev. Cyberther. Telemed.* 11, 43–47.
- Rohit, F., Kulathumani, V., Kavi, R., Elwarfalli, I., Kecojovic, V., and Nimbarte, A. (2017). Real-time drowsiness detection using wearable, lightweight brain sensing headbands. *IET Intell. Transp. Syst.* 11, 255–263. doi: 10.1049/iet-its.2016.0183
- Rundo, F., Rinella, S., Massimino, S., Coco, M., Fallica, G., Parenti, R., et al. (2019). An innovative deep learning algorithm for drowsiness detection from EEG signal. *Computation* 7:13. doi: 10.3390/computation7010013
- Sadeghi, K., Banerjee, A., Sohankar, J., and Gupta, S. K. (2016). “Safedrive: an autonomous driver safety application in aware cities,” in *Proceedings of the IEEE International Conference on Pervasive Computing and Communication Workshops* (Sydney, NSW).
- Saichoo, T., and Boonbrahm, P. (2019). Brain computer interface for real-time driver drowsiness detection. *Thai J. Phys.* 36, 1–8.
- Salehi, M., Mackellar, G., and Leckie, C. (2015). “Car racing driver distraction detection using brain eeg,” in *Workshop on Large-Scale Sports Analytics in conjunction with the 21st ACM SIGKDD Conference on Knowledge Discovery and Data Mining (KDD-2015)*.
- Sarno, R., Nugraha, B. T., Munawar, M. N., Sarno, R., Nugraha, B. T., and Munawar, M. N. (2016). Real time fatigue-driver detection from electroencephalography using Emotiv EPOC+. *Int. Rev. Comput. Softw.* 11, 214–223. doi: 10.15866/irecos.v11i3.8562
- Sawangjai, P. H., Leelaarporn, P., Kongwudhikunakorn, S., and Wilaiprasitporn, T. (2019). Consumer grade eeg measuring sensors as research tools: a review. *IEEE Sens. J.* 20, 3996–4024. doi: 10.1109/JSEN.2019.2962874
- Sawicki, D., Wolska, A., Roslon, P., and Ordysinski, S. (2016). New EEG measure of the alertness analyzed by Emotiv EPOC in a real working environment. *Neurotechnix* 2016, 35–42. doi: 10.5220/0006041200350042
- Sethi, C., Dabas, H., Dua, C., Dalawat, M., and Sethia, D. (2018). “EEG-based attention feedback to improve focus in E-learning,” in *Proceedings of the International Conference on Computer Science and Artificial Intelligence* (Shenzhen), 321–326.
- Shabani, H., Mikaili, M., and Noori, S. M. (2016). Assessment of recurrence quantification analysis (RQA) of EEG for development of a novel drowsiness detection system. *Biomed. Eng. Lett.* 6, 196–204. doi: 10.1007/s13534-016-0223-5
- Shen, J., Li, B., and Shi, X. (2017). Real-time detection of human drowsiness via a portable brain-computer interface. *Open J. Appl. Sci.* 7:98. doi: 10.4236/ojapps.2017.73009
- Shin, I., Setiawan, B., Samopa, F., Suryotrisongko, H., Atletiko, F. J., and Wibowo, R. P. (2013). “Development of drowsiness detection system with analyzing attention and meditation wave using support vector machine method,” in *Proceedings of the ISICO* (Bali).
- Solaz, J., Laparra-Hernández, J., Bande, D., Rodríguez, N., Veleff, S., Gerpe, J., et al. (2016). Drowsiness detection based on the analysis of breathing rate obtained from real-time image recognition. *Transport. Res. Proc.* 14, 3867–3876. doi: 10.1016/j.trpro.2016.05.472
- Suprihadi, T., and Karyono, K. (2014). “DROWTION: Driver drowsiness detection software using MINDWAVE,” in *Proceedings of the International Conference*

- on *Industrial Automation, Information and Communications Technology* (Bali), 141–144.
- Tan, B. H. (2012). *Using a low-cost EEG sensor to detect mental states* [Dissertation]. Carnegie Mellon University, Pittsburgh, PA, United States.
- Tan, C. W., Salehi, M., and Mackellar, G. (2020). Detecting driver's distraction using long-term recurrent convolutional network. *arXiv [Preprint]*. arXiv 2004.11839.
- Teo, J., and Chia, J. T. (2018). "EEG-based excitement detection in immersive environments: an improved deep learning approach," in *AIP Conference Proceeding* (Penang).
- US Dot National Highway Traffic Safety Administration (2018). *2017 Fatal Motor Vehicle Crashes: Overview*. DOT HS 812 60.
- Van Hal, B., Rhodes, S., Dunne, B., and Bossemeyer, R. (2014). "Low-cost EEG-based sleep detection," in *Proceedings of the Annual International Conference of the IEEE Engineering in Medicine and Biology Society* (Chicago).
- Vuckovic, A., Radivojevic, V., Chen, A. C., and Popovic, D. (2002). Automatic recognition of alertness and drowsiness from EEG by an artificial neural network. *Med. Eng. Phys.* 24, 349–360. doi: 10.1016/S1350-4533(02)00030-9
- Wang, D., Chen, J., Zhao, D., Dai, F., Zheng, C., and Wu, X. (2017). Monitoring workers' attention and vigilance in construction activities through a wireless and wearable electroencephalography system. *Automat. Construct.* 82, 122–137. doi: 10.1016/j.autcon.2017.02.001
- Wang, F., Lin, J., Wang, W., and Wang, H. (2015). "EEG-based mental fatigue assessment during driving by using sample entropy and rhythm energy," in *Proceedings of the IEEE International Conference on Cyber Technology in Automation, Control, and Intelligent Systems* (Xi'an), 1906–1911.
- Wang, J. S. (2011). *Effectiveness of Stability Control Systems for Truck Tractors*. National Highway Traffic Safety Administration, HS-8114S37.
- Wei, C. S. (2017). *Towards Brain Decoding for Real-World Drowsiness Detection*. San Diego, CA: UC San Diego.
- Wei, C. S., Wang, Y. T., Lin, C. T., and Jung, T. P. (2018). "Toward drowsiness detection using non-hair-bearing EEG-based brain-computer interfaces," in *IEEE Transactions on Neural Systems and Rehabilitation Engineering* (San Diego, CA), 400–406.
- Wexler, A., and Thibault, R. (2019). Mind-reading or misleading? Assessing direct-to-consumer Electroencephalography (EEG) devices marketed for wellness and their ethical and regulatory implications. *J. Cogn. Enhancement* 3, 131–137. doi: 10.1007/s41465-018-0091-2
- Wilaprasitporn, T., and Yagi, T. (2016). "Feasibility study of drowsiness detection using hybrid brain-computer interface," in *Proceedings of the International Convention on Rehabilitation Engineering & Assistive Technology* (Singapore: Singapore Therapeutic, Assistive & Rehabilitative Technologies (START) Centre), 1–4.
- Yin, Y., Zhu, Y., Xiong, S., and Zhang, J. (2011). "Drowsiness detection from EEG spectrum analysis," in *Informatics in Control, Automation and Robotics*, eds J. Andrade Cetto, J.-L. Ferrier, J. Pereira, and J. Filipe (Berlin: Springer) 753–759.
- Zhang, X., Li, J., Liu, Y., Zhang, Z., Wang, Z., Luo, D., et al. (2017). Design of a fatigue detection system for high-speed trains based on driver vigilance using a wireless wearable EEG. *Sensors* 17:486. doi: 10.3390/s17030486

Conflict of Interest: The authors declare that the research was conducted in the absence of any commercial or financial relationships that could be construed as a potential conflict of interest.

Copyright © 2020 LaRocco, Le and Paeng. This is an open-access article distributed under the terms of the Creative Commons Attribution License (CC BY). The use, distribution or reproduction in other forums is permitted, provided the original author(s) and the copyright owner(s) are credited and that the original publication in this journal is cited, in accordance with accepted academic practice. No use, distribution or reproduction is permitted which does not comply with these terms.



Connectome-Based Model Predicts Deep Brain Stimulation Outcome in Parkinson's Disease

Ruihong Shang¹, Le He², Xiaodong Ma³, Yu Ma^{4*} and Xuesong Li^{1*}

¹ School of Computer Science and Technology, Beijing Institute of Technology, Beijing, China, ² Department of Biomedical Engineering, Center for Biomedical Imaging Research, School of Medicine, Tsinghua University, Beijing, China, ³ Center for Magnetic Resonance Research, University of Minnesota, Minneapolis, MN, United States, ⁴ Department of Neurosurgery, Tsinghua University Yuquan Hospital, Beijing, China

OPEN ACCESS

Edited by:

Rong Chen,
University of Maryland, Baltimore,
United States

Reviewed by:

Aristide Merola,
The Ohio State University,
United States

Bin Wang,
Taiyuan University of
Technology, China

*Correspondence:

Xuesong Li
lixuesong@bit.edu.cn
Yu Ma
mayu@tsinghua.edu.cn

Received: 11 June 2020

Accepted: 15 September 2020

Published: 28 October 2020

Citation:

Shang R, He L, Ma X, Ma Y and Li X
(2020) Connectome-Based Model
Predicts Deep Brain Stimulation
Outcome in Parkinson's Disease.
Front. Comput. Neurosci. 14:571527.
doi: 10.3389/fncom.2020.571527

Subthalamic nucleus deep brain stimulation (STN-DBS) is an effective invasive treatment for advanced Parkinson's disease (PD) at present. Due to the invasiveness and cost of operations, a reliable tool is required to predict the outcome of therapy in the clinical decision-making process. This work aims to investigate whether the topological network of functional connectivity states can predict the outcome of DBS without medication. Fifty patients were recruited to extract the features of the brain related to the improvement rate of PD after STN-DBS and to train the machine learning model that can predict the therapy's effect. The functional connectivity analyses suggested that the GBRT model performed best with Pearson's correlations of $r = 0.65$, $p = 2.58E-07$ in medication-off condition. The connections between middle frontal gyrus (MFG) and inferior temporal gyrus (ITG) contribute most in the GBRT model.

Keywords: deep brain stimulation (DBS) surgery, Parkinson's disease, machine learning, brain network, rs-fMRI

INTRODUCTION

Parkinson's disease (PD) is a common neurodegenerative disorder with a wide range of motor and non-motor symptoms, such as cognitive impairment, autonomic dysfunction, disorders of sleep, depression, or hyposmia, which lead to a severe burden for the patients and their caregivers (Poewe et al., 2017). It is considered that PD arises from dysfunction in several neural networks. Thilo van Eimeren et al. confirmed that the medial prefrontal cortex and rostral ventromedial caudate nucleus were functionally disconnected in PD (Thilo van Eimeren et al., 2009). Hammond et al. found that PD patients showed abnormally synchronized oscillatory activity at multiple levels of the basal ganglia (BG)–cortical loop (Hammond et al., 2007).

To cure PD, highly efficacious therapies, such as pharmacological dopamine substitution, have been adapted widely (Poewe et al., 2017). The use of levodopa as dopamine-replacement therapy is highly effective in ameliorating the symptoms of the disease (Fahn et al., 2004) through changing the motor cortex hypoactivation in the supplementary motor area and the primary motor cortex (Buhmann et al., 2003). Deep brain stimulation (DBS) at high frequency was firstly used in 1997 to replace thalamotomy in treating the characteristic tremor of PD and has subsequently been applied to the pallidum and the subthalamic nucleus (STN) (Benabid, 2003). It is reported that neurostimulation of STN was more effective than medical management alone (Deuschl et al., 2006).

DBS therapy is an invasive and costly procedure, and its outcome differs in patients with PD (Cury et al., 2014). While a growing body of research suggests that variability in treatment response

links up with individual differences in neurological function (Hartmann et al., 2016), the search for brain network-based biomarkers can yield a reliable indicator for future treatment response in this respect. The identification of brain-based predictors of PD can not only expand existing biological knowledge of neurodegenerative pathophysiology but also inform real-world clinical practice by assignment of patients to make decisions based on individual patterns of neural function or biomarkers.

Nowadays, powerful neuroimaging methods, such as magnetic resonance imaging (MRI), establish accurate and high-precision observation from the view of neuronal activities (Cohen et al., 1993). In particular, the application of functional magnetic resonance imaging (fMRI) in neuroscience has offered a way to assess the status of functional systems, which can reveal relationships between brain activity and treatment response, such as obsessive-compulsive disorder (Figuee et al., 2013), depression (Guo et al., 2012), pediatric anxiety disorders (McClure et al., 2007), etc. Neuroimaging studies have also identified impairments in the corticostriatal network pathways and the related neural circuits in patients with PD (Hacker et al., 2012).

Moreover, studies of large-scale network analysis using graph theory-based approaches revealed disruptions in the topological properties of brain networks in PD patients. For example, it was found that PD patients had lower clustering coefficient and local efficiency than control subjects, which can contribute to identifying and tracking PD (Luo et al., 2015). Kim et al. found that PD was related to the temporal properties of brain functional connectivity states as well as the variability of network topological organization using resting state fMRI (rs-fMRI) (Kim et al., 2017). These findings of graph theory-based analysis of fMRI in PD give us insights into the possibility of predicting the outcome after DBS with brain networks.

It is confirmed that specific connectivity profiles encompassing frontothalamic streamlines correlated with clinical response, which can guide surgeons to locate DBS electrode in surgery (Horn et al., 2017). There is also a series of specific patterns of the brain that can enhance the clinical care of DBS, such as frontal white matter architecture in curing major depression (Coenen et al., 2019) and posterior thalamus (Tha) in treating essential tremor (Al-Fatly et al., 2019). With these approaches, surgery can be utilized easily, and the sophisticated relationship between the effectiveness of operation and the intrinsic brain connectome can be discovered.

Machine learning as a data-driven technique can use spatiotemporal information to extract the stable whole-brain patterns that are present in MRI data. Because machine learning is effective in automating the process of building models that relate neural activity to symptoms, it has been attempted to use machine learning for predicting response after DBS (Bermudez et al., 2019; Habets et al., 2019).

In this paper, we aimed at building a model to predict the outcome (percentage change in the Unified Parkinson's Disease Rating Scale (UPDRS)-III score) after DBS through functional brain connectivity. We hypothesized that the outcome of stimulation based on whole-brain networks; thus, functional connectivity profiles would predict the individual outcomes of

DBS for PD. The results suggested that the model was capable to predict the DBS outcome, and that the most contributive connections to the prediction were detected.

MATERIALS AND METHODS

Participants and Assessment

This study included 50 patients aged from 50 to 77 (mean age = 60.24 ± 7.84 years) with a final clinic diagnosis of PD. They were recruited from Tsinghua University Yuquan Hospital, Beijing, China, and their disease severities were assessed according to the motor section of the Movement Disorder Society (MDS) UPDRS-III (Antonini et al., 2013). All of them received preoperative MRI and evaluation of dopaminergic responsiveness, and they were considered suitable to DBS surgery according to acute levodopa challenge test (Defer et al., 1999; Rodriguez et al., 2007). The assessing procedure was conducted by a specialist with more than 10 years of experience. All participants were informed about the procedures in this protocol and provided informed consent before the experiment. The research protocol was approved by the Ethics Committee of Tsinghua University Yuquan Hospital.

To be noted, the DBS outcome measure was measured as percentage change in UPDRS-III score comparing postoperative ON DBS to preoperative baseline. The baseline UPDRS-III score was 43.9 ± 12.1 , and the UPDRS improvement rate with DBS was $65.2 \pm 20.6\%$.

Surgical Procedure

DBS surgery was performed under local anesthesia, using the Leksell stereotactic frame (Elekta AB, Stockholm, Sweden). Two STN-DBS electrodes (PINS L301; Beijing, China) were placed in both hemispheres. During the operation, a single unit of microelectrode kept stimulating and recording continuously to evaluate and confirm the site with the best clinical results. After the lead placement was confirmed, the electrodes were connected to a pulse generator (G102R; Pinchi, Beijing, China), which was implanted subcutaneously in the right subclavian region. During surgery, MRI scanning was used for both preoperative targeting and immediate postoperative verification (Foltynie and Hariz, 2010). It was ensured that electrode contacts were well-sited within the STN.

Image Acquisition

MRI scans were conducted 2–3 days before the operational therapy for all PD patients, and each patient was scanned after withdrawal from levodopa for more than 12 h.

Imaging data were collected on a 3T Philips Achieva MRI scanner (Philips Healthcare, Best, The Netherlands) with a 32-channel head coil. Participants were instructed to keep their eyes open and not to think about anything specific during the rs-fMRI scan. Head motion was controlled by fixing their heads using headphone and sponge during scanning. Resting state blood oxygenation-level-dependent (BOLD) signals were collected using the following parameters: 35 axial slices, repetition time (TR) = 2,000 ms, the number of volumes = 240, echo time (TE) = 30 ms, flip angle (FA) = 90° , slice thickness = 4.0 mm,

gap = 0.8 mm, acquisition matrix = 64×64 , and field of view (FOV) = $224 \times 224 \text{ mm}^2$.

Image Preprocessing and Brain Network Construction

Whole-brain functional networks were constructed using SPM 12 and GREYNA software (Wang et al., 2015). The following pre-processing steps were taken: (1) the first 10 volumes of each scan were discarded for magnetization equilibration, (2) data were realigned to the first volume to correct for head motions, (3) bottom-up slice-timing correction was applied, (4) functional images were co-registered to subject-space (the same participant's T1-weighted structural image), then spatial normalization was conducted to acquire Montreal Neurological Institute (MNI) template space, and (5) spatial smoothing was performed at 4 mm full-width half maximum (FWHM) Gaussian kernel. According to the Brainnetome Atlas (BNA) (Fan et al., 2016), we segmented the whole brain into 246 regions, including 210 cortical and 36 subcortical regions. Each region served as one node of functional brain networks, and it can also be regarded as a region of interest (ROI). The mean time series of each ROI was obtained by averaging the BOLD time series over all voxels within that region. The edges of functional brain networks were computed by Pearson correlation coefficients between ROIs.

The T1-weighted volume MRI data and fMRI data were used for DBS lead localization, and this protocol followed the steps in the manual of Lead-DBS (Horn and Kühn, 2015). Images were normalized into ICBM 2009b NLIN asymmetric space using the DISTAL Minimal atlas (Ewert et al., 2017), and DBS electrode contacts were localized within MNI space using Lead-DBS software (www.lead-dbs.org) (Horn and Kühn, 2015).

Connectome-Based Predictive Modeling

According to the BNA, we acquired 30,135 connectivities between ROIs, and the dimension space of connectivity matrix is so large that it can lead to a serious overfitting problem. Therefore, feature preparation was conducted on connectivity between ROIs. To be more specific, we narrowed down the feature space of sparse matrixes through random forest algorithm, which is a multivariate supervised approach that can retain essential pre-surgical features.

As shown in **Figure 1**, our process of learning and predicting mainly includes four parts: (1) all participants were scanned by an MRI scanner to acquire BOLD time series in rs-fMRI, (2) the functional connectivity network was constructed through computing the Pearson correlation coefficients between ROIs, (3) feature selection was applied, and (4) use machine learning method to train the predictive model.

Six predictive models were implemented in this study, including linear regression models with Ordinary Least Squares (OLS) (Goldberger, 1964), ridge regression (Tibshirani, 1996b), or least absolute shrinkage and selection operator (lasso) (Tibshirani, 1996a) and non-linear regression models with Support Vector Regression (SVR) (Drucker et al., 1997), Gradient Boost Regression Tree (GBRT) (Friedman, 2001), or reformed random forest named Extremely Randomized Trees (ERT) (Geurts et al., 2006). We used nested cross-validation, which

included outer Leave-One-Out-Cross-Validation (LOOCV) and inner 5-fold cross-validation (5F-CV), to quantify the prediction accuracy. The inner 5F-CV was used to determine the optimal parameters (e.g., α , λ) for six machine learning algorithms, and outer LOOCV was applied to evaluate the generalizability of the model.

In the inner 5F-CV, we used grid search method to find the best estimator for six models and evaluated each estimator by measuring the prediction error of the model. Then, we acquired six models with suitable estimator to predict the outcome of DBS surgery and choose the most predictive model to conduct connection analysis accordingly.

Because the dataset size is limited compared with tens of thousands of features in PD patients' brain, a Leave-One-Out-Cross-Validation (LOOCV) was used in the outer loop to maximize the prediction model to learn existing data (Kohavi, 1995). In the LOOCV, one sample was used as validation data, and the other samples were used as training data. In the dataset with n subjects, the data of $n-1$ subjects were used as input to train the model, and this process was repeated n times with different left-one-out subjects, generating the estimated percentage changes of UPDRS-III score, identified functional connectivity and their corresponding weights in the training model. This allows us to investigate the biological characteristic of these connections between ROIs by analyzing important connections and nodes chosen by machine learning model.

RESULTS

DBS Lead Placement

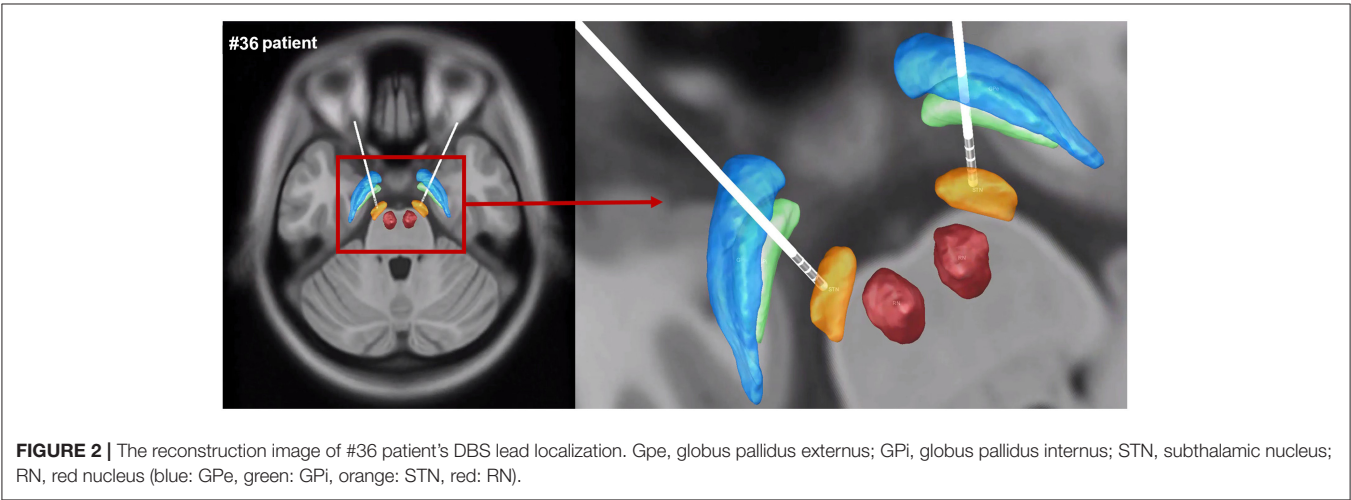
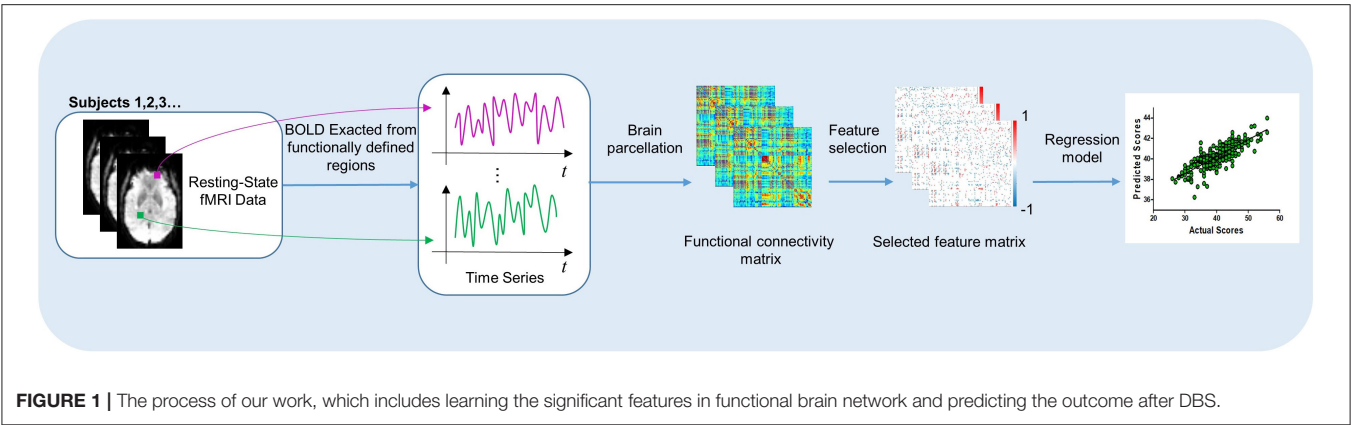
The electrode contacts were well-sited within the STN, and DBS lead localization was reconstructed using Lead-DBS. The reconstruction image of #36 patient was shown as an example in **Figure 2**.

Feature Selection and Connection Analysis

By choosing BNA-based functional connectivity matrix, we acquired 30,135 pairs of connections by removing the repeated connections from the 246×246 combinations in whole-brain connections for each subject. As mentioned in the Materials and Methods section, we used random forest to exclude redundant connections. Finally, the data showed that there were 242 connections for predicting the outcome of DBS without levodopa.

Predicting the Individual Outcome of DBS With PD

Six models (OLS/ridge regression/lasso/SVR/GBRT/ERT) were implemented for the prediction of the DBS outcome. To test the reliability of our connectome-based predictive model, we employed an outer LOOCV analysis to predict the improvement rate in UPDRS-III score after DBS. Four indicators [i.e., Pearson's r , Pearson's p , mean absolute error (MAE), and mean square error (MSE)] were utilized to measure the performance of each predicting model, shown in **Table 1**. Pearson's r is an indicator to measure the correlations between two objects, whereas Pearson's p -value corresponds to a test for whether



the correlation was significantly different from zero ($p < 0.05$ was considered statistically significant). We also used MAE (Willmott and Matsuura, 2005) and MSE (Imbens et al., 2005) to describe the average model-performance error. The correlations between predicted percentage change in UPDRS-III score and actual percentage change in UPDRS-III score were significant in our model based on functional connectivity. The best fitting model came from the GBRT model with Pearson correlations of $r = 0.65$, $p = 2.58E-07$ in medication-off condition, shown in **Figure 3**. In addition, the Bonferroni correction (Abdi, 2007) was used in performing multiple tests, and the Pearson's p was less than the stricter threshold of 0.001.

Connections Contributing to Prediction

Based on stable prediction, further brain analysis could be conducted by the GBRT model. For better interpretation, we grouped the 246 ROIs into 24 gyri as defined by BNA and calculated the top 11 predictive connections between 24 gyri, shown in **Figure 4A**. The gyri of each brain hemisphere were further divided into five lobes, and the predictive connections selected by the GBRT model from the perspective of the lobes were shown in **Figure 4B**.

TABLE 1 | Performance of six models in predicting the improvement rate in UPDRS-III score by using nested cross-validation.

Model	MAE	MSE	r	p -value
OLS	21.14	862.94	0.05	0.75
Ridge regression	17.57	573.95	0.14	0.35
Lasso regression	14.29	411.83	0.33	0.02
GBRT	12.40	240.74	0.65	2.58E-07
SVR	16.06	398.57	0.28	0.05
ERT	13.12	282.13	0.59	6.67E-06

In predicting the outcome of DBS without levodopa, middle frontal gyrus (MFG), inferior temporal gyrus (ITG), superior frontal gyrus (SFG), and Tha show more connections than other regions. The top 11 predictive connections were shown in **Table 2**. The connections of cross-brain regions, such as MFG and ITG, precuneus (Pcun), and posterior superior temporal sulcus (pSTS), exerted an enormous function on medication-off condition.

DISCUSSION

The actual outcome of PD patients was based on their motor and non-motor symptoms. To assess the condition of PD patients, there were the Hoehn and Yahr (H&Y) scale (Ramaker et al., 2002) for quantifying disease stage, MDS-UPDRS (Goetz et al., 2008) for assessing the patient’s condition clinically, Beck Depression Inventory (Beck et al., 1988) for measuring the patient’s degree of depression, and Mini-Mental State Examination (Folstein et al., 1983) for intellectual impairment. The objective of this study was to explore the

relationship between brain connectivity and DBS outcome regarding the motor symptoms among PD patients. UPDRS-III provides a useful severity measure on the motor symptoms of

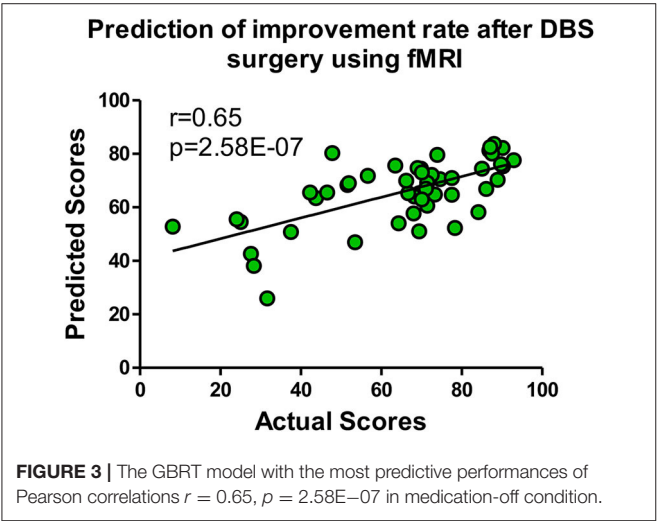
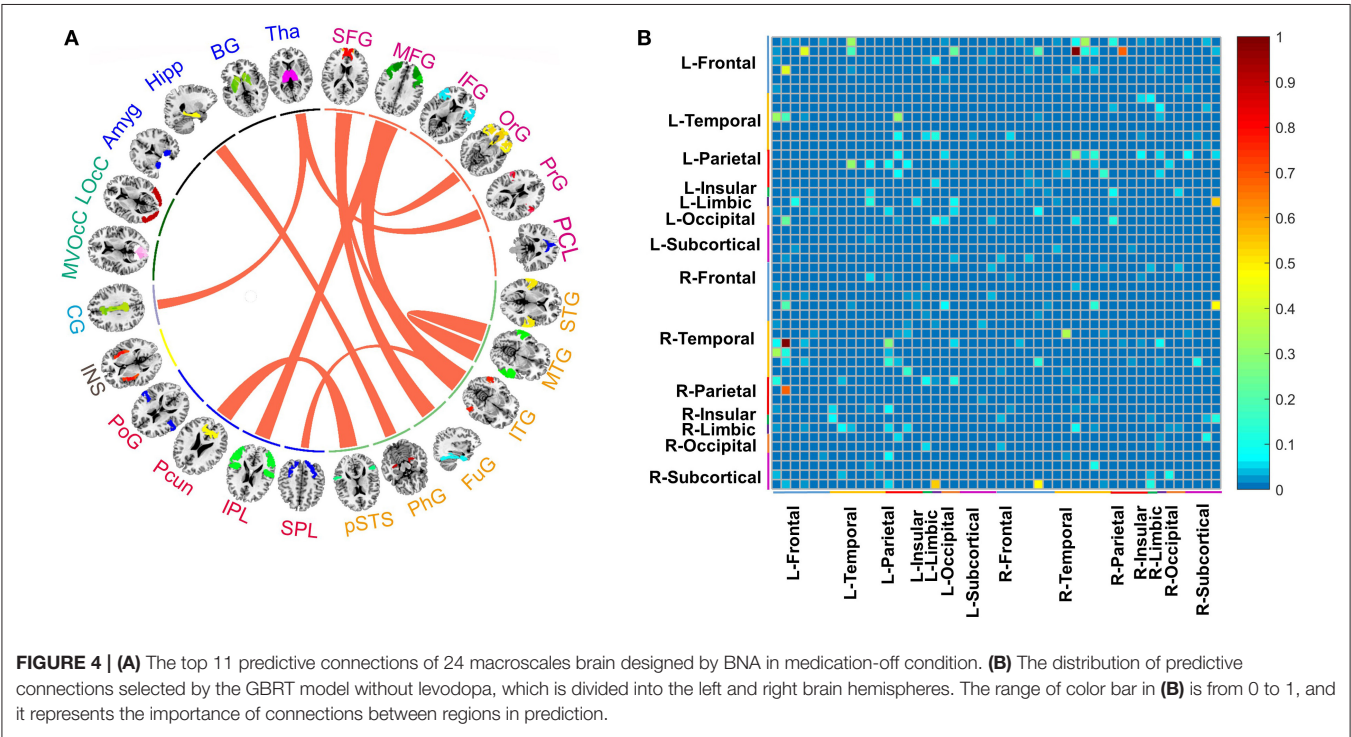


TABLE 2 | The top 11 connections in the prediction of improvement rate in UPDRS-III score after the deep brain stimulation operation in medication-off condition.

ID	Node name	ID	Node name
1	Superior frontal gyrus (SFG)	9	Inferior temporal gyrus (ITG)
1	Superior frontal gyrus (SFG)	10	Fusiform gyrus (FuG)
2	Middle frontal gyrus (MFG)	4	Orbital gyrus (OrG)
2	Middle frontal gyrus (MFG)	9	Inferior temporal gyrus (ITG)
2	Middle frontal gyrus (MFG)	14	Inferior parietal lobule (IPL)
5	Precentral gyrus (PrG)	24	Thalamus (Tha)
8	Middle temporal gyrus (MTG)	8	Middle temporal gyrus (MTG)
9	Inferior temporal gyrus (ITG)	13	Superior parietal lobule (SPL)
11	Parahippocampal gyrus (PhG)	22	Hippocampus (Hipp)
12	Posterior superior temporal sulcus (pSTS)	15	Precuneus (Pcun)
18	Cingulate gyrus (CG)	24	Thalamus (Tha)

1–6: frontal, 7–12: temporal, 13–16: parietal, 17: insular lobe, 18: limbic lobe, 19–20: occipital lobe, 21–24: subcortical nuclei.



PD (Tison et al., 2002), and it was reliable (Metman et al., 2004). Therefore, the DBS outcome in this study was measured as the percentage change in UPDRS-III score.

Based on the results of 50 PD patients in this study, we were able to characterize networks that can predict the recovery after the DBS therapy. These network features played significant roles in training the machine learning model. In PD patients treated by DBS without levodopa, the connections of the MFG to ITG, Pkun to pSTS, and internal connection in middle temporal gyrus (MTG) were found to provide top contribution in the GBRT model to the prediction of operation therapy. These findings provide new evidence that the functional connectivity has an effect on predicting the DBS operation outcome in PD patients before the operation. This progress may potentially help reduce the loss of money and the trauma of body in patients with unsatisfactory DBS response (Ellis et al., 2008).

As a white matter lesion associated with motor and cognitive symptoms (Gattellaro et al., 2009), PD is related to topological properties (Olde Dubbelink et al., 2013), through which the effectiveness of DBS can be assessed (i.e., global efficiency, clustering coefficient, and small-worldness) (van Hartevelt et al., 2014). Moreover, the predictive value of connectivity-informed brain stimulation for DBS can be seen in obsessive-compulsive disorder (Baldermann et al., 2019), resistant depression (Johansen-Berg et al., 2007), and tremor disorder (Middlebrooks et al., 2018). These results indicated that it might be feasible to predict the outcome of PD patients treated by DBS.

There are already previous studies related to PD that present results similar to our work. Brain activity in the right ITG and MFG was also found related to gait in PD (Wang et al., 2016). Comparing with healthy controls, PD patients showed increased functional connectivity in ITG (Yang et al., 2016). Furthermore, Grafton et al. found that effective DBS can smoothen the overactivity in bilateral rostral ITG of PD patients toward a more normal pattern (Grafton et al., 2006), which suggested that the pattern of ITG may be a biomarker indicating the outcome of DBS. It was reported that gray matter atrophy or cortical thinning in MFG is related to PD (Brenneis et al., 2003; Biundo et al., 2015), and that it can also be a predictor of conversion to dementia in PD patients (Song et al., 2011). These findings were consistent with our results that ITG and MFG showed more connectivity with other gyri and the connections between ITG and MFG have significant contribution in the model predicting the outcome of DBS in medication-off condition.

It has been confirmed that PD patients exhibited decreased short-range functional connectivity densities in SFG (Zhang et al., 2015). SFG is one of the most important gyri for executive control (Kendi et al., 2008), and cortical atrophy in SFG can affect the motor cortex (Possin et al., 2013). Similar to SFG, Pkun is also associated with network modulation in the treatment of PD patients. In PD patients, the functional connectivity between Pkun and motor system is decreased (Thibes et al., 2017), and the metabolic in Pkun increased after STN-DBS according to the study based on PET (Asanuma et al., 2006). The association between DBS outcome and SFG and Pkun is congruent with the results of prior studies.

The current study indicated that the frontal lobe and temporal lobe play an important role in predicting DBS's effect. Among the top 11 predictive connections, there are one or both ends of 17 connections distributed in the frontal lobe and temporal lobe. Kostić et al. have also found that a specific pattern of brain network damage involving the frontal and parietal cortices occurs in patients with freezing of gait (Kostić et al., 2012). It was also reported that a lack of adequate frontal activation was found to be related to PD patients (Jahanshahi et al., 2010), and that the modulation by STN-DBS was found to be correlated to the suppression of alpha and beta oscillations in the temporal area based on a MEG study (Cao et al., 2017). By comparing six machine learning models, the GBRT regression model was able to estimate the improvement rate of UPDRS-III score after DBS most accurately. The GBRT regression model (Friedman, 2001) is an ensemble of weak prediction models (decision trees) based on gradient boosting. GBRT sequentially adds small trees (low depth) with high bias, so that it can better fit target. It has been widely used in many fields of regression problems because of its high prediction accuracy. To conclude, GBRT regression offers many advantages over the traditional multiple-regression models, with the ability of processing non-linear data. Besides the GBRT model, the ERT model also showed excellent prediction. In the two collections of top 11 connections selected by the GBRT and ERT regression models, respectively, 10 connections were the same (**Supplementary Table 1**), which also verified the accuracy of the GBRT model in prediction.

It has several limitations when interpreting the findings in our study. First, there are some factors that influence variables during the operation, such as surgical instruments, doctors' operations, etc. These factors have not been fully considered. Second, due to the difficulty in obtaining the data clinically, the amount of sample is still small from the perspective of machine learning, which may cause errors. In further research with larger dataset of more PD patients carried out DBS surgery, more predictive patterns can be found, and there can be more comprehensive evaluation before surgery.

CONCLUSION

In this study, we investigated the relationship between functional connectivity and outcome of DBS therapy in 50 PD patients. Using machine learning models, we demonstrated that the functional network can predict the outcome of operation therapy. The GBRT model is the most effective machine learning model with Pearson correlations $r = 0.65$, $p = 2.58E-07$ in medication-off condition, and the most contributable connections for models were identified.

DATA AVAILABILITY STATEMENT

The datasets generated for this study are available on request to the corresponding author.

ETHICS STATEMENT

The studies involving human participants were reviewed and approved by the Ethics Committee of Tsinghua University Yuquan Hospital. The patients/participants provided their written informed consent to participate in this study.

AUTHOR CONTRIBUTIONS

XL, YM, and RS conceived the research project. XL supervised the research project. LH and YM processed the raw Parkinson's disease dataset. XM, XL, and RS conducted the computational analyses. RS, XM, and XL wrote this manuscript. All the authors discussed the experimental results and commented on the manuscript.

REFERENCES

- Abdi, H. (2007). Bonferroni and Šidák corrections for multiple comparisons. *Encyclopedia Meas. Stat.* 3, 103–107.
- Al-Fatly, B., Ewert, S., Kübler, D., Kroneberg, D., Horn, A., and Kuhn, A. A. (2019). Connectivity profile of thalamic deep brain stimulation to effectively treat essential tremor. *Brain* 142, 3086–3098. doi: 10.1093/brain/awz236
- Antonini, A., Abbruzzese, G., Ferini-Strambi, L., Tilley, B., Huang, J., Stebbins, G. T., et al. (2013). Validation of the Italian version of the movement disorder society—unified Parkinson's disease rating scale. *Neurol. Sci.* 34, 683–687. doi: 10.1007/s10072-012-1112-z
- Asanuma, K., Tang, C., Ma, Y., Dhawan, V., Mattis, P., Edwards, C., et al. (2006). Network modulation in the treatment of Parkinson's disease. *Brain* 129, 2667–2678. doi: 10.1093/brain/awl162
- Baldermann, J. C., Melzer, C., Zapf, A., Kohl, S., Timmermann, L., Tittgemeyer, M., et al. (2019). Connectivity profile predictive of effective deep brain stimulation in obsessive-compulsive disorder. *Biol. Psychiatr.* 85, 735–743. doi: 10.1016/j.biopsych.2018.12.019
- Beck, A. T., Steer, R. A., and Carbin, M. G. (1988). Psychometric properties of the Beck depression inventory: twenty-five years of evaluation. *Clin. Psychol. Rev.* 8, 77–100. doi: 10.1016/0272-7358(88)90050-5
- Benabid, A. L. (2003). Deep brain stimulation for Parkinson's disease. *Curr. Opin. Neurobiol.* 13, 696–706. doi: 10.1016/j.conb.2003.11.001
- Bermudez, C., Rodriguez, W., Huo, Y., Hainline, A. E., Li, R., Shults, R., et al. (2019). Towards machine learning prediction of deep brain stimulation (DBS) intra-operative efficacy maps. *Proc. SPIE Int. Soc. Opt. Eng.* 10949:1094922. doi: 10.1117/12.2509728
- Biundo, R., Weis, L., Facchini, S., Formento-Dojot, P., Vallelunga, A., Pilleri, M., et al. (2015). Patterns of cortical thickness associated with impulse control disorders in Parkinson's disease. *Mov. Disord.* 30, 688–695. doi: 10.1002/mds.26154
- Brenneis, C., Seppi, K., Schocke, M. F., Müller, J., Luginger, E., Bösch, S., et al. (2003). Voxel-based morphometry detects cortical atrophy in the Parkinson variant of multiple system atrophy. *Mov. Disord.* 18, 1132–1138. doi: 10.1002/mds.10502
- Buhmann, C., Glauche, V., Stürenburg, H., Oechsner, M., Weiller, C., and Büchel, C. (2003). Pharmacologically modulated fMRI—cortical responsiveness to levodopa in drug-naïve hemiparkinsonian patients. *Brain* 126, 451–461. doi: 10.1093/brain/awg033
- Cao, C.-Y., Zeng, K., Li, D.-Y., Zhan, S.-K., Li, X.-L., and Sun, B.-M. (2017). Modulations on cortical oscillations by subthalamic deep brain stimulation in patients with Parkinson disease: a MEG study. *Neurosci. Lett.* 636, 95–100. doi: 10.1016/j.neulet.2016.11.009
- Coenen, V. A., Schlaepfer, T. E., Bewernick, B. H., Kilian, H., Kaller, C. P., Urbach, H., et al. (2019). Frontal white matter architecture predicts efficacy of deep brain stimulation in major depression. *Transl. Psychiatr.* 9:197. doi: 10.1038/s41398-019-0540-4
- Cohen, J. D., Noll, D. C., Schneider, W. (1993). Functional magnetic resonance imaging: overview and methods for psychological research.

FUNDING

This work was supported by the National Key R&D Program of China (no. 2018YFC0115400), Beihang University & Capital Medical University Advanced Innovation Center for Big Data-Based Precision Medicine Plan (BHME-201907), and Beijing Institute of Technology Research Fund Program for Young Scholars.

SUPPLEMENTARY MATERIAL

The Supplementary Material for this article can be found online at: <https://www.frontiersin.org/articles/10.3389/fncom.2020.571527/full#supplementary-material>

- Behav. Res. Methods Instrument. Comput.* 25, 101–113. doi: 10.3758/BF03204483
- Cury, R. G., Galhardoni, R., Fonoff, E. T., dos Santos Ghilardi, M. G., Fonoff, F., Arnaut, D., et al. (2014). Effects of deep brain stimulation on pain and other nonmotor symptoms in Parkinson disease. *Neurology* 83, 1403–1409. doi: 10.1212/WNL.0000000000000887
- Defer, G. L., Widner, H., Marié, R. M., Rémy, P., and Levivier, M. (1999). Core assessment program for surgical interventional therapies in Parkinson's disease (CAPSIT-PD). *Mov. Disord.* 14, 572–584.
- Deuschl, G., Schade-Brittinger, C., Krack, P., Volkmann, J., Schäfer, H., Bötzel, K., et al. (2006). A randomized trial of deep-brain stimulation for Parkinson's disease. *N. Engl. J. Med.* 355, 896–908. doi: 10.1056/NEJMoa060281
- Drucker, H., Burges, C. J., Kaufman, L., Smola, A. J., and Vapnik, V. (1997). "Support vector regression machines," in *Advances in Neural Information Processing Systems* (Denver, CO: NIPS Conference), 155–161. Available online at: <https://www.datalearner.com/conference/nips/60000133>
- Ellis, T.-M., Foote, K. D., Fernandez, H. H., Sudhyadhom, A., Rodriguez, R. L., Zeilman, P., et al. (2008). Reoperation for suboptimal outcomes after deep brain stimulation surgery. *Neurosurgery* 63, 754–761. doi: 10.1227/01.NEU.0000325492.58799.35
- Ewert, S., Plettig, P., Li, N., Chakravarty, M. M., Collins, D. L., Herrington, T. M., et al. (2017). Toward defining deep brain stimulation targets in MNI space: a subcortical atlas based on multimodal MRI, histology and structural connectivity. *Neuroimage* 170, 271–282. doi: 10.1016/j.neuroimage.2017.05.015
- Fahn, S., Oakes, D., Shoulson, I., Kieburtz, K., Rudolph, A., Lang, A., et al. (2004). Levodopa and the progression of Parkinson's disease. *N. Engl. J. Med.* 351, 2498–2508. doi: 10.1056/NEJMoa033447
- Fan, L., Hai, L., Zhuo, J., Yu, Z., Wang, J., Chen, L., et al. (2016). The human brainnetome atlas: a new brain atlas based on connectional architecture. *Cereb. Cortex* 26, 3508–3526. doi: 10.1093/cercor/bhw157
- Figee, M., Luigjes, J., Smolders, R., Valencia-Alfonso, C.-E., van Wingen, G., de Kwaastienet, B., et al. (2013). Deep brain stimulation restores frontostriatal network activity in obsessive-compulsive disorder. *Nat. Neurosci.* 16, 386–387. doi: 10.1038/nn.3344
- Folstein, M. F., Robins, L. N., and Helzer, J. E. (1983). The mini-mental state examination. *Arch. Gen. Psychiatr.* 40, 812–812. doi: 10.1001/archpsyc.1983.01790060110016
- Foltynie, T., and Hariz, M. I. (2010). Surgical management of Parkinson's disease. *Expert Rev. Neurother.* 10, 903–914. doi: 10.1586/ern.10.68
- Friedman, J. H. (2001). Greedy function approximation: a gradient boosting machine. *Ann. Stat.* 29, 1189–1232. doi: 10.1214/aos/1013203451
- Gattellaro, G., Minati, L., Grisoli, M., Mariani, C., Carella, F., Osio, M., et al. (2009). White matter involvement in idiopathic Parkinson disease: a diffusion tensor imaging study. *Am. J. Neuroradiol.* 30, 1222–1226. doi: 10.3174/ajnr.A1556
- Geurts, P., Ernst, D., and Wehenkel, L. (2006). Extremely randomized trees. *Mach. Learn.* 63, 3–42. doi: 10.1007/s10994-006-6226-1
- Goetz, C. G., Tilley, B. C., Shaftman, S. R., Stebbins, G. T., Fahn, S., Martinez-Martin, P., et al. (2008). Movement disorder society-sponsored revision of the

- Unified Parkinson's disease rating scale (MDS-UPDRS): scale presentation and clinimetric testing results. *Mov. Disord.* 23, 2129–2170. doi: 10.1002/mds.22340
- Goldberger, A. S. (1964). *Econometric Theory*. New York, NY: Wiley.
- Grafton, S., Turner, R., Desmurget, M., Bakay, R., Delong, M., Vitek, J., et al. (2006). Normalizing motor-related brain activity: subthalamic nucleus stimulation in Parkinson disease. *Neurology* 66, 1192–1199. doi: 10.1212/01.wnl.0000214237.58321.c3
- Guo, W.-B., Liu, F., Xue, Z.-M., Xu, X.-J., Wu, R.-R., Ma, C.-Q., et al. (2012). Alterations of the amplitude of low-frequency fluctuations in treatment-resistant and treatment-response depression: a resting-state fMRI study. *Prog. Neuropsychopharmacol. Biol. Psychiatr.* 37, 153–160. doi: 10.1016/j.pnpb.2012.01.011
- Habets, J. G., Duits, A. A., Sijben, L. C., de Greef, B., Mulders, A., Temel, Y., et al. (2019). Machine learning prediction of motor response after deep brain stimulation in Parkinson's disease. *Medrxiv* 19006841. doi: 10.1101/19006841
- Hacker, C. D., Perlmuter, J. S., Criswell, S. R., Ances, B. M., and Snyder, A. Z. (2012). Resting state functional connectivity of the striatum in Parkinson's disease. *Brain* 135, 3699–3711. doi: 10.1093/brain/awb281
- Hammond, C., Bergman, H., and Brown, P. (2007). Pathological synchronization in Parkinson's disease: networks, models and treatments. *Trends Neurosci.* 30, 357–364. doi: 10.1016/j.tins.2007.05.004
- Hartmann, C. J., Lujan, J. L., Chaturvedi, A., Goodman, W. K., Okun, M. S., McIntyre, C. C., et al. (2016). Tractography activation patterns in dorsolateral prefrontal cortex suggest better clinical responses in OCD DBS. *Front. Neurosci.* 9:519. doi: 10.3389/fnins.2015.00519
- Horn, A., and Kühn, A. A. (2015). Lead-DBS: a toolbox for deep brain stimulation electrode localizations and visualizations. *Neuroimage* 107, 127–135. doi: 10.1016/j.neuroimage.2014.12.002
- Horn, A., Reich, M., Vorwerk, J., Li, N., Wenzel, G., Fang, Q., et al. (2017). Connectivity predicts deep brain stimulation outcome in parkinson disease. *Ann. Neurol.* 82, 67–78. doi: 10.1002/ana.24974
- Imbens, G. W., Newey, W. K., and Ridder, G. (2005). Mean-Square-Error Calculations for Average Treatment Effects. IEPW Working Paper No. 05.34. doi: 10.2139/ssrn.820205
- Jahanshahi, M., Jones, C. R. G., Zijlmans, J., Katzenschlager, R., Lee, L., Quinn, N., et al. (2010). Dopaminergic modulation of striato-frontal connectivity during motor timing in Parkinson's disease. *Brain* 133, 727–745. doi: 10.1093/brain/awq012
- Johansen-Berg, H., Gutman, D., Behrens, T., Matthews, P., Rushworth, M., Katz, E., et al. (2007). Anatomical connectivity of the subgenual cingulate region targeted with deep brain stimulation for treatment-resistant depression. *Cereb. Cortex* 18, 1374–1383. doi: 10.1093/cercor/bhm167
- Kendi, A. T. K., Lehericy, S., Luciana, M., Ugurbil, K., and Tuite, P. (2008). Altered diffusion in the frontal lobe in Parkinson disease. *Am. J. Neuroradiol.* 29, 501–505. doi: 10.3174/ajnr.A0850
- Kim, J., Criado, M., Cho, S. S., Díez-Cirarda, M., Mihaescu, A., Coakeley, S., et al. (2017). Abnormal intrinsic brain functional network dynamics in Parkinson's disease. *Brain* 140, 2955–2967. doi: 10.1093/brain/awx233
- Kohavi, R. (1995). "A study of cross-validation and bootstrap for accuracy estimation and model selection," in *IJCAI* (Montréal, QC), 1137–1145. Available online at: http://www.researchgate.net/publication/265370033_IJCAI-95_Proceedings_of_the_14th_international_joint_conference_on_artificial_intelligence_Montreal_Canada_August_20-25_1995
- Kostić, V. S., Agosta, F., Pievani, M., Stefanova, E., Ječmenica-Lukić, M., Scarale, A., et al. (2012). Pattern of brain tissue loss associated with freezing of gait in Parkinson disease. *Neurology* 78, 409–416. doi: 10.1212/WNL.0b013e318245d23c
- Luo, C. Y., Guo, X. Y., Song, W., Chen, Q., Cao, B., Yang, J., et al. (2015). Functional connectome assessed using graph theory in drug-naive Parkinson's disease. *J. Neurol.* 262, 1557–1567. doi: 10.1007/s00415-015-7750-3
- McClure, E. B., Adler, A., Monk, C. S., Cameron, J., Smith, S., Nelson, E. E., et al. (2007). fMRI predictors of treatment outcome in pediatric anxiety disorders. *Psychopharmacology* 191, 97–105. doi: 10.1007/s00213-006-0542-9
- Metman, L. V., Myre, B., Verwey, N., Hassin-Baer, S., Arzbaecher, J., Sierens, D., et al. (2004). Test-retest reliability of UPDRS-III, dyskinesia scales, and timed motor tests in patients with advanced Parkinson's disease: an argument against multiple baseline assessments. *Mov. Disord.* 19, 1079–1084. doi: 10.1002/mds.20101
- Middlebrooks, E. H., Tuna, I. S., Almeida, L., Grewal, S. S., Wong, J., Heckman, M. G., et al. (2018). Structural connectivity-based segmentation of the thalamus and prediction of tremor improvement following thalamic deep brain stimulation of the ventral intermediate nucleus. *Neuroimage Clin.* 20, 1266–1273. doi: 10.1016/j.nicl.2018.10.009
- Olde Dubbelink, K. T., Hillebrand, A., Stoffers, D., Deijen, J. B., Twisk, J. W., Stam, C. J., et al. (2013). Disrupted brain network topology in Parkinson's disease: a longitudinal magnetoencephalography study. *Brain* 137, 197–207. doi: 10.1093/brain/awt316
- Poewe, W., Seppi, K., Tanner, C. M., Halliday, G. M., Brundin, P., Volkmann, J., et al. (2017). Parkinson disease. *Nat. Rev. Dis. Primers* 3:17013. doi: 10.1038/nrdp.2017.13
- Possin, K. L., Kang, G. A., Guo, C., Fine, E. M., Trujillo, A. J., Racine, C. A., et al. (2013). Rivastigmine is associated with restoration of left frontal brain activity in Parkinson's disease. *Mov. Disord.* 28, 1384–1390. doi: 10.1002/mds.25575
- Ramaker, C., Marinus, J., Stiggelbout, A. M., and van Hilten, B. J. (2002). Systematic evaluation of rating scales for impairment and disability in Parkinson's disease. *Mov. Disord.* 17, 867–876. doi: 10.1002/mds.10248
- Rodriguez, R. L., Fernandez, H. H., Haq, I., and Okun, M. S. (2007). Pearls in patient selection for deep brain stimulation. *Neurologist* 13, 253–260. doi: 10.1097/NRL.0b013e318095a4d5
- Song, S. K., Lee, J. E., Park, H. J., Sohn, Y. H., Lee, J. D., and Lee, P. H. (2011). The pattern of cortical atrophy in patients with Parkinson's disease according to cognitive status. *Mov. Disord.* 26, 289–296. doi: 10.1002/mds.23477
- Thibes, R. B., Novaes, N. P., Lucato, L. T., Campanholo, K. R., Melo, L. M., Leite, C. C., et al. (2017). Altered functional connectivity between precuneus and motor systems in Parkinson's disease patients. *Brain Connect.* 7, 643–647. doi: 10.1089/brain.2017.0534
- Tibshirani, R. (1996a). Regression shrinkage and selection via the Lasso. *J. R. Stat. Soc. Ser. B.* 58, 267–288.
- Tibshirani, R. (1996b). Regression shrinkage and selection via the Lasso: a retrospective. *J. R. Stat. Soc. Ser. B.* 73, 273–282.
- Tison, F., Yekhelef, F., Chrysostome, V., Balestre, E., Quinn, N. P., Poewe, W., et al. (2002). Parkinsonism in multiple system atrophy: natural history, severity (UPDRS-III), and disability assessment compared with Parkinson's disease. *Mov. Disord.* 17, 701–709. doi: 10.1002/mds.10171
- van Eimeren, T., Monchi, O., Ballanger, B., and Strafella, A. P. (2009). Dysfunction of the default mode network in Parkinson disease. *Arch. Neurol.* 66, 877–883. doi: 10.1001/archneurol.2009.97
- van Hartevelt, T. J., Cabral, J., Deco, G., Möller, A., Green, A. L., Aziz, T. Z., et al. (2014). Neural plasticity in human brain connectivity: the effects of long term deep brain stimulation of the subthalamic nucleus in Parkinson's disease. *PLoS ONE* 9:e86496. doi: 10.1371/journal.pone.0086496
- Wang, J. H., Wang, X. D., Xia, M. R., Liao, X. H., Evans, A., and He, Y. (2015). GREYNA: a graph theoretical network analysis toolbox for imaging connectomics. *Front. Hum. Neurosci.* 9:458. doi: 10.3389/fnhum.2015.00458
- Wang, M., Jiang, S., Yuan, Y., Zhang, L., Ding, J., Wang, J., et al. (2016). Alterations of functional and structural connectivity of freezing of gait in Parkinson's disease. *J. Neurol.* 263, 1583–1592. doi: 10.1007/s00415-016-8174-4
- Willmott, C. J., and Matsuura, K. (2005). Advantages of the mean absolute error (MAE) over the root mean square error (RMSE) in assessing average model performance. *Clim. Res.* 30, 79–82. doi: 10.3354/cr030079
- Yang, W., Liu, B., Huang, B., Huang, R., Wang, L., Zhang, Y., et al. (2016). Altered resting-state functional connectivity of the striatum in Parkinson's disease after levodopa administration. *PLoS ONE* 11:e0161935. doi: 10.1371/journal.pone.0161935
- Zhang, J., Bi, W., Zhang, Y., Zhu, M., Zhang, Y., Feng, H., et al. (2015). Abnormal functional connectivity density in Parkinson's disease. *Behav. Brain Res.* 280, 113–118. doi: 10.1016/j.bbr.2014.12.007

Conflict of Interest: The authors declare that the research was conducted in the absence of any commercial or financial relationships that could be construed as a potential conflict of interest.

Copyright © 2020 Shang, He, Ma, Ma and Li. This is an open-access article distributed under the terms of the Creative Commons Attribution License (CC BY). The use, distribution or reproduction in other forums is permitted, provided the original author(s) and the copyright owner(s) are credited and that the original publication in this journal is cited, in accordance with accepted academic practice. No use, distribution or reproduction is permitted which does not comply with these terms.



Effects of Visual Attentional Load on the Tactile Sensory Memory Indexed by Somatosensory Mismatch Negativity

Xin He¹, Jian Zhang^{2*}, Zhilin Zhang³, Ritsu Go^{2,4}, Jinglong Wu^{2,4}, Chunlin Li⁵, Kai Gan⁶ and Duanduan Chen¹

¹School of Life Science, Beijing Institute of Technology, Beijing, China, ²Intelligent Robotics Institute, School of Mechatronical Engineering, Beijing Institute of Technology, Beijing, China, ³Department of Psychiatry, Graduate School of Medicine, Kyoto University, Kyoto, Japan, ⁴Key Laboratory of Biomimetic Robots and Systems, Ministry of Education, Beijing, China, ⁵School of Biomedical Engineering, Capital Medical University, Beijing, China, ⁶Guangdong Country Garden School, Guangdong, China

OPEN ACCESS

Edited by:

Rong Chen,
University of Maryland, United States

Reviewed by:

Xinjun Sheng,
Shanghai Jiao Tong University, China
Maria L. Bringas,
University of Electronic Science and
Technology of China, China

*Correspondence:

Jian Zhang
zhangjian2023@bit.edu.cn

Received: 22 June 2020

Accepted: 22 October 2020

Published: 25 November 2020

Citation:

He X, Zhang J, Zhang Z, Go R, Wu J, Li C, Gan K and Chen D (2020) Effects of Visual Attentional Load on the Tactile Sensory Memory Indexed by Somatosensory Mismatch Negativity. *Front. Integr. Neurosci.* 14:575078. doi: 10.3389/fninf.2020.575078

Auditory sensory memory indexed by mismatch negativity has been broadly studied over the past century, but far less attention has been directed to tactile sensory memory. To investigate whether tactile sensory memory is affected by attention, we recorded somatosensory mismatch negativity (sMMN) from 24 healthy adults in two experiments to distinguish sustained attention from non-sustained attention. Using the roving somatosensory oddball paradigm, we analyzed the average dynamic changes in the amplitude and latency of sMMN amplitude and found a clear sMMN component at the central region at a 100–300 ms interval. The sMMN amplitude, which indexes the early detection of tactile stimuli with the sensory memory trace, was larger in the tactile attentional task. Additionally, the sMMN latency increased with the increasing visual attentional load, which indicates a decay of tactile sensory memory. Our results indicate that the more attention resources are allocated for a tactile sensation, the more favorable it is to the generation of tactile sensory memory.

Keywords: tactile sensory memory, attention, somatosensory mismatch negativity (sMMN), electroencephalogram (EEG), perceptual load theory

INTRODUCTION

The skin covering the body's surface contacts the external environment directly, and tactile sensations have large influences on human perception (Gallace et al., 2007). The human brain automatically encodes information from multiple tactile sensations over a short period in a real-time buffer. The tactile sensory memory described above allows us to focus on one event while still being aware of and able to process tactile events in the wider surroundings. Additionally, tactile sensory memory can be used in clinical applications (e.g., developmental coordination disorder, paralysis, and coma) to help patients improve tactile sensations or to predict the recovery of awareness. However, little attention has been paid to the topic of tactile sensory memory.

Sensory memory was originally described by Atkinson and Shiffrin (1968) using a multistore model of memory. Compared to short and long-term memory, sensory memory is an automatic and parallel preconscious response that temporarily stores incoming sensory information. This type of memory lasts only seconds and appears to show a rapidly decaying effect (Gallace and Spence, 2009). Electroencephalography (EEG) can provide high temporal information of neural components related to perception and represent various stages of information processing, and studies have used MMN to research the temporal dynamics of sensory memory (Bartha-Doering et al., 2015).

Since mismatch negativity (MMN) was first discovered by Näätänen et al. (1978), it has been suggested that MMN is generated by an automatic neural mismatch process, which consists of a memory trace that encodes the physical features of the standard stimulus (Näätänen et al., 1978, 1993; Näätänen and Michie, 1979). The MMN can be recorded when the memory trace of a repeated stimulus has not decayed (Bartha-Doering et al., 2015). Consistent with this view, previous studies showed that increasing the interstimulus offset-to-onset interval (ISI) leads to a reduction in MMN amplitude (Mantysalo and Naatanen, 1987; Bottcherghandor and Ullsperger, 1992; Cowan et al., 1993; Winkler et al., 2002). So, the MMN operates at the sensory memory level.

Usually, tactile sensory memory is accessed by behavioral tasks, for example, using a sensitivity index to measure the accuracy rate on a memory set (Creelman and Macmillan, 2004; Ito et al., 2020). However, when involving in these tasks, sufficient motivation and adequate attention would be needed. So, a more objective indicator is proposed as an index of sensory memory is the MMN. Previous studies showed that the MMN is elicited irrespective of where the subject or patient's attention is directed (Näätänen et al., 1993, 2007). Similar to the results of adult studies, prominent MMN signals can also be obtained from all waking and sleep states in infants (Cheour et al., 2000). Therefore, this pre-attentive and sensory-specific neural component provides a relatively independent relationship between attention and the sensory memory neural pathway for research.

Tactile sensory memory is considered to be outside of cognitive control; therefore, whether it is affected or modulated by attention remains unknown. Based on the comparison of sensory memory representations from preceding stimuli with that of a current deviant stimulus, some studies have proposed that MMN is unaffected by attention (Näätänen et al., 1978, 1980; Sams et al., 1984). However, Woldorff et al. (1991) carried out a dual dichotic listening experiment and found that attended tones can be distinguished from unattended tones by both ears of entry and pitch cues. They found that MMN in the unattended-channel deviant was markedly reduced compared with that in the attended-channel deviant (Woldorff et al., 1991). Subsequently, Näätänen et al. (1993) also found that the MMN intensity deviation was attenuated in the absence of attention. These studies provided the first evidence that an early sensory level in unattended channels can be attenuated or gated under highly focused attention. However, the attention of a different modality set has not been established. Other research has focused

on the effects of visual attention load on auditory MMN. In that study, subjects performed a speeded letter-detection task under different attentional loads in visual modality and a simultaneous auditory oddball task. The results did not show an effect of attention on MMN. However, a follow-up meta-analysis study suggested that demanding visual tasks do reduce auditory MMN (Wiens et al., 2016). In support of these findings, recent studies found that a high visual attention load strongly reduced auditory sensory detection ability (Macdonald and Lavie, 2011; Raveh and Lavie, 2015; Szychowska et al., 2017). Moreover, somatosensory ERP studies showed that high mental workload would decrease exogenous tactile stimuli processing, but the tactile analysis was about the late positive potential component or somatosensory P2 (Sugimoto and Katayama, 2013; Mun et al., 2017). Nevertheless, other studies have reached the opposite opinion. Zhang et al. (2006) evaluated a task in which the visual attention load was parametrically manipulated by varying the number of tracked targets (Zhang et al., 2006). They found that increasing visual attention load increased auditory MMN. Overall, evidence concerning the effect of attention load on sensory memory is mixed. A large body of empirical studies over the past century has focused on the neural mechanisms associated with auditory and visual sensory memory, but few studies have focused on tactile sensory memory, particularly the effect of attention on tactile sensory memory.

In this experiment, the somatosensory mismatch negativity (sMMN) was used to measure the effects in two visual attentional tasks in case that an overlap exists between the attention pathway and the sensory memory process in a single modality (Näätänen and Gaillard, 1983). By using roving somatosensory oddball task (RSOT), which is a variant of oddball paradigm, the sMMN can be obtained by subtracting the event-related response to the standard event from the response to the deviant event (Garrido et al., 2009). To consider both sustained attention and non-sustained attention, weighting pictures and tracking balls were included in visual stimuli (Zhang et al., 2006; Debettencourt et al., 2015). And different difficulties of the visual target were used to better manipulate the process of attracting attention. The current study was aimed to investigate whether tactile sensory memory is affected by attention and analyze which pattern exists between tactile sensory memory and attention.

MATERIALS AND METHODS

Experiment 1

Participants

Twelve healthy right-handed volunteers (mean age 25.3 ± 3.2 years, three females and nine males) participated in the experiment. One participant was rejected due to poor data caused by head movements. None of the participants had a history of neurological disorders or other illnesses. All the participants had either normal or corrected-to-normal vision and normal hearing. All the participants provided written informed consent before the experiment, which was approved by the ethical committee at the Beijing Institute of Technology (2017SY38).

Stimuli and Experiment Paradigm

Visual stimuli consisted of grayscale photographs of male or female faces and outdoor scenes. These images were combined into composite stimuli by averaging pixel intensities using various weightings (for example, 20% face–80% scene; Debettencourt et al., 2015). There were three types of pictures: 20% face–80% scene, 50% face–50% scene, and 100% face (**Figure 1A**). In addition to female faces, there were also male faces integrated with the picture, and distinguishing the gender face was a key task. Every picture was presented for 1 s. All the visual stimuli were displayed in the center of the screen at a visual angle of $10^\circ \times 10^\circ$ from a viewing distance of 55 cm.

The tactile stimuli were delivered by a self-designed rigid string pressure device. The stimulus onset asynchrony (SOA) was fixed at 1 s, and the duration of each stimulus was 0.1 s. The output pressure was 1.5 N and the diameter of the rigid string was 1.5 mm. Only the rigid string part was used for delivering the stimulus to participants, the other part of the device (e.g., the pump) was placed outside the shielding room, effectively reduce the experimental irrelevant interference.

A RSOT was performed on participants in parallel with the visual stimuli. Trains of stimuli were delivered consecutively and alternatively between the subjects' index and little fingertips of the left hand (**Figure 1B**). And the number of successive same-stimulus trials in a train was presented varied pseudo-randomly between four to seven. The first stimulus in each new train was modeled as "deviant," after four to seven repetitions, the last stimulus was modeled as "standard." So deviant and standard stimuli have the same physical properties, differing only in the number of repetitions, eliminating the interference of stimulating physical characteristics on brain responses.

Experiment Procedure

Participants performed the rapid gender face detection task. Whenever a target face (e.g., female face) was shown in the picture, they were instructed to press a left mouse button with their right hand as soon as possible but to ignore the tactile stimuli delivered on the left hand. To avoid any influence on tactile stimuli from pressing the button, no key tasks (female faces) appeared during the standard stimulus, deviation stimulus, and the stimulus preceding the standard stimulus. The total percentage of key task responses was 20%. In the control group, participants were instructed to fixate on the cross at the central site of the screen while counting the number of stimuli changes between their index and little fingers.

The experiment included four types of blocks (20% face, 50% face, 100% face, cross); each block consisted of 600 tactile trials (60 standard tactile stimuli and 60 deviants in each block, respectively). The first trial delivered on the index or little fingertip was randomized within each block and counterbalanced between blocks to eliminate order effects. In all the blocks, participants were seated in a chair in a sound-attenuated and electrically shielded room. Participants rested for 2 min between blocks. Within the task blocks, participants were asked to ignore the tactile stimuli and focus on the center of the visual field to attempt to detect the face stimuli as accurately as possible.

They were also asked to minimize eye movements during the experiment.

Experiment 2

Participants

Twelve healthy right-handed volunteers (mean age 25.1 ± 3.6 , two females and 10 males) participated in the experiment. Two participants were rejected due to poor data caused by head movements. The participants had no history of neurological disorders or other illnesses. All participants had normal or corrected to normal vision and normal hearing. All the participants provided written informed consent before the experiment, which was approved by the ethical committee at the Beijing Institute of Technology (2017SY38).

Stimuli and Experiment Paradigm

The tactile stimuli settings were the same as those in experiment 1. For the visual stimuli, we attracted attention by presenting visual targets of varying difficulty in a visual stream. Ten bouncing balls (each 1° in diameter) moved independently at a constant velocity (2° per second) within a dark gray square (10° in both width and height). The balls moved smoothly, and there was no sudden shift in their motion. The green balls continued to move along their original path when they collided with each other but were reflected at the original speed when they impacted a screen boundary (with the reflection angle equal to the incident angle). An eye-fixation point was presented in the center of the square. Ten green balls in Brownian motion moved during the first 2.5 s of each block to engage the subject's attention. A variable number (1, 3, or 5) of balls then turned red for 2 s and then turned back to green for the next 21 s. Therefore, the attentive tracking period lasted for 21 s (**Figure 2**). Then, the previously reddened balls turned red again for 2.5 s, and the participants were instructed to press the mouse button to respond whether they were tracking the right target. The entire block lasted for 30 s (2 s for rest).

Experiment Procedure

The participants needed to remember which ball(s) turned red, and followed ball(s) during the tracking period. And participants were instructed to press the mouse button (the left mouse button for yes, the right mouse button for no) with the right hand to respond whether they were identical to the tracked targets when the ball(s) turned red again. And they were instructed to fixate their gaze on the fixation point and to avoid eye shaking far away from the square during the attentive tracking period.

The entire experiment consisted of two task sessions and one control session (no red ball). Each task session consisted of 30 blocks (10 blocks per task condition) and lasted for 15 min. There were no differences between the two task sessions. The standard and deviant tactile stimuli were administered only during the tracking period. During the task sessions, they were asked to ignore the tactile stimuli and focus on the center of the visual field to track the balls as accurately as possible. The control session included ten green moving balls and the participants were instructed to keep their eyes on the screen but count the number of stimuli exchanges between their index and little

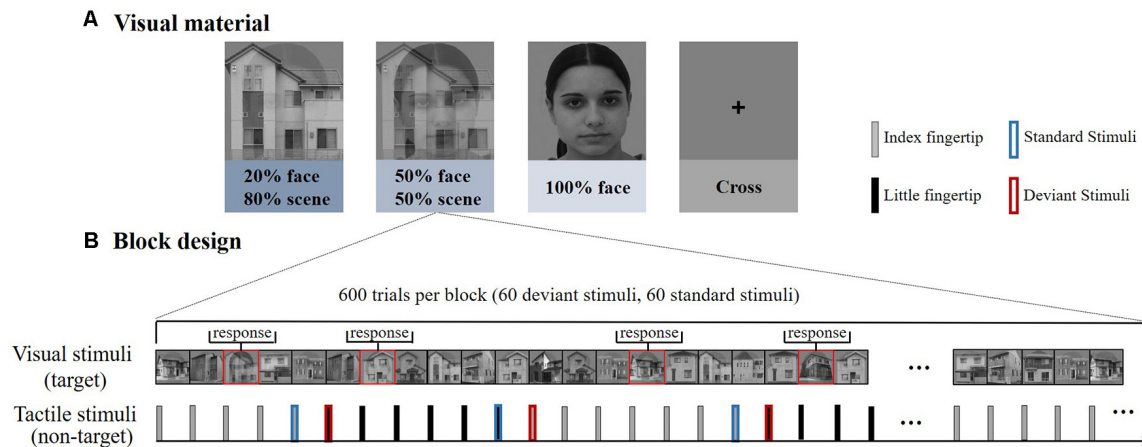


FIGURE 1 | (A) Experiment 1 consisted of four types of blocks according to the different difficulties of visual materials. The house images were photos taken in Okayama City. The face images were obtained from the FEI face database (<https://fei.edu.br/~cet/facedatabase.html>). **(B)** Each block consisted of 600 trials, including 60 deviant stimuli and 60 standard stimuli. The visual stimuli and tactile stimuli were presented simultaneously.

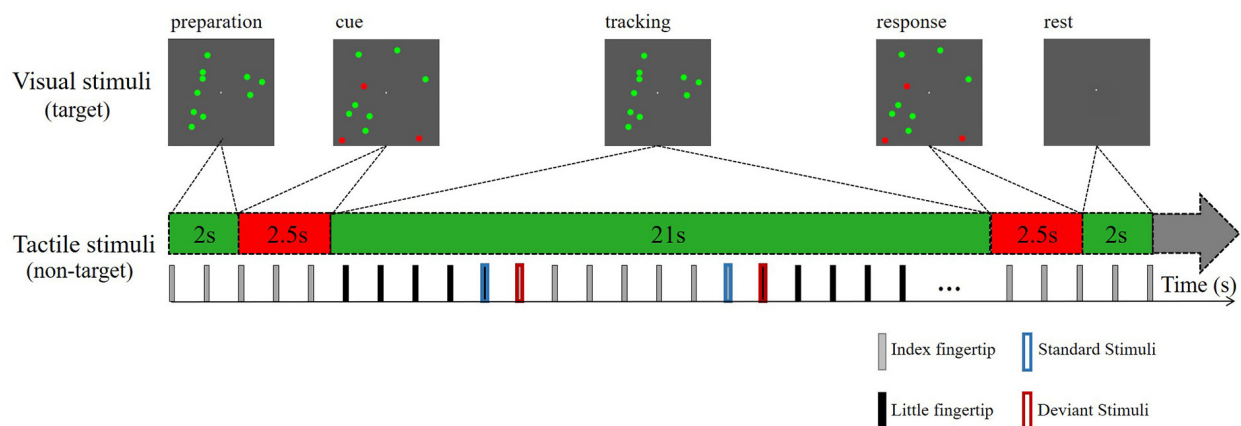


FIGURE 2 | Schematic depiction of the attentive tracking task. Experiment 2 consisted of tracking three different numbers of balls during a task session lasting for 30 s. The task session was repeated twice. The participants were instructed to maintain sustained attention on the tracking tasks, ignoring the tactile stimuli.

fingers. They were also asked to minimize their eye movements during the experiment.

EEG Recording and Processing

The subjects' EEGs were recorded continuously (at a sampling rate of 1,000 Hz) with a SynAmps RT amplifier system using an electrode cap with 64 Ag/AgCl electrodes placed according to the 10-20 system (NeuroScan Labs, El Paso, USA). VEOG and HEOG were recorded with two extra pairs of electrodes, one placed above and below the left eye, and the other placed on the lateral sites of eyes. The electrode impedance was kept below 5 k Ω .

Preprocessing and initial analysis of the EEG signals was performed using the EEGLAB 13.5.4b toolbox¹ (Swartz Center for Computational Neuroscience, La Jolla, CA, USA;

Delorme and Makeig, 2004) implemented in MATLAB R2014a (MathWorks Inc., Natick, MA, USA). A bandpass filter (zero phase shift, cutoff frequency 30 Hz, roll-off 12 dB/octave) was used offline on the continuous data. The reference was converted to bilateral mastoids. One and two subjects were rejected in experiment 1 and experiment 2, respectively, due to poor data caused by head movements. Independent component analysis (ICA) was used to identify and remove eye movements and other artifacts (Jung et al., 2001). Then, epochs with a duration of 1,000 ms were extracted from the continuous EEG data; each epoch extended from -200 to 800 ms relative to stimulus onset. Baseline correction was applied in a time window of 200 ms before stimulus onset. Finally, ERPs were generated separately for the index and little fingers by averaging the preprocess data epochs.

¹<http://scn.ucsd.edu/eeGLAB/>

ERP Analysis

The sMMN was calculated by subtracting the ERP waveform elicited by the standard stimuli from those elicited by the deviant stimuli. RSOT was used to avoid the difference in the physical properties between the deviant and standard stimuli. According to previous studies (Hu et al., 2013), the analysis of sMMN focused on the central scalp regions between 100 and 300 ms, and specific electrodes were selected. Point-wise paired *t*-tests were used between responses to standards and deviants in the 100–300 ms time window. For sMMN peak amplitude analysis, the negative peak in the difference wave was identified after point-wise paired *t*-tests for each participant. For sMMN latency analysis, sMMN peak latency was quantified as the latency from stimulus onset to the negative peak for each participant. And the peak amplitude and latency of sMMN were compared between conditions. In experiment 1, facial stimuli were shown to the participants, so the ERP component of N170 was extracted in a time window of 150 to 200 ms of standard stimuli to assess the degree of participants' attention.

Statistical Analysis

SPSS version 20.0 was used for the statistical analyses. The average sMMN waveforms of four conditions were compared. For each condition, point-wise paired *t*-tests were performed on the standard and deviant stimuli to verify that sMMN was elicited. The peak amplitudes and latency between different visual attentional conditions were tested for normality and normalized before statistical analysis and assessed *via* one-way ANOVA with Bonferroni corrections at $p < 0.05$.

RESULTS

Experiment 1

Behavioral Data

To determine the degree of attention, the accuracy and reaction time to the target stimuli were evaluated. As expected, an increase in task difficulty was associated with a decline in accuracy (mean \pm SD: 20% face, 0.745 ± 0.200 ; 50% face, 0.962 ± 0.029 ; and 100% face, 0.977 ± 0.023) and an increase in reaction time (mean \pm SD: 20% face, 637 ± 37.4 ; 50% face, 519 ± 26.8 ; and 100% face, 488 ± 21.3). There were significant effects on accuracy, reaction time and ratio of them (accuracy: $F_{(2,30)} = 14.96$, $p < 0.001$; reaction time: $F_{(2,30)} = 141.05$, $p < 0.001$; ratio: $F_{(2,30)} = 70.48$, $p < 0.001$), as illustrated in Figure 3.

Event-Related Potentials

N170

Figure 4 shows the grand averaged N170 at the electrode of CPZ. All three conditions elicited the N170 component in the standard stimuli. The one-way ANOVA for the N170 of peak amplitude showed a significant difference between the task conditions and the control condition for both the index and little fingers (index finger: $F_{(3,40)} = 7.118$, $p = 0.001$; little finger: $F_{(3,40)} = 4.395$, $p = 0.009$, respectively). Neither the index nor the little finger data showed any significant difference between task conditions, but there was an ascending tendency of N170 as the

facial intensities increased. These results indicated that the visual stimuli were effective and that the attention load might increase with decreasing facial intensities.

sMMN

Figure 5 presents the responses to the standard and deviant stimuli and different waves at FC4 for the index and little fingers and their scalp topographic distributions in the 100–300 ms interval. A clear negative-trending ERP response to the tactile deviant stimuli was observed approximately 100–300 ms after stimulus onset. The difference between deviant and standard stimuli was tested by paired-samples *t*-tests in the time range of 100–300 ms to verify the generation of sMMN. The sMMN was generated in both four conditions as shown in gray zones in Figure 5. As shown in the scalp topographic distributions, sMMN is also distributed at the frontal and central regions.

As shown in Figure 6, there was a significant main effect between the task conditions and the control condition, showing that the control condition elicited larger sMMN than did the task conditions in the index finger ($F_{(3,40)} = 8.982$, $p < 0.001$). Regarding the sMMN latency, there was a significant difference in the little finger ($F_{(2,30)} = 7.169$, $p = 0.003$). A Bonferroni-corrected pairwise comparison indicated significant differences in 50% face and 100% face ($p < 0.05$). Although we did not find significant latency differences for the index finger, we did find a similar tendency across the task conditions. Therefore, for both index and little fingers, there is a tendency that the sMMN latency becomes longer as the task becomes more difficult.

Experiment 2

Behavioral Data

To determine the degree of attention, the accuracy and reaction time of target stimuli were evaluated. As shown in Figure 7, increasing task difficulty was associated with declining accuracy (mean \pm SD: 5 balls 0.675 ± 0.165 ; 3 balls, 0.830 ± 0.132 ; and 1 ball, 0.973 ± 0.045) and increasing reaction time (mean \pm SD: 5 balls 1.383 ± 0.507 ; 3 balls, 1.206 ± 0.415 ; and 1 ball, 1.192 ± 0.441). There were significant effects on accuracy, reaction time and ratio of them (accuracy: $F_{(2,27)} = 15.67$, $p < 0.001$; reaction time: $F_{(2,27)} = 4.01$, $p = 0.36$; ratio: $F_{(2,27)} = 16.83$, $p < 0.001$), as illustrated in Figure 7.

Event-Related Potentials

Figure 8 presents the responses to standard and deviant stimuli and different waves at FC4 for index and little fingers with their scalp topographic distribution in a time window of 100 to 300 ms. The difference between deviant and standard stimuli was tested by paired-samples *t*-tests in the time range of 100–300 ms to verify the generation of sMMN. The sMMN was generated in both four conditions as shown in gray zones in Figure 8. As shown in the scalp topographic distributions, sMMN is also distributed at the frontal and central regions. Compared with experiment 1, the negative-going ERP response to the tactile deviant stimuli was smaller.

As illustrated in Figure 9, there was a significant main effect of the amplitude of sMMN between task conditions and control condition, showing that control condition elicited larger sMMN than any task conditions (index finger: $F_{(3,36)} = 30.124$, $p < 0.001$;

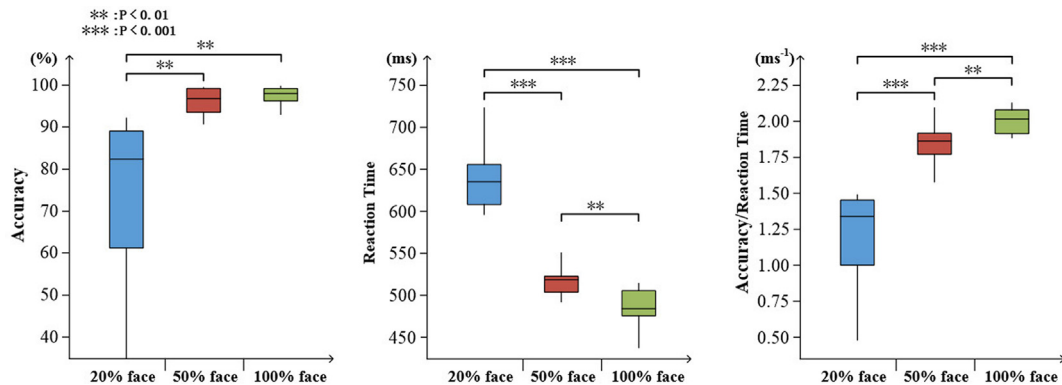


FIGURE 3 | Visualized behavioral data. Statistical analysis for accuracy, reaction time, and the ratio of accuracy to reaction time (** $p < 0.01$; *** $p < 0.001$).

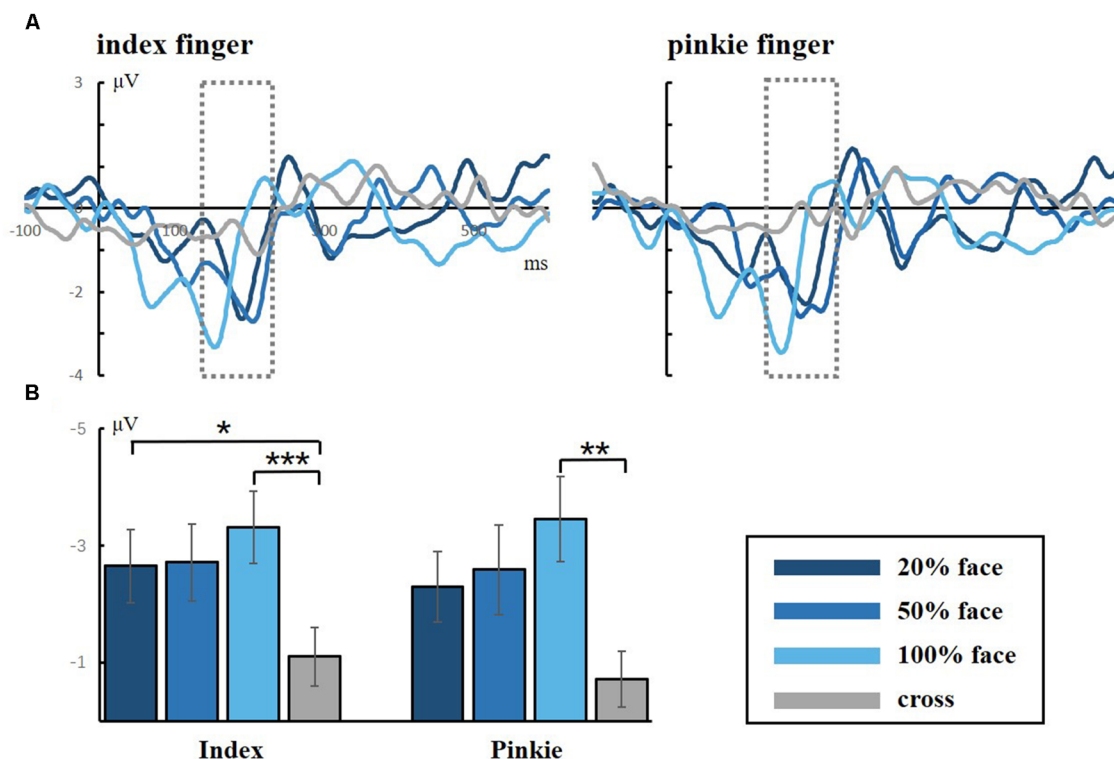


FIGURE 4 | (A) Grand averaged responses to facial stimuli for the index and little fingers in the occipital lobe (electrode CPZ). The gray dotted lines frame the ERP component of N170, which is a facial-specific component. (B) Statistical analysis for the N170 peak amplitude (* $p < 0.05$; ** $p < 0.01$; *** $p < 0.001$).

little finger: $F_{(3,36)} = 13.134$, $p < 0.001$). For the latency of sMMN, neither the index nor little fingers differed between task conditions. However, there is a tendency that the more difficult the task was, the longer latency was, as in experiment 1.

DISCUSSION

This study aimed to investigate the effect of attention on tactile sensory memory. We conducted two experiments and recorded

sMMN at three different difficulty levels of visual target tasks. We found that the sMMN amplitude was the largest when subjects were focused on the tactile stimuli in both types of experiments but there was no significant difference based on the visual attention load tasks. However, there is an increasing latency tendency of sMMN under increasing visual task loads.

The first study of sMMN was reported that it can be elicited in the response to a change in vibration frequency (24 and 240 Hz) or spatial location (middle finger and thumb;

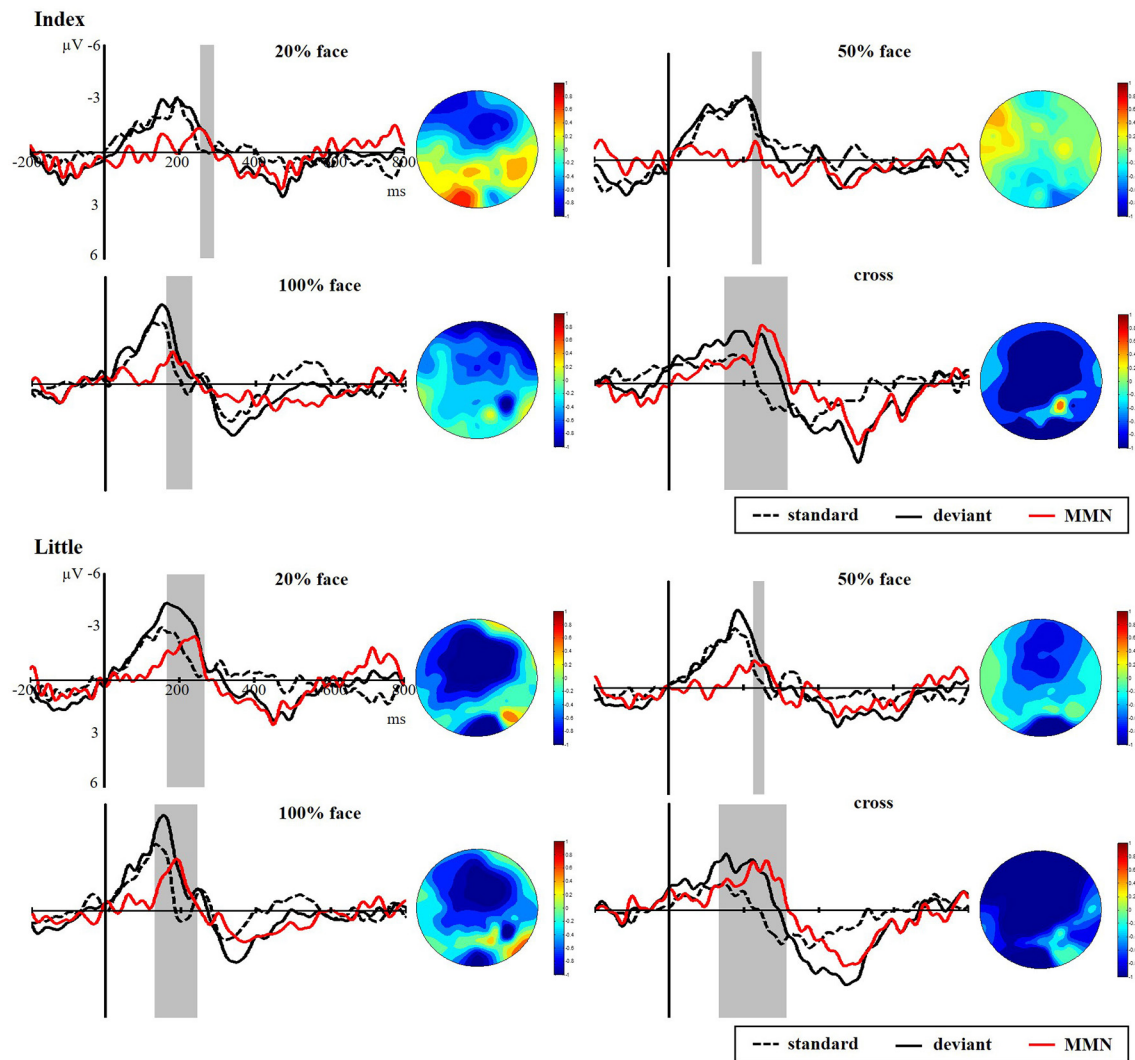


FIGURE 5 | Grand average ERPs of standard (dotted line) and deviant (solid line) stimuli at the FC4 electrode site. Somatosensory mismatch negativity (sMMN; red line) obtained by subtracting the waveforms of the standard stimuli from waveforms of the deviant stimuli. The gray area superimposes on the waveform represent the time window of sMMN, showing the significant differences between the standard and deviant stimuli as revealed by the point-wise paired *t*-tests ($p < 0.05$). The scalp topographic distributions are shown beside the waveforms of ERPs for time windows of 100–300 ms.

Kekoni et al., 1997). Also, different durations of vibrotactile stimulus pairings to the fingertip can elicit an sMMN (Spackman et al., 2007). In our study, the sMMN was elicited by a change between the index and little fingertips. So, the sMMN could be stimulated by multiple stimuli of different physical characteristics, which facilitates the study of tactile sensory memory. Previous studies have investigated whether sMMN is elicited by changes to the fingers in the frontal and central regions between 100–300 ms (Hu et al., 2013; Strommer et al., 2014; Naeije et al., 2018; Zhang et al., 2019). The sMMN responses and topographies presented in this study are similar to those of previous studies. Additionally, the facial specificity component of N170 decreases as the facial intensities decrease (Bentin et al., 1996). In both sustained attention and non-sustained attention, the sMMN was elicited, tactile sensory memory can

emerge in both states. But compared with experiment 1, the standard stimulus of high visual attention load in experiment 2 is nearly zero. One possible explanation is that the visual attention components continue to activate during the entire task.

Given that sMMN represents a sensory memory, we hypothesized that attention affects tactile sensory memory. Consistent with previous studies (Woldorff et al., 1991; Näätänen et al., 1993), the sMMN is significantly more negative when attention is focused completely on the tactile stimuli. This indicates that tactile sensory memory can be enhanced under a highly focused attentional state. In the non-attention task, subjects were instructed to focus on the visual targets, ignoring the tactile stimuli. That attentional resources are transferred to the visual modality to avoiding the overlapping of attention and tactile memory sensory resources in the same modality.

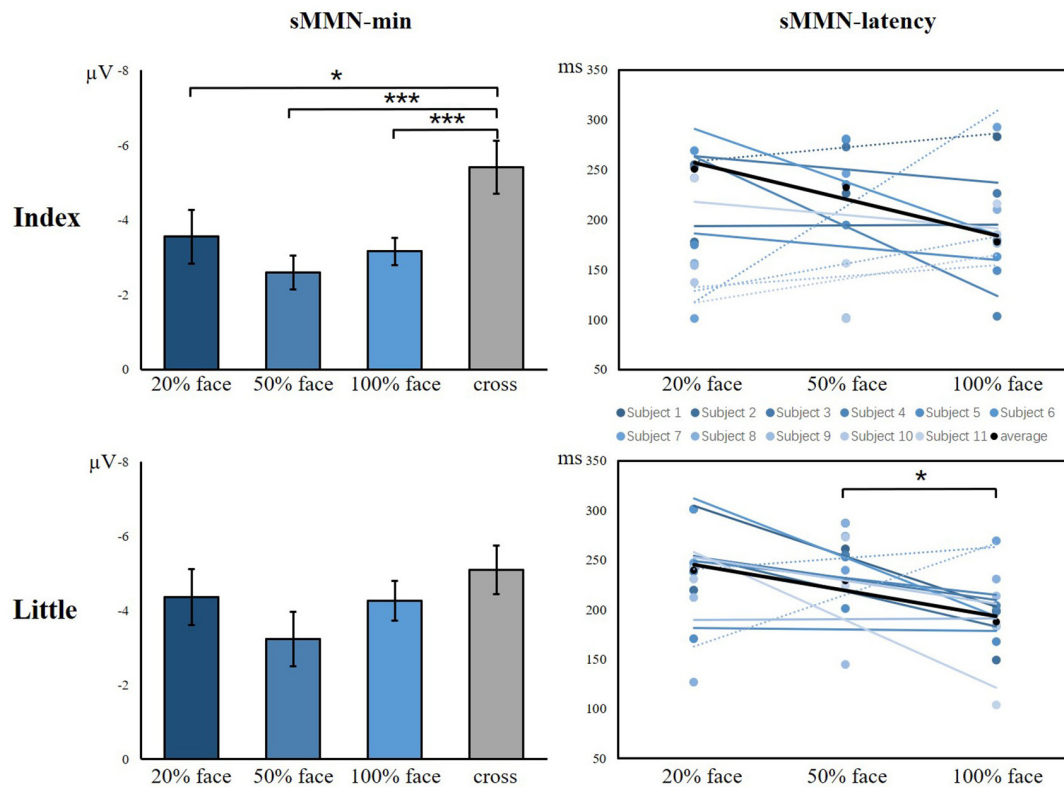


FIGURE 6 | The minimum amplitude and latency of the grand averaged sMMN for the index and little fingers. The sMMN-min compares the differences between task conditions and control conditions. The sMMN latency compares differences between task conditions and the latency trend of all participants are shown (* $p < 0.05$; *** $p < 0.001$).

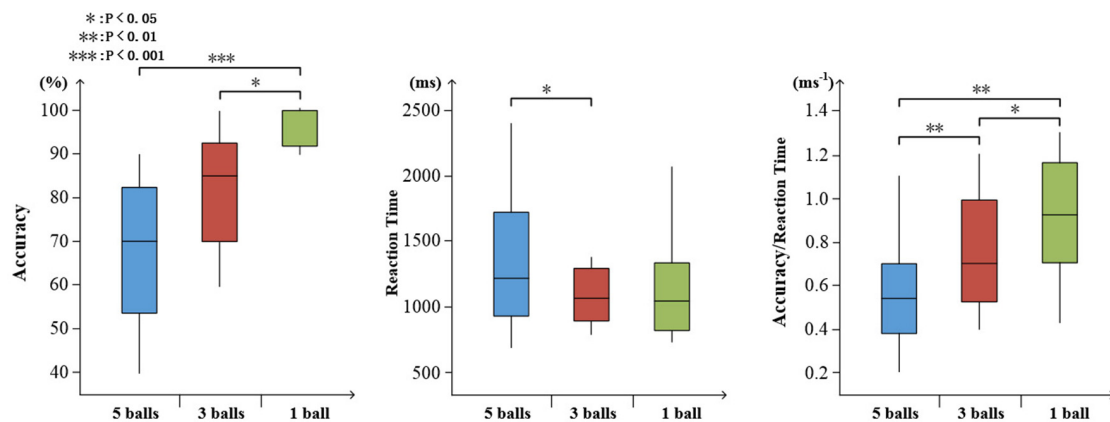


FIGURE 7 | Visualized behavioral data. Statistical analysis for accuracy, reaction time, and the ratio of accuracy to reaction time (* $p < 0.05$; ** $p < 0.01$; *** $p < 0.001$).

Under different visual attentional task loads, auditory MMN may be either increased or decreased, as reported in previous studies. Here, we might have found a new and different pattern in the somatosensory system: rather than attenuating or enhancing neural responses to the task-irrelevant, the tactile sensory memory process was prolonged, and attention had no

effect on their intensity. The relationship between MMN latency and pre-attentive sensory memory was reported by Tiitinen et al. (1994), who found that MMN latency could be used to predict the behavioral response latency, which was explained as originating from the pre-attentive sensory memory mechanism. MMN latency has been shown to indicate a recognition of the time

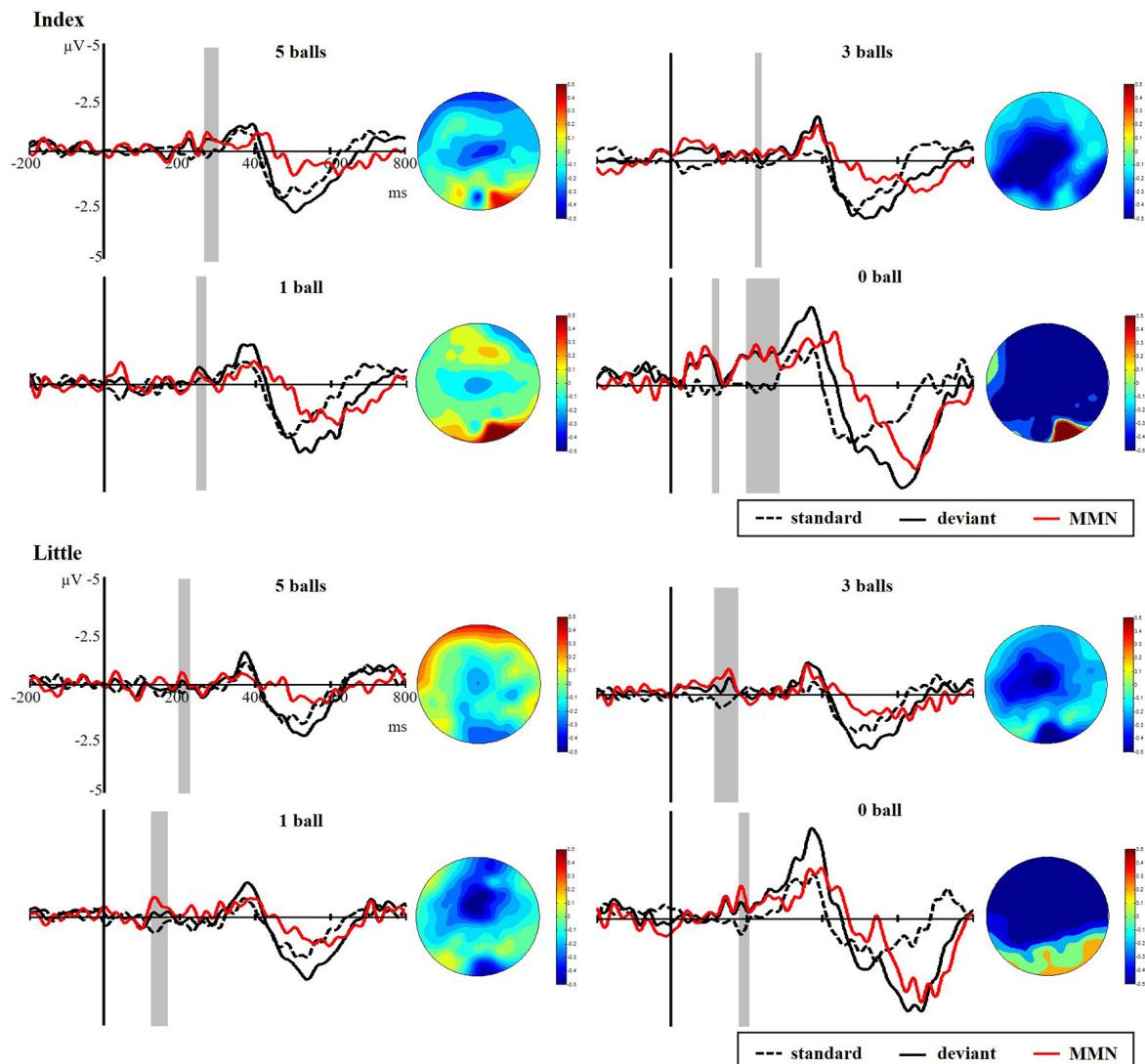


FIGURE 8 | Grand average ERPs of standard (dotted line) and deviant (solid line) stimuli at the FC4 electrode site. The sMMN (red line) was obtained by subtracting the waveforms of the standard stimuli from waveforms of the deviant stimuli. The gray area superimposes on the waveform represent the time window of sMMN, showing the significant difference between standard and deviant stimuli as revealed by the point-wise paired *t*-tests. Scalp topographic distributions are shown beside the waveforms of ERPs with time windows of 100–300 ms.

of the difference between deviant and standard representations (Picton et al., 2000). Thus, reduced MMN latency may indicate a briefer involvement of the comparison process (Horton et al., 2011). And the other way around increased sMMN latency may suggest a decay of the sensory memory trace (Bartha-Doering et al., 2015). When fewer attentional resources are allocated to the tactile modality, the sMMN latency is longer, which indicates that attention may contribute to the formation of tactile sensory memory.

In both the attention and non-attention tasks, the results are broadly consistent with perceptual load theory: attention resources distributed between targets and distractors are limited (Woldorff et al., 1991; Lavie, 1995, 2010; Lavie et al., 2004). The distractors are processed less when the

main task consumes all the available attention resources. Previous studies also showed that early somatosensory processing was diminished under visual load (Jones and Forster, 2013). In the present study, when subjects were instructed to count the number of stimuli exchanges between their index and little fingers during the attention task, more resources were allocated to predict errors. In this case, the sMMN amplitude, which indexes the early detection of irregular changes, would be larger. Consistently, increasing the attention load on the visual stimuli leads to increasing somatosensory memory coding time associated with detecting the incoming information regularities. It seems that our brain continues to monitor the environment, but it postpones task-irrelevant information.

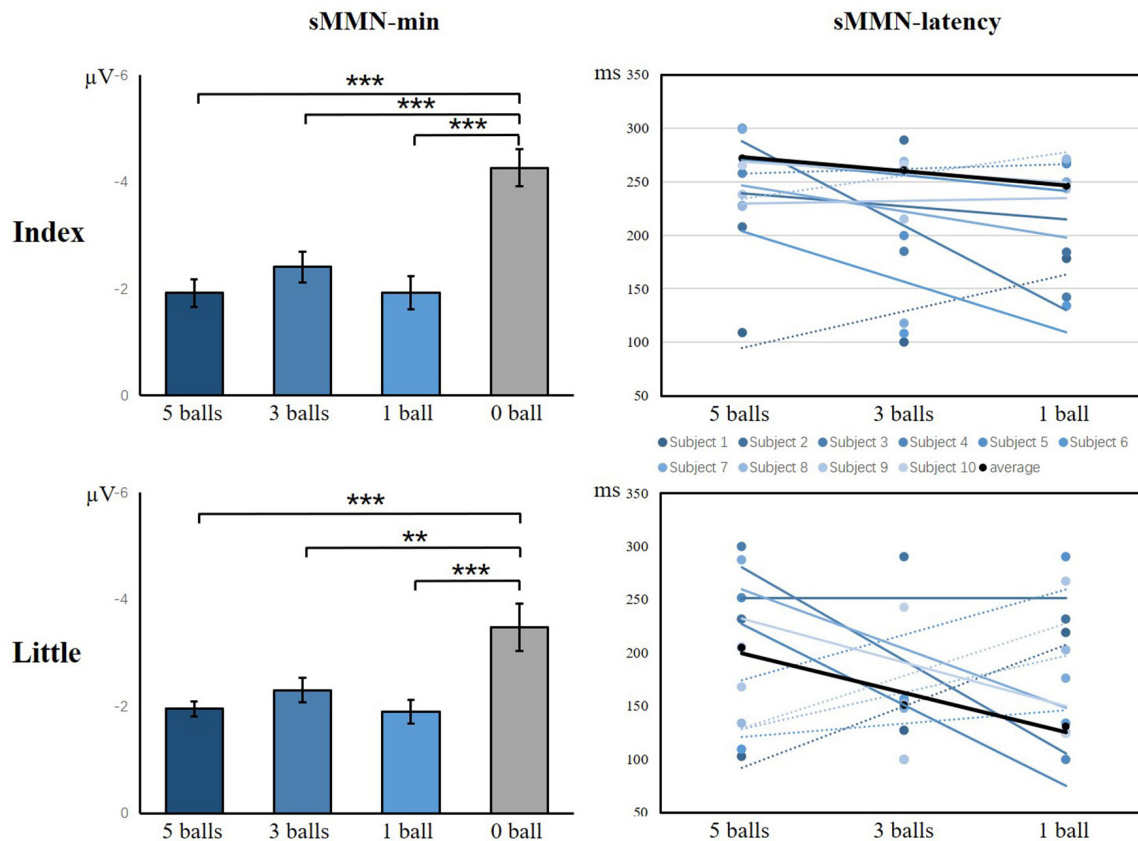


FIGURE 9 | The minimum amplitude and latency of the grand averaged sMMN for the index and little fingers. The sMMN-min compares the differences between task conditions and control conditions. The sMMN latency compares differences between task conditions and the latency trend of all participants are shown (** $p < 0.01$; *** $p < 0.001$).

Previous work showed that tactile memory can be subdivided into several functionally distinct neurocognitive subsystems, and a multi-sensory information processing network appears to play a leading role in the storage of tactile information (Gallace and Spence, 2009). Another study revealed that memory adapting properties and sensory memory capacities are presented in both the SI and SII areas, which can be considered as a model of sensory memory construction (Bradley et al., 2016). Early studies utilized a cross-modal visuo-haptic delay task to record the spikes from Brodmann's areas 3a, 3b, 1, and 2 of monkeys and found that certain cells changed their firing frequency when they reacted to tactile objects during the presentation of a visual cue (Zhou and Fuster, 1997, 2000). The authors suggested that certain neurons are involved in responding to both tactile and visual information and that these might form part of the cross-modal memory network, which indicates that at least part of the neural network involved in the memory storage of tactile stimuli might be shared among different sensory modalities. So, some of the neurons in this cross-modal memory network might be involved in forming the generators of sMMN, and these might be the sources of multi-sensory attention that affect tactile sensory memory. However, this inference is based on previous studies,

further research can operate at a neural level to investigate this assumption.

To summarize, our results demonstrate that the more attentional resources that are allocated to tactile sensation, the more favorable conditions are for generating tactile sensory memory. Here, we acknowledge some limitations: there are no significant correlations between the behavioral results and sMMN features, we will continue to further study the brain mechanism of tactile sensory memory, hoping to find better features to explain the relationship between behavioral results and brain mechanisms. Although we set up a gradient for the visual attention load and found the tendencies of N170 and sMMN in our results, a better understanding of the effects on attention and sensory memory requires further research using a better method for attracting attention. To date, the brain mechanism of tactile sensory memory has not been fully elucidated. Our research provides some evidence; however, this area still requires further exploration.

DATA AVAILABILITY STATEMENT

The raw data supporting the conclusions of this article will be made available by the authors, without undue reservation.

ETHICS STATEMENT

The studies involving human participants were reviewed and approved by Beijing Institute of Technology (2017SY38). The patients/participants provided their written informed consent to participate in this study. Written informed consent was obtained from the individual(s) for the publication of any potentially identifiable images or data included in this article.

AUTHOR CONTRIBUTIONS

XH: analyzed and interpreted the data, wrote the article, and performed the experiments. JZ and ZZ: conceived and designed the experiments, and performed the experiments. CL, DC,

and KG: revised the article. RG and JW: approved the final version. All authors contributed to the article and approved the submitted version.

FUNDING

This work was supported by the National Key R&D Program of China (grant number 2018YFC1314502), the National Natural Science Foundation of China (grant numbers 61727807, 61633018, and 81771909), China Postdoctoral Science Foundation (grant number 2020TQ0040), the Beijing Municipal Science & Technology Commission (grant numbers Z181100003118007 and Z191100010618004) and the Beijing Nova Program (grant number Z181100006218008).

REFERENCES

- Atkinson, R. C., and Shiffrin, R. M. (1968). Human memory: a proposed system and its control processes. *Psychol. Learn. Motiv.* 2, 89–195.
- Bartha-Doering, L., Deuster, D., Giordano, V., Zehnhoﬀ-Dinnesen, A. A., and Dobel, C. (2015). A systematic review of the mismatch negativity as an index for auditory sensory memory: from basic research to clinical and developmental perspectives. *Psychophysiology* 52, 1115–1130. doi: 10.1111/psyp.12459
- Bentin, S., Allison, T., Puce, A., Perez, E., and McCarthy, G. (1996). Electrophysiological studies of face perception in humans. *J. Cogn. Neurosci.* 8, 551–565. doi: 10.1162/jocn.1996.8.6.551
- Bottcherghandor, C., and Ullsperger, P. (1992). Mismatch negativity in event-related potentials to auditory-stimuli as a function of varying interstimulus-interval. *Psychophysiology* 29, 546–554. doi: 10.1111/j.1469-8986.1992.tb02028.x
- Bradley, C., Joyce, N., and Garcia-Larrea, L. (2016). Adaptation in human somatosensory cortex as a model of sensory memory construction: a study using high-density EEG. *Brain Struct. Funct.* 221, 421–431. doi: 10.1007/s00429-014-0915-5
- Cheour, M., Leppänen, P. H., and Kraus, N. (2000). Mismatch negativity (MMN) as a tool for investigating auditory discrimination and sensory memory in infants and children. *Clin. Neurophysiol.* 111, 4–16. doi: 10.1016/S1388-2457(99)00191-1
- Cowan, N., Winkler, I., Teder, W., and Naatanen, R. (1993). Memory prerequisites of mismatch negativity in the auditory event-related potential (ERP). *J. Exp. Psychol. Learn. Mem. Cogn.* 19, 909–921. doi: 10.1037/0278-7393.19.4.909
- Creelman, C. D. and Macmillan, N. A. (2004). *Detection Theory: A User's Guide*. New York, NY: Psychology Press
- Debettencourt, M. T., Cohen, J. D., Lee, R. F., Norman, K. A., and Turk-Browne, N. B. (2015). Closed-loop training of attention with real-time brain imaging. *Nat. Neurosci.* 18, 470–475. doi: 10.1038/nn.3940
- Delorme, A., and Makeig, S. (2004). EEGLAB: an open source toolbox for analysis of single-trial EEG dynamics including independent component analysis. *J. Neurosci. Methods* 134, 9–21. doi: 10.1016/j.jneumeth.2003.10.009
- Gallace, A., and Spence, C. (2009). The cognitive and neural correlates of tactile memory. *Psychol. Bull.* 135, 380–406. doi: 10.1037/a0015325
- Gallace, A., Tan, H. Z., and Spence, C. (2007). The body surface as a communication system: the state of the art after 50 years. *Presence: Teleoperators Virtual Environ.* 16, 655–676. doi: 10.1162/pres.16.6.655
- Garrido, M. I., Kilner, J. M., Stephan, K. E., and Friston, K. J. (2009). The mismatch negativity: a review of underlying mechanisms. *Clin. Neurophysiol.* 120, 453–463. doi: 10.1016/j.clinph.2008.11.029
- Horton, J., Millar, A., Labelle, A., and Knott, V. J. (2011). MMN responsivity to manipulations of frequency and duration deviants in chronic, clozapine-treated schizophrenia patients. *Schizophr. Res.* 126, 202–211. doi: 10.1016/j.schres.2010.11.028
- Hu, L., Zhao, C., Li, H., and Valentini, E. (2013). Mismatch responses evoked by nociceptive stimuli. *Psychophysiology* 50, 158–173. doi: 10.1111/psyp.12000
- Ito, T., Bai, J., and Ostry, D. J. (2020). Contribution of sensory memory to speech motor learning. *J. Neurophysiol.* 124, 1103–1109. doi: 10.1152/jn.00457.2020
- Jones, A., and Forster, B. (2013). Lost in vision: ERP correlates of exogenous tactile attention when engaging in a visual task. *Neuropsychologia* 51, 675–685. doi: 10.1016/j.neuropsychologia.2013.01.010
- Jung, T. P., Makeig, S., Westerfield, M., Townsend, J., Courchesne, E., and Sejnowski, T. J. (2001). Analysis and visualization of single-trial event-related potentials. *Hum. Brain Mapp.* 14, 166–185. doi: 10.1002/hbm.1050
- Kekoni, J., Hamalainen, H., Saarinen, M., Grohn, J., Reinikainen, K., Lehtokoski, A., et al. (1997). Rate effect and mismatch responses in the somatosensory system: ERP-recordings in humans. *Biol. Psychol.* 18, 125–142. doi: 10.1016/s0301-0511(97)05249-6
- Lavie, N. (1995). Perceptual load as a necessary condition for selective attention. *J. Exp. Psychol. Hum. Percept. Perform.* 21, 451–468. doi: 10.1037/0096-1523.21.3.451
- Lavie, N. (2010). Attention, distraction and cognitive control under load. *Curr. Dir. Psychol.* 19, 143–148. doi: 10.1177/0963721410370295
- Lavie, N., Hirst, A., de Fockert, J. W., and Viding, E. (2004). Load theory of selective attention and cognitive control. *J. Exp. Psychol. Gen.* 133, 339–354. doi: 10.1037/0096-3445.133.3.339
- Macdonald, J. S. P., and Lavie, N. (2011). Visual perceptual load induces inattentional deafness. *Atten. Percept. Psychophys.* 73, 1780–1789. doi: 10.3758/s13414-011-0144-4
- Mantysalo, S., and Naatanen, R. (1987). The duration of a neuronal trace of an auditory stimulus as indicated by event-related potentials. *Biol. Psychol.* 24, 183–195. doi: 10.1016/0301-0511(87)90001-9
- Mun, S., Whang, M., Park, S., and Park, M. C. (2017). Effects of mental workload on involuntary attention: a somatosensory ERP study. *Neuropsychologia* 106, 7–20. doi: 10.1016/j.neuropsychologia.2017.08.021
- Näätänen, R., and Gaillard, A. W. K. (1983). The orienting reflex and the N2 deflection of the event-related potential (ERP). *Adv. Psychol.* 10, 119–141. doi: 10.1016/S0166-4115(08)62036-1
- Näätänen, R., Gaillard, A. W. K., and Mäntysalo, S. (1980). Brain potential correlates of voluntary and involuntary attention. *Prog. Brain Res.* 54, 343–348. doi: 10.1016/S0079-6123(08)61645-3
- Näätänen, R., Gaillard, A. W., and Mäntysalo, S. (1978). Early selective-attention effect on evoked potential reinterpreted. *Acta Psychol.* 42, 313–329. doi: 10.1016/0001-6918(78)90006-9
- Näätänen, R., and Michie, P. T. (1979). Early selective-attention effects on the evoked potential: a critical review and reinterpretation. *Biol. Psychol.* 8, 81–136. doi: 10.1016/0301-0511(79)90053-x
- Näätänen, R., Paavilainen, P., Rinne, T., and Alho, K. (2007). The mismatch negativity (MMN) in basic research of central auditory processing: a review. *Clin. Neurophysiol.* 118, 2544–2590. doi: 10.1016/j.clinph.2007.04.026
- Näätänen, R., Paavilainen, P., Tiitinen, H., Jiang, D., and Alho, K. (1993). Attention and mismatch negativity. *Psychophysiology* 30, 436–450. doi: 10.1111/j.1469-8986.1993.tb02067.x

- Naeije, G., Vaulet, T., Wens, V., Marty, B., Goldman, S., and De Tiege, X. (2018). Neural basis of early somatosensory change detection: a magnetoencephalography study. *Brain Topog.* 31, 242–256. doi: 10.1007/s10548-017-0591-x
- Picton, T. W., Alain, C., Otten, L., Ritter, W., and Achim, A. (2000). Mismatch negativity: different water in the same river. *Audiol. Neurotol.* 5, 111–139. doi: 10.1159/000013875
- Raveh, D., and Lavie, N. (2015). Load-induced inattentional deafness. *Atten. Percept. Psychophys.* 77, 483–492. doi: 10.3758/s13414-014-0776-2
- Sams, M., Alho, K., and Naatanen, R. (1984). Short-term habituation and dishabituation of the mismatch negativity of the ERP. *Psychophysiology* 21, 434–441. doi: 10.1111/j.1469-8986.1984.tb00223.x
- Spackman, L. A., Boyd, S. G., and Towell, A. (2007). Effects of stimulus frequency and duration on somatosensory discrimination responses. *Exp. Brain Res.* 177, 21–30. doi: 10.1007/s00221-006-0650-0
- Strommer, J. M., Tarkka, I. M., and Astikainen, P. (2014). Somatosensory mismatch response in young and elderly adults. *Front. Aging Neurosci.* 6:293. doi: 10.3389/fnagi.2014.00293
- Sugimoto, F., and Katayama, J. (2013). Somatosensory P2 reflects resource allocation in a game task: assessment with an irrelevant probe technique using electrical probe stimuli to shoulders. *Int. J. Psychophysiol.* 87, 200–204. doi: 10.1016/j.ijpsycho.2013.01.007
- Szychowska, M., Eklund, R., Nilsson, M. E., and Wiens, S. (2017). Effects of sound pressure level and visual perceptual load on the auditory mismatch negativity. *Neurosci. Lett.* 640, 37–41. doi: 10.1016/j.neulet.2017.01.001
- Tiitinen, H., May, P., Reinikainen, K., and Naatanen, R. (1994). Attentive novelty detection in humans is governed by pre-attentive sensory memory. *Nature* 372, 90–92. doi: 10.1038/372090a0
- Wiens, S. S., Szychowska, M., and Nilsson, M. E. (2016). Visual task demands and the auditory mismatch negativity: an empirical study and a meta-analysis. *PLoS One* 11:e0146567. doi: 10.1371/journal.pone.0146567
- Winkler, I., Korzyukov, O., Gumenyuk, V., Cowan, N., Linkenkaer-Hansen, K., Ilmoniemi, R. J., et al. (2002). Temporary and longer term retention of acoustic information. *Psychophysiology* 39, 530–534. doi: 10.1017/S0048577201393186
- Woldorff, M. G., Hackley, S. A., and Hillyard, S. A. (1991). The effects of channel-selective attention on the mismatch negativity wave elicited by deviant tones. *Psychophysiology* 28, 30–42. doi: 10.1111/j.1469-8986.1991.tb03384.x
- Zhang, P., Chen, X. C., Yuan, P., Zhang, D. R., and He, S. (2006). The effect of visuospatial attentional load on the processing of irrelevant acoustic distractors. *NeuroImage* 33, 715–724. doi: 10.1016/j.neuroimage.2006.07.015
- Zhang, Z. L., Guo, G. X., Zhang, J., Li, C. L., Huang, Q., Go, R. S., et al. (2019). Do theta oscillations explain the somatosensory change detection mechanism? *Biol. Psychol.* 143, 103–112. doi: 10.1016/j.biopsycho.2019.02.001
- Zhou, Y. D., and Fuster, J. M. (1997). Neuronal activity of somatosensory cortex in a cross-modal (visuo-haptic) memory task. *Exp. Brain Res.* 116, 551–555. doi: 10.1007/PL00005783
- Zhou, Y. D., and Fuster, J. M. (2000). Visuo-tactile cross-modal associations in cortical somatosensory cells. *Proc. Natl. Acad. Sci. U S A* 97, 9777–9782. doi: 10.1073/pnas.97.17.9777

Conflict of Interest: The authors declare that the research was conducted in the absence of any commercial or financial relationships that could be construed as a potential conflict of interest.

Copyright © 2020 He, Zhang, Zhang, Go, Wu, Li, Gan and Chen. This is an open-access article distributed under the terms of the Creative Commons Attribution License (CC BY). The use, distribution or reproduction in other forums is permitted, provided the original author(s) and the copyright owner(s) are credited and that the original publication in this journal is cited, in accordance with accepted academic practice. No use, distribution or reproduction is permitted which does not comply with these terms.



A Spelling Paradigm With an Added Red Dot Improved the P300 Speller System Performance

Yan Wu, Weiwei Zhou, Zhaohua Lu and Qi Li*

School of Computer Science and Technology, Changchun University of Science and Technology, Changchun, China

OPEN ACCESS

Edited by:

Tianyi Yan,
Beijing Institute of Technology, China

Reviewed by:

Minpeng Xu,
Tianjin University, China
Jing Jin,
East China University of Science and
Technology, China
Bin Wang,
Taiyuan University of
Technology, China

*Correspondence:

Qi Li
liqi@cust.edu.cn

Received: 30 July 2020

Accepted: 02 November 2020

Published: 03 December 2020

Citation:

Wu Y, Zhou W, Lu Z and Li Q (2020) A
Spelling Paradigm With an Added Red
Dot Improved the P300 Speller
System Performance.
Front. Neuroinform. 14:589169.
doi: 10.3389/fninf.2020.589169

The traditional P300 speller system uses the flashing row or column spelling paradigm. However, the classification accuracy and information transfer rate of the P300 speller are not adequate for real-world application. To improve the performance of the P300 speller, we devised a new spelling paradigm in which the flashing row or column of a virtual character matrix is covered by a translucent green circle with a red dot in either the upper or lower half (GC-RD spelling paradigm). We compared the event-related potential (ERP) waveforms with a control paradigm (GC spelling paradigm), in which the flashing row or column of a virtual character matrix was covered by a translucent green circle only. Our experimental results showed that the amplitude of P3a at the parietal area and P3b at the frontal-central-parietal areas evoked by the GC-RD paradigm were significantly greater than those induced by the GC paradigm. Higher classification accuracy and information transmission rates were also obtained in the GC-RD system. Our results indicated that the added red dots increased attention and visuospatial information, resulting in an amplitude increase in both P3a and P3b, thereby improving the performance of the P300 speller system.

Keywords: brain-computer interface (BCI), P300 speller, visuospatial information, spelling paradigm, event-related potential

INTRODUCTION

Brain-computer interface (BCI) systems allow people to communicate without using their muscles, which provides a direct communication pathway for patients with severe amyotrophic lateral sclerosis (ALS) and other locked-in syndromes (LIS) (Sellers and Donchin, 2006; Kubler and Birbaumer, 2008). An ERP is a response of the brain to an external stimulus, which is generally used to implement a BCI system. The P300 is an ERP component generated from the observation of a rare or odd event and manifests as a positive waveform appearing around 300 ms after presentation of the stimulus (Bernat et al., 2001). In 1988, Farwell and Donchin described a BCI system, known as the P300 speller, which allows the patient to spell characters by detecting the P300 potential (Farwell and Donchin, 1988). In the P300 speller, a 6×6 matrix of characters is displayed on a screen, and the rows and columns of the matrix are intensified (flashed) one after another in a pseudo-random order. When users wish to output a target character, they need to only focus on the desired target character. When the row or column containing the target character is intensified, which has a one-sixth probability and constitutes a rare event, a P300 potential is elicited. Thus, the target character is determined by the row and the column that elicited a P300 potential. Several

studies have attempted to improve the spelling accuracy and speed of the P300 speller. However, its performance is still unable to meet the requirements of a real-world application (Kaufmann et al., 2011; Aya et al., 2018; Philip and George, 2020; Xu et al., 2020).

Eliciting larger amplitudes of ERP such as P300, to improve the performance of character recognition, is a key direction for optimizing BCIs (Aya et al., 2018; Xiao et al., 2019). Previous studies have indicated that focusing attention on external stimuli improves the processing of visual information in the nervous system and can significantly modulate the visual stimulus response (Posner, 1980; Mangun, 1995). Further, the resource quantity expended on concentrating attention directly affects the excitability of brain activity and resulting features of the evoked waveform (Berti, 2016). Lakey et al. (2011) reported that heightening subjects' attention with a short session of mindfulness meditation can elicit larger P300 amplitude. Additionally, researchers have shown that there is a reciprocal relation between the concentration of attentional resources and the scope or size of the attentional focus (Eriksen and Yeh, 1985; Xu et al., 2018). When attention is paid to a small spatial scope, the stimulus is allocated more visual processing resources, resulting in a greater ability of the brain to process and discriminate the stimulus (Rincover and Ducharme, 1987).

Stimuli containing spatial information can elicit larger ERP amplitudes than those without. A previous study found that a stimulus located above or below the central fixation point elicited a larger P300 amplitude than one located at the central fixation point (Abramov et al., 2017). Several studies reported that when the appearance of the target was predictable, subjective efforts in perceptual processing and attention orientation were small, resulting in the reduction of the target P300 amplitude (Sutton et al., 1965; Hugdahl and Nordby, 1994). Therefore, we speculated that changing the visuospatial location to reduce the probability of the target appearance could also increase the P300 amplitude.

Green has been shown to be a color that helps the perceivers maintain attention on a task (Xia et al., 2018). Studies have investigated the combining of characters or stimulus images with green backgrounds to modify spelling paradigms and found that they improved not only the comfort level of subjects but also the performance of the P300 speller (Li et al., 2015; Lu et al., 2019).

In the present study, we proposed a new spelling paradigm to attract more attention from subjects and increase visuospatial information, in which the flashing row or column of a virtual character matrix was overlaid with a translucent green circle in which a red dot was positioned in either the upper or lower half (GC-RD spelling paradigm). The red dot resulted in a smaller focus scope, and its appearance in either the upper or lower half of the green circle reduced the probability of its manifestation. The control spelling paradigm was that the flashing row or column of the virtual character matrix was covered by a translucent green circle only (GC spelling paradigm). We compared ERP waveforms and the spelling performances of the P300 speller between the two paradigms to verify whether the GC-RD spelling paradigm would improve the performance of the P300 speller system.

MATERIALS AND METHODS

Participants

Eleven college student volunteers (two female and nine male; mean age, 20 ± 2 years old) participated in the study. Participants signed their written informed consent after receiving a full explanation of the purpose and requirements of the study. All participants were right handed and had normal or corrected-to-normal vision. Two of the participants had previously participated in a similar experiment, while the others had no prior BCI experience. The study was approved by the ethics committee of Changchun University of Science and Technology.

The Spelling Paradigm

In both the GC-RD and GC paradigms, a 6×7 character matrix with 26 letters, 10 numerals (0–9), and four symbols is presented on a monitor (**Figure 1**). The size of each character is $1.2^\circ \times 1.2^\circ$ (1.5×1.5 cm), and the distance between each character is $3.5^\circ \times 2.5^\circ$ (4.5×3 cm). To mitigate the problem of adjacency flashing, we pseudo-randomly intensified a set of characters (six or seven) that scattered as far away as possible. The intensified characters were selected according to the rows and columns of a virtual 6×7 character matrix as shown in **Figure 2**.

In the GC-RD paradigm, characters are covered by green circles with a red dot while intensified. The red dot appears in the upper (**Figure 1A**, left) or lower (**Figure 1A**, right) half of the green circle. The position of the red dots is the same for all intensified stimuli in each flash. The GC paradigm is similar to the GC-RD paradigm but without the red dot (**Figure 1B**). The interstimulus interval (ISI) was 250 ms, in which each character was covered by a green circle with (GC-RD paradigm) or without (GC paradigm) a red dot for 200 ms and then reverted to a gray character for 50 ms.

Procedure

The study was conducted in a dimly lit, sound-attenuated, and electrically shielded room. Participants sat ~ 90 cm in front of a monitor. Each participant participated in two experiments: Exp. 1 (GC-RD spelling paradigm) and Exp. 2 (GC spelling paradigm). Each experiment consisted of four sessions in which the subjects were required to output four words with five different characters; each session included five runs to output the five characters. Eight sessions of two experiments were conducted in a pseudo-random order to avoid learning effects. Thirteen flashes corresponding to the six rows and seven columns were defined as a sequence. In each run, the sequence was repeated eight times. Thus, each run consisted of 104 flashes of row or column to output a target character (**Figure 3**). In Exp. 1, the 13 flashes in a sequence comprised six occasions when the red dot was in the upper half of the green circle and seven when it was in the lower half.

During the experiments, subjects were instructed to avoid unnecessary movement including blinking, to pay attention to the target character, and to silently count the number of target character flashes. In Exp. 1, participants were specifically told to concentrate their attention on the red dot rather than on the whole green circle. Subjects were allowed to take a 5-min break between two sessions.

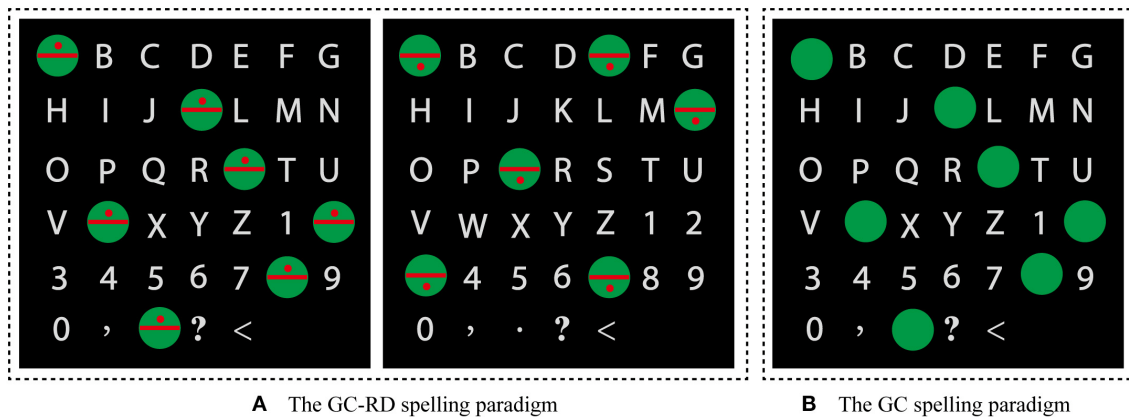


FIGURE 1 | The spelling paradigms. **(A)** The GC-RD spelling paradigm: the red dot appears in the upper (left picture) or lower half (right picture) of the green circle. **(B)** The GC spelling paradigm.



FIGURE 2 | The 6 × 7 virtual character matrix.

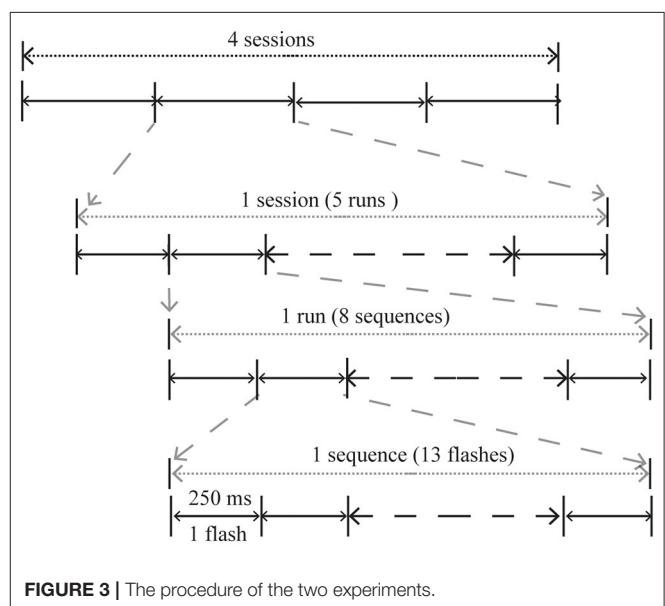


FIGURE 3 | The procedure of the two experiments.

impedance of these electrodes was kept below 5 k Ω . All data were digitized at a rate of 250 Hz.

Data Acquisition

Electroencephalograph (EEG) data from 14 channels (F3, Fz, F4, C3, Cz, C4, P3, Pz, P4, P7, P8, O1, Oz, and O2) were recorded by a SynAmps2 EEG amplifier (SynAmps 2, NeuroScan Inc., and Abbottsford, Australia) with the left mastoid as the ground and the right mastoid as reference. Horizontal eye movements were measured by placing two horizontal electrooculogram (HEOG) electrodes at the corners of the left and right eyes. Two vertical electrooculogram (VEOG) electrodes were placed ~1 cm above and 1 cm below the left eye to record vertical eye movements. In data preprocessing, the EEG signals that were contaminated by EOG were corrected using a regression analysis algorithm. The

Data Processing and Analysis

The raw EEG data were filtered between 0.1 and 30 Hz using a third-order Butterworth band pass filter. The EEG signals were then divided into epochs from 100 ms before the onset of each flashing to 800 ms after the onset, and baseline corrections were made against −100–0 ms. Amplitudes of the P3a and P3b components in the two time windows at 14 of the electrode channels were analyzed with a 2 (spelling paradigms: GC-RD vs. GC) × 14 (electrode channels) repeated measures analysis of variance (ANOVA). The Greenhouse–Geisser Epsilon correction was applied to adjust the degrees of freedom of the F ratios, if necessary. Because a greater difference between target and

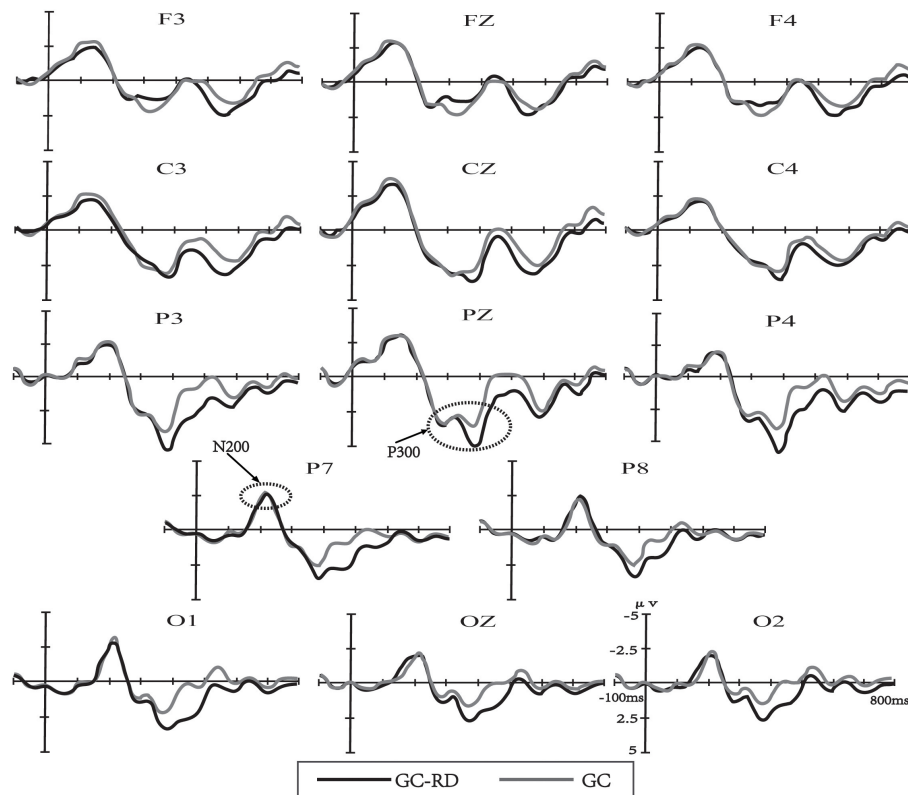


FIGURE 4 | Superimposed grand average waveforms elicited by target trials from 11 students in the GC-RD and GC spelling paradigms. The P300 potential (Pz) and N200 component (P7) are circled.

nontarget trials simplifies their classification, the difference waveforms ($ERP_{\text{Target}} - ERP_{\text{nontarget}}$) for both experiments were obtained by subtracting ERP waveforms elicited by nontarget trials from those elicited by target trials.

Classification Scheme

The EEG data were classified using Bayesian linear discriminant analysis (BLDA). BLDA is an extension of Fisher's linear discriminant analysis, which avoids overfitting due to high-dimensional and possibly noisy datasets (Jin et al., 2010, 2015). The details of the algorithm have been published (Lei et al., 2009), and many studies have shown that BLDA achieves perfect results in P300 detection (Jin et al., 2012, 2014). We used fourfold cross-validation to calculate individual spelling accuracy, successively choosing one of the four sessions as the test set and the remaining three as the training sets, thus obtaining the accuracy of the test set. Individual accuracy was obtained by averaging the four results for each participant.

Information Transfer Rate

The information transmission rate (ITR) was first described by Wolpaw et al. (1998) and is used to evaluate the communication performance of a BCI system. ITR (bit/min) refers to the amount of information that can be transmitted per minute, with the

calculation formula as follows:

$$B = \log_2 N + P \log_2 P + (1 - P) \log_2 \frac{1 - P}{N - 1} \quad (1)$$

$$ITR (\text{bits/min}) = B \times \frac{60}{T} \quad (2)$$

where N is the number of possible choices within a sequence, and P is the target identification accuracy. B (bit/trial) is the number of bits per trial transmission, and T (seconds/character) is the time needed to output each character.

In addition, because of low signal-to-noise ratios, we calculated and compared the classification accuracy and ITR with different sequence numbers to investigate the effects of changing the number of averaged sequences.

RESULTS

Figure 4 shows the grand-average waveform elicited by target trials from 11 students in two spelling paradigms. Positive deflections were clearly observed at the central area (C3, CZ, and C4), parietal area (P7, P3, PZ, P4, and P8), and occipital area (O1, OZ, and O2) in both paradigms, indicating the P300 potential ERP component (Polich, 2007). In addition, a clear negative waveform was observed around 200 ms at the bilateral temporal area (P7 and P8) and occipital area (O1, Oz, and O2).

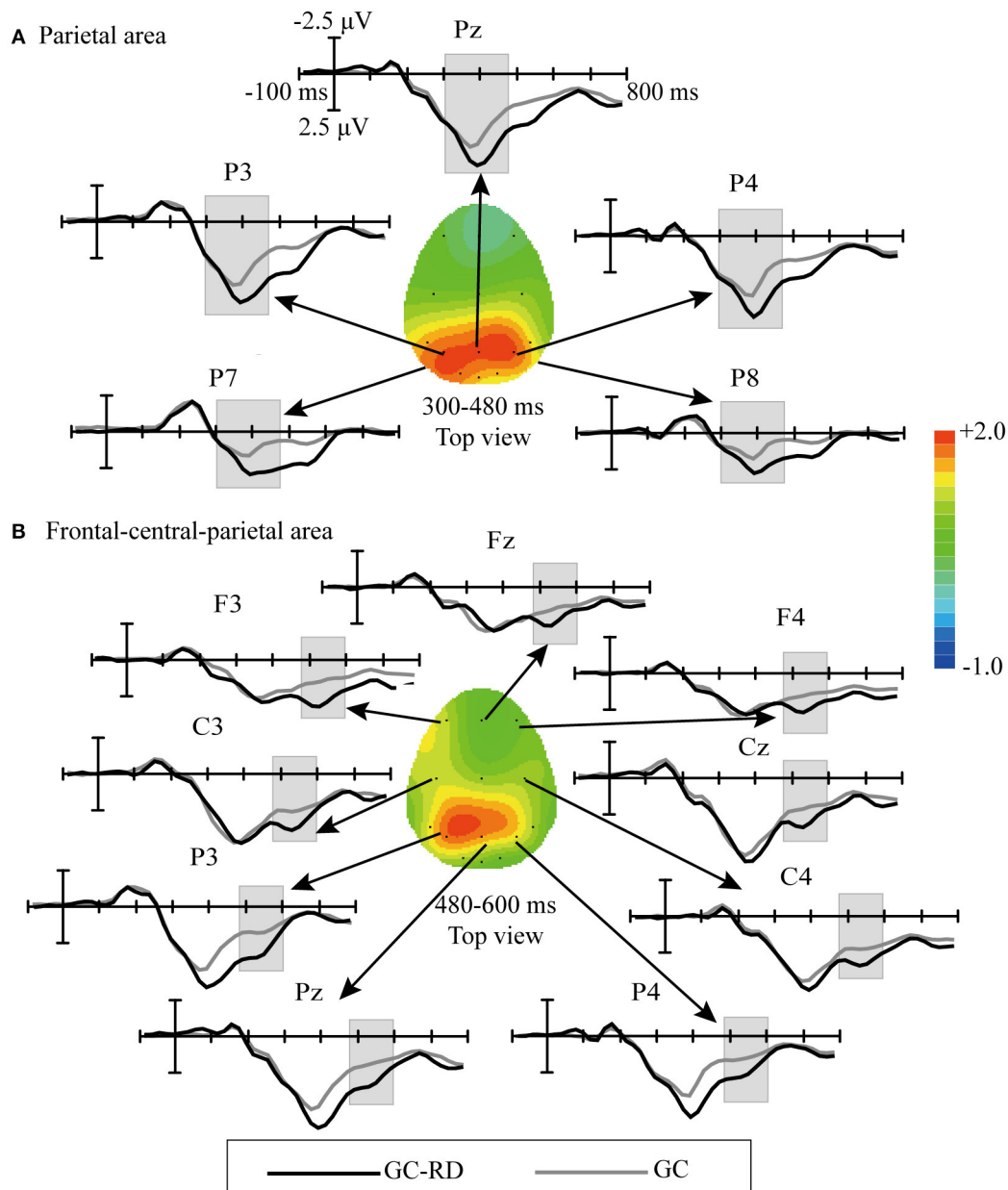


FIGURE 5 | Comparison of difference waveforms of event-related potential (ERP) by subtracting the ERPs of the GC spelling paradigm from those of the GC-RD spelling paradigm ($ERP_{\text{Target}} - ERP_{\text{Nontarget}}$) and scalp topographies for double difference waveforms obtained by subtracting the ($ERP_{\text{Target}} - ERP_{\text{Nontarget}}$) waveforms for the GC spelling paradigm from those of the GC-RD spelling paradigm. **(A)** Parietal area at 300–480 ms; **(B)** Frontal-central-parietal areas at 480–600 ms.

in both paradigms; this is likely to be the N200 component (Reza et al., 2007).

The GC-RD spelling paradigm stimulus elicited a higher P300 potential than the GC spelling paradigm at the central, parietal, and occipital areas (**Figure 4**). A biphasic positive component between 250 and 500 ms was visible with two peaks: the first peak between 250 and 350 ms and the second peak between 350 and 450 ms. The first positive deflection may be P3a potential and the second may be P3b potential (Berti, 2016).

Analysis of the difference waveforms ($ERP_{\text{Target}} - ERP_{\text{Nontarget}}$) between the GC-RD and GC spelling paradigms showed significant differences for P3a in 300–480 ms at P7, P3, Pz, P4, and P8 [$F_{(1,10)} = 25.5111$, $P = 0.001$] and for P3b in 480–600 ms at F3, Fz, F4, C3, Cz, C4, P3, Pz, and P4 [$F_{(1,10)} = 6.654$, $P = 0.03$]. The significant difference amplitudes of P3a were mainly at the parietal areas (**Figure 5A**), while the significant difference amplitudes of P3b were at the frontal-central-parietal areas (**Figure 5B**).

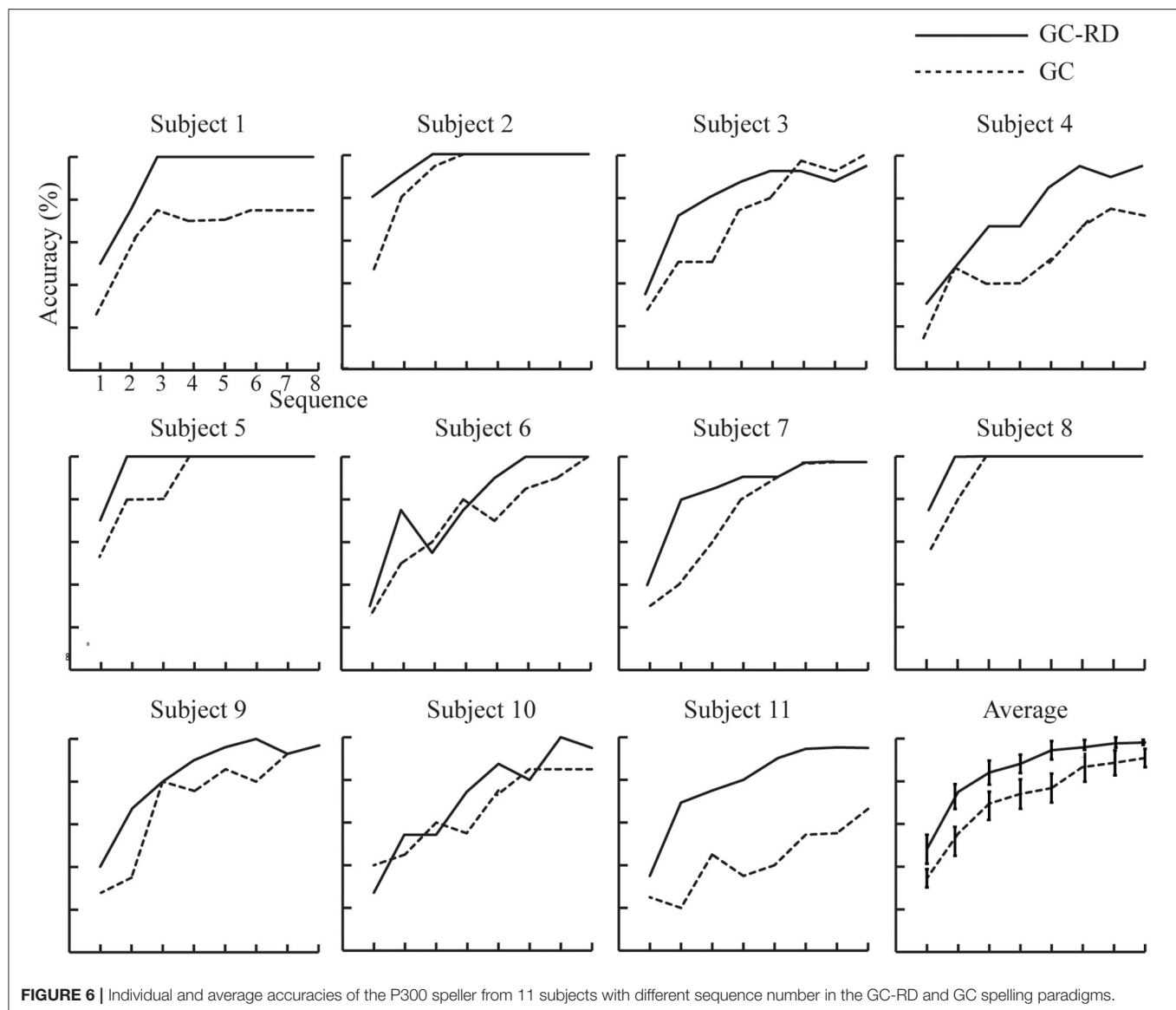


FIGURE 6 | Individual and average accuracies of the P300 speller from 11 subjects with different sequence number in the GC-RD and GC spelling paradigms.

Based on the ERP analysis, we intercepted 160–688 ms from the –100–800 ms data for feature extraction from 11 channels (F3, Fz, F4, C3, Cz, C4, P3, Pz, P4, P7, and P8) to reduce the computational time, in which the significant differences of the ERP waveforms were observed (Li et al., 2015). The intercepted EEG data were downsampled from 250 to 62.5 Hz by selecting every fourth sample from the filtered EEG signals. This decreased the number of waveform points to 33. Therefore, the size of the feature vector was 33×11 , with 11 denoting the number of electrodes and 33 denoting the number of sample points in each flashing.

Figure 6 shows the individual and average accuracies; accuracy increased as sequence number increased for both spelling paradigms. The average classification accuracy of the GC-RD spelling paradigm was higher than that of the GC spelling paradigm at all sequence numbers. In the GC-RD

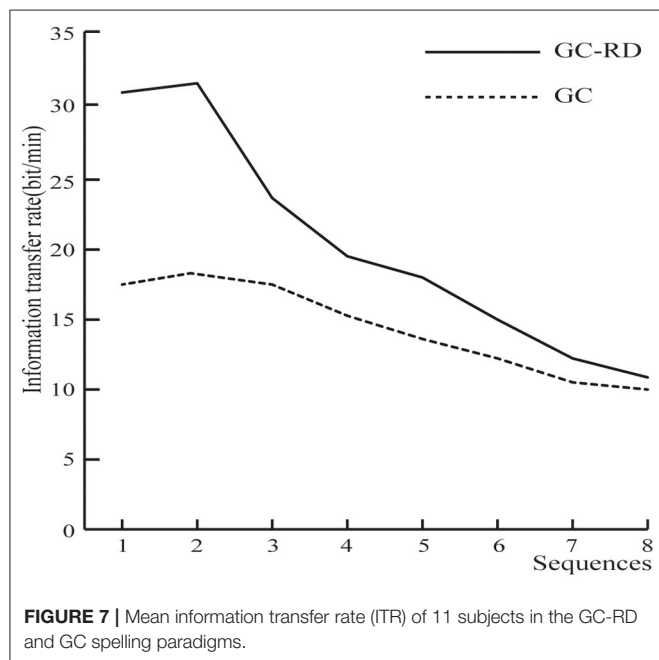
spelling paradigm, the classification accuracy of five subjects (subjects 1, 2, 5, 6, and 8) reached 100% with an average sequence of 3.2. Before statistically comparing classification accuracy and ITR, we verified that the data were normally distributed by a one-sample Kolmogorov–Smirnov test (Jin et al., 2014). A paired sample *t*-test was then conducted to compare the accuracy between GC and GC-RD spelling paradigms at each sequence. Results of the *t*-tests showed that the GC-RD spelling paradigm was significantly more accurate than the GC spelling paradigm at sequences 1–7 (**Table 1**).

The mean ITR of the GC-RD spelling paradigm was higher than that of the GC paradigm for all sequences (**Figure 7**). The paired sample *t*-test for the ITR at each sequence between GC-RD and GC spelling paradigms was also conducted. Results showed that the differences were significant for sequences 1–7 (**Table 2**).

TABLE 1 | Results of paired sample *t*-tests comparing accuracy between the GC-RD and GC spelling paradigm at each sequence time.

	Sequence							
	1**	2**	3**	4**	5*	6*	7*	8
GC	33.64 (± 3.99)	53.18 (± 6.00)	67.73 (± 5.89)	73.18 (± 6.88)	79.09 (± 6.10)	85 (± 4.57)	86.82 (± 4.17)	89.55 (± 4.07)
GC-RD	47.27 (± 5.74)	75 (± 5.18)	81.82 (± 5.10)	87.73 (± 3.59)	92.27 (± 2.17)	95.45 (± 1.84)	95.91 (± 1.63)	97.27 (± 0.79)

** $p < 0.01$, * $p < 0.05$.



DISCUSSION

Larger ERP amplitudes improve the performance of the P300 speller system. Our new GC-RD spelling paradigm is designed to enhance the attention of subjects on the target stimulus and to increase the visuospatial information. We compared the ERP amplitude, classification accuracy, and ITR between the GC-RD spelling paradigm and control paradigm (GC spelling paradigm).

A previous work has found that the P300 speller system's performance can be improved by enhancing the difference between target and nontarget trials (Jin et al., 2012). Therefore, we compared the waveforms ($ERP_{\text{Target}} - ERP_{\text{Nontarget}}$) elicited in the GC-RD and GC spelling paradigms (Figure 5) and found two significant differences. The first was between 300 and 480 ms at the parietal area (Figure 5A), which is thought to be the P3a subcomponent of P300 (Polich, 2007). The P3a waveform usually occurs when subjects react to novel or small probability stimuli and is found at the frontal-central-parietal areas between 200 and 500 ms (Daffner et al., 2003; Berti, 2016; Li et al., 2019). The target stimuli in both the GC-RD and GC spelling paradigms elicited clear P3a components at the

frontal-central-parietal areas, which is consistent with results of previous studies (Polich, 2007; Berti, 2016). The amplitude of P3a with a significant difference between GC-RD and GC spelling paradigms was found only at the parietal areas. Studies have suggested that the parietal area is activated when visual stimuli with spatial information are presented (Baumgartner et al., 2018) and when stimuli are located at the left and right sides of the screen (Wang et al., 2015), indicating that the parietal area is activated by visuospatial features. In a study of visuospatial information processing during attentional tasks, Abramov et al. (2017) found that target stimuli above or below the central fixation point elicited larger P300 amplitude at Pz (parietal area) than those without spatial information. At the same time, the analog ERP component was detected at Fz (frontal area) for stimuli with and without spatial information. This indicates that the increased P300 amplitude at Pz reflects the processing of visuospatial information about the target position during attentional tasks. In our GC-RD spelling paradigm, the red dot appeared randomly above or below the center of the green circle. This elicited a significantly increased P3a amplitude at parietal areas compared to the GC spelling paradigm. The increased P3a amplitude at the parietal area reflects brain processing of visuospatial information.

The second significant difference between GC and GC-RD was during 480–600 ms at the frontal-central-parietal areas (Figure 5B); this may be the P3b component, another subcomponent of P300. An early study showed that P3b appears in the frontal-central-parietal areas when attentional resources activate working memory, and the amplitude of P3b is influenced by the allocation of attentional resources to update working memory (Stevens, 1999), i.e., the P3b amplitude increases when cognitive demands are related to working memory (Li et al., 2019). Compared with the GC spelling paradigm, the positioning of the red dot in GC-RD imposed additional cognitive demands for the updating of working memory, which translated to significantly increased P3b amplitudes. Our findings are consistent with the study of Li et al. (2019), in which subjects were asked to pay attention not only to the number of target flashes but also to the color of the stimulus. Our GC-RD spelling paradigm deliberately added a red dot to the green circle to help subjects focus better on a small scope stimulus.

In addition, because the upper and lower positioning of the red dots in the green circle were random in the GC-RD paradigm, the probability of the target stimulus manifesting, decreased. Specifically, inclusion of the dots reduced the probability of the target stimulus manifesting from 2/13 (six rows or seven columns flashing) by 50%, to 1/13. Studies have consistently shown that

TABLE 2 | Paired sample *t*-test results of information transmission rate (ITR) between the GC-RD and GC spelling paradigms at each sequence time.

	Sequence							
	1**	2**	3**	4**	5*	6*	7*	8
GC	17.85 (±3.37)	18.44 (±3.15)	17.81 (±2.50)	15.36 (±2.21)	13.72 (±1.61)	12.65 (±1.09)	11.18 (±0.85)	10.35 (±0.77)
GC-RD	30.80 (±5.94)	31.12 (±3.51)	23.96 (±2.46)	19.86 (±1.39)	17.16 (±0.74)	15.19 (±0.52)	13.13 (±0.42)	11.74 (±0.20)

***p* < 0.01, **p* < 0.05.

the smaller the probability of the target stimulus appearing, the higher the level of the elicited P300 amplitude (Katayama and Polich, 1996). This is likely to be the reason that the GC-RD spelling paradigm elicited an increased P300 amplitude and improved the performance of the P300 speller system.

The ERP amplitude evoked by the GC-RD spelling paradigm was higher than that induced by the GC spelling paradigm. In addition the GC-RD spelling paradigm enhanced the difference between target and nontarget waveform and improved the classification accuracy (Jin et al., 2014). As expected, the average accuracies of the GC-RD spelling paradigm were higher than those of the GC spelling paradigm at each sequence (Figure 6). Moreover, there were significant differences in accuracy between the paradigms at all sequences (*p* < 0.05, Table 1) except sequence 8. Similarly, the ITR of the GC-RD spelling paradigm was significantly greater than that of the GC spelling paradigm at all sequences except sequence 8 (*p* < 0.05, Table 2). We also found that the improvements in ITR were even stronger at the first four sequences (*p* < 0.01), especially at sequence 2 (*p* < 0.0005). Thus, our results indicated that the GC-RD spelling paradigm significantly improved the performance of the P300 speller. Moreover, the results of accuracy and ITR further verify that the increased amplitude of waveforms (ERP_{Target} – ERP_{Nontarget}) can improve the performance of the P300 spelling system. The ITR is an important statistical metric for the performance of the P300 speller system (Zhang et al., 2012). As we know, the ITR depends on both classification accuracy and the time to output a character based on the ITR calculation formula. The time to output a character is determined by the number of averaged sequences. As the number of averaged sequences reduces, the signal-to-noise ratio inevitably decreases and results in a decrease in classification accuracy. Therefore, classification accuracy and the number of averaged sequences must be weighed for obtaining a higher ITR (Li et al., 2015).

CONCLUSION

This study investigated whether the new GC-RD spelling paradigm with small size and visuospatial information could

improve the performance of the P300 speller. The results demonstrated that the GC-RD spelling paradigm enhanced the amplitude of the P300 potential and improved the classification accuracy and ITR at most sequence numbers compared with the GC spelling paradigm.

DATA AVAILABILITY STATEMENT

The raw data supporting the conclusions of this article will be made available by the authors, without undue reservation.

ETHICS STATEMENT

The studies involving human participants were reviewed and approved by The Ethics Committee of Changchun University of Science and Technology. The patients/participants provided their written informed consent to participate in this study.

AUTHOR CONTRIBUTIONS

YW is responsible for experimental design. WZ is responsible for the implementation of the experiment. ZL is responsible for data analysis. QL is responsible for the overall idea of experimental design. All authors contributed to the article and approved the submitted version.

FUNDING

This work was financially supported by the National Natural Science Foundation of China (grant numbers 61806025 and 61773076) and the Jilin Scientific and Technological Development Program (grant numbers 20190302072GX, 20200802004GH, and 20190201192JC).

SUPPLEMENTARY MATERIAL

The Supplementary Material for this article can be found online at: <https://www.frontiersin.org/articles/10.3389/fninf.2020.589169/full#supplementary-material>

REFERENCES

- Abramov, D. M., Pontes, M., Pontes, A. T., Mourao-Junior, C. A., Vieira, J., Quero Cunha, C., et al. (2017). Visuospatial information processing load and the ratio between parietal cue and target P3 amplitudes in the Attentional Network Test. *Neurosci. Lett.* 647, 91–96. doi: 10.1016/j.neulet.2017.03.031
- Aya, R., Mihaly, B., Piotr, S., Felix, G., Abdul, S., and Ivan, V. (2018). Brain-computer interface spellers: a review. *Brain Sci.* 8, 57. doi: 10.3390/brainsci8040057
- Baumgartner, H. M., Grauly, C. J., Hillyard, S. A., and Pitts, M. A. (2018). Does spatial attention modulate the earliest component of the visual evoked potential? *Cogn. Neurosci.* 9, 4–19. doi: 10.1080/17588928.2017.1333490

- Bernat, E., Shevrin, H., and Snodgrass, M. (2001). Subliminal visual oddball stimuli evoke a P300 component. *Clin. Neurophysiol.* 112, 159–171. doi: 10.1016/S1388-2457(00)00445-4
- Berti, S. (2016). Switching attention within working memory is reflected in the P3a component of the human event-related brain potential. *Front. Hum. Neurosci.* 9, 701. doi: 10.3389/fnhum.2015.00701
- Daffner, K. R., Scinto, L. F. M., Weitzman, A. M., Faust, R., Rentz, D. M., Budson, A. E., et al. (2003). Frontal and parietal components of a cerebral network mediating voluntary attention to novel events. *J. Cogn. Neurosci.* 15, 294–313. doi: 10.1162/089892903321208213
- Eriksen, C. W., and Yeh, Y. Y. (1985). Allocation of attention in the visual field. *J. Exp. Psychol. Hum. Percept. Perform.* 11, 583–597. doi: 10.1037/0096-1523.11.5.583
- Farwell, L. A., and Donchin, E. (1988). Talking off the top of your head: toward a mental prosthesis utilizing event-related brain potentials. *Electroencephalogr. Clin. Neurophysiol.* 70, 510–523. doi: 10.1016/0013-4694(88)90149-6
- Hugdahl, K., and Nordby, H. (1994). Electrophysiological correlates to cued attentional shifts in the visual and auditory modalities. *Behav. Biol.* 62, 21–32. doi: 10.1016/S0163-1047(05)80055-X
- Jin, J., Allison, B. Z., Brunner, C., Wang, B., Wang, X., Zhang, J., et al. (2010). P300 Chinese input system based on Bayesian LDA. *Biomed. Eng.* 55, 5–18. doi: 10.1515/bmt.2010.003
- Jin, J., Allison, B. Z., Kaufmann, T., Kubler, A., Zhang, Y., Wang, X., et al. (2012). The changing face of P300 BCIs: a comparison of stimulus changes in a P300 BCI involving faces, emotion, and movement. *PLoS ONE* 7, e49688. doi: 10.1371/journal.pone.0049688
- Jin, J., Daly, I., Zhang, Y., Wang, X., and Cichocki, A. (2014). An optimized ERP brain-computer interface based on facial expression changes. *J. Neural Eng.* 11, 036004. doi: 10.1088/1741-2560/11/3/036004
- Jin, J., Sellers, E. W., Zhou, S., Zhang, Y., Wang, X., and Cichocki, A. (2015). A P300 brain-computer interface based on a modification of the mismatch negativity paradigm. *Int. J. Neural Syst.* 25, 1550011. doi: 10.1142/S0129065715500112
- Katayama, J., and Polich, J. (1996). P300, probability, and the three-tone paradigm. *Electroencephalogr. Clin. Neurophysiol.* 100, 555–562. doi: 10.1016/S0168-5597(96)95171-0
- Kaufmann, T., Schulz, S. M., Grunzinger, C., and Kubler, A. (2011). Flashing characters with famous faces improves ERP-based brain-computer interface performance. *J. Neural Eng.* 8, 056016. doi: 10.1088/1741-2560/8/5/056016
- Kubler, A., and Birbaumer, N. (2008). Brain-computer interfaces and communication in paralysis: extinction of goal directed thinking in completely paralysed patients? *Clin. Neurophysiol.* 119, 2658–2666. doi: 10.1016/j.clinph.2008.06.019
- Lakey, C. E., Berry, D. R., and Sellers, E. W. (2011). Manipulating attention via mindfulness induction improves P300-based brain-computer interface performance. *J. Neural Eng.* 8:025019. doi: 10.1088/1741-2560/8/2/025019
- Lei, X., Yang, P., and Yao, D. (2009). An empirical bayesian framework for brain-computer interfaces. *IEEE Trans. Neural Syst. Rehab. Eng.* 17, 521–529. doi: 10.1109/TNSRE.2009.2027705
- Li, Q., Liu, S., Li, J., and Bai, O. (2015). Use of a green familiar faces paradigm improves P300-speller brain-computer interface performance. *PLoS ONE* 10, e0130325. doi: 10.1371/journal.pone.0130325
- Li, Q., Lu, Z., Gao, N., and Yang, J. (2019). Optimizing the performance of the visual P300-speller through active mental tasks based on color distinction and modulation of task difficulty. *Front. Hum. Neurosci.* 13, 130. doi: 10.3389/fnhum.2019.00130
- Lu, Z., Li, Q., Gao, N., Yang, J., and Bai, O. (2019). A novel audiovisual P300-speller paradigm based on cross-modal spatial and semantic congruence. *Front. Neurosci.* 13, 1040. doi: 10.3389/fnins.2019.01040
- Mangun, G. R. (1995). Neural mechanisms of visual selective attention. *Psychophysiology* 32, 4–18. doi: 10.1111/j.1469-8986.1995.tb03400.x
- Philip, J. T., and George, S. T. (2020). Visual P300 mind-speller brain-computer interfaces: a walk through the recent developments with special focus on classification algorithms. *Clin. EEG Neurosci.* 51, 19–33. doi: 10.1177/1550059419842753
- Polich, J. (2007). Updating P300: an integrative theory of P3a and P3b. *Clin. Neurophysiol.* 118, 2128–2148. doi: 10.1016/j.clinph.2007.04.019
- Posner, M. I. (1980). Orienting of attention. *Q. J. Exp. Psychol.* 32, 3–25. doi: 10.1080/00335558008248231
- Reza, M. F., Ikoma, K., Ito, T., Ogawa, T., and Mano, Y. (2007). N200 latency and P300 amplitude in depressed mood post-traumatic brain injury patients. *Neuropsychol. Rehabil.* 17, 723–734. doi: 10.1080/09602010601082441
- Rincover, A., and Ducharme, J. M. (1987). Variables influencing stimulus overselectivity and “tunnel vision” in developmentally delayed children. *Am. J. Ment. Defic.* 91, 422–430.
- Sellers, E. W., and Donchin, E. (2006). A P300-based brain-computer interface: initial tests by ALS patients. *Clin. Neurophysiol.* 117, 538–548. doi: 10.1016/j.clinph.2005.06.027
- Stevens, C. F. (1999). Memory: from mind to molecules. *Nat. Med.* 5, 1343–1344. doi: 10.1038/70903
- Sutton, S., Braren, M., Zubin, J., and John, E. R. (1965). Evoked-potential correlates of stimulus uncertainty. *Science* 150, 1187–1188. doi: 10.1126/science.150.3700.1187
- Wang, F., He, Y., Pan, J., Xie, Q., Yu, R., Zhang, R., et al. (2015). A novel audiovisual brain-computer interface and its application in awareness detection. *Sci. Rep.* 5, 9962. doi: 10.1038/srep12592
- Wolpaw, J. R., Ramoser, H., McFarland, D. J., and Pfurtscheller, G. (1998). EEG-based communication: improved accuracy by response verification. *IEEE Trans. Rehab. Eng.* 6, 326–333. doi: 10.1109/86.712231
- Xia, T., Qi, Z., Shi, J., Zhang, M., and Luo, W. (2018). The early facilitative and late contextual specific effect of the color red on attentional processing. *Front. Hum. Neurosci.* 12, 224. doi: 10.3389/fnhum.2018.00224
- Xiao, X., Xu, M., Jin, J., Wang, Y., Jung, T., and Ming, D. (2019). Discriminative canonical pattern matching for single-trial classification of ERP components. *IEEE Trans. Biomed. Eng.* 67, 2266–2275. doi: 10.1109/TBME.2019.2958641
- Xu, M., Han, J., Wang, Y., Jung, T., and Ming, D. (2020). Implementing over 100 command codes for a high-speed hybrid brain-computer interface using concurrent P300 and SSVEP features. *IEEE Trans. Biomed. Eng.* 1, 1–10. doi: 10.1109/TBME.2020.2975614
- Xu, M., Xiao, X., Wang, Y., Qi, H., Jung, T., and Ming, D. (2018). A brain-computer interface based on miniature-event-related potentials induced by very small lateral visual stimuli. *IEEE Trans. Biomed. Eng.* 65, 1166–1175. doi: 10.1109/TBME.2018.2799661
- Zhang, Y., Zhao, Q., Jin, J., Wang, X., and Cichocki, A. (2012). A novel BCI based on ERP components sensitive to configural processing of human faces. *J. Neural Eng.* 9, 026018. doi: 10.1088/1741-2560/9/2/026018
- Zhu, J., Wang, X. Q., He, X., Hu, Y. Y., Li, F., Liu, M. F., et al. (2019). Affective and cognitive empathy in pre-teachers with strong or weak professional identity: an ERP Study. *Front. Hum. Neurosci.* 13, 175. doi: 10.3389/fnhum.2019.00175

Conflict of Interest: The authors declare that the research was conducted in the absence of any commercial or financial relationships that could be construed as a potential conflict of interest.

Copyright © 2020 Wu, Zhou, Lu and Li. This is an open-access article distributed under the terms of the Creative Commons Attribution License (CC BY). The use, distribution or reproduction in other forums is permitted, provided the original author(s) and the copyright owner(s) are credited and that the original publication in this journal is cited, in accordance with accepted academic practice. No use, distribution or reproduction is permitted which does not comply with these terms.



Development of a Non-invasive Deep Brain Stimulator With Precise Positioning and Real-Time Monitoring of Bioimpedance

Heng Wang¹, Zhongyan Shi², Weiqian Sun², Jianxu Zhang¹, Jing Wang³, Yue Shi⁴, Ruoshui Yang¹, Chunlin Li⁵, Duanduan Chen^{2*}, Jinglong Wu^{1,6*}, Guo Gongyao² and Yifei Xu²

¹ School of Mechatronic Engineering, Beijing Institute of Technology, Beijing, China, ² School of Life Science, Beijing Institute of Technology, Beijing, China, ³ Department of Health Management, Aerospace Center Hospital, Peking University Aerospace School of Clinical Medicine, Beijing, China, ⁴ Beijing Big-IQ Medical Equipment Co., Ltd., Beijing, China, ⁵ School of Biomedical Engineering, Capital Medical University, Beijing, China, ⁶ Graduate School of Interdisciplinary Science and Engineering in Health Systems, Okayama University, Okayama, Japan

OPEN ACCESS

Edited by:

Rong Chen,
University of Maryland, Baltimore,
United States

Reviewed by:

Richard Bayford,
Middlesex University, United Kingdom
Stavros I. Dimitriadis,
Cardiff University, United Kingdom

*Correspondence:

Duanduan Chen
duanduan@bit.edu.cn
Jinglong Wu
wujinglong5@gmail.com

Received: 19 June 2020

Accepted: 29 October 2020

Published: 08 December 2020

Citation:

Wang H, Shi Z, Sun W, Zhang J, Wang J, Shi Y, Yang R, Li C, Chen D, Wu J, Gongyao G and Xu Y (2020) Development of a Non-invasive Deep Brain Stimulator With Precise Positioning and Real-Time Monitoring of Bioimpedance. *Front. Neuroinform.* 14:574189. doi: 10.3389/fninf.2020.574189

Methods by which to achieve non-invasive deep brain stimulation via temporally interfering with electric fields have been proposed, but the precision of the positioning of the stimulation and the reliability and stability of the outputs require improvement. In this study, a temporally interfering electrical stimulator was developed based on a neuromodulation technique using the interference modulation waveform produced by several high-frequency electrical stimuli to treat neurodegenerative diseases. The device and auxiliary software constitute a non-invasive neuromodulation system. The technical problems related to the multichannel high-precision output of the device were solved by an analog phase accumulator and a special driving circuit to reduce crosstalk. The function of measuring bioimpedance in real time was integrated into the stimulator to improve effectiveness. Finite element simulation and phantom measurements were performed to find the functional relations among the target coordinates, current ratio, and electrode position in the simplified model. Then, an appropriate approach was proposed to find electrode configurations for desired target locations in a detailed and realistic mouse model. A mouse validation experiment was carried out under the guidance of a simulation, and the reliability and positioning accuracy of temporally interfering electric stimulators were verified. Stimulator improvement and precision positioning solutions promise opportunities for further studies of temporally interfering electrical stimulation.

Keywords: electrical stimulation, temporally interfering, finite element method, simulation, mouse

INTRODUCTION

Considering the challenges associated with an aging society, brain diseases have increasingly serious negative effects on human life (Cole and Franke, 2017). Continued investigation into therapies for brain diseases should be encouraged to expand indications and improve effectiveness (Buss et al., 2019). As a typical neurosurgical procedure, DBS has been used to cure abnormal neuronal firing patterns that result from certain diseases, such as Parkinson's disease, essential tremors, and dystonia (Flora et al., 2010; Miocinovic et al., 2013). However, careful wound care and personal hygiene are needed to protect DBS hardware and to avoid additional negative

impacts after the surgery (Umemura et al., 2003; Blomstedt and Hariz, 2006; Batra et al., 2016). Studies on non-invasive brain stimulation that does not require built-in hardware are accumulating rapidly. Transcranial direct current stimulation (tDCS) and transcranial alternating current stimulation (tACS) are common non-invasive tools that use weak electric currents to painlessly and non-invasively regulate human neural activity and are widely employed in many research areas (Ali et al., 2013; Schulz et al., 2013; Tavakoli and Kyongsik, 2017). Due to the characteristics of current transmission, these non-invasive electrical stimulation methods have a qualified stimulation effect on superficial brain areas, but it is difficult to reach deep targets accurately via these techniques.

In 2017, Cell magazine reported a temporally interfering electrical stimulation technology using multiple high-frequency alternating currents to recruit neural firing (Grossman et al., 2017). Compared with common non-invasive electrical stimulation, time-interfering electrical stimulation can directly reach deep brain regions without affecting shallow brain regions. However, as a new technology, the stimulator needs to be improved to help researchers make it more efficient and convenient to use for temporally interfering electrical stimulation. The stimulus effect is based on the envelope modulation of the electric field, and the envelope will appear seriously distorted or too small if one of the loads is too large. Therefore, for the stimulator, real-time measurements of biological impedance between electrodes and warnings of potential overloading are necessary. In addition, the positional accuracy of temporally interfering electrical stimulation is jointly determined by the electrode position and the current amplitude ratio. An existing study has described methods by which to move the position of the target of temporally interfering electrical stimulation, and a helpful rule for adjusting the location of the electrical stimulation target was proposed—the wider the electrode spacing is, the deeper the stimulation target depth (Grossman et al., 2017). However, an accurate positioning scheme for specific targets is lacking, and the qualitative rule cannot be directly used to calculate the location of the electrode. Several studies have used arrays of scalp electrodes, with each electrode optimized to target a desired location in the human brain (Huang and Parra, 2019). The electrode array optimization method may not be appropriate in a mouse model because of the small size of the mouse head and the fact that the electrodes cannot be shrunk indefinitely. The number of electrodes in the preset electrode array is not large enough.

In this study, a powerful temporally interfering stimulator was developed. In terms of accuracy, we did the following work. First, we solved the problem of crosstalk between channels through a circuit design and improved the accuracy of each circuit stimulation signal. Second, to avoid the waveform distortion and amplitude decrease caused by excessive impedance, a bioimpedance measurement module was designed. Due to these two developments, the stimulator has advantages in terms of precision. To form modulation envelope waves with accurate frequency characteristics through the interference of kHz differential frequency currents, the kHz-level sinusoidal electrical stimulation signal of the electrical stimulator must

have ultrahigh parameter control accuracy. The device that we designed adopts graphical user interface control and integrates a bioimpedance measurement function. The amplitude, frequency, sinusoidal phase, and transition time can be precisely controlled to ensure the stability and controllability of the complex intracranial electric field interference. Based on the idea that biological impedance varies with the excitation frequency (Stroud et al., 1995), the appropriate carrier frequency can be selected to achieve a small current loss.

We conducted a simulation analysis and a phantom measurement proof to study the functional relationships among the target location, the electrode location, and the current ratio in temporally interfering stimulation. The functional relationship between the electrode spacing and the stimulus depth was fitted to locate the longitudinal coordinate of the target. In addition, the functional relationship between the amplitude ratio of the currents and the transverse coordinate of the target was fitted to assist in locating the transverse target coordinate. By solving these functions, the electrode arrangement can be directly determined according to the coordinates of the target. Then, we formed a set of feasible schemes by which to achieve accurate positioning in a simplified and realistic mouse model. Based on the positioning functions and the mouse model simulation, the auxiliary software was designed to help target the desired location in the mouse brain. In this way, it is convenient to use the temporally interfering stimulation system in mouse experiments for those who are not interested in modeling and simulation. Finally, a small region of the mouse motor cortex associated with shoulder movement was successfully located and activated in the mouse experiment. The experiments demonstrated that the electrical stimulator could effectively modulate mouse neurons by enveloping the electric field, and the localization accuracy was as expected.

MATERIALS AND METHODS

The experimental protocol was approved by the ethics committee of Capital Medical University and was in accordance with the Declaration of Helsinki.

Implementation of the Temporally Interfering Stimulation System

Figure 1 shows the conceptual block diagram and photos of the temporally interfering neuromodulation system, including the auxiliary software, electrical stimulator, and experimental platform. The auxiliary software can control the stimulus parameters, record experimental data, and assist in target navigation (**Figure 1A**). The stimulation parameters, such as the frequency, amplitude, and offset, can also be set on the touch panel of the stimulator. There are two main functions of the stimulator (**Figure 1B**). One is to provide multichannel, high-precision, and high-frequency output. The other is to measure the bioimpedance synchronously between the stimulation electrodes. When the system works, two sets of high-frequency electrical stimuli are applied to mice via the electrodes, and feedback signals are concurrently collected for impedance measurement

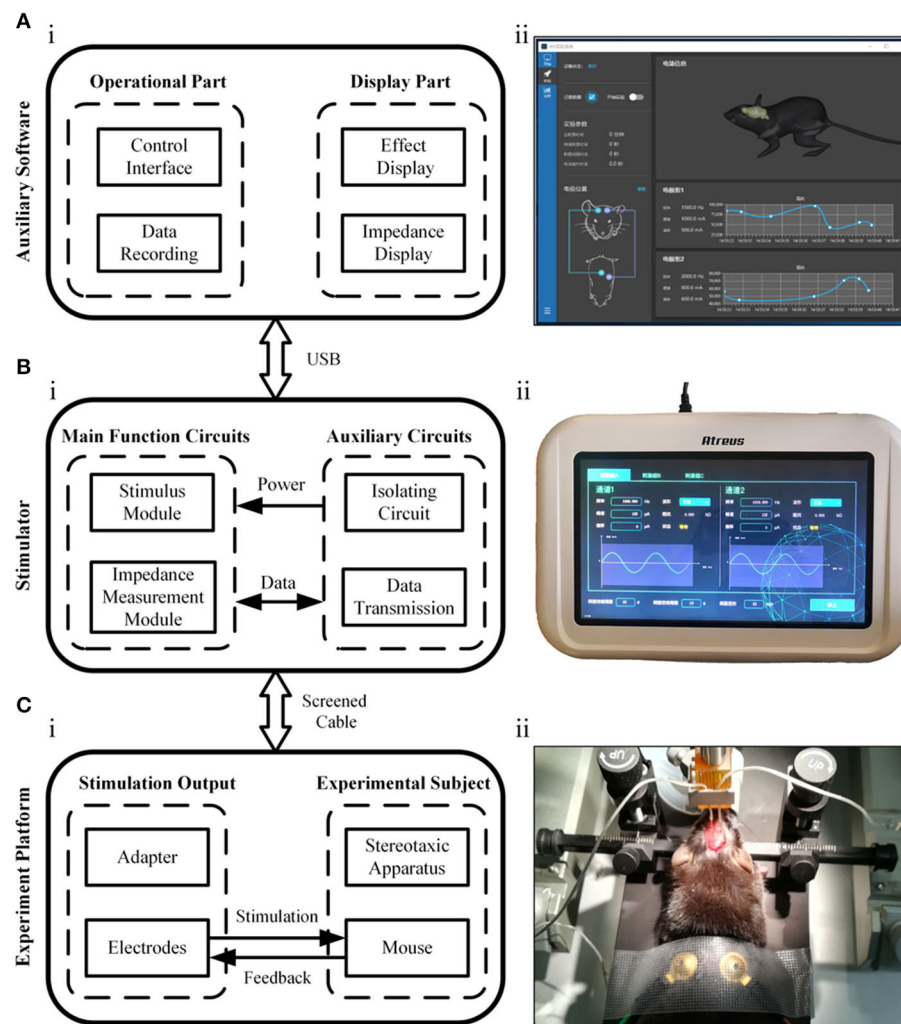


FIGURE 1 | Illustration of the neuromodulation system. **(A)** The auxiliary software. **(B)** The electrical stimulator. **(C)** The experimental platform.

(Figure 1C). The electrical stimulator has a modular design, with extra functionality loaded on demand (Figure 2).

Implementation of High-Precision Output

The temporally interfering electrical stimulation scheme in this study is based on two high-frequency, accurate alternating currents. In this study, an analog phase accumulator was used to achieve a high-precision sine wave. Since STM32 MCU has no special phase accumulator digital-to-analog converter (DAC), the principle of the phase accumulator can be simulated by software. This process was performed by a system that contained the following main components: a numerically controlled oscillator (NCO), a frequency and phase modulator, SIN ROM, a digital-to-analog converter, and a regulator. The DAC was configured for single-ended operation. The simulation process was achieved by continuously updating the output data to the direct memory access (DMA). After optimization, the test could be performed in 1,000 ns for each output but in 522 ns for each data-generation

instance. Up to 52.2% of the CPU was utilized. When using two channels, the output frequency could be reduced to 250 kHz. To prevent the user from reducing the frequency too much, all subordinate machines were cross-connected; that is, the output of the original 1–2 channels was provided by subordinate machine 1, whose output was jointly provided by subordinate machines 1 and 4 after using this algorithm.

Implementation of Bioimpedance Measurements

The biologically complex impedance measurement technique used in this study collects the potential signal produced by the corresponding frequency stimulation. The measured bioimpedance was the sum of the tissue impedance and the electrode contact impedance. The process used to implement the bioimpedance measurement function was as follows. First, the electrical signal output module of the electric stimulator was programmed to provide a weak sinusoidal signal to the electrode group attached to the subject, and the feedback

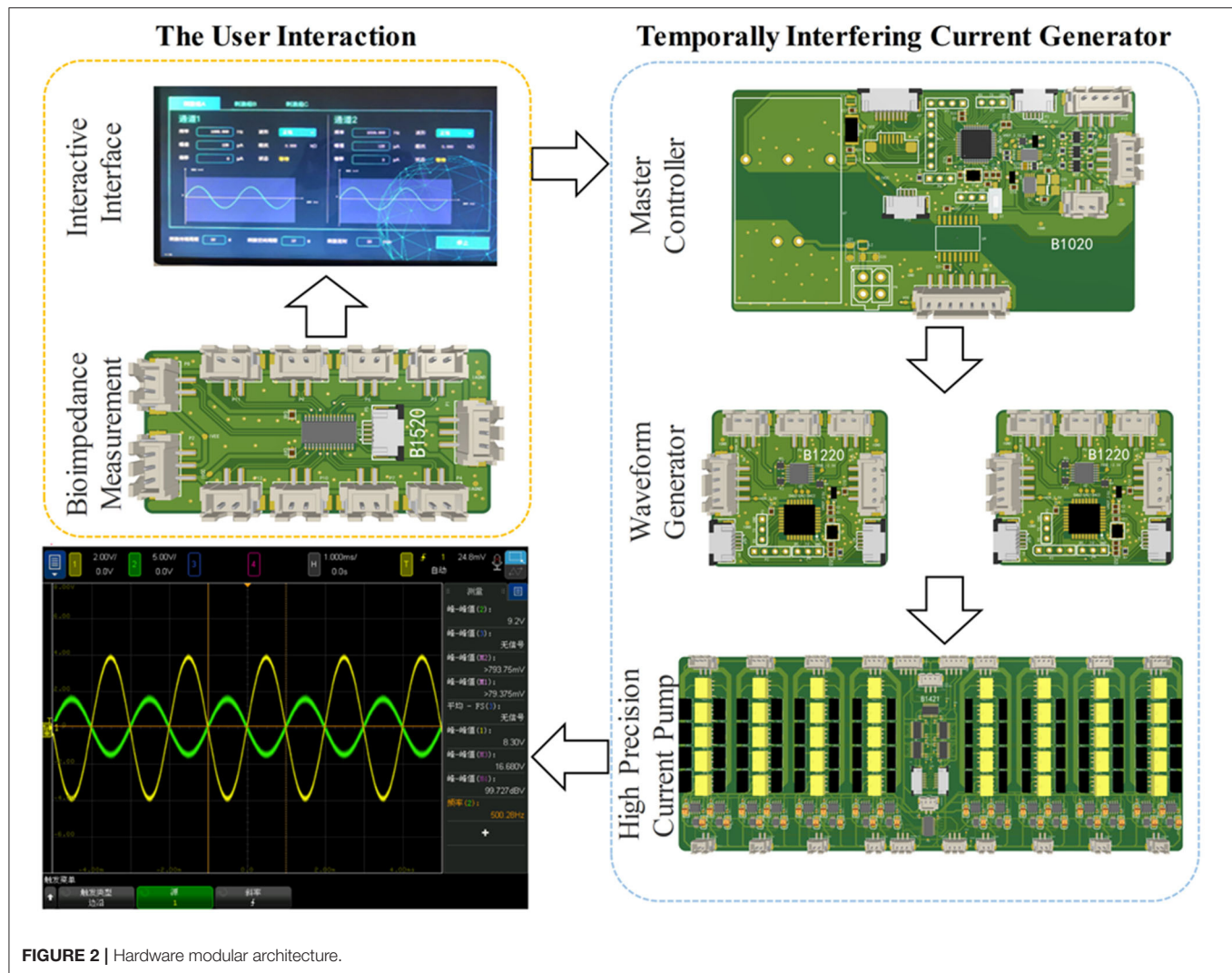


FIGURE 2 | Hardware modular architecture.

signal was collected at the same time. Then, discrete Fourier transform arithmetic was used to calculate the real and imaginary parts of the signal (Yang et al., 2017). The real part R and imaginary part I can be converted into amplitude and phase information by Equations (1) and (2). Using this method, the device can measure the impedance of $100\ \Omega$ – $10\ \text{M}\ \Omega$ values and achieve a system accuracy as high as 0.5% (Analog Devices Inc., 2005–2011). The function of bioimpedance measurement helps ensure the accuracy of the waveform in the electrical stimulation experiment, thus ensuring the effect of the electrical stimulation. The circuit design details are shown in the **Supplementary Figure 2**.

$$\text{Magnitude} = \sqrt{R^2 + I^2} \quad (1)$$

$$\text{Phase} = \tan^{-1}(I/R) \quad (2)$$

Inhibition of Crosstalk Between Channels

The output circuit of the temporally interfering electrical stimulator consists of three parts: an amplifying circuit, a reverse dual-current pump, and a limiter circuit. In the temporal

interfering electrical stimulation, the current flows not only from the output electrode to the reference electrode but also from the electrodes of the other channels, which results in serious current crosstalk between channels. To maintain the independence of the channel outputs, anti-phase current drive technology was used as shown in the **Supplementary Figure 3**. Each channel contains two current sources that remain in the opposite phase. In this way, the current between the channels can be balanced to eliminate crosstalk.

Electrical Stimulator Test

First, a resin phantom was made to test the output performance of the electrical stimulator. The phantom was a 50 mm-diameter cylindrical container filled with a solution with a conductivity set to $\sim 0.333\ \text{S m}^{-1}$, and the bottom was covered with holes as fixing points for electrodes. The crosstalk between channels was obtained by analyzing the potential data from the stimulating electrodes (**Figures 4Ai, Bi**). Second, the load capacity of the electrical stimulator was tested with resistors. We selected 0.5, 1, 1.5, and 2 mA as the current output amplitudes and used

gradually increasing resistance as the load. In this process, an ammeter was used to measure the real current output. The critical load values were also recorded. To test the bioimpedance measurement function of the device, we performed three types of load tests—resistance, resistance–capacitance, and mouse—and measured the impedance changes under different excitation frequencies (Figures 5A–C). The first two loads were standard models, and the impedance changes followed physical characteristics that made it easy to determine whether the device measurements were accurate. Third, by comparing the simulated distribution of the electric field envelope amplitude with the measured distribution, the reliability of the temporally interfering electrical stimulator could be confirmed. To obtain the simulated envelope amplitude distribution map, a two-dimensional 50 mm-diameter circular model containing 1,222 grids and 652 nodes was established (Figure 6Ai). The model has been validated for grid independence. The material of the model was set to be uniform and isotropic, and the conductivity was set to 0.333 S m^{-1} , which was consistent with the phantom. Two pairs of electrodes were symmetrically placed on the periphery of the model. A sinusoidal waveform current (0.5 mA, 1 kHz) was applied to the electrodes on the left. Another current (0.5 mA, 1.01 kHz) was applied on the right. The measured electric field strength was calculated by Equation (3) to obtain the electric field envelope amplitude.

$$\left| \vec{E}_{AM}(\vec{n}, \vec{r}) \right| = \left| \left(\vec{E}_1(\vec{r}) + \vec{E}_2(\vec{r}) \right) \cdot \vec{n} \right| - \left| \left(\vec{E}_1(\vec{r}) - \vec{E}_2(\vec{r}) \right) \cdot \vec{n} \right| \quad (3)$$

E_1 and E_2 represent the fields generated by the first and the second electrode pairs, respectively; n is a unit vector along the direction studied; and r represents the location. Then, we drew the simulated distribution map of the envelope amplitude of the electric field intensity.

To obtain the measured envelope amplitude distribution map of electric field intensity, a phantom and an oscilloscope were used (Figure 6B), an alternating current (0.5 mA, 1 kHz) was applied to the left two electrodes. Another current (0.5 mA, 1.01 kHz) was applied on the right. The potential difference ΔV of every two adjacent positions was measured by an oscilloscope, and the electric field intensity E was calculated by equation $E(t) = V(t)/S$, where S is the distance between the two electrodes inserted at the tested positions. We used the Hilbert transform to process the data of the electric field intensity along the X and Y directions and calculated the envelope amplitude. Then, the measured distribution map of the envelope amplitude could be drawn.

Accurate Control of the Electrical Stimulation Target

A study of electrical stimulation simulation showed that CSF had a shunt effect on the stimulating current, and the higher the conductivity of CSF, the more obvious the shunt effect was. However, there was no gross change in the current flow patterns through the brain (Jiang et al., 2020). Therefore, even with CSF shunting, electrical stimulation could still reach the target in

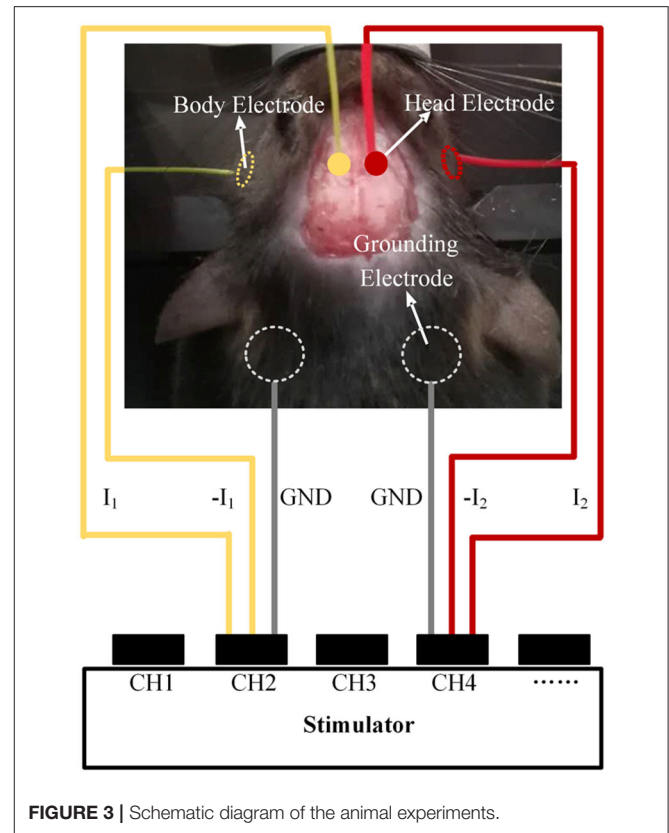


FIGURE 3 | Schematic diagram of the animal experiments.

the brain and showed little effect on the intensity distribution of stimulation in the brain regions. Considering that the CSF layer in mice is too thin to be modeled, we constructed a layered finite element model containing 56,000 grids, including the scalp, skull, and brain, based on the MRI and CT data of the mouse (Figure 8A). The material of each layer was set to be uniform and isotropic, and the conductivity was set to 0.333, 0.0083, and 0.333 S m^{-1} , corresponding to the scalp, skull, and brain, respectively (Grossman et al., 2017). To reduce the computational load, a layered elliptic cylinder model was constructed according to the shape of the coronal plane of the mouse head (Figure 7). The major axis of the ellipse was $2a$, the minor axis was $2b$, and the thickness of the first layer was 0.44 mm, as in the mouse skull. Afterward, the layered elliptic cylinder model was further simplified into a layered circular cylinder model by keeping the curvature radius unchanged, with the radius $R = a^{2/b}$. Taking the radial electric field stimulation as the most important part, we analyzed the distribution diagram of the electric field enveloping intensity in this direction. We conducted multiple sets of simulations to find the relationship between the target depth and the electrode distance of the electrical stimulation in an ideal layered circular cylinder model. In addition, the transverse coordinates of the target were expected to be correlated with the electrode position. The results of the simplified model were applied to the individual mouse model to verify the validity of the rule. The simulation results were used in the software of a temporally interfering electrical stimulation system, with which

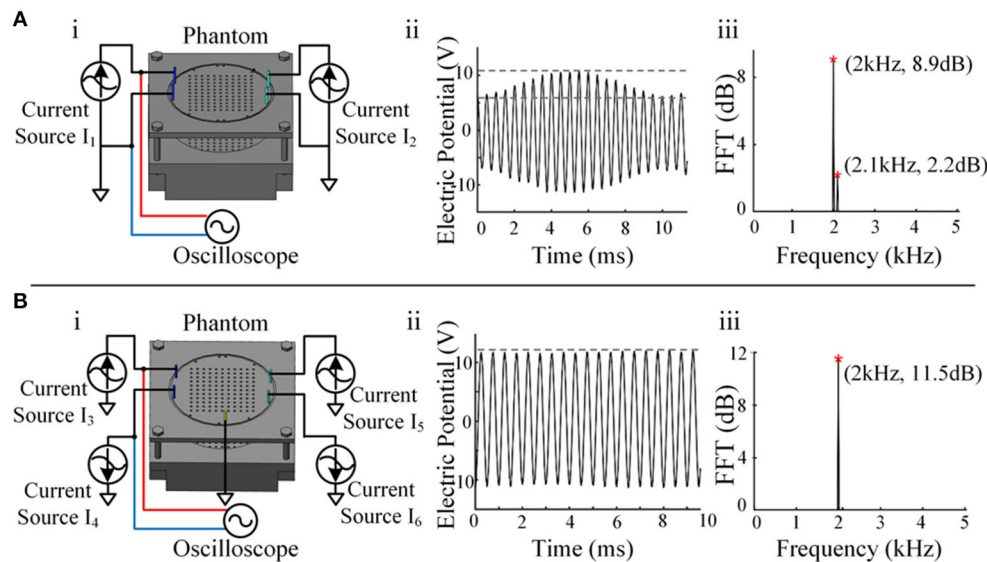


FIGURE 4 | Crosstalk testing between channels. **(A)** i, Schematic diagram of a single-current source drive. ii, The waveform between the two electrodes of a single-current source output channel. iii, Spectrum analysis result of a single-current source output channel. **(B)** i, Schematic diagram of the reverse dual-current source drive. ii, The waveform between the two electrodes of the dual-current source output channel. iii, Spectrum analysis result of the dual-current source output channel.

we predicted and adjusted the electrode positions to accurately stimulate the target.

Mouse Experiment

Ten male C57BL/6 mice were subjected to electrical stimulation in the motor cortex to activate neurons to cause evoked movements. The motor cortex area related to the shoulder is $\sim 1 \times 1$ mm, and we selected it as a target of temporally interfering electrical stimulation (Tennant et al., 2011). The target position relative to the bregma was AP -0.5 mm and ML 0.75 mm. Overall swinging of the mouse front paw should be observed as the target phenomenon. To prepare for the experiment, the mice were anesthetized with isoflurane, and surgery was performed to expose the skull and bregma. In addition, the cheeks of the mice were shaved. The electrical stimulation experiment was performed immediately after preparation, and the mice were maintained under continuous anesthesia with 1–1.5% (vol/vol) isoflurane in oxygen. Two 1 mm-diameter head electrodes with conductive paste were attached to the surface of the skull. Two 2 mm-diameter body electrodes with conductive gel were attached to the cheek of the mouse, spaced ~ 1 cm apart. Two 5 mm-diameter grounding electrodes were placed on the shaved chest, spaced ~ 0.8 cm apart. The electrode configurations were determined through simulation in the mouse model. The two head electrodes were set mediolaterally at -0.55 and 2.05 mm and anteroposteriorly at -0.5 mm relative to the bregma. Each of the two kHz alternating currents were applied to the mouse simultaneously through the head electrode and the body electrode connected to the electrical stimulator (Figure 3).

First, we performed a stimulation experiment with alternating currents of I₁ and I₂ (1 kHz $50 \mu\text{A}$, 1.002 kHz $50 \mu\text{A}$). If a

2 Hz overall swing of the contralateral forepaw was not observed, the sum of the current amplitudes I₁ + I₂ was increased by a gradient of $50 \mu\text{A}$. In the process, the positioning of the target could also be finetuned by adjusting the proportion between the two currents. Then, we recorded the lowest I₁ + I₂ that evoked contralateral forepaw movement. Movement of the ipsilateral forepaw during stimulation was also recorded. Finally, we changed the frequency of I₂ to 1.005 kHz and 1 kHz and recorded the experimental phenomena.

RESULTS

Performance Test of the Electrical Stimulator

Implementation of High-Precision Output

Four electrodes were applied in the phantom (Figure 4Ai), and an electrical stimulator channel was used to output 2 kHz on the left and 2.1 kHz on the right via another channel. The waveform shows the interference state of two sine waves between the two electrodes (Figure 4Aii). After spectral analysis, the two components of 2 and 2.1 kHz could be clearly observed, indicating that there was mutual interference between the two channels (Figure 4Aiii).

The waveform between the two electrodes presented a relatively standard sine wave (Figure 4Bii), and only the composition of 2 kHz was seen after spectral analysis, indicating that the crosstalk between the two channels was reduced significantly (Figure 4Biii). In this way, channel-to-channel isolation for high-quality current output was achieved. A single-channel current source drive can remain stable when stimulated by a single channel, but serious crosstalk occurs

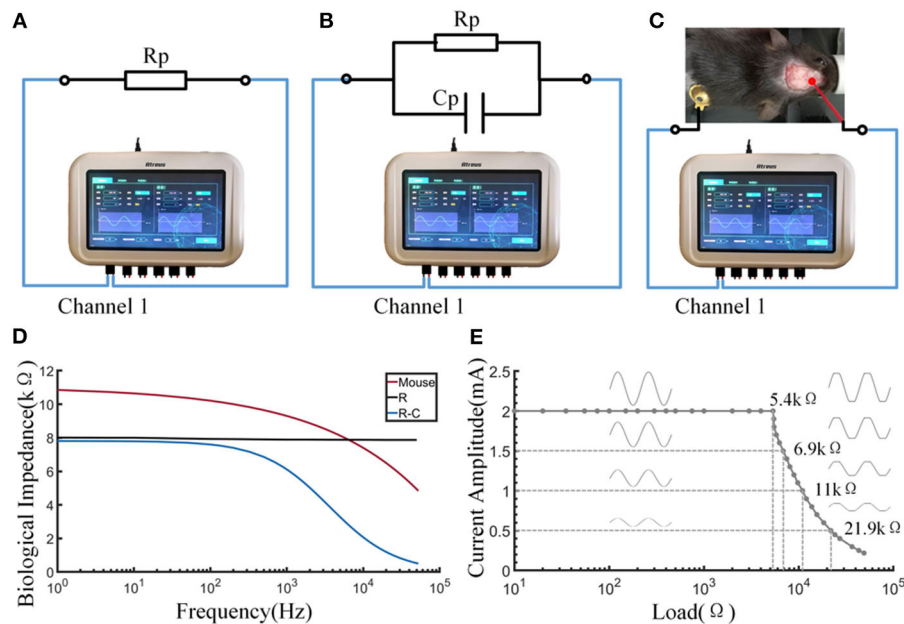


FIGURE 5 | Output and impedance measurement performance of the stimulator. **(A)** Schematic diagram of measuring the resistance by the stimulator. **(B)** Schematic diagram of measuring the resistance-capacitance by the stimulator. **(C)** Schematic diagram of measuring the bioimpedance of a mouse by the stimulator. **(D)** The curve of impedance by excitation frequency. **(E)** The load curve of the stimulator.

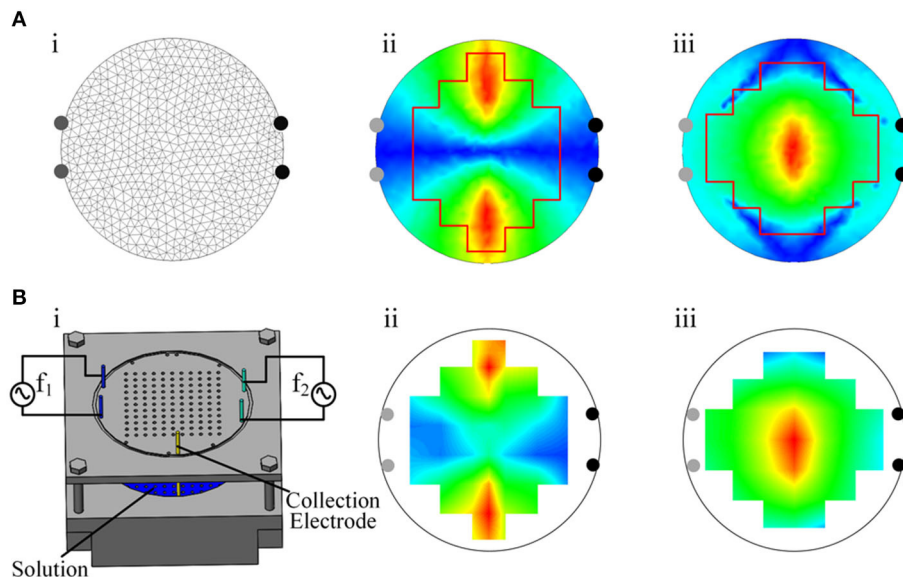


FIGURE 6 | Measured and simulated distribution of the envelope amplitude. **(A)** i, Two-dimensional finite element model. ii, Simulated distribution of the envelope amplitude of the electric field intensity in the X-axis direction. iii, Simulated distribution of the envelope amplitude of the electric field intensity in the Y-axis direction. **(B)** i, Phantom. ii, Measured distribution of the envelope amplitude of the electric field intensity in the X-axis direction. iii, Measured distribution of the envelope amplitude of the electric field intensity in the Y-axis direction.

when it is stimulated by dual channels simultaneously, as temporally interfering electrical stimulation occurs. Reverse dual-current pump drive technology successfully solved the crosstalk problem.

Output Performance Testing

The output waveform of the electric stimulator produced accurate signals when the load did not exceed the range (Figure 5E). The electrical stimulator could provide a standard

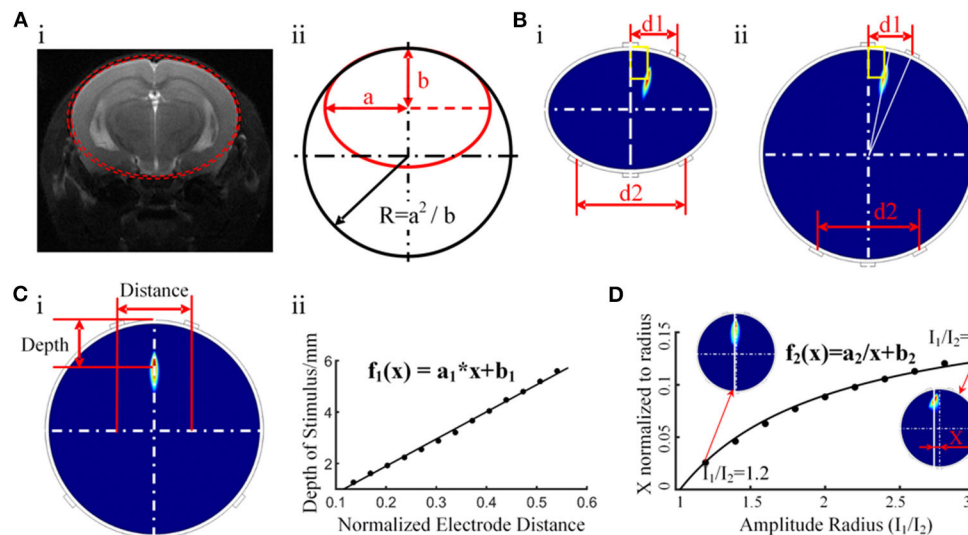


FIGURE 7 | Initial target positioning via a simplified cylindrical model. **(A)** i, The ellipse model constructed with MRI data. ii, Further simplified circular model. **(B)** i, Distribution of the electric field envelope amplitude in the elliptic cylinder model. ii, Distribution of the electric field envelope amplitude in the circular cylinder model. **(C)** Functional relationship between the depth of the temporally interfering stimulation target and the distance between the head electrodes. **(D)** Relationship between the amplitude ratio (I_1/I_2) and the peak envelope amplitude position.

sinusoidal signal of 2 mA amplitude within the load range of 0–5.4 k Ω . Waveform distortion occurred if the load was exceeded, as shown by a series of tests with various resistances. The load capacity decreased as the set current increased. In terms of the biological impedance measurement function of the device, three types of impedance—resistance, resistance-capacitance, and mouse body—were tested (**Figures 5A–C**). Electrodes were placed on the skull and body of the mice, which was consistent with the electrical stimulation. The impedance of 8 k Ω resistance did not change with the excitation frequency, and the impedance of the resistor-capacitor load decreased with increasing excitation frequency and closely matched the result of the calculation formula $Z = R/(1+j \times R \times \omega \times C)$. This result indicates that the biological impedance measurement function of the equipment is qualified. Impedance measurements in mice showed that impedance values decreased as the frequency increased, somewhat similar to the resistance-capacitance model (**Figure 5D**).

Comparison of Simulation Calculations and Stimulation Measurements

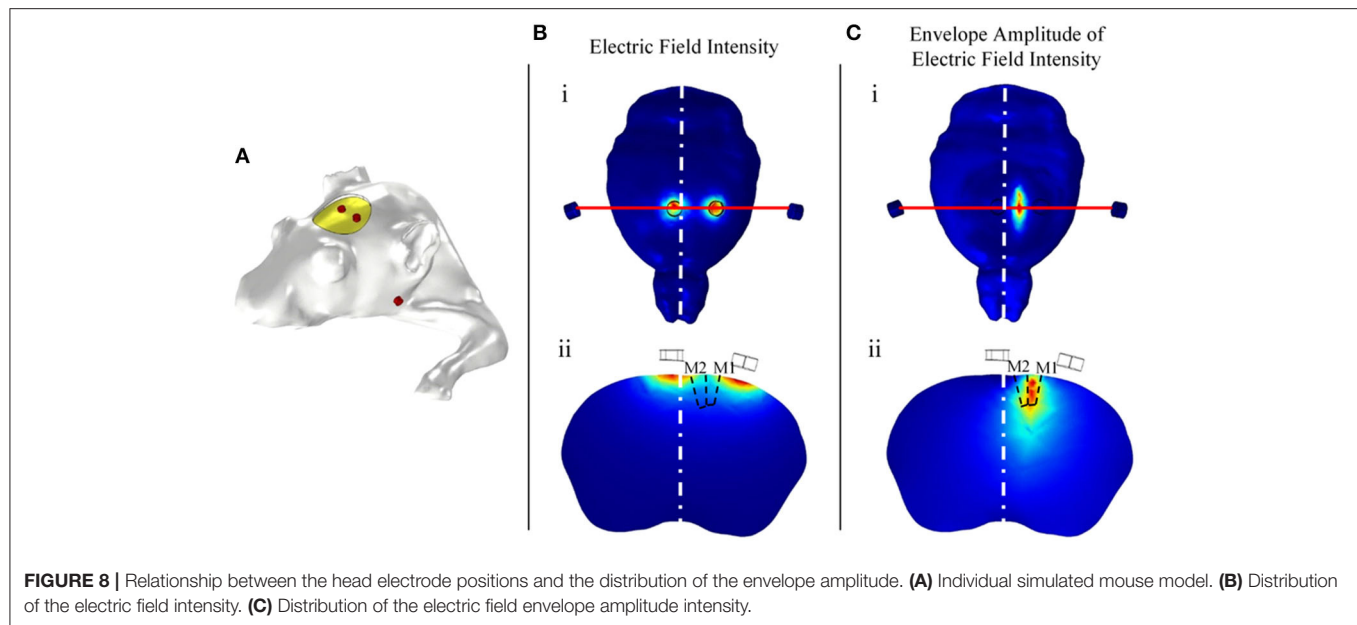
In this study, we simulated the envelope amplitude on a 2-dimensional circular model and compared the distribution map with the phantom-measured result. The simulated and measured results were based on the model and the phantom (**Figures 6Ai,Bi**). The X-axis direction and the Y-axis direction were chosen as the focus directions of the electric field intensity. Upon comparing the measured distribution map of the envelope amplitude of the electric field (**Figures 6Aii,iii**) with the simulated one (**Figures 6Bii,iii**), similar distributions and the same legend were found. The unification of the two types of envelope amplitude distributions demonstrated

the accuracy of the electrical stimulator output. This result confirmed the reliability of the electrical stimulator from a comprehensive perspective.

Mouse Experiment

Simulation Prediction of Electrode Positions

The motor cortex target position of the mouse experiment relative to the bregma was AP –0.5 mm and ML 0.75 mm, and the depth was 0.44 ± 0.8 mm (the thickness of the mouse skull was 0.44 mm, and 0.8 mm corresponded to the mid-layer to deep-layer V) (Tennant et al., 2011; Lapchak et al., 2015). We simplified the coronal plane of mice into a two-layer elliptic model and then further simplified it into a circular model by keeping the maximum curvature radius unchanged and radius $R = a^2/b$ (**Figure 7A**). The major axis of the ellipse was $2a$, the minor axis was $2b$, and the radius of the circular model was R . According to the MRI images of the mouse brain, we measured the coronal section at AP 0.5 mm and determined that $a = 4.1$ mm, $b = 3.6$ mm, and $R = 4.7$ mm. The thickness of the first layer was 0.44 mm, which was the same as that of the mouse skull, and the conductivity was 0.0083 S m^{-1} . The second layer represented the brain, with a conductivity of 0.333 S m^{-1} . The simulated targets of the elliptic and circular models were the same as the same electrode position and current parameters (**Figure 7B**). In addition, when two current amplitudes are the same, the radial electric field envelope distribution will be in the middle of the two nearest electrodes. In the circular model, there is a linear relationship between the depth of the target of the electrical stimulation and the distance between two relatively close electrodes. The specific functional relationship was established (**Figure 7C**), with $a_1 = 0.6343$ and $b_1 = -0.0773$. According to the functional relationship, the electrode



distance should be 2.6 mm to stimulate a target with a depth of 1.24 mm. Therefore, the two head electrodes should be set mediolaterally at -0.55 mm and anteroposteriorly at -0.5 mm and mediolaterally at 2.05 mm and anteroposteriorly at -0.5 mm relative to the bregma.

In contrast to ordinary electrical stimulation, in which the stimulation target can only be changed by adjusting the electrode position, temporally interfering electrical stimulation can conveniently adjust the coordinates of the stimulation area by changing the amplitude ratio between the two currents. A cylindrical simulation model was built to study the effect of the current amplitude ratio on the location of the peak envelope amplitude area. Upon keeping the electrode position unchanged and adjusting the ratio of the current amplitude, the peak stimulation area moved along the X-axis and maintained a stable position along the Y-axis. Through the function-fitting analysis of the ratio of the current amplitude and peak area position, a function with good coincidence was found (**Figure 7D**), with $a_2 = -0.1906$ and $b_2 = 0.1853$. Based on this finding, adjusting the current ratio is proposed to control the lateral location of the peak stimulation region. Together with the rule indicating that the longitudinal depth position is controlled by adjusting the spacing of the head electrodes, the function can make target positioning more convenient.

The above simulation results regarding electrode positions in the simplified model require simulation verification in an individualized mouse model. The individualized mouse model uses the mouse bregma as the coordinate origin. According to the simulation results of the simplified model, 1 mm diameter electrodes were placed at positions $(2.05, 0, -0.5)$ and $(-0.55, 0, 0.5)$. Two body electrodes were placed symmetrically on the cheeks of the mice. The simulation results show that the radial electric field envelope amplitude was the largest in the section

in which the electrode was placed (**Figures 8B,C**). The electric field of the electric stimulation under the head electrode was the largest, but the maximum amplitude of the electric field envelope as an effective stimulation occurred in the middle between the head electrodes. The simulation results show that the coordinates of the region with the largest envelope amplitude were $(0.71, -1.12, -0.57)$, with a deviation of 0.15 mm from the target point $(0.75, -1.25, 0.5)$.

Mouse Stimulation Experiment

Electrodes were placed according to the simulation result to stimulate the target in a mouse stimulation experiment. I1 (1 kHz) and I2 (1.002 kHz) were supplied by the stimulator. The experimental phenomena and electrical stimulation parameters are shown in **Table 1**. The result shows that every mouse experienced evoked movements in the forepaw on the contralateral side, and the frequency of the periodic movement was equal to the frequency difference between the two channels. The mouse forepaw moved only as a whole, and smaller joints such as the wrist or elbow did not move. This finding suggests that the electrical stimulator activated mouse neurons and successfully targeted the 1×1 mm motor cortex related to shoulder movement. In addition, I1 (1 kHz) and I2 (1.005 kHz) were also used to stimulate the mouse, and higher-frequency evoked movements were observed. However, I1 (1 kHz) and I2 (1 kHz) caused no experimental phenomena.

DISCUSSION

In this study, we developed a multichannel temporally interfering electrical stimulation system with a target positioning function. The real-time bioimpedance measurement function of the stimulator ensures that the actual stimulation is accurate and

TABLE 1 | Experimental data of mice.

No.	Current amplitude I1/I2 (μ A)	Whether contralateral forepaw shook	Whether ipsilateral forepaw shook
1	200/150	YES	NO
2	200/200	YES	NO
3	150/150	YES	NO
4	150/150	YES	NO
5	200/150	YES	NO
6	150/150	YES	NO
7	150/150	YES	NO
8	200/200	YES	NO
9	150/200	YES	NO
10	200/200	YES	NO

as expected. In terms of the accurate target positioning, we constructed individualized mouse models, performed finite element analysis of the electric field, and successfully simplified the simulation using cylinder models of layered ellipses and layered circles. We found the functional relationship between the stimulus depth and the electrode spacing, as well as the relationship between the target abscissa and amplitude ratio. These findings can help users achieve target positioning in mice without the heavy work of modeling and simulation. The mouse experiment showed that the stimulation system could indeed activate mouse neurons, and the accuracy of target localization was satisfactory.

In most studies of tACS, 10–40 Hz and 0.4–1 mA currents are used (Antal et al., 2008; Zaehle et al., 2010; Paulus, 2011). In addition, 140 Hz tACS on the primary motor cortex has been shown to result in nonlinear excitatory modulation of cortical tissue (Moliadze et al., 2012). All these studies used a one-channel electrical stimulator (Version DC-Stimulator-Plus, NeuroConn) to provide stimulation with adjustable frequencies up to 250 Hz. In addition, tRNS can also be considered a type of tACS, with frequencies varying from 0.1 to 640 Hz (Terney et al., 2008). The sampling rate of the electrical stimulator (Version Eldith DC-Stimulator-Plus, NeuroConn) used in this tRNS study was 1,280 samples/s, with frequencies adjustable up to half of the sampling rate, i.e., 640 Hz. These stimulators can only provide low-frequency signals. Later studies found that stimulation at 2 and 5 kHz produced lasting changes in the motor cortical excitability, which was attributed to the modulation of neuronal membrane activity (Herrmann et al., 2013). The kHz stimulation was applied over the M1 using a DS5 isolated bipolar constant current stimulator (Digitimer, Welwyn Garden City) connected via a cable to the input of a waveform generator (Peak Tech, Ahrensburg) (Chaieb et al., 2011). These existing devices cannot provide temporally interfering stimulation due to the weaknesses of the frequency range, channel number, and resolution, etc. Since the real modulating effect of time-interfering electrical stimulation on neurons is the modulating wave of two different kHz sinusoidal signals, this modulation process should not take place between the circuits of the equipment. In this work, high-quality current output was achieved

using a reverse dual-current pump to restrain the crosstalk between channels.

The bioimpedance between electrodes during temporally interfering stimulation affects the actual distribution of the amplitude of the electrical stimulation. Theoretically, the electrical stimulation provided by the electric stimulator is a constant current source. However, due to the limited driving voltage, the biological impedance of each electric stimulation must be less than the limit load to ensure the signal stability of the constant current source, which is a feature of any electrical stimulation device. If the biological impedance between the two electrodes in one circuit exceeds the load limit, the actual current amplitude will be smaller than the preset current, and the target of the differential frequency stimulation will also be shifted toward this circuit current, as shown in the **Supplementary Figure 3**. In addition, if the bioimpedance is increased significantly during the electrical stimulation, this indicates that part of the electrode has bad contact, which will also affect the accuracy of the target location of the electrical stimulation, as shown in the **Supplementary Figure 4**. The bioimpedance measurement function can detect this condition early in the experiment and monitor the changes in impedance during the process of electrical stimulation in real time to ensure the effect of electrical stimulation. In the mouse experiment, we observed that the stimulation effect was better when the bioimpedance of each channel was small and not significantly different. In addition, bioimpedance decreased with an increase in the stimulation frequency in the common case (Rodriguez et al., 2016), indicating that the method of using a high-frequency current to modulate a low-frequency stimulation signal may be conducive to penetrating the barriers of the scalp, skull, and CSF.

In research on the mouse brain, the usual anchor point of the mouse head is a vertex on the skull called bregma. The bregma was also used as a reference point for the location of electrodes in the mouse electrical stimulation experiment in this study, so invasive treatment of the mouse scalp was required. However, the electrical stimulation itself is non-invasive, and in experiments on larger animals or humans, non-invasive methods can be used to stimulate the target. The following simulation results can be used as evidence. The simulation results shown in **Supplementary Figure 5** show that the effects of non-invasive and invasive stimulation are similar.

Accurate stimulation of the target brain region is crucial for the application of electrical stimulation, and numerous studies on simulation localization for tDCS and tACS have been published (Datta et al., 2009; Edwards et al., 2013). In some studies, hundreds of electrodes are calculated to find optimal electrode configurations (Huang and Parra, 2019). The positioning accuracy depends on the use of a large number of electrodes, but only a few electrodes can be placed on the mouse skull, even if the electrodes are designed to be 1 mm in diameter. Based on the shape characteristics of the mouse head and brain, we found that the most effective point of stimulation always appeared on the same plane as the electrodes, so the three-dimensional individualized simulation navigation could be simplified into a columnar

model simulation calculation according to the shape of the coronal plane. In this way, we could obtain electrode position prediction results by the functional relationship between the target coordinates, the electrode position and the amplitude ratio. Then, the target was further navigated in a three-dimensional, individualized model of the mouse, and the electrode positions were fine-tuned according to the simulation results.

Previous studies have shown that high-frequency electrical stimulation has an activating effect on neurons, which is based on its effect on cell membranes (Chaieb et al., 2011; Herrmann et al., 2013). The regulatory effect of low-frequency electrical stimulation on brain rhythms and networks has been recognized (Ali et al., 2013; Fröhlich, 2015), but kHz stimulation has shown no such effect. Time-interfering electrical stimulation, with the characteristics of both high-frequency and low-frequency electrical stimulation, may provide many opportunities for future research and is expected to more efficiently regulate brain function. Further studies, such as fMRI and behavioral experiments, will be meaningful and necessary for analyzing the changes in brain rhythms and networks derived from time-interfering electrical stimulation.

CONCLUSION

In this study, we designed a temporal interference electrical stimulator in which technologies such as analog phase accumulation, reverse current pump driving, and spectral analysis were used to solve the problems of accurate output, crosstalk between channels, and bioimpedance measurements. The output performance of the device was confirmed by testing the load capacity and SNR of the device. A functional test of the bioimpedance measurement was performed under resistance and resistance-capacitance loads and in the mouse body. The uniformity of the measured and simulated distributions of the envelope amplitude exhibited the feasibility of temporally interfering electrical stimulation and the reliability of the stimulator. Through the simulation of idealized models and individualized mouse models, we achieved the precise positioning of temporally interfering stimulation targets. The functional relationship between the stimulus depth and the electrode spacing and the relationship between the target abscissa and amplitude ratio that we found can help users achieve target positioning in mice without modeling and simulation. Finally, we conducted a mouse experiment, and evoked movement was observed in the contralateral forepaw; that is, the temporally interfering stimulator succeeded in activating mouse neurons and achieved positioning accuracy in the mouse experiment. In summary, the performance and experimental effectiveness of the electrical stimulator have been verified in this study, and this type of stimulation, with both high-frequency and low-frequency electrical stimulation characteristics, provides many opportunities for future research. Further research should be carried out utilizing this electrical stimulator. If necessary,

we will be able to provide equipment to research teams that need it.

DATA AVAILABILITY STATEMENT

The original contributions presented in the study are included in the article/**Supplementary Materials**, further inquiries can be directed to the corresponding author/s.

ETHICS STATEMENT

The animal study was reviewed and approved by Ethics Committee of Beijing Tiantan Hospital affiliated to Capital Medical University, Beijing Tiantan Hospital.

AUTHOR CONTRIBUTIONS

HW, DC, and JWu contributed to the conception of the study. WS, JZ, and JWa performed the experiment. ZS and CL contributed significantly to the analysis and manuscript preparation. RY, YS, GG, and YX helped perform the analysis through constructive discussion. All authors contributed to the article and approved the submitted version.

FUNDING

This work was supported by the National Key Research and Development Program of China under grant 2018YFC0115400, the National Natural Science Foundation of China (Grant Nos. 61727807, 81970404, and 81771909), the Beijing Municipal Science and Technology Commission (Z191100010618004), and the Beijing Nova Program (Z181100006218008). This work was also supported by JSPS KAKENHI Grant Numbers 18K18835, 18H01411, and 19KK0099.

SUPPLEMENTARY MATERIAL

The Supplementary Material for this article can be found online at: <https://www.frontiersin.org/articles/10.3389/fninf.2020.574189/full#supplementary-material>

Supplementary Figure 1 | Impedance measurement circuit. **(A)** Feedback signal transmission circuit. **(B)** Signal regulation circuit.

Supplementary Figure 2 | Multichannel high-SNR output circuit.

Supplementary Figure 3 | Influence of additional impedance on the target location.

Supplementary Figure 4 | Influence of poor electrode contact on electrical stimulation. **(A)** There was complete contact between the electrodes and the mouse. **(B)** The condition in which a portion of the area between the electrodes and the mouse was in poor contact led to a decrease in the stimulus amplitude. **(C)** The condition in which a portion of the area between the electrodes and the mouse was in poor contact led to a right shift of the target.

Supplementary Figure 5 | Comparison between non-invasive and invasive temporally interfering electrical stimulation. **(A)** Non-invasive model. **(B)** Invasive model. **(C)** Distribution of the stimulus intensity of the non-invasive model. **(D)** Distribution of the stimulus intensity of the invasive model.

REFERENCES

- Ali, M. M., Sellers, K. K., and Frohlich, F. (2013). Transcranial alternating current stimulation modulates large-scale cortical network activity by network resonance. *J. Neurosci.* 33, 11262–11275. doi: 10.1523/JNEUROSCI.5867-12.2013
- Analog Devices Inc. (2005–2011). *AD5933 Data Sheet*.
- Antal, A., Boros, K., Poreisz, C., Chaieb, L., Terney, D., and Paulus, W. (2008). Comparatively weak after-effects of transcranial alternating current stimulation (tACS) on cortical excitability in humans. *Brain Stimul.* 1, 97–105. doi: 10.1016/j.brs.2007.10.001
- Batra, V., Guerin, G. F., Goeders, N. E., and Wilden, J. A. (2016). A general method for evaluating deep brain stimulation effects on intravenous methamphetamine self-administration. *J. Vis. Exp.* 1, 75–81. doi: 10.3791/53266
- Blomstedt, P., and Hariz, M. I. (2006). Are complications less common in deep brain stimulation than in ablative procedures for movement disorders? *Stereotact. Funct. Neurosurg.* 84, 72–81. doi: 10.1159/000094035
- Buss, S. S., Fried, P. J., and Pascual-Leone, A. (2019). Therapeutic non-invasive brain stimulation in Alzheimer's disease and related dementias. *Curr. Opin. Neurol.* 32, 292–304. doi: 10.1097/WCO.0000000000000669
- Chaieb, L., Antal, A., and Paulus, W. (2011). Transcranial alternating current stimulation in the low kHz range increases motor cortex excitability. *Restor. Neurol. Neurosci.* 29:167. doi: 10.3233/RNN-2011-0589
- Cole, J. H., and Franke, K. (2017). Predicting age using neuroimaging: innovative brain ageing biomarkers. *Trends Neurosci.* 40, 681–90. doi: 10.1016/j.tins.2017.10.001
- Datta, A., Bansal, V., Diaz, J., Patel, J., Reato, D., and Bikson, M. (2009). Gyri-precise head model of transcranial direct current stimulation: Improved spatial focality using a ring electrode versus conventional rectangular pad. *Brain Stimul.* 2, 201–207. doi: 10.1016/j.brs.2009.03.005
- Edwards, D., Cortes, M., Datta, A., Minhas, P., Wassermann, E. M., and Bikson, M. (2013). Physiological and modeling evidence for focal transcranial electrical brain stimulation in humans: a basis for high-definition tDCS. *Neuroimage.* 74, 266–275. doi: 10.1016/j.neuroimage.2013.01.042
- Flora, E. D., Perera, C. L., Cameron, A. L., and Maddern, G. J. (2010). Deep brain stimulation for essential tremor: a systematic review. *Mov. Disord.* 25, 1550–1559. doi: 10.1002/mds.23195
- Fröhlich, F. (2015). Experiments and models of cortical oscillations as a target for non-invasive brain stimulation. *Progr. Brain Res.* 222, 41–73. doi: 10.1016/j.pbr.2015.07.025
- Grossman, N., Bono, D., Dedic, N., Kodandaramaiah, S. B., Rudenko, A., Suk, H. J., et al. (2017). Non-invasive deep brain stimulation via temporally interfering electric fields. *Cell* 169, 1029–1041.e16. doi: 10.1016/j.cell.2017.05.024
- Herrmann, C. S., Rach, S., Neuling, T., and Strüder, D. (2013). Transcranial alternating current stimulation: a review of the underlying mechanisms and modulation of cognitive processes. *Front. Hum. Neurosci.* 2013:7. doi: 10.3389/fnhum.2013.00279
- Huang, Y., and Parra, L. C. (2019). Can transcranial electric stimulation with multiple electrodes reach deep targets. *Brain Stimul.* 12, 30–40. doi: 10.1016/j.brs.2018.09.010
- Jiang, J., Truong, D. Q., Esmailpour, Z., Huang, Y., Badran, B. W., and Bikson, M. (2020). Enhanced tES and tDCS computational models by meninges emulation. *J. Neural Eng.* 17:016027. doi: 10.1088/1741-2552/ab549d
- Lapchak, P. A., Boitano, P. D., Butte, P. V., Fisher, D. J., Hölscher, T., Ley, E. J., et al. (2015). Transcranial near-infrared laser transmission (NILT) Profiles (800 nm): systematic comparison in four common research species. *PLoS ONE.* 10:e0127580. doi: 10.1371/journal.pone.0127580
- Miocinovic, S., Somayajula, S., Chitnis, S., and Vitek, J. L. (2013). History, applications, and mechanisms of deep brain stimulation. *JAMA Neurol.* 70:163. doi: 10.1001/2013.jamaneurol.45
- Moliadze, V., Antal, A., and Paulus, W. (2012). Close to threshold transcranial electrical stimulation preferentially activates inhibitory networks before switching to excitation with higher intensities. *Brain Stimul.* 5, 505–511. doi: 10.1016/j.brs.2011.11.004
- Paulus, W. (2011). Transcranial electrical stimulation (tES-tDCS; tRNS, tACS) methods. *Neuropsychol. Rehabil.* 21, 602–617. doi: 10.1080/09602011.2011.557292
- Rodriguez, S., Ollmar, S., Waqar, M., and Rusu, A. (2016). A batteryless sensor ASIC for implantable bio-impedance applications. *IEEE Transact. Biomed. Circ. Syst.* 10, 533–544. doi: 10.1109/TBCAS.2015.2456242
- Schulz, R., Gerloff, C., and Hummel, F. C. (2013). Non-invasive brain stimulation in neurological diseases. *Neuropharmacology.* 64, 579–587. doi: 10.1016/j.neuropharm.2012.05.016
- Stroud, D. B., Cornish, B. H., Thomas, B. J., and Ward, L. C. (1995). The use of Cole-Cole plots to compare two multi-frequency bioimpedance instruments. *Clin. Nutr.* 14, 307–311. doi: 10.1016/S0261-5614(95)80069-7
- Tavakoli, A. V., and Kyongsik, Y. (2017). Transcranial alternating current stimulation (tACS) mechanisms and protocols. *Front. Cell. Neurosci.* 11:214. doi: 10.3389/fncel.2017.00214
- Tennant, K. A., Adkins, D. L., Donlan, N. A., Asay, A. L., Thomas, N., Kleim, J. A., et al. (2011). The organization of the forelimb representation of the C57BL/6 mouse motor cortex as defined by intracortical microstimulation and cytoarchitecture. *Cerebral Cortex* 21, 865–876. doi: 10.1093/cercor/bhq159
- Terney, D., Chaieb, L., Moliadze, V., Antal, A., and Paulus, W. (2008). Increasing human brain excitability by transcranial high-frequency random noise stimulation. *J. Neurosci.* 28, 14147–14155. doi: 10.1523/JNEUROSCI.4248-08.2008
- Umehura, A., Jaggi, J. L., Hurtig, H. I., Siderowf, A. D., Colcher, A., Stern, M. B., et al. (2003). Deep brain stimulation for movement disorders: morbidity and mortality in 109 patients. *J. Neurosurg.* 98, 779–784. doi: 10.3171/jns.2003.98.4.0779
- Yang, L., Liu, W., Chen, R., Zhang, G., Li, W., Fu, F., et al. (2017). *In vivo* bioimpedance spectroscopy characterization of healthy, hemorrhagic and ischemic rabbit brain within 10 Hz–1 MHz. *Sensors* 17:791. doi: 10.3390/s17040791
- Zaehle, T., Rach, S., and Herrmann, C. S. (2010). Transcranial alternating current stimulation enhances individual alpha activity in human EEG. *PLoS ONE* 5, 1–7. doi: 10.1371/journal.pone.0013766

Conflict of Interest: YS was employed by the company Beijing Big-IQ Medical Equipment Co., Ltd.

The remaining authors declare that the research was conducted in the absence of any commercial or financial relationships that could be construed as a potential conflict of interest.

Copyright © 2020 Wang, Shi, Sun, Zhang, Wang, Shi, Yang, Li, Chen, Wu, Gongyao and Xu. This is an open-access article distributed under the terms of the Creative Commons Attribution License (CC BY). The use, distribution or reproduction in other forums is permitted, provided the original author(s) and the copyright owner(s) are credited and that the original publication in this journal is cited, in accordance with accepted academic practice. No use, distribution or reproduction is permitted which does not comply with these terms.



Biosignal-Based Attention Monitoring to Support Nuclear Operator Safety-Relevant Tasks

Jung Hwan Kim¹, Chul Min Kim¹, Eun-Soo Jung² and Man-Sung Yim^{1*}

¹ Department of Nuclear and Quantum Engineering, Korea Advanced Institute of Science and Technology, Daejeon, South Korea, ² Technology Research, Samsung SDS, Seoul, South Korea

OPEN ACCESS

Edited by:

Tianyi Yan,
Beijing Institute of Technology, China

Reviewed by:

Songyun Xie,
Northwestern Polytechnical University,
China

Daya Shankar Gupta,
Camden County College,
United States

*Correspondence:

Man-Sung Yim
msyim@kaist.ac.kr

Received: 19 August 2020

Accepted: 18 November 2020

Published: 21 December 2020

Citation:

Kim JH, Kim CM, Jung E-S and
Yim M-S (2020) Biosignal-Based
Attention Monitoring to Support
Nuclear Operator Safety-Relevant
Tasks.
Front. Comput. Neurosci. 14:596531.
doi: 10.3389/fncom.2020.596531

In the main control room (MCR) of a nuclear power plant (NPP), the quality of an operator's performance can depend on their level of attention to the task. Insufficient operator attention accounted for more than 26% of the total causes of human errors and is the highest category for errors. It is therefore necessary to check whether operators are sufficiently attentive either as supervisors or peers during reactor operation. Recently, digital control technologies have been introduced to the operating environment of an NPP MCR. These upgrades are expected to enhance plant and operator performance. At the same time, because personal computers are used in the advanced MCR, the operators perform more cognitive works than physical work. However, operators may not consciously check fellow operators' attention in this environment indicating potentially higher importance of the role of operator attention. Therefore, remote measurement of an operator's attention in real time would be a useful tool, providing feedback to supervisors. The objective of this study is to investigate the development of quantitative indicators that can identify an operator's attention, to diagnose or detect a lack of operator attention thus preventing potential human errors in advanced MCRs. To establish a robust baseline of operator attention, this study used two of the widely used biosignals: electroencephalography (EEG) and eye movement. We designed an experiment to collect EEG and eye movements of the subjects who were monitoring and diagnosing nuclear operator safety-relevant tasks. There was a statistically significant difference between biosignals with and without appropriate attention. Furthermore, an average classification accuracy of about 90% was obtained by the k-nearest neighbors and support vector machine classifiers with a few EEG and eye movements features. Potential applications of EEG and eye movement measures in monitoring and diagnosis tasks in an NPP MCR are also discussed.

Keywords: electroencephalography, eye movements, machine learning, attention, human error, nuclear safety

1. INTRODUCTION

Attention is an important cognitive resource for information processing directly affecting the quality of task performance (Wickens et al., 1998). According to the Nuclear Event Evaluation Database (NEED), a database developed by Korea Institute of Nuclear Safety (KINS), approximately 20% of the unplanned nuclear power plant (NPP) shutdowns between 2000 and 2011 in Korea were due to human errors (Lee et al., 2017). The operator's insufficient attention

accounted for more than 26% of the total cause of human errors, which takes the biggest portion. Hence, the decreased attention of an NPP main control room (MCR) operator could lead to a decrease in their situational awareness, which could result in a poor reactor operating performance and ultimately cause critical human errors.

Recently developed NPP designs include fully digitalized instrumentation and control (I&C). These upgrades are expected to enhance plant and operator performance. Advanced MCRs based on digital I&C technology create a completely different operating environment from the existing MCR configurations (Choi et al., 2019).

MCR operators are required to monitor several information sources, such as indicators, alarms, controllers, and mimic displays, but they have a limited capacity of attention (Wickens et al., 1998; Ha et al., 2016). Selective attention to important information is therefore required to effectively understand the current reactor operating status (Mumaw et al., 2000). MCR operators therefore allocate their attention resources and selectively pay attention to relevant and important information to understand the system status.

MCR operators' tasks involve cognitive activities of monitoring and detecting the environment, diagnosing situations, and decision making (Yang et al., 2017; Kim and Seong, 2019). MCR operators generally monitor the plant status and diagnose and respond to the plant status for abnormal operation (Kim et al., 2020b).

There is a direct relationship between operation and attention, and that is why either a supervisor or peers observe other operators to check whether they are sufficiently attentive. However, this method requires significant labor and may be subjective. The problem could be exacerbated in an advanced MCR, where personal computer-based workstations make it difficult for a supervisor to detect fellow operators' attention states (Savchenko et al., 2017). In this situation, remote measurement of attention would be a useful tool providing real-time feedback to the supervisor.

Recently, the analysis of electroencephalography (EEG) and eye movements have been used to assess variations in the attention state of subjects during the execution of cognitive tasks in various fields (Jung et al., 2017, 2019; Kim et al., 2018; Pei et al., 2018).

Liu et al. (2013) determined whether students remain attentive throughout instruction during the learning process based on their EEG signals. To describe the learning environment, Standard English class material was used as experiment material. A classification accuracy of 76% was obtained through the support vector machine. The authors explained that if teachers identify whether students are attentive, they can remind students to remain focused, thereby improving students' learning effects.

Heuer and Hallowell (2015) suggested the eye movement method to index attention allocation in people with aphasia. Auditory sentence comprehension and visual search tasks were performed. The authors observed differences in attention allocation between groups with and without aphasia depends on task complexity in single- and dual-task conditions. They suggested that utilizing information

from eye movements has promising potential for clinical assessment applications.

Pallavi and Harish (2016) implemented a driver's attention monitoring system using EEG signals. The EEG signals were monitored and analyzed by using a brain sense headband that transmits the information to the controller wirelessly using the Bluetooth module. The warning tone would be triggered to prevent accidents when the drowsiness condition occurred to the driver. The authors explained that their EEG based-attention monitoring system can be used to indicate driving attention and drowsiness.

To date, the potential benefits of studying EEG and eye movements together to understand operator's attention in NPP tasks has not been pursued. As MCR operators perform cognitive activities by using information obtained through visual channels, we evaluated the use of both EEG signals and eye movements (as supportive biosignal) to establish a robust baseline to determine the plausibility of developing an attention monitoring system in this paper. Using two sets of data to monitor human attention may help to improve the accuracy in model predictions and contribute to overall human error reduction.

In this research, performing nuclear tasks based on the use of a nuclear simulator was investigated. Although this is not completely the same as with the tasks of a professional MCR operator in NPP, this could provide similar environment of an MCR operator and raise the level of psychological involvement of the subjects during the experiments. To reflect and mimic operations in an advanced MCR, this study designed general tasks and nuclear simulator tasks as the basis for collecting relevant EEG and eye movement data. The collected data were analyzed for feature extraction and classification model development based on the use of machine learning algorithms.

2. METHODS

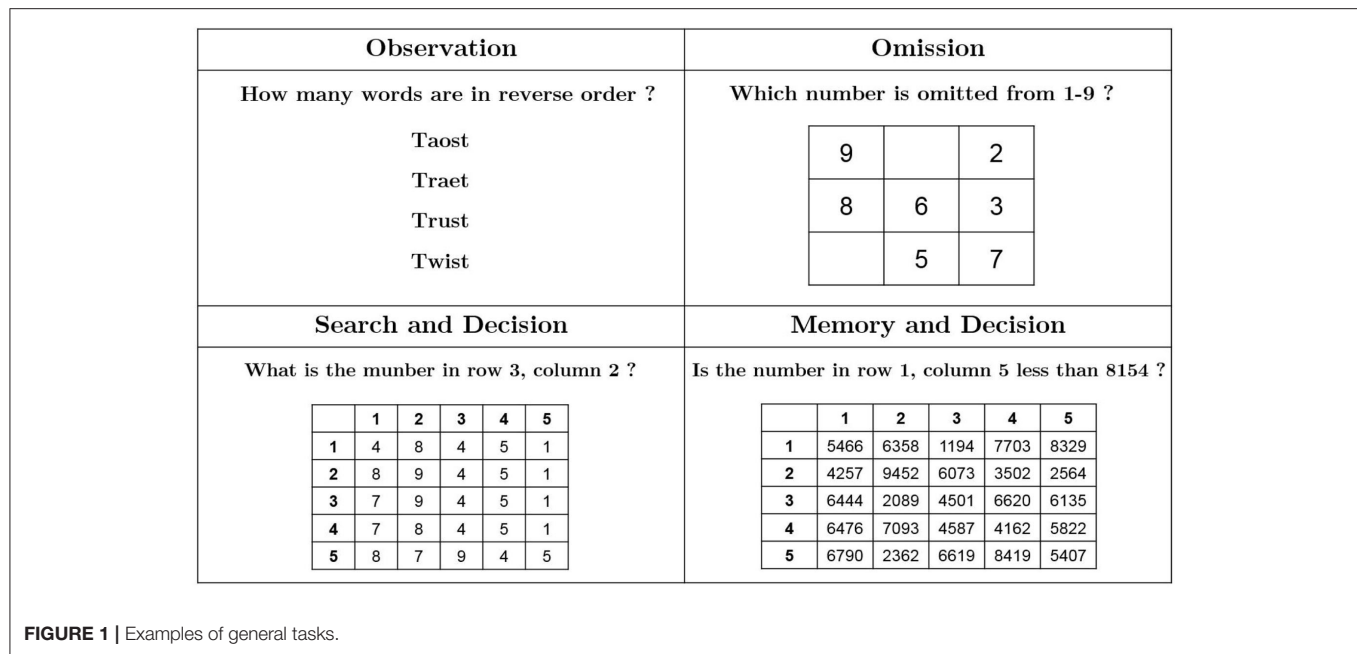
This study constructed a hypothesis to investigate the identification of the attention of advanced MCR operators. The hypothesis is that there will be a significant difference in an operator's biosignals between the presence and absence of attention while performing general tasks as well as the tasks related to nuclear reactor operations.

2.1. Experimental Design

To test this hypothesis, study subjects were asked 38 questions as general tasks and 72 questions specific to nuclear reactor operations based on the use of the nuclear simulator. EEG and eye movement data were collected during the experimental sessions and analyzed with respect to the testing hypothesis.

2.1.1. General Tasks

Oh and Lee (2013) investigated the potential causes of human errors in an advanced MCR where PC-soft controls are heavily relied on for reactor operation. They found that observation, omission, search and decision, and memory and decision failures are four major factors related to human errors. The authors also designed four experimental tasks to investigate the role of these factors. These tasks were used with slight modification



in the current study as general task questions. Examples of these questions are illustrated in **Figure 1**. For example, the observation trial questions ask the subject how many words in a list (“taost,” “traet,” “trust,” “twist”) have typographical errors [answer: two words (toast and treat) have typographical errors]. The omission trial questions ask the subject to find the omitted numbers from a matrix where the numbers between 1 and 9 are presented in a random order. The search and decision trial questions ask the subject to check the number in a specific position in a 5X5 matrix. The memory and decision trial questions ask the subject to recall a specified number in a 5X5 matrix and compare it with the number provided. A total of 38 questions were used in the general task session, including eight observation trials, six omission trials, 16 search and decision trials, and eight memory and decision trials.

As shown in **Figure 2**, each trial followed the same sequence of screen changes: a fixation cross to prepare the subject for the trial, a blank screen, a question (e.g., “What is the number in row 3, column 5?”), a blank screen, a picture related to the question (e.g., a matrix of numbers with 5 rows and 5 columns), a blank screen, an answer to the question provided by the instructor (in each trial, the subjects answered the trial questions and were given an opportunity to compare their answer with the answer provided by the instructor.), and a blank screen followed by a two checklist questions to be answered by the subject via keyboard. The first checklist question was “Was there an error in the instructor’s answer?” with the choice of yes or no. The second question was “How attentive were you in answering the previous question?” with these multiple-choice options: very attentive, moderately attentive, somewhat attentive, only slightly attentive, or not at all attentive.

2.1.2. Nuclear Simulator Tasks

The second group of trials used soft controls in an advanced MCR mock-up called the Windows-based Nuclear Plant Performance Analyzer (Win-NPA). Win-NPA is a compact nuclear simulator capable of simulating 53 malfunctions in nuclear reactor operations (Kim et al., 2000; Sohn et al., 2011). Although the simulator is not a full scope simulator, many researchers have used it to simulate operations in an advanced MCR (Choi et al., 2018; Kim et al., 2020c). The interface of the Win-NPA is fully digitalized to make the experimental environment similar to the environment in an advanced MCR.

Various types of human error can occur in an advanced NPP MCR. This study examines operation omission, wrong object selection, and wrong operation as part of conducting nuclear simulator tasks (Kim et al., in press). Operation omission can be defined as failing to execute a step in an operating procedure (e.g., mistakenly taking steps 1, 2, 4, and 5 in a procedure, leaving out step 3). Wrong object selection is a failure to select a target object and instead select a different object. An example of the wrong operation is pressing an “OPEN” button instead of a “CLOSE” button.

The types of scenarios used in the experiment in association with identifying human error occurrence were normal operating scenarios (i.e., startup and shutdown) as well as two accident scenarios [i.e., a loss of coolant accident (LOCA) and a steam generator tube rupture (SGTR)]. If a LOCA occurs in an NPP, the pressurizer’s (PZR’s) pressure, temperature, and the water level will decrease, and containment radiation will increase. Similarly, if an SGTR occurs in an NPP, the PZR’s pressure, temperature, and the water level will decrease, and the steam generator (SG) water level will increase. Prior to the experiment, the subjects were instructed that it was training session for education to avoid the higher workload or decision burden for accident scenarios.

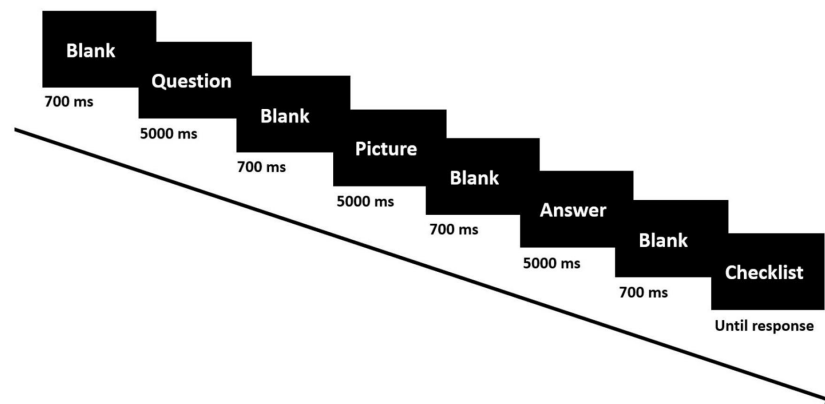


FIGURE 2 | Experiment paradigm of general tasks.

To focus on evaluating the attention of the subjects, the scenarios used in the experiment was not required to recover the accident but was required to monitor and diagnose the situation.

To analyze the cognitive behavior of the subjects during the trials, this study defined four groups of areas of interest (AOI, or specific operating parameters of interest) as shown in the red rectangles of **Figure 3**; these are (1) pressure, wide-range water level, and narrow-range water level of SG1, (2) pressure, wide-range water level, and narrow-range water level of SG2, (3) PZR pressure and water level, and (4) reactor power. Furthermore, there is an additional condition that insert a broken indicator (BI) to make deviations from the training contents. While faced with a scenario (normal operation, LOCA, or SGTR), the subject must focus on the four groups of AOI to monitor indicators or find a BI. Collectively, this study provides 18 startup scenarios, 18 shutdown scenarios, 18 LOCA scenarios, and 18 SGTR with each having six scenarios of finding BIs.

Each subject acted as an operator, specifically a reactor operator or a turbine operator. Each subject took part in a session of 72 operator action trials, 36 involving normal scenarios, and 36 involving the two accident scenarios. As shown in **Figure 4**, each trial followed this screen sequence: a fixation cross to prepare the subject for the trial, a blank screen, a question (e.g., “Can you find a broken indicator?”), a blank screen, a video related to the question (e.g., a video of the LOCA scenario), a blank screen, the instructor’s answer [e.g., PZR pressure indicator is broken (PZR P is BI)], a blank screen, a checklist with two questions to be answered by the subject via keyboard. As in the case of the general task session, the first checklist question was “Was there an error in the supervisor’s answer?” with the choice of yes or no. The second question was “How attentive were you in answering the previous question?” with these multiple-choice options: very attentive, moderately attentive, somewhat attentive, only slightly attentive, or not at all attentive.

As the study requires labeling of the experimental data as either presence of attention (PoA) or absence of attention (AoA) for classification model development, the answers to the checklist questions were used to identify the attention levels of the subjects during the experimental sessions.

2.2. Subjects of the Experiment

Because the tasks performed in this study require sufficient knowledge in nuclear reactor systems, the experimental subjects were recruited among the college/graduate students majoring in nuclear engineering. It was required for the subjects to have completed one of the two courses: “Introduction to Nuclear Engineering” or “System Engineering of Nuclear Power Plants.” In the end, 30 volunteer students (27 male and three female) from the Department of Nuclear and Quantum Engineering at Korea Advanced Institute of Science and Technology (KAIST) participated in the experiments. They were also screened against a history of eye problems, neurological disorders, mental disorders, or alcohol or drug dependence. None of the students were disqualified from the screening.

Before conducting the experimental sessions, the research staff explained the experimental procedures to the subjects, as required by the KAIST Institutional Review Board (IRB) guideline. The subjects read an information sheet and signed an agreement regarding the data collection process. All subjects were required to sleep more than 6 h and not to drink caffeine or alcohol for at least 24 h before the experiment.

Prior to performing the experiment, there was a 30 min training session by the experiment instructors, who have considerable expertise with the Win-NPA system. This training session included conducting simple tasks to show how to monitor and diagnose simulator scenarios. The actual experiment was conducted only for the subjects who answered more than six out of eight questions correctly in the pre-test. It turned out that one student did not pass the pre-test. After further studies, the student was qualified and participated in the experiment.

2.3. System Architecture for Classification

2.3.1. Data Acquisition

Studies indicate that among various frequency bands of EEG, an increase in the gamma band and a decrease in the alpha band are associated with subjects’ paying attention to tasks (Pascucci et al., 2018). In eye movements, an increase in the fixation count and fixation duration is often referred to as an increase

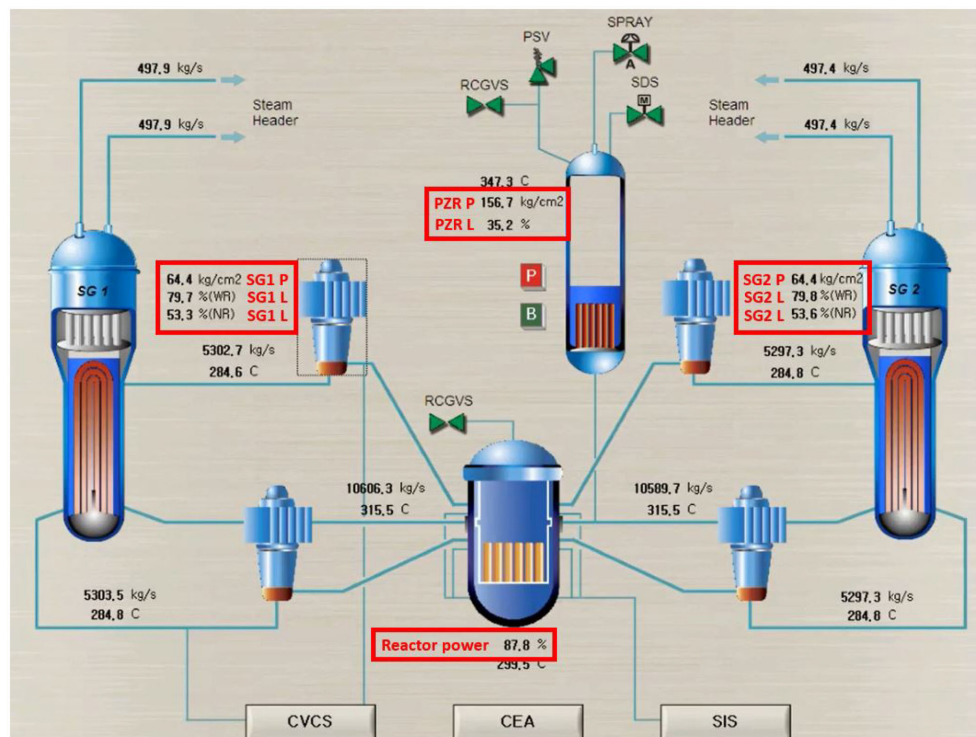


FIGURE 3 | Schematic diagram of nuclear simulator tasks with four groups of AOI.

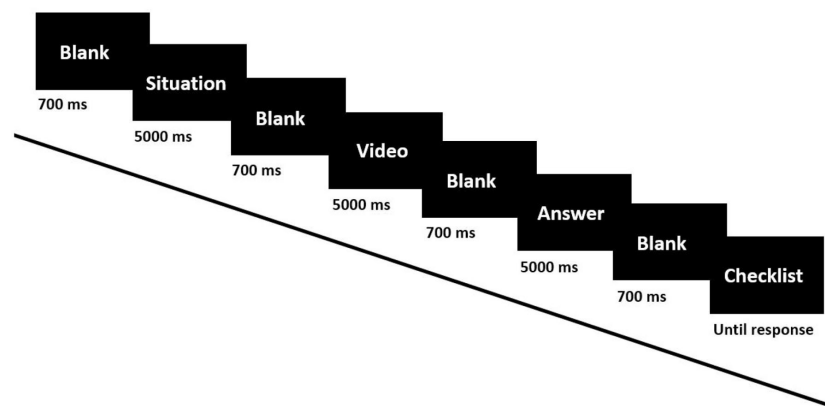


FIGURE 4 | Experiment paradigm of nuclear simulator tasks.

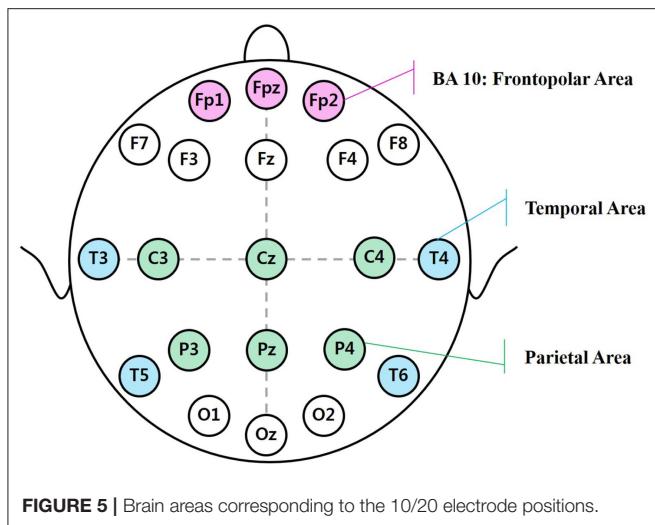
in the attention level (Holmqvist et al., 2011). Based on these observations, we acquired the relevant EEG and eye movement data to evaluate the attention status of the subjects.

EEG signals were measured using a Neuron-spectrum 4/P (Neurosoft Ltd., Russia). Each subject was fitted with an Ag/AgCl electrode cap arranged with an extended international 10-20 system. The EEG data from 21 channels (Fp1, Fp2, Fpz, F3, F4, F7, F8, Fz, C3, C4, Cz, T3, T4, T5, T6, P3, P4, Pz, O1, O2, and Oz) were recorded, as shown in **Figure 5**, at a sampling rate of 500 Hz. Reference electrodes were placed on both earlobes. During

the experiment, the electrode impedances of all the channels were kept below 5 kΩ.

The eye movements were measured by using a Tobii X120 eye tracker. The eye tracker was located beneath the computer monitor, monitoring the subject's field of vision. The seating position was adjusted according to the subject's height. Since the eye tracker is non-invasive and operates remotely, the device did not interfere with the subject's task performance.

After adjusting the seating position, the Tobii X120 was calibrated. Calibration required the subjects to move their eyes



to five specific spots, i.e., each of the four corners and the center of the monitor screen. These eye movements were tracked using a standard five-point calibration option in the Tobii Eye Tracker Extension for Presentation software. Eye movement was recorded with a sampling frequency of 120 Hz. Because EEG and eye movement data collection are sensitive to light and sound, the experimental environment blocked light and sound to support the subject's concentration. The EEG and eye movement data were synchronized in time by using the Neurobehavioral Systems presentation software.

2.3.2. Channel Selection

The EEG signals are generally categorized as delta (δ), theta (θ), alpha (α), beta (β), and gamma (γ) based on signal frequencies (Zeng et al., 2015). The δ frequency (1–4 Hz) appears in cognitive processes related to the detection of salient stimuli in the environment. The θ frequency (4–8 Hz) is related to visual selective attention. The α frequency (8–13 Hz) primarily reflects visual processing in the brain (Klimesch et al., 2011). The β frequency (13–30 Hz) focuses on neural correlates of attention and concentration (Wang et al., 2017). The γ frequency (30–50 Hz) reflects working memory and attention (Klimesch et al., 2008). These EEG indicators were measured on various parts of the brain to represent different brain functions. This study focused on describing functions related to the frontal, temporal, and parietal lobes as well as the Brodmann Areas (BAs).

As shown in **Figure 5**, each area of the brain is responsible for a specific function. The frontal lobes play a role in many processes, such as motivation, intention, attention, and concentration. The temporal lobes are believed to be of central importance in memory processing and discrimination of complex visual stimuli (Klimesch et al., 1994). The parietal lobes are associated with the detection of salient new events in the environment and in sustaining attention on task goals. BA 10 is the frontopolar area responsible for central executive processes such as memory, emotion, and integration of the information (Peng et al., 2018).

The brain areas that correspond to the 10/20 electrode positions can vary and include the frontal area (with Fp1, Fp2, FpZ, F3, F4, F7, F8, Fz, C3, C4, and Cz), the temporal area (with T3, T4, T5, and T6), the parietal area (with C3, C4, Cz, P3, P4, and Pz), and the BA 10 area (with Fp1, Fp2, and FpZ).

2.3.3. EEG and Eye Movement Preprocessing

To remove artifacts in the collected EEG data, data preprocessing was performed based on Makoto's preprocessing pipeline using EEGLAB (Delorme and Makeig, 2004). The line noise was removed by the CleanLine plugin (Mullen, 2012). Bad channels were rejected using the Clean Rawdata plugin, and continuous data were corrected using artifact subspace reconstruction (ASR). The Adaptive Mixture Independent Component Analysis (AMICA) program and the postAmicaUtility toolbox were used for independent component analysis (ICA) (Palmer et al., 2012). The artifacts from body movement, rolling eyeballs, and blinking were excluded from the analysis based on visual inspections of each component.

The preprocessed data were divided into 38 epochs of 5 s for each general task and 72 epochs of 5 s for each nuclear simulator task. A total of 110 epochs of 5 s per channel were collected and used for subsequent analysis.

The eye movement data are made up of x, y coordinates with each data point's associated timestamp. These raw data were used to obtain information about fixation count and fixation duration. Preprocessing of eye movement data includes conversion of gaze position data from pixels to millimeters, removal of blinks and artifacts, and removal of outliers.

2.3.4. Feature Extraction

To support the development of a machine learning algorithm, this study extracted a set of features that describe subjects' EEG and eye movement responses. These features were then used to classify the presence and absence of attention using the classification model. The EEG features used were extracted from the frequency domain (Tang et al., 2013).

The frequency domain features were calculated using the Discrete Fourier Transform (DFT). The transformed data were categorized into five frequency bands, δ , θ , α , β , and γ . A relative power value was calculated for each channel by dividing the power of each frequency band by the total power from the five frequency bands.

In the case of eye movement data, fixation was defined as a pause, of 150 ms, in eye movement over a specific region of the visual field. In the nuclear simulator tasks, a question was asked referring to four groups of AOI (SG1, SG2, PZR, and reactor power). All fixations occurring during the 5 s video relevant to the question were measured but only the fixations on specific group of AOI were considered for analysis. If the subject looked at other groups of AOI, these fixations were not included in the analysis. The analysis consisted of calculating the total number of fixations on the relevant group of AOI and the time duration of these fixations per task.

This study used each of the five frequency domain features from each channel of the EEG measurements and two features extracted from the eye movement data as summarized in **Table 1**.

TABLE 1 | Features extracted from the EEG and eye movement data.

Biosignals	Feature types	Extracted features
EEG	Frequency domain	Relative power of δ , θ , α , β , and γ
Eye movements	Fixation domain	Total number of fixations in the relevant AOI (fixation) and total time spent on the relevant AOI fixation (duration)

TABLE 2 | *P*-values for the EEG indicators showing differences between the AoA class and the PoA class for all general tasks while viewing pictures.

Indicator	Frontal	Temporal	Parietal	BA 10
Relative power of δ	0.633	0.587	0.545	0.535
Relative power of θ	0.420	0.597	0.606	0.011*
Relative power of α	0.008*	0.521	0.242	0.587
Relative power of β	0.010*	0.229	0.304	0.143
Relative power of γ	0.372	0.521	0.457	0.592

P-values less than 0.05 are identified with an asterisk.

3. RESULTS

3.1. Statistical Analysis

Using the answers to the two checklist questions in both the general and nuclear simulator task sessions, this study labeled the collected EEG signals and eye movement data into the PoA class and the AoA class. Trials with the answer “very attentive” and “moderately attentive” with correct responses for the task were labeled as the PoA class, and those with “somewhat attentive” were not used in the classification. The AoA class was defined for the following two conditions. First, the trials with the answer “only slightly attentive” or “not at all attentive” in the second question of the checklist were labeled as the AoA class regardless of the correctness of the answer to the first question. Also, the cases with incorrect responses to the first question of the checklist were also labeled as the AoA class by assuming that the wrong answer was due to a lack of attention. This may involve misclassification as the subject could have answered the question wrong under full attention. But the number of cases under this category was very small and is not expected to affect the outcome of the study. In summary, there were 2656 PoA cases, 578 AoA cases, 12 cases of potential misclassification, and 54 removed cases due to artifact removal. To examine the effect of possible misclassification with the 12 cases, this set was treated as both the AoA class and the PoA class in the analysis. The results showed statistically insignificant difference with and without these 12 cases both in the analysis of the general tasks and the nuclear simulator tasks.

The results from the Welch's *t*-test for the general task questions are shown in **Table 2**. Results indicated that statistically significant differences exist in several of the EEG signals between the AoA class and the PoA class. These EEG signals were the relative power of the α and β bands from the frontal lobes and the relative power of the θ band from the BA 10. As mentioned above, frontal lobes are related to attention and concentration, and BA

TABLE 3 | *P*-values for the EEG indicators showing differences between the AoA class and the PoA class for all Win-NPA tasks while watching videos.

Indicator	Frontal	Temporal	Parietal	BA 10
Relative power of δ	0.214	0.051	0.036*	0.546
Relative power of θ	0.576	0.995	0.638	0.131
Relative power of α	0.662	0.051	0.619	0.039*
Relative power of β	0.598	0.003*	0.041*	0.462
Relative power of γ	0.443	0.015*	0.057	0.019*

P-values less than 0.05 are identified with an asterisk.

10 is responsible for memory and integration of information. The α , β , and θ bands are related to visual processing, concentration, and visual selective attention, respectively. As shown in **Figure 6**, the θ band was significantly increased across the BA 10 in the AoA class. Also, the α band was significantly increased and the β band was significantly decreased across frontal lobes in the AoA class.

The EEG signals collected during the Win-NPA tasks also showed significant differences (based on the Welch's *t*-test) between the AoA class and the PoA class as shown in **Table 3**. Because visual processing of information is important cognitive activities during the nuclear simulator session, EEG signals recorded from the brain regions related to visual processing, such as on temporal lobes and parietal lobes, showed significant differences between the AoA class and the PoA class. Also, EEG signals from BA 10, which is associated with memory and integration of information showed a significant difference between the AoA class and the PoA class, similar to the observations from the general tasks. As shown in **Figure 7**, the δ band was significantly decreased across parietal in the AoA class while watching the videos. The α band was significantly increased across BA 10 in the AoA class. This result is consistent with previous studies that alpha desynchronization promotes information processing in the brain (Klimesch, 2012). Similarly, the β band was significantly increased across temporal and parietal lobes in the AoA class. The γ band was significantly decreased across temporal and BA 10 in the AoA class.

As shown in **Tables 2, 3**, the number of statistically significant indicators was three in the general tasks and six in the nuclear simulator tasks. The fact that the nuclear simulator tasks required professional knowledge and higher concentration levels compared to the general tasks may have resulted in a larger number of significant indicators between the AoA class and the PoA class in the nuclear simulator tasks. Additionally, it is noticeable that, unlike the general tasks, the nuclear simulator tasks showed statistically significant differences in the EEG signals from the temporal and parietal lobes, which are related to visual attention.

The observed differences in the attention level between the AoA class and the PoA class during the general tasks and nuclear simulator tasks were utilized for classification model development by applying machine learning algorithms.

3.2. Classification

Feature selection is the process of selecting a subset of features that contribute the most to the construction of the classification model through including and excluding features present in the data. The feature selection was achieved by using the default parameters of the Variable Selection using Random Forests (varSelRF) technique (Diaz-Uriarte, 2007). The varSelRF uses both backwards variable elimination and selection based on the potentially highly correlated variables. As described in the feature extraction section, five features from the frequency domain in the EEG data and two features from eye movement data were used for classification.

To classify the data, both the classifiers of the k-nearest neighbors (kNN) and support vector machine (SVM) were used. These classifiers are widely used in various fields to classify EEG data (López-Gil et al., 2016). The kNN is a supervised learning algorithm for classifying objects based on the closest training data in the feature space. As a non-parametric method, it performs classification based on comparing testing data with training data. The SVM is a supervised learning algorithm and formulates a separating hyperplane. The method is applied to solve a quadratic optimization problem in the feature space. Kernel SVM finds the optimum hyperplane into a higher dimensional space, which ensures that the distance between margins is maximum. This study specifically used the radial basis function (RBF) kernel to project input vectors into a Gaussian space.

30% of the study observations were randomly selected and used as testing data, and 70% of the observations were used as

training data for classification model development. The average classification accuracy using the developed model was calculated through the classification results of testing data.

Table 4 summarizes the results as classification accuracy of the developed model for the case of the general tasks. The classification accuracy was calculated as an average across the total brain, frontal lobes, and BA 10 based on statistical analysis. When the five EEG frequency domain features were used, the average classification accuracies of the kNN and SVM classifiers were 84.6–86.7 and 87.0–87.4%, respectively. From the results, it is noticeable that the average classification accuracy of using BA 10 data only is comparable to that of using the total brain and frontal lobes data, which use a greater number of channels.

Table 5 summarizes the average classification accuracy of the developed model between the AoA class and the PoA class in the nuclear simulator tasks. The classification accuracy was calculated as an average across the total brain, temporal lobes, parietal lobes, and BA 10 based on statistical analysis. When

TABLE 4 | Average classification accuracy of the AoA class and the PoA class in the general tasks using the frequency domain features (Unit: %).

Brain areas	kNN	SVM
Total brain	85.8	87.4
Frontal lobes	86.7	87.0
BA 10	84.6	87.2

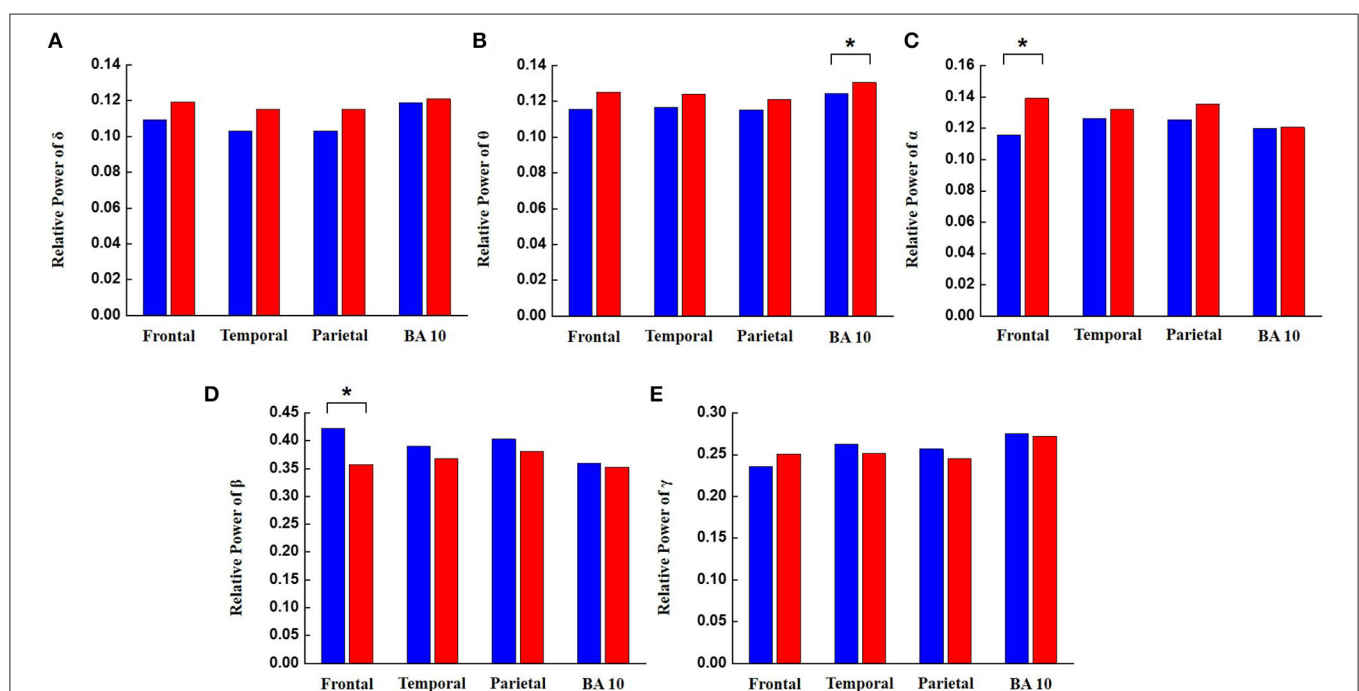


FIGURE 6 | The relative power of EEG frequency bands between the AoA class and the PoA class in different regions of the brain for all general tasks. Blue bars represent the PoA class and the red bars represent the AoA class. Brain areas with P -values less than 0.05 are identified with an asterisk. (A) Relative power of delta, (B) relative power of theta, (C) relative power of alpha, (D) relative power of beta, and (E) relative power of gamma.

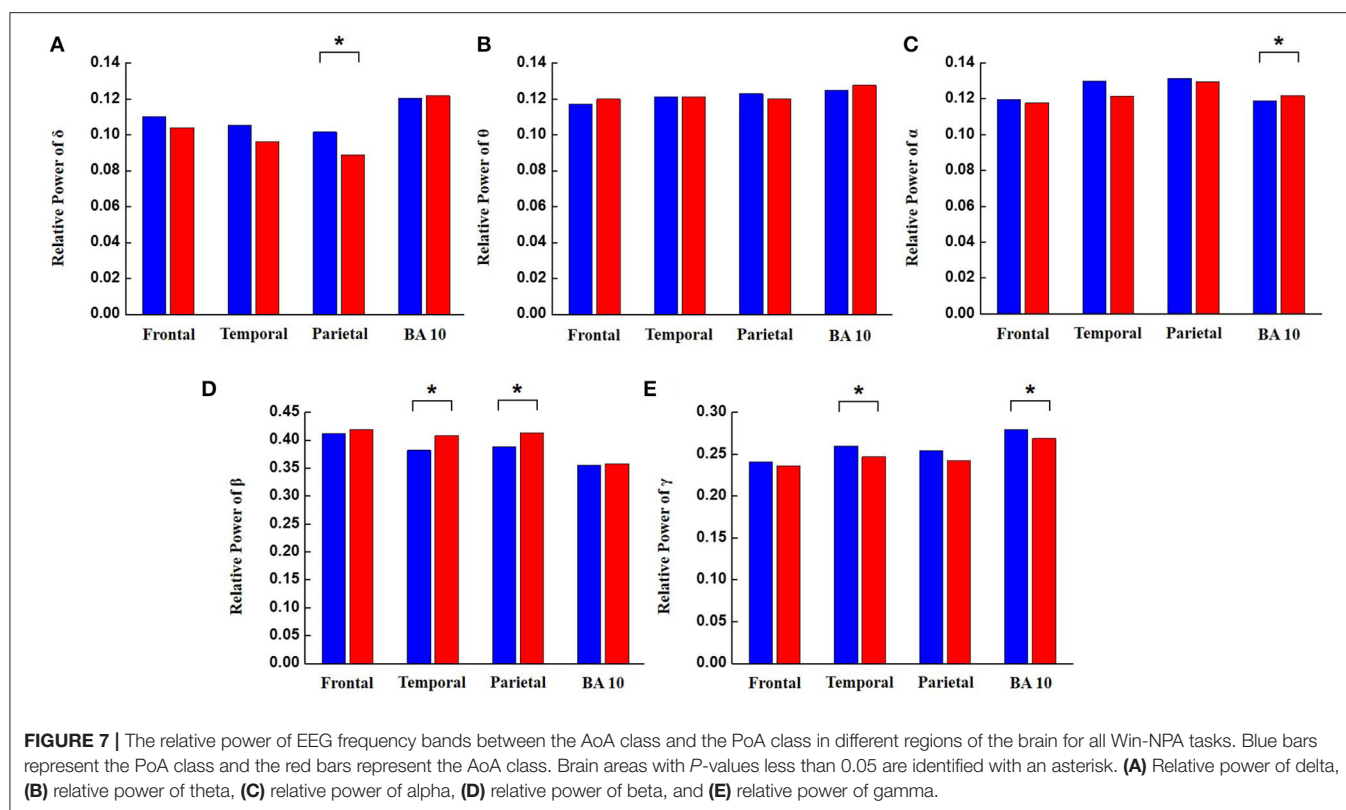


TABLE 5 | Average classification accuracy of the AoA class and the PoA class in the nuclear simulator tasks using the frequency domain features (Unit: %).

Brain areas	kNN	SVM
Total brain	86.5	87.8
Temporal lobes	86.5	87.6
Parietal lobes	86.2	87.4
BA 10	86.8	87.2

the five EEG frequency domain features were used, the average classification accuracies of the kNN and SVM classifiers were 86.2–86.8 and 87.2–87.8%, respectively. From the results, it is also noticeable that the average classification accuracy of using the BA 10 data is comparable to that of using the data from the total brain, temporal lobes, and parietal lobes which use a larger number of channels. The BA 10 is related to visual processing and attention functions.

The results again confirm that visual processing and attention play an important role in understanding visual-based nuclear relevant tasks. On the basis of statistical analysis and classification results from the general tasks and the nuclear simulator tasks, the null hypothesis is rejected.

This study also compared the average classification accuracy between the case of using only the EEG data and the case of using both the EEG and eye movement data. **Table 6** summarizes the comparison of the average classification accuracy of the AoA class

TABLE 6 | Average classification accuracy in the total brain when using EEG only and when using EEG with eye movements in the nuclear simulator tasks using the frequency domain features (Unit: %).

Biosignals	kNN	SVM
EEG	86.5	87.8
EEG with eye movements	89.1	90.1

and the PoA class between the two cases in the nuclear simulator tasks. The average classification accuracy was calculated for the total brain area.

The average classification accuracies of the kNN and SVM classifiers were about 86–87% for the use of EEG data only, and 89–90% for the combined use of the EEG and eye movement data, respectively. The average classification accuracy of using both the EEG and eye movement data is about 3% higher than using only the EEG data. Although the increase is not great, these results may indicate the potential of the eye movement data as the supportive biosignal to evaluate MCR operators' attention.

4. DISCUSSION

4.1. Applications

The proposed system could be utilized to provide a real-time monitoring of the attention levels of nuclear reactor operators during operations in the MCR. Such monitoring capability may help to enhance overall performance of the reactor operating

team without interfering with their operating duties or functions. Such capability may also provide opportunities to prevent or detect human errors, particularly in terms of an advanced NPP MCR.

Applying the proposed concept in an NPP MCR requires a high degree of information security in data utilization. The process of obtaining and transmitting EEG and eye movement data should be protected to prevent tampering or unauthorized acquisition of the data. For this reason, application of the proposed system to an advanced MCR can be through wired data transmission in conjunction with a secure USB or using the Intranet or using one-way data transmission and reception (this is because Wi-Fi and Bluetooth tools are not allowed in NPPs).

Another application of the proposed approach is to support operator training. The operators' performance during training sessions can be monitored in real-time as suggested in the study. Based on the analysis of the data, individually tailored recommendations can be provided to the trainees conserving the privacy of the data. Also, effectiveness of the existing training programs can be assessed by using the proposed approaches for program enhancement.

4.2. Biosignal and Channel Selection

In this study, use of all the available EEG channels and their potentially associated features were not considered under the consideration of avoiding overfitting of the machine learning algorithm. In fact, taking economic and ergonomic aspects into consideration, recording a full set of EEG data may not be desirable (Kim et al., 2020a). To examine this point, this study compared the EEG results from the total brain (21 channels) to the BA 10 (three channels: Fp1, Fp2, and Fpz).

Comparison of the classification accuracies from using various brain channel data indicated that using all available data or channels was not necessary for the given task, i.e., classification of attention levels. As shown in **Table 5**, the average classification accuracies of using only the BA 10 data are comparable to those of using the total brain data. This suggests that an EEG measurement implementation in the form of helmets may be possible with the use of only the BA 10 channels. Such implementation could suffice the data required for the advanced MCR application.

Furthermore, the average classification accuracy of the developed model from the combined use of the EEG and eye movement data was just 3% higher than the case of using the EEG data only (**Table 6**). Although the increase in classification accuracy is not significant from the use of additional eye movement data, the use of eye movement data may be important for human error reduction as looking at the right AOI is an important part of decision making by a nuclear operator.

While this study indicated the plausibility of using the EEG and eye movement data for attention monitoring based on mockup tasks with students as subjects, future study will consider using a full-scale simulator with professional reactor operators.

5. CONCLUSION

This study investigated the development of biosignal-based attention monitoring system for the purpose of preventing human error at NPP MCR. The system is based on a classification model for the presence or absence of operator attention. We designed general tasks and nuclear simulator tasks mimicking the situations in NPP MCR as the basis of model development. During these tasks, each subject's attention levels were examined and analyzed from their biosignals to develop the classification model. The biosignals used were the five frequency band EEG data and eye movement data. Through the use of the developed model, we demonstrated that the presence or absence of human attention can be classified with up to 90% in accuracy. The proposed methods could be adopted to other industrial applications for the purpose of human performance enhancement and/or human error reduction based on attention monitoring.

DATA AVAILABILITY STATEMENT

The original contributions presented in the study are included in the article/supplementary material, further inquiries can be directed to the corresponding author/s.

ETHICS STATEMENT

The studies involving human participants were reviewed and approved by Korea Advanced Institute of Science and Technology (KAIST) Institutional Review Board (IRB) guideline. The patients/participants provided their written informed consent to participate in this study.

AUTHOR CONTRIBUTIONS

JK carried out the conception and design of study, acquisition of data, analysis and interpretation of data, and drafting of the manuscript. CK performed the acquisition, analysis, and interpretation of data. E-SJ was responsible for the design of an experiment and the drafting of the manuscript. M-SY supervised, interpreted data, and revised the manuscript critically for important intellectual content. All authors contributed to the article and approved the submitted version.

FUNDING

This work was supported by the Nuclear Safety Research Program through the Korea Foundation Of Nuclear Safety (KoFONS) using the financial resource granted by the Nuclear Safety and Security Commission (NSSC) of the Republic of Korea (No. 2003023).

REFERENCES

- Choi, J., Kim, H., Jung, W., and Lee, S. J. (2019). Analysis of interface management tasks in a digital main control room. *Nuclear Eng. Technol.* 51, 1554–1560. doi: 10.1016/j.net.2019.04.010
- Choi, M. K., Lee, S. M., Ha, J. S., and Seong, P. H. (2018). Development of an EEG-based workload measurement method in nuclear power plants. *Ann. Nuclear Energy* 111, 595–607. doi: 10.1016/j.anucene.2017.08.032
- Delorme, A., and Makeig, S. (2004). EEGLAB: an open source toolbox for analysis of single-trial EEG dynamics including independent component analysis. *J. Neurosci. Methods* 134, 9–21. doi: 10.1016/j.jneumeth.2003.10.009
- Diaz-Uriarte, R. (2007). GeneSrf and varSelRF: a web-based tool and R package for gene selection and classification using random forest. *BMC Bioinform.* 8:328. doi: 10.1186/1471-2105-8-328
- Ha, J. S., Byon, Y.-J., Baek, J., and Seong, P. H. (2016). Method for inference of operators' thoughts from eye movement data in nuclear power plants. *Nuclear Eng. Technol.* 48, 129–143. doi: 10.1016/j.net.2015.09.004
- Heuer, S., and Hallowell, B. (2015). A novel eye-tracking method to assess attention allocation in individuals with and without aphasia using a dual-task paradigm. *J. Commun. Disord.* 55, 15–30. doi: 10.1016/j.jcomdis.2015.01.005
- Holmqvist, K., Nyström, M., Andersson, R., Dewhurst, R., Jarodzka, H., and Van de Weijer, J. (2011). *Eye Tracking: A Comprehensive Guide to Methods and Measures*. Oxford: Oxford University Press.
- Jung, E.-S., Dong, S.-Y., and Lee, S.-Y. (2019). Neural correlates of variations in human trust in human-like machines during non-reciprocal interactions. *Sci. Rep.* 9, 1–10. doi: 10.1038/s41598-019-46098-8
- Jung, E.-S., Lee, D.-G., Lee, K., and Lee, S.-Y. (2017). Temporally robust eye movements through task priming and self-referential stimuli. *Sci. Rep.* 7, 1–11. doi: 10.1038/s41598-017-07641-7
- Kim, J. H., Kim, C. M., Lee, Y. H., and Yim, M.-S. (in press). Electroencephalography-based intention monitoring to support nuclear operators' communications for safety-relevant tasks. *Nuclear Technol.* doi: 10.1080/00295450.2020.1837583
- Kim, J. H., Kim, C. M., and Yim, M.-S. (2020a). An investigation of insider threat mitigation based on EEG signal classification. *Sensors* 20:6365. doi: 10.3390/s20216365
- Kim, J. H., Suh, Y. A., and Yim, M. S. (2018). "An investigation of human error identification based on bio-monitoring system (EEG and ECG analysis)," in *2018 International Conference on Applied Human Factors and Ergonomics* (Orlando, FL), 145–151. doi: 10.1007/978-3-319-94866-9_14
- Kim, J. M., Lee, G., Lee, C., and Lee, S. J. (2020b). Abnormality diagnosis model for nuclear power plants using two-stage gated recurrent units. *Nuclear Eng. Technol.* 52, 2009–2016. doi: 10.1016/j.net.2020.02.002
- Kim, S. H., Kim, H. H., Song, I. H., Hong, E. Y., and Oh, Y. T. (2000). *Development of the Nuclear Plant Analyzer for Korean Standard Nuclear Power Plants*. Technical report, Korea Power Engineering Company (KOEPC).
- Kim, T. J., Lee, C., Kang, S. K., Choi, M. K., and Seong, P. H. (2020c). An empirical study of the personality effects on diagnosis performance of human operators in unexpected plant conditions of NPPs. *Ann. Nuclear Energy* 145:107557. doi: 10.1016/j.anucene.2020.107557
- Kim, T. J., and Seong, P. H. (2019). Influencing factors on situation assessment of human operators in unexpected plant conditions. *Ann. Nuclear Energy* 132, 526–536. doi: 10.1016/j.anucene.2019.06.051
- Klimesch, W. (2012). Alpha-band oscillations, attention, and controlled access to stored information. *Trends Cogn. Sci.* 16, 606–617. doi: 10.1016/j.tics.2012.10.007
- Klimesch, W., Fellinger, R., and Freunberger, R. (2011). Alpha oscillations and early stages of visual encoding. *Front. Psychol.* 2:118. doi: 10.3389/fpsyg.2011.00118
- Klimesch, W., Freunberger, R., Sauseng, P., and Gruber, W. (2008). A short review of slow phase synchronization and memory: evidence for control processes in different memory systems? *Brain Res.* 1235, 31–44. doi: 10.1016/j.brainres.2008.06.049
- Klimesch, W., Schimke, H., and Schwaiger, J. (1994). Episodic and semantic memory: an analysis in the EEG theta and alpha band. *Electroencephalogr. Clin. Neurophysiol.* 91, 428–441. doi: 10.1016/0013-4694(94)90164-3
- Lee, H. C., Jang, T. I., Kim, S. K., Kim, C. H., Lee, Y. H., Park, G. O., et al. (2017). *Development of Human Error Countermeasures for Nuclear Safety*. Technical report, Korea Atomic Energy Research Institute (KAERI).
- Liu, N.-H., Chiang, C.-Y., and Chu, H.-C. (2013). Recognizing the degree of human attention using EEG signals from mobile sensors. *Sensors* 13, 10273–10286. doi: 10.3390/s130810273
- López-Gil, J.-M., Virgili-Gomá, J., Gil, R., Guilera, T., Batalla, I., Soler-González, J., et al. (2016). Method for improving EEG based emotion recognition by combining it with synchronized biometric and eye tracking technologies in a non-invasive and low cost way. *Front. Comput. Neurosci.* 10:85. doi: 10.3389/fncom.2016.00119
- Mullen, T. (2012). *CleanLine EEGLAB Plugin*. San Diego, CA: Neuroimaging Informatics Tools and Resources Clearinghouse (NITRC).
- Mumaw, R. J., Roth, E. M., Vicente, K. J., and Burns, C. M. (2000). There is more to monitoring a nuclear power plant than meets the eye. *Human Fact.* 42, 36–55. doi: 10.1518/001872000779656651
- Oh, Y. J., and Lee, Y. H. (2013). Human error identification based on EEG analysis for the introduction of digital devices in nuclear power plants. *J. Ergon. Soc. Korea* 32, 27–36. doi: 10.5143/JESK.2013.32.1.27
- Pallavi, T., and Harish, G. (2016). "Implementation of EEG based driver's attention tracking and habitats monitoring system," in *2016 International Conference on Communication and Electronics Systems (ICCES)* (Coimbatore). doi: 10.1109/CESYS.2016.7889852
- Palmer, J. A., Kreutz-Delgado, K., and Makeig, S. (2012). *AMICA: An Adaptive Mixture of Independent Component Analyzers with Shared Components*. Technical report, Swartz Center for Computational Neuroscience, University of California San Diego, San Diego, CA.
- Pascucci, D., Hervais-Adelman, A., and Plomp, G. (2018). Gating by induced A-Γ asynchrony in selective attention. *Hum. Brain Mapp.* 39, 3854–3870. doi: 10.1002/hbm.24216
- Pei, G., Wu, J., Chen, D., Guo, G., Liu, S., Hong, M., et al. (2018). Effects of an integrated neurofeedback system with dry electrodes: EEG acquisition and cognition assessment. *Sensors* 18:3396. doi: 10.3390/s18103396
- Peng, K., Steele, S. C., Becerra, L., and Borsook, D. (2018). Brodmann area 10: collating, integrating and high level processing of nociception and pain. *Prog. Neurobiol.* 161, 1–22. doi: 10.1016/j.pneurobio.2017.11.004
- Savchenko, K., Medema, H., Boring, R., and Ulrich, T. (2017). "Comparison of mutual awareness in analog vs. digital control rooms," in *2017 International Conference on Applied Human Factors and Ergonomics* (Los Angeles, CA), 192–199. doi: 10.1007/978-3-319-60645-3_19
- Sohn, S.-W., Song, I.-H., Jeong, S.-C., Sohn, J.-J., and Kim, E.-K. (2011). *Development of a Performance Validation Tool for NSSS Control System*. Technical report, Korea Power Engineering Company (KOEPC).
- Tang, X., Xia, L., Liu, W., Peng, Y., Chen, D., Gao, T., et al. (2013). Analysis of frequency domain of EEG signals in clinical location of epileptic focus. *Clin. EEG Neurosci.* 44, 25–30. doi: 10.1177/1550059412451215
- Wang, L., Wang, W., Yan, T., Song, J., Yang, W., Wang, B., et al. (2017). Beta-band functional connectivity influences audiovisual integration in older age: an EEG study. *Front. Aging Neurosci.* 9:239. doi: 10.3389/fnagi.2017.00239
- Wickens, C. D., Gordon, S. E., and Liu, Y. (1998). *An Introduction to Human Factors Engineering*. New York, NY: Longman.
- Yang, J., Kim, T., and Kim, J. (2017). Analysis of errors of commission for a CE type plant with the advanced control room in the full power condition. *Ann. Nuclear Energy* 105, 184–195. doi: 10.1016/j.anucene.2017.03.019
- Zeng, K., Wang, Y., Ouyang, G., Bian, Z., Wang, L., and Li, X. (2015). Complex network analysis of resting state EEG in amnesic mild cognitive impairment patients with type 2 diabetes. *Front. Comput. Neurosci.* 9:133. doi: 10.3389/fncom.2015.00133

Conflict of Interest: E-SJ was employed by company Samsung SDS.

The remaining authors declare that the research was conducted in the absence of any commercial or financial relationships that could be construed as a potential conflict of interest.

Copyright © 2020 Kim, Kim, Jung and Yim. This is an open-access article distributed under the terms of the Creative Commons Attribution License (CC BY). The use, distribution or reproduction in other forums is permitted, provided the original author(s) and the copyright owner(s) are credited and that the original publication in this journal is cited, in accordance with accepted academic practice. No use, distribution or reproduction is permitted which does not comply with these terms.



Alternation of Resting-State Functional Connectivity Between Visual Cortex and Hypothalamus in Guinea Pigs With Experimental Glucocorticoid Enhanced Myopia After the Treatment of Electroacupuncture

OPEN ACCESS

Edited by:

Jinghao Zhou,
University of Maryland, Baltimore,
United States

Reviewed by:

Yong Li,
Shanghai Jiao Tong University, China
Yuchun Tang,
Shandong University, China

*Correspondence:

Wenjun Jiang
liz_jiang@139.com
Hongsheng Bi
hongshengbi1@163.com

[†]These authors have contributed
equally to this work and share first
authorship

Received: 03 July 2020

Accepted: 07 December 2020

Published: 13 January 2021

Citation:

Zhang T, Jiang Q, Xu F, Zhang R,
Liu D, Guo D, Wu J, Wen Y, Wang X,
Jiang W and Bi H (2021) Alternation of
Resting-State Functional Connectivity
Between Visual Cortex and
Hypothalamus in Guinea Pigs With
Experimental Glucocorticoid
Enhanced Myopia After the Treatment
of Electroacupuncture.
Front. Neuroinform. 14:579769.
doi: 10.3389/fninf.2020.579769

Tao Zhang^{1†}, Qian Jiang^{2†}, Furu Xu^{2†}, Ruixue Zhang², Dezheng Liu², Dadong Guo³,
Jianfeng Wu², Ying Wen⁴, Xingrong Wang⁴, Wenjun Jiang^{3*} and Hongsheng Bi^{3*}

¹ The First College of Clinical Medicine, Shandong University of Traditional Chinese Medicine, Jinan, China, ² Department of Ophthalmology and Optometry, Shandong University of Traditional Chinese Medicine, Jinan, China, ³ Shandong Province Key Laboratory of Integrated Traditional Chinese and Western Medicine for Prevention and Therapy of Ocular Disease, Eye Institute of Shandong University of Traditional Chinese Medicine, Jinan, China, ⁴ Affiliated Eye Hospital of Shandong University of Traditional Chinese Medicine, Jinan, China

Excessive glucocorticoids (GC) may lead to the aggravation of several basic diseases including myopia, due to plasma hormone imbalances associated with the hypothalamic–pituitary–adrenal axis (HPAA). Electroacupuncture (EA) is an effective therapeutic method to treat many diseases, although it remains unclear whether EA at acupoints on the foot or back would be effective in treating eye diseases. It was recently found that visual cortex activity for responses to visual stimuli with spatial frequency and resting-state functional connectivity (FC) between the supramarginal gyrus and rostralateral prefrontal cortex was significantly reduced in patients with high myopia. The present study aims to investigate the role of the alternation of resting-state FC among the bilateral visual cortex and hypothalamus in exerting anti-myopia effects of EA in GC-enhanced lens-induced myopic (LIM) guinea pigs such that the mechanisms of EA to treat GC-enhanced myopia at Shenshu (BL23) acupoints can be probed. To confirm the effects of EA, ocular parameters including axial length and GC-associated physiological parameters such as animal appearance, behavior, bodyweight, and levels of four HPAA-associated plasma hormones [free triiodothyronine (FT3), free thyroxine (FT4), estradiol (E2), and testosterone (T)] were also collected. Increased resting-state FC between the left and right visual cortex was detected in GC-enhanced lens-induced myopic guinea pigs with EA at BL23 acupoints (LIM+GC+EA) guinea pigs compared to GC-enhanced lens-induced myopic guinea pigs with EA at sham acupoints (LIM+GC+Sham) guinea pigs, as well as suppressed myopia and recovery of symptoms

initially caused by overdose of GC. Recovered symptoms included improved animal appearance, behavior, bodyweight, and HPAA-associated plasma hormone levels were observed after 4 weeks of EA treatment. In contrast, the LIM+GC+Sham group showed decreased FC with elongation of axial length for myopization as compared to the control group and LIM group and exhibited a deterioration in physiological parameters including reduced body weight and balance disruption in the four measured HPAA-associated plasma hormones. Our findings suggest that EA could effectively treat GC-enhanced myopia by increasing resting-state FC between the left and right visual cortices, which may be pivotal to further understanding the application and mechanisms of EA in treating GC-enhanced myopia.

Keywords: functional connectivity, resting-state fMRI, neuroimaging, electroacupuncture, glucocorticoid, myopia

INTRODUCTION

High myopia is a major public health concern, often accompanied by several severe comorbidities, including retinal detachment, cataracts, and glaucoma due to the elongation of axial length (Rudnicka et al., 2016; Morgan et al., 2018). Currently, excessive myopic axial length elongation and increased risk of irreversible visual impairment have been found in experimental lens-induced myopia after intraperitoneal injection of the glucocorticoids (GC) (Ding et al., 2018). The imbalance of four plasma hormones associated with the hypothalamic–pituitary–adrenal axis (HPAA), including free triiodothyronine (FT3), free thyroxine (FT4), estradiol (E2), and testosterone (T), is often caused by excess GC. Excess GC also causes deteriorated physical conditions as well as a reduction in body weight and then resulted in enhancement of basic disorders, such as arthritis and diabetes (De Bosscher and Haegeman, 2009; Lu et al., 2011; Vieira et al., 2011; Wang et al., 2015; Ferreira et al., 2016; Oray et al., 2016; Xia et al., 2017; Yan et al., 2017; Hasona, 2018; Panettieri et al., 2019). Interestingly, electroacupuncture (EA) has been proven to be an effective therapeutic method to treat GC-induced diseases at the Shenshu (BL23) acupoint which was located adjacent to the second lumbar vertebra on the back (Wang et al., 2015; Feng et al., 2018).

Using resting-state functional MRI (rsfMRI), functional connectivity (FC) between brain regions can be assessed by analyzing the temporal relationships of blood oxygen level-dependent (BOLD) fluctuations between brain regions (Chong et al., 2019; O'Neill et al., 2019). In recent years, various studies utilized rsfMRI to investigate the underlying mechanisms of eye diseases including myopia and amblyopia (Hu et al., 2018; Dai et al., 2019). Previous studies reported that visual cortex activity for responses to visual stimuli with spatial frequency, and resting-state FC between the supramarginal gyrus and the rostralateral prefrontal cortex, was significantly reduced in high-myopia patients (Zhai et al., 2016; Mirzajani et al., 2017). It was also reported that FC density significantly decreased in the posterior cingulate cortex/precuneus (PCC/preCun) (Zhai et al., 2016). However, the role of resting-state FC between the left and right visual cortex on the treatment of high myopia has not yet been explored.

Consequently, there is considerable interest in discovering means to explore whether EA would affect brain function in treating GC-enhanced eye diseases at BL23 acupoints located on the back. In the present study, we aimed to investigate alternation of resting-state FC between the visual cortex and hypothalamus to assess the effects of EA at BL23 acupoints on the treatment of GC enhanced myopia in guinea pigs. We also measured myopia-related ocular parameters including axial length, and GC-associated physiological parameters including animal appearance, behavior, body weight, and levels of four plasma hormones related to the HPAA (FT3, FT4, E2, and T). Our study may provide insights in deepening understanding of the mechanisms of acupuncture in the treatment of GC-enhanced eye diseases at acupoints far from the eyes.

MATERIALS AND METHODS

Animals

Sixty male pigmented guinea pigs (*Cavia porcellus*) at the age of 2–3 weeks were obtained from the Jinan Xijueling Laboratory Animal Ltd. (Jinan, China) and raised in the animal lab center within the Eye Institute of Shandong University of Traditional Chinese Medicine. Food and water for the guinea pigs were available *ad libitum*, and the room temperature was maintained at 22°C. The guinea pigs were reared in plastic cages (15 cm × 26 cm × 32 cm) under a 12/12 h light–dark cycle. The average light in the cage was ~300 lux. All experimental protocols and animal handling procedures were approved by the ethics committee of the Eye Institute of Shandong University of Traditional Chinese Medicine (2017-002)s and were in accordance with the statement of the Association for Research in Vision and Ophthalmology for the use of animals in vision and ophthalmological research.

GC Administration and LIM Establishment

The guinea pigs were randomly divided into four groups: control, LIM, LIM+GC+Sham, and LIM+GC+EA. The control group includes animals with no treatment ($n = 15$), and the LIM group comprises of animals with lens-induced unilateral myopization by goggles with a refractive power of -10 diopters glued onto the orbital rim of right eyes ($n = 15$). The LIM+GC+Sham group includes animals with lens-induced unilateral myopization of the

right eyes and intraperitoneal injection of hydrocortisone in a dose of 10 mg/kg once daily (8:00–10:00 a.m.) for 2 consecutive weeks and then followed in a dose of 5 mg·kg⁻¹ for the next 4 consecutive weeks to maintain the treatment effect, with EA at sham acupoints ($n = 15$), and the LIM+GC+EA group includes animals with lens-induced unilateral myopization of the right eyes and intraperitoneal injection of hydrocortisone in a dose of 10 mg/kg once daily (8:00–10:00 a.m.) for 2 consecutive weeks and then followed in a dose of 5 mg·kg⁻¹ for the next 4 consecutive weeks to maintain the treatment effect, with EA at bilateral BL23 acupoints ($n = 15$).

The animals underwent body weight measurement at baseline and at each follow-up examination. The sonographic ocular biometry for axial length measurement was also collected by A/B-mode scan (oscillator frequency: 11 MHz; Quantel Co., Les Ulis, France) at these time points. One drop of 1% cyclopentolate hydrochloride (Alcon, USA) was applied to both eyes to achieve a completely dilated pupil and cycloplegia.

Electroacupuncture

After the combined treatment of lens-induced myopia and intraperitoneal injection of hydrocortisone for 2 consecutive weeks, the guinea pigs in the LIM+GC+EA group received EA at the bilateral BL23 point for 30 min a day for 4 consecutive weeks. BL23 is located adjacent to the second lumbar vertebra on the back (Xiang et al., 2019). The guinea pigs in the LIM+GC+Sham group were treated with EA at a sham point, which was set to the “degenerated tail” on the gluteus muscle, a point further away from the traditional meridians (Wang et al., 2007). The animals were lightly immobilized using a manufactured apparatus to minimize restraint stress, and acupuncture needles (40 mm in length, 0.30 mm in diameter) were bilaterally inserted to a depth of 8 mm at BL23 once a day (2:00 p.m.). Acupuncture needles were stimulated with an electrical-stimulator (Suzhou Medical Appliance Factory of China, Model SDZ-V), and parameters were set as continuous wave electrical pulses (0.1 ms duration), with a frequency 2 Hz and an intensity of 2 mA.

Serum Collection and Radioimmunoassay

The blood was drawn by cardiac puncture under anesthesia at 2 p.m. at the 0, 2, and 6 week intervals. Plasma FT3, FT4, E2, and T concentrations were determined in duplicate using standard radioimmunoassay (RIA) techniques by means of 125I-RIA kits with detection limits of 5×10^{-13} M, 1×10^{-12} M, 7.7×10^{-12} M, and 6.6×10^{-11} M, respectively. The different concentrations of the various hormones were measured using a gamma counter (GC-911, Anhui Ustc Zonkia Scientific Instruments Co., Ltd, China). The experimental steps were performed according to the protocols of the kits: (1) 125I FT3 and FT4 RIA kits (North Biotechnology Research Institute, Beijing) and (2) 125I E2 and T RIA kits (Tianjin JiuDing Medicine Bio-Engineering Co., Ltd, Tianjin).

MRI

Each group included six randomly selected guinea pigs for MRI after 4 weeks of EA. MRI was performed on a BioSpec 70/20 animal MRI system (Bruker BioSpin) equipped with a 7.0-T

magnet with a horizontal bore 20 cm in diameter. The operating system was ParaVision 6.0.1, and the maximum gradient strength of the gradient system was 100 mT/m, using a low-temperature phased array receiver coil. During MRI, low-dose isoflurane (Ruiward Life Technology Co., Ltd., Shenzhen, China) was used (3.5% for induction and 1.5% for maintenance), which was slightly adjusted throughout the experiment to maintain a stable breathing frequency of 90 bpm. The animal respiratory rate was monitored using a PC-SAM Small Animal Monitor (SA Instruments). The four groups of guinea pigs were each placed in a separate animal bed equipped with circulating warm water to ensure that body temperature was maintained at 37–38°C through the heated animal bed.

Anatomical images covering the entire guinea pig brain were acquired using a multislice rapid acquisition with a relaxation enhancement sequence with repetition time (TR) = 175 ms, echo time (TE) = 4.5 ms, effective echo time (TE eff) 36 ms, number of averages (NA) = 1, and number of repetitions (NR) = 4, matrix dimension (MD) = 256 * 256, pixel dimensions (V) = 50 * 50 mm², slice thickness (STH) = 1 mm, interslice distance (ISD) = 1 mm, and number of slices (NSI) = 30.

For fMRI, gradient-echo echo-planar imaging (EPI) was used with TR = 1,500 ms, TE = 20 ms, number of repetition (NR) = 180, NA = 1, MD = 256 * 256, pixel dimensions = 25 * 220 mm², slice thickness = 1 mm, interslice distance = 1 mm, number of slices = 30.

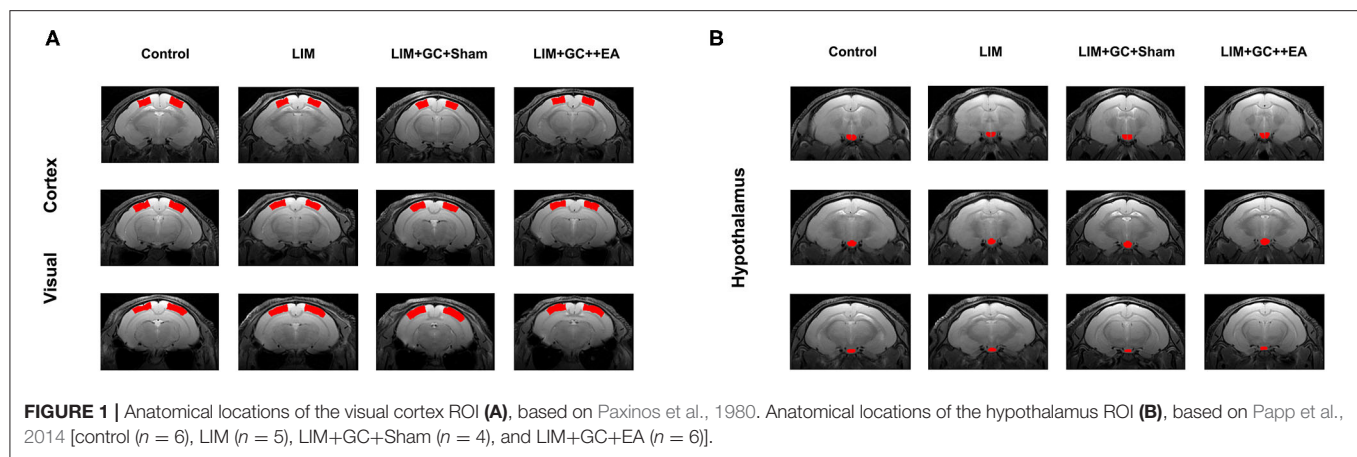
MRI Data Analysis

We segmented the label of the visual cortex and hypothalamus manually according to the sixth edition of The Rat Brain in Stereotaxic Coordinates (Figure 1). For a subject's high-resolution T2 anatomical image, we manually performed skull-stripping to remove non-brain tissues. The next step was inhomogeneity correction. Subsequently, a control subject's brain was chosen as the brain template. We registered each subject's T2 volume to the brain template using non-linear registration. Using the transformation generated by the registration algorithm, the subject's visual cortex region (left and right) and the hypothalamus were segmented (Valdes-Hernandez et al., 2011).

The rsfMRI images were realigned and corrected for slice timing. Afterward, a base EPI volume was extracted and skull stripping was performed to remove non-brain tissues. Linear detrending was applied for the removal of a systematic linear trend (Zerbi et al., 2014). The data was then band-pass filtered using a range between 0.01 and 0.3 Hz (Zerbi et al., 2018), and the subject's T2 volume was co-registered to the subject's fMRI base EPI volume. The visual cortex and the hypothalamus in the native fMR space were labeled based on the transformation generated by the registration algorithm. The left and right visual cortex and the hypothalamus were region-of-interests (ROIs), and the mean time courses of these three ROIs were extracted. The pairwise correlation coefficient among the ROIs was calculated to assess the functional connectivity between a brain region pair.

Statistical Analysis

SPSS software (Version 21.0) was used to perform statistical analyses. All data were expressed as mean \pm SEM. An



independent sample *t*-test was used to detect differences between groups. Statistical significance was considered when $P < 0.05$.

RESULTS

Changes in Morphological Behavior, Body Weight, and Hormone Levels

At baseline, all groups had similar morphological behavior, body weight, and hormone levels of FT3, FT4, T, and E2 (Figures 2B–F). After 2 weeks of treatment, GC-treated groups (LIM+GC+Sham and LIM+GC+EA) showed deteriorated animal appearance such as dull coats, shivering, and decreased activity when compared to the LIM group and the control group. In addition, the GC-treated groups (LIM+GC+Sham and LIM+GC+EA) showed significantly decreased body weight when compared to the LIM group and the control group (Figure 2B). No significant differences were observed between LIM and controls (Figure 2B). The GC-treated groups (LIM+GC+Sham and LIM+GC+EA) also had significantly decreased concentrations of FT3, FT4, and T and significantly increased concentrations of E2 compared to LIM and control groups (Figures 2C–F).

After 4 weeks of EA treatment (at the time point of “6 weeks,” as EA treatment was conducted after 2 weeks of LIM+GC treatment), the LIM+GC+EA group showed significantly increased body weight compared to the LIM+GC+Sham group, suggesting the GC-induced symptoms were ameliorated by EA (Figures 2A,B). In addition, the LIM+GC+EA guinea pigs also showed significantly increased FT3, FT4, and T concentrations with significantly decreased E2 when compared to the LIM+GC+Sham group (Figures 2C–F).

Changes of Axial Length

At baseline, a similar mean axial length of right eyes (treated) and left eyes (untreated) was observed in all groups (Table 1, Figure 3). In the control group, mean axial length of right (treated) eyes increased from 7.77 ± 0.07 mm (mean \pm standard deviation) at baseline to 8.62 ± 0.12 mm at the end of follow-up, and mean axial length of left (untreated) eyes increased from 7.79 ± 0.03 at baseline to 8.64 ± 0.07 mm at the end of follow-up. There was no significant difference between treated and

untreated eyes (Table 1). In the LIM group, the mean axial length of right eyes (treated) was significantly longer after 2 weeks of treatment compared to the control group (LIM group vs. control group, 8.20 ± 0.04 mm vs. 8.11 ± 0.04 mm, $P < 0.001$) and this increase continued in a time-dependent manner (Table 1, Figure 3A).

In groups with unilateral lens-induced myopization and intraperitoneal injection of hydrocortisone (LIM+GC+Sham and LIM+GC+EA), the mean axial lengths of the right eyes (treated eyes) were significantly longer compared to the LIM group after combined treatment of GC and lens-induced myopization for 2 weeks, thus suggesting that excess GC significantly increased the degree of lens-induced myopia [(LIM+GC+Sham group vs. LIM group, 8.26 ± 0.10 mm vs. 8.20 ± 0.04 mm, $P < 0.05$; LIM+GC+EA group vs. LIM group, 8.26 ± 0.07 mm vs. 8.20 ± 0.04 mm, $P < 0.05$] (Table 1, Figure 3A). However, there was no significant difference in axial length between LIM+GC+Sham and LIM+GC+EA at that time point (LIM+GC+EA vs. LIM+GC+Sham, 8.26 ± 0.10 mm vs. 8.26 ± 0.07 mm, $P = 0.833$) (Table 1, Figure 3A).

Interestingly, after the treatment of EA at BL23 for 4 weeks, the axial length of the right eyes was significantly shorter in the LIM+GC+EA group compared to the LIM+GC+Sham group (LIM+GC+EA vs. LIM+GC+Sham, 8.79 ± 0.07 mm vs. 8.87 ± 0.04 mm, $P < 0.05$) (Table 1, Figure 3A). No significant difference was found in the axial lengths of the left eyes (untreated eyes) among each group at any time interval (Table 1, Figure 3B).

Altered Resting-State FC

Among the four groups, control ($n = 6$), LIM ($n = 5$), LIM+GC+Sham ($n = 4$), and LIM+GC+EA ($n = 6$), there were significant differences across the groups, as shown through linear regression modeling ($p = 0.05$). As shown in Figure 4, we found that the FC between the left and right visual cortices of the LIM group was significantly lower than that of the control ($p = 0.02$). The FC of the visual cortex of the LIM+GC+Sham group was also lower than that of control ($p = 0.03$). Of note, the FC of visual cortex of the LIM+GC+EA group is higher than that of LIM and LIM+GC+Sham groups. The difference in FC between the visual cortices was not significant between control and LIM+GC+EA; no significant difference between the LIM

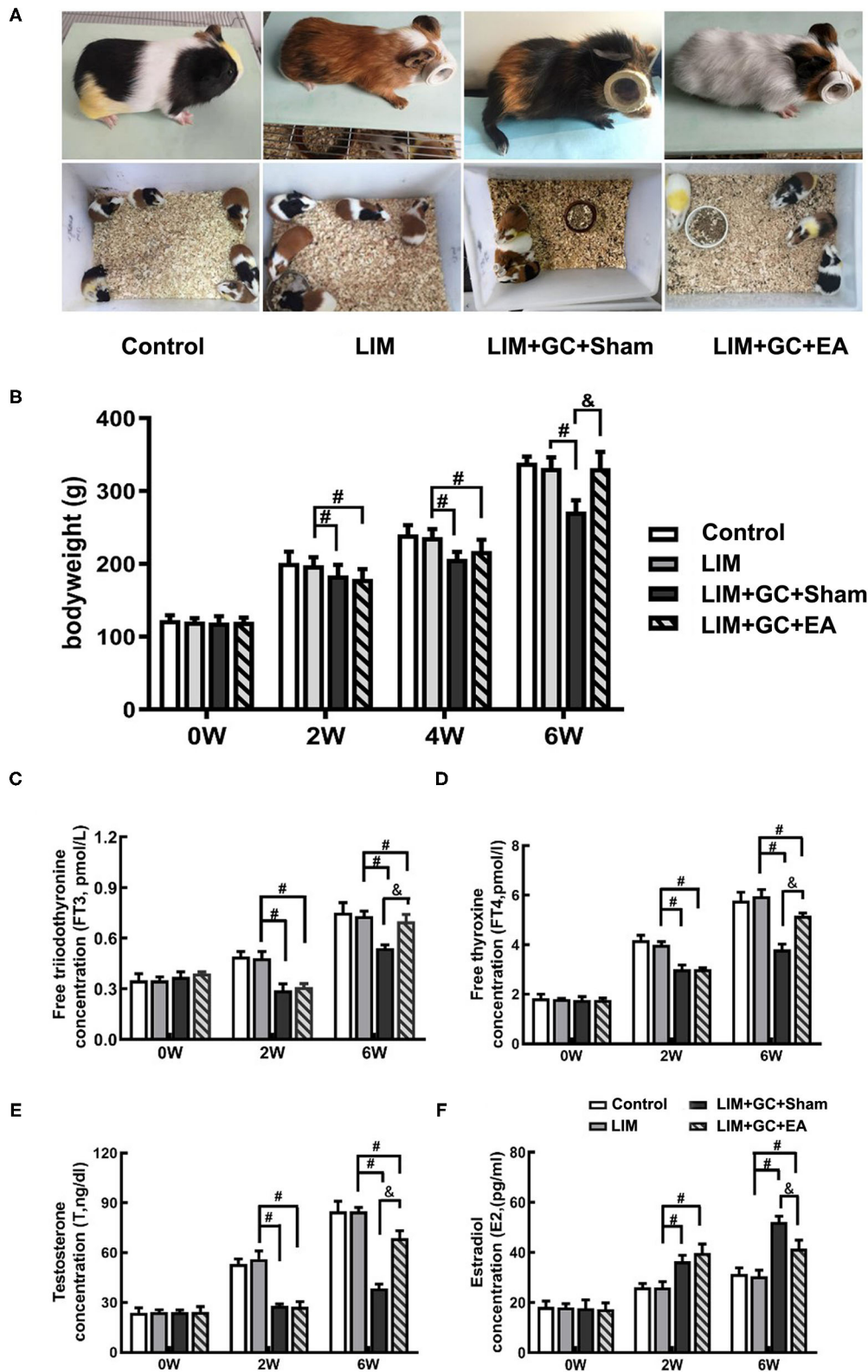
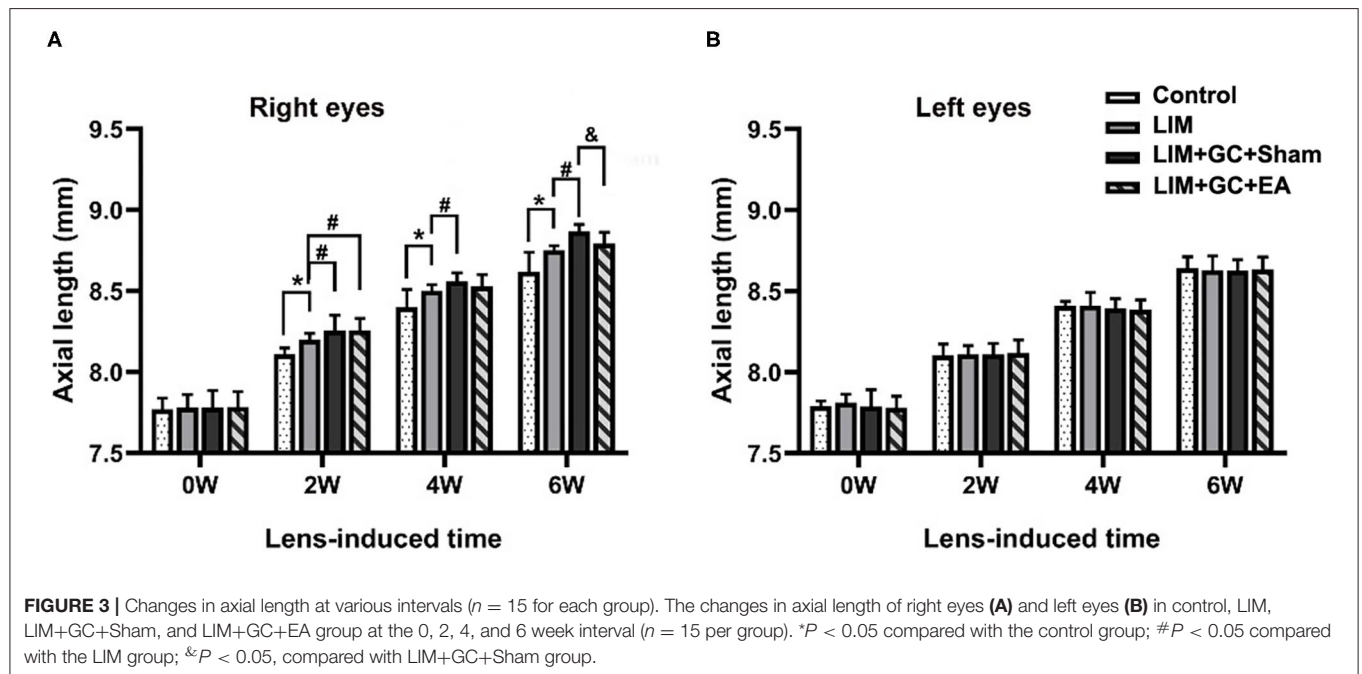


FIGURE 2 | The change in morphological behavior, body weight, and hormone level ($n = 15$ for each group). The changes in morphological behavior after the treatment for 6 w (A), and alterations of body weight (B) and hormones, including FT3 (C), FT4 (D), T (E), and E2 (F) in serum in all time intervals. # $P < 0.05$ compared with the LIM group; & $P < 0.05$, compared with LIM+GC+Sham group.

TABLE 1 | Sonographic biometric measurements (mean \pm standard deviation; OD: right eyes; OS: right eyes).

Group	Time (week)	OD (mm)				OS (mm)			
		Vitreous cavity length	Anterior chamber depth	Lens thickness	Axial length	Vitreous cavity length	Anterior chamber depth	Lens thickness	Axial length
Control	0	3.42 \pm 0.05	1.16 \pm 0.01	3.18 \pm 0.05	7.77 \pm 0.07	3.43 \pm 0.06	1.17 \pm 0.02	3.19 \pm 0.02	7.79 \pm 0.03
	2	3.49 \pm 0.03	1.22 \pm 0.03	3.40 \pm 0.02	8.11 \pm 0.04	3.50 \pm 0.05	1.20 \pm 0.03	3.40 \pm 0.04	8.10 \pm 0.07
	4	3.58 \pm 0.09	1.23 \pm 0.02	3.60 \pm 0.05	8.40 \pm 0.11	3.59 \pm 0.04	1.23 \pm 0.01	3.59 \pm 0.04	8.41 \pm 0.03
	6	3.63 \pm 0.07	1.26 \pm 0.02	3.73 \pm 0.06	8.62 \pm 0.12	3.67 \pm 0.06	1.25 \pm 0.03	3.72 \pm 0.04	8.64 \pm 0.07
LIM	0	3.42 \pm 0.05	1.16 \pm 0.03	3.18 \pm 0.04	7.78 \pm 0.08	3.44 \pm 0.04	1.17 \pm 0.02	3.20 \pm 0.04	7.81 \pm 0.05
	2	3.55 \pm 0.04*	1.21 \pm 0.04	3.45 \pm 0.03	8.20 \pm 0.04*	3.50 \pm 0.05	1.20 \pm 0.03	3.41 \pm 0.03	8.11 \pm 0.05
	4	3.65 \pm 0.03*	1.22 \pm 0.03	3.63 \pm 0.04	8.50 \pm 0.04*	3.57 \pm 0.06	1.23 \pm 0.02	3.61 \pm 0.03	8.41 \pm 0.08
	6	3.74 \pm 0.02*	1.26 \pm 0.02	3.75 \pm 0.03	8.75 \pm 0.03*	3.65 \pm 0.09	1.25 \pm 0.03	3.73 \pm 0.03	8.63 \pm 0.09
LIM+GC+Sham	0	3.43 \pm 0.08	1.16 \pm 0.03	3.18 \pm 0.07	7.78 \pm 0.10	3.43 \pm 0.05	1.16 \pm 0.03	3.20 \pm 0.07	7.79 \pm 0.10
	2	3.57 \pm 0.04*, #	1.21 \pm 0.02	3.47 \pm 0.08*	8.26 \pm 0.10*	3.50 \pm 0.04	1.21 \pm 0.03	3.41 \pm 0.04	8.11 \pm 0.07
	4	3.69 \pm 0.03*, #	1.24 \pm 0.02	3.64 \pm 0.05	8.56 \pm 0.05*	3.57 \pm 0.03	1.24 \pm 0.02	3.59 \pm 0.04	8.40 \pm 0.06
	6	3.85 \pm 0.04*, #	1.26 \pm 0.02	3.77 \pm 0.03	8.87 \pm 0.04*, #	3.64 \pm 0.05	1.26 \pm 0.02	3.73 \pm 0.06	8.63 \pm 0.07
LIM+GC+EA	0	3.43 \pm 0.06	1.16 \pm 0.03	3.19 \pm 0.05	7.78 \pm 0.10	3.42 \pm 0.05	1.16 \pm 0.03	3.20 \pm 0.05	7.78 \pm 0.07
	2	3.57 \pm 0.04*, #	1.20 \pm 0.02	3.48 \pm 0.06*	8.26 \pm 0.07*	3.52 \pm 0.06	1.19 \pm 0.02	3.41 \pm 0.06	8.12 \pm 0.08
	4	3.68 \pm 0.03*	1.23 \pm 0.02	3.63 \pm 0.04	8.54 \pm 0.03*	3.56 \pm 0.06	1.23 \pm 0.02	3.60 \pm 0.06	8.39 \pm 0.06
	6	3.79 \pm 0.05*, &	1.26 \pm 0.04	3.74 \pm 0.05	8.79 \pm 0.07*, &	3.66 \pm 0.08	1.25 \pm 0.03	3.73 \pm 0.06	8.63 \pm 0.08

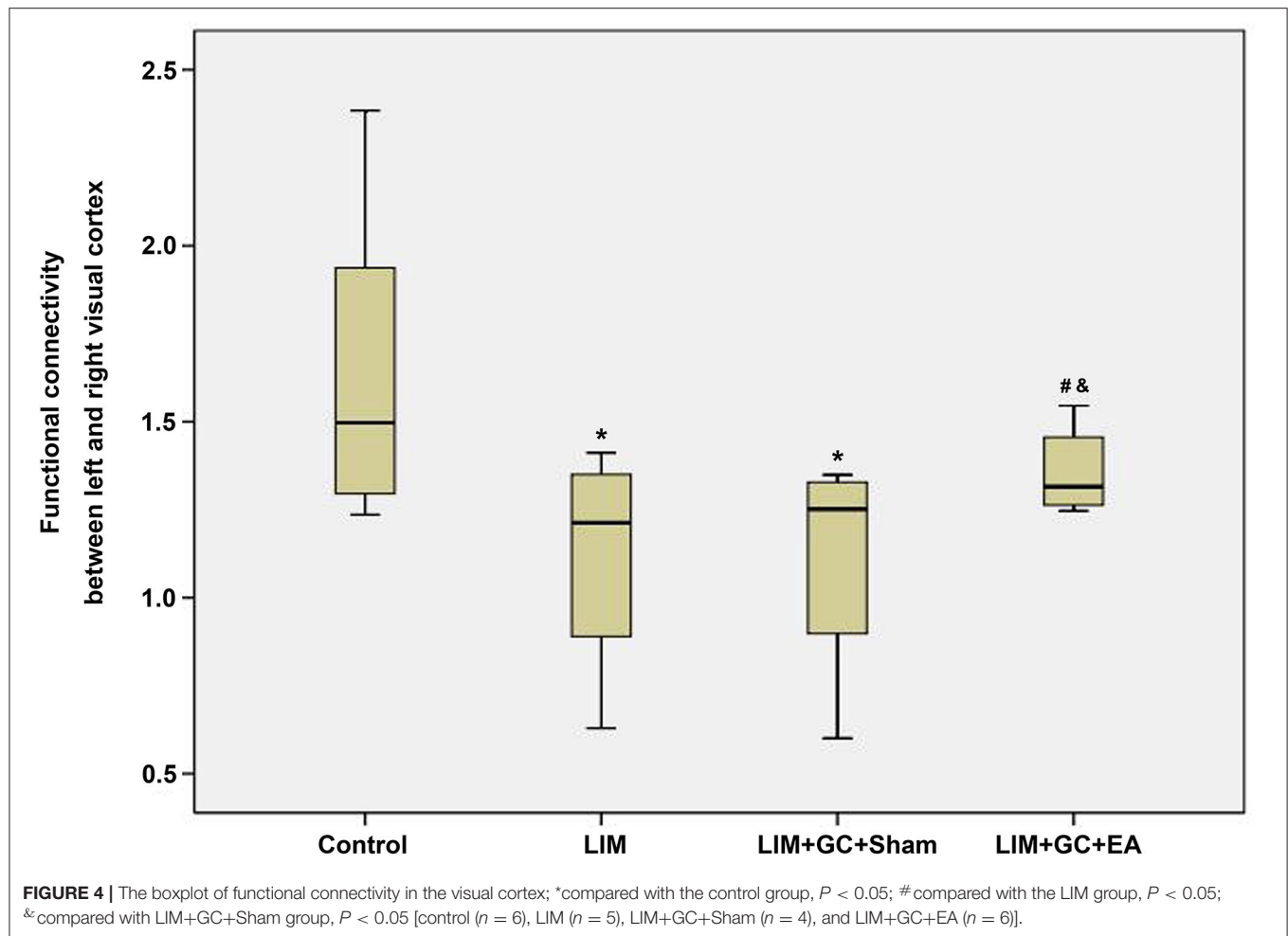
* $P < 0.05$ compared with the control group; # $P < 0.05$ compared with the LIM group; & $P < 0.05$, compared with the LIM+GC+Sham group ($n = 15$).



group and the LIM+GC+Sham group was found either ($p > 0.05$). Meanwhile, we did not find any significant difference for FC between the hypothalamus and each side of the visual cortex among all the four groups.

To further elucidate the relationship of FC between the visual cortex and parameters of animals, we conducted regression

analyses between them. Results from the analyses showed a positive association between FC of the visual cortex and bodyweight, FT3 and T, whereas a negative association was found between FC of the visual cortex and E2 or axial length (Figure 5). However, no significant relationship was found between FC of the visual cortex and FT4.



DISCUSSION

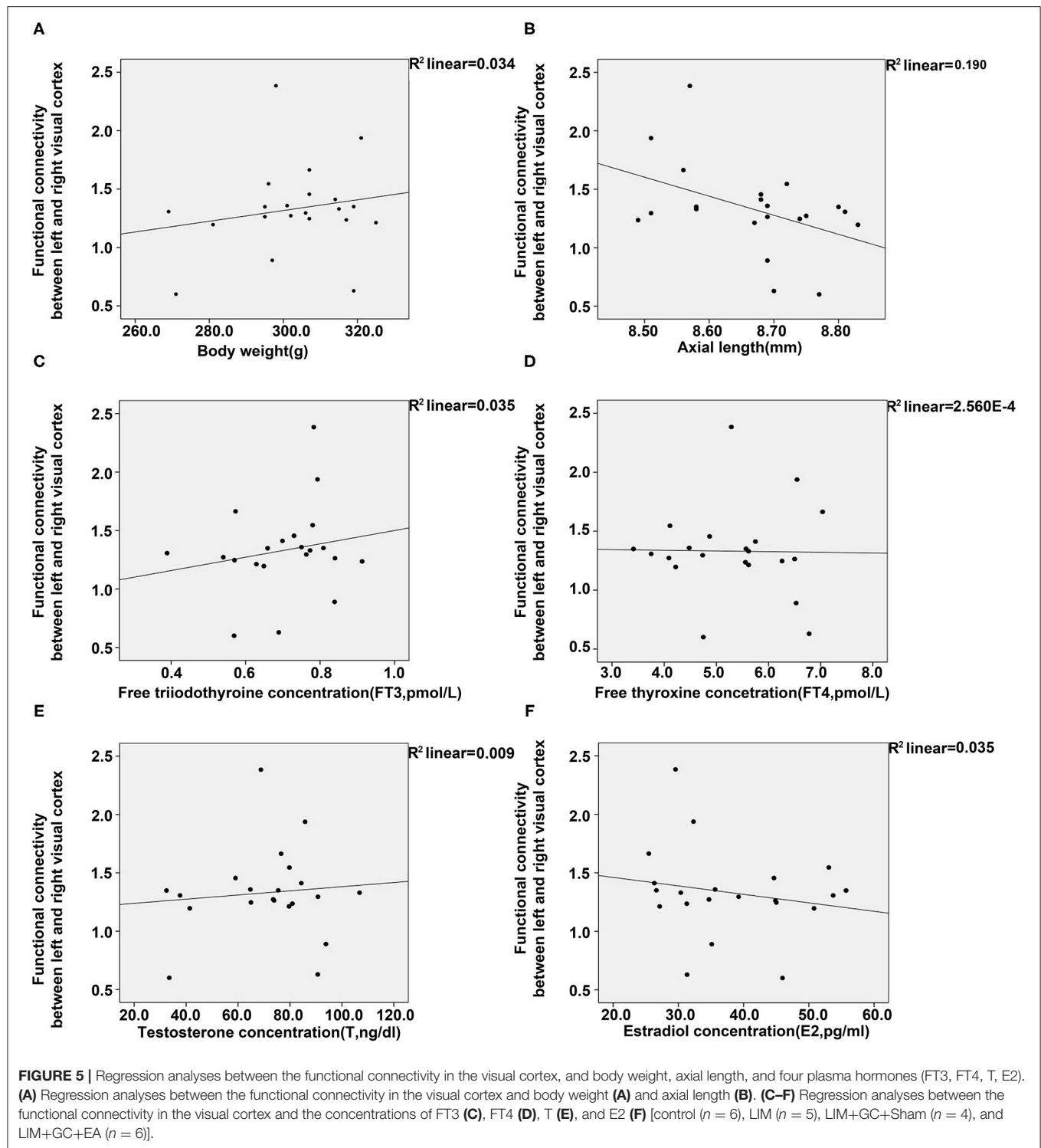
The prevalence of myopia has markedly increased within the past three decades, especially in China. The main characteristic of myopia is the irreversible elongation of axial length, resulting in many severe visual impairments including myopic macular degeneration, glaucoma, and even blind (Rudnicka et al., 2016; Morgan et al., 2018). In addition, overdose of GC could also induce excessive myopic axial length elongation and imbalance of four plasma hormones associated with hypothalamic–pituitary–adrenal axis (HPAA), including E2, T, FT3, and FT4 (Ding et al., 2018). The receptors of E2 and T are widely expressed in various ocular tissues (Wickham et al., 1998, 2000; Suzuki et al., 2001).

The guinea pigs have been a classic model to evaluate the effects of various therapeutic methods on myopia as well as its complications. Similar to the process of eye development in human beings, guinea pigs show hyperopia at birth and then rapidly become emmetropia within the first 3 weeks (21 days) of age (Shan et al., 2018). Their eyes have a more similar structure and biometric changes in the development of myopia as human beings, compared to other experimental model animals such as chicks and mice as well (Wu et al., 2020). In the present study,

a low dose of isoflurane was used to maintain stable breathing frequency in anesthetized animals, and low-dose isoflurane maintained the resting-state networks of anesthetized animals to be similar to wake ones in rats and mice. The protection in resting-state neuron activity may result from a moderate systemic vasodilator effect due to increasing resting blood flow from low-dose isoflurane (Iida et al., 1998; Guilfoyle et al., 2013; Zhou et al., 2014). Moreover, isoflurane was not reported to be a risk factor for GC signaling or myopiazation, suggesting that it would be suitable for the application in the present study. Due to the relative ease in signal acquisition and proficiency of rsfMRI technology to measure the functional connectivity (FC) between functional areas of the brain in different populations, we choose the axial length and the resting-state functional connectivity using rsfMRI technology to assess the effects of EA at BL23 on GC-enhanced myopia. It strongly suggested that FC between the visual cortices played an important role in myopiazation.

FC in the Myopic Guinea Pig's Brain

It has been demonstrated that the amplitude of low-frequency fluctuation values in high-myopia patients are reduced in the right cerebellum anterior lobe/calcarine/bilateral



parahippocampal gyrus, bilateral posterior cingulate cortex, and bilateral middle cingulate cortex, while they are significantly increased in the left optic radiation, bilateral frontal parietal cortex, and left primary motor cortex (M1)/primary somatosensory cortex (S1) (Huang et al.,

2016; Cheng et al., 2020). Meanwhile, it was found that the high myopia exhibited significantly decreased short- and long-range FC densities in the posterior cingulate cortex/precuneus (PCC/preCun), with a similar result reported in amblyopia patients, which showed decreased

FC between the PCC/preCun and bilateral primary visual areas (Ding et al., 2013; Zhai et al., 2016).

Our results indicated that FC between the visual cortex in the LIM+GC+Sham group and LIM group was significantly lower compared to the control group with the elongation of axial length. It exhibited many similarities with previous studies. It was reported that expression of neurotransmitters and their receptors changed in the primary visual cortex during the development of myopia (Zhao et al., 2017). Researches found that induced high myopia caused a significant reduction in the visual cortex activity by presenting a high range of spatial frequencies using functional MRI compared to the normal vision state (Mirzajani et al., 2017). Meanwhile, a resting-state functional magnetic resonance imaging study also demonstrated that low/moderate myopia and high myopia will lead to decreased neuronal and physiological activities in the primary visual cortex by studying the amplitude of low-frequency fluctuations (Cheng et al., 2020).

Effect of Excess GC on HPA and Myopia

Evidence has shown that excessive GC resulted in deterioration of various diseases including arthritis and myopia through affecting secretion of certain hormones including FT3, FT4, E2, and T secreted from the hypothalamic pituitary target gland (adrenal, thyroid, and gonad) axis into target gland (Yang et al., 2008; Pace et al., 2009; Ding et al., 2018). It was found that concentrations of FT3, FT4, and T decreased while E2 elevated after the treatment of GC in the present study. These findings are consistent with previous studies that intraperitoneal injection of hydrocortisone, a type of GC, results in deteriorated animal appearance and a reduced body weight, accompanied with the suppression of the HPA function by affecting the HPA plasma hormone expression (Yang et al., 2008; Zhao et al., 2013, 2016). Besides, E2, as a member of estrogen, was reported to be a modulating factor that maintains the biomechanical properties and stability of the cornea and upregulate MMP-2 activity and protein expression in human retinal pigment epithelium cells, whereas T acted as an androgen of the steroid family and was reported to be associated with the biochemical characteristics of the sclera, the aqueous outflow pathway, and the iris/ciliary body (Knepper et al., 1985; Marin-Castano et al., 2003; Song et al., 2014). Also, cortisol administration elevated both the default mode network and salience network activity to a normal level to treat traumatic stress disorder and anxiety (Soravia et al., 2018). Also, it was found that intraperitoneal injection of GC can enhance myopic shift and axial elongation in guinea pigs with lens-induced myopia (Ding et al., 2018). These symptoms were also defined as “kidney-yang deficiency” in traditional Chinese medicine, which could be effectively treated by EA (Shen, 1999).

Previous studies showed that rapid intravenous infusion of hydrocortisone significantly increased the fMRI BOLD signal within the hippocampus in a time-dependent manner (Symonds et al., 2012). Additionally, it was also found that increased endogenous GC can elevate the resting-state FC of brain regions highly expressing GC receptors, such as the medial prefrontal cortex and medial temporal lobe (Stomby et al., 2019). Nevertheless, only FC between visual cortices was found to

be significantly associated with alteration of levels of HPA-associated hormones including FT3, T, and E2 in the serum, instead of FC between the hypothalamus and each side of the visual cortex. It might also be suggested that neuron signals between the hypothalamus and visual cortex may be through some unknown intermediate medium. Moreover, FT3 rather than FT4 played an important role in the relationship between GC and FC of the visual cortex.

Effects of EA on the Brain

Increasing evidence demonstrates that acupuncture at acupoints located in the body such as the limbs and trunk could effectively treat nervous system diseases including stroke, migraines, motor system diseases, and other diseases such as functional dyspepsia, hypertension, overweight and Crohn's disease (Cai et al., 2018). It was reported that acupuncture could effectively enhance the FC between left primary motor area and left inferior frontal gyrus to promote the compensatory response to treat refractory facial paralysis, and enhance the functional connectivity between the precentral gyrus and the hippocampus in the Alzheimer disease patients (Zheng et al., 2018; Ma et al., 2019). Acupuncture could effectively enhance the FC between the left primary motor area and left inferior frontal gyrus to promote the compensatory response, increase connectivity between the periaqueductal gray, anterior cingulate cortex, left posterior cingulate cortex, right anterior insula, limbic/paralimbic, and precuneus, and adjust the limbic-paralimbic-neocortical network, brainstem, cerebellum, and subcortical and hippocampus brain areas (Cai et al., 2018).

Researches have shown that EA at acupoints located near the eyes, including Hegu (LI4) and Taiyang (EX-HN5), was effective to improve myopia by downregulating the level of retinal GABA in a myopic guinea pig model (Sha et al., 2015). It was also found that the stimulation of acupoints in the body, such as LR3 located on the feet, activated some areas of the visual cortex (Liu et al., 2012). With the development of rsfMRI technology, more research has focused on exploring different mechanisms of treatment including acupuncture for eye diseases such as high myopia, amblyopia, and blindness, by measuring FC between brain regions (Huang et al., 2016; Mendola et al., 2018; Wen et al., 2018). It was well established that the development of myopia is highly associated with alteration of function of visual cortex (Mirzajani et al., 2017). In the present study, our data revealed that EA at BL23 acupoints, located adjacent to the second lumbar vertebra on the back, could effectively suppress the elongation of axial length induced by a combination of treatment of GC and negative lens through recovering the balance of HPA-associated plasma hormones and effectively recovering FC between the visual cortex of LIM+GC animals to normal levels, providing strong support to the notion that FC is related to the mechanism of acupuncture. It was consistent with the previous studies that acupuncture at a group of acupoints including BL23 as one of the major acupoints could relieve the symptoms of many disorders by improving the cerebral hemodynamics and cognitive deficits in the hippocampal CA1 region and rebalancing HPA-associated plasma hormones including E2, T, CORT, LH, and GnRH, or

inhibiting the expression of orexin in the lateral hypothalamus (Wang et al., 2017, 2020; Zhang et al., 2017; Ji et al., 2019; Jing et al., 2020). Despite the limited research conducted on elucidating the effects of stimulating the BL23 acupoint as a single point to cure Kidney Yang deficiency-associated disorders, it was once reported that acupuncture at BL23 could effectively treat senescence-accelerated mice by increasing levels of serum hormone T (Zhang et al., 2009). These results would provide further evidence for the hypothesis that acupuncture could treat visual impairments including high myopia, through the alteration of the function of the visual cortex at acupoints located far from the eyes.

Nevertheless, several limitations of the study should be mentioned. First, there have been no brain atlases on guinea pigs so far. We therefore performed the MRI data analysis according to the rat brain atlas. Second, the fMRI image in this study was relatively low, so a higher image resolution would definitely strengthen our conclusion. Third, the specific mechanism of glucocorticoids aggravating the development of myopia needs further exploration.

In summary, EA could effectively treat GC-enhanced myopia by increasing resting-state FC between the left and right visual cortices at BL23, which may be pivotal in understanding the underlying mechanisms of EA in the treatment of GC-enhanced myopia.

DATA AVAILABILITY STATEMENT

The original contributions presented in the study are included in the article/supplementary material, further inquiries can be directed to the corresponding author/s.

REFERENCES

- Cai, R. L., Shen, G. M., Wang, H., and Guan, Y. Y. (2018). Brain functional connectivity network studies of acupuncture: a systematic review on resting-state fMRI. *J. Integr. Med.* 16, 26–33. doi: 10.1016/j.joim.2017.12.002
- Cheng, Y., Huang, X., Hu, Y. X., Huang, M. H., Yang, B., Zhou, F. Q., et al. (2020). Comparison of intrinsic brain activity in individuals with low/moderate myopia versus high myopia revealed by the amplitude of low-frequency fluctuations. *Acta Radiol.* 61, 496–507. doi: 10.1177/0284185119867633
- Chong, C. D., Schwedt, T. J., and Hougaard, A. (2019). Brain functional connectivity in headache disorders: a narrative review of MRI investigations. *J. Cereb. Blood Flow Metab.* 39, 650–669. doi: 10.1177/0271678X17740794
- Dai, P., Zhang, J., Wu, J., Chen, Z., Zou, B., Wu, Y., et al. (2019). Altered spontaneous brain activity of children with unilateral amblyopia: a resting state fMRI study. *Neural Plast* 2019:3681430. doi: 10.1155/2019/3681430
- De Bosscher, K., and Haegeman, G. (2009). Minireview: latest perspectives on antiinflammatory actions of glucocorticoids. *Mol. Endocrinol.* 23, 281–291. doi: 10.1210/me.2008-0283
- Ding, K., Liu, Y., Yan, X., Lin, X., and Jiang, T. (2013). Altered functional connectivity of the primary visual cortex in subjects with amblyopia. *Neural Plast* 2013:612086. doi: 10.1155/2013/612086
- Ding, M., Guo, D., Wu, J., Ye, X., Zhang, Y., Sha, F., et al. (2018). Effects of glucocorticoid on the eye development in guinea pigs. *Steroids* 139, 1–9. doi: 10.1016/j.steroids.2018.09.008
- Feng, Y., Fang, Y., Wang, Y., and Hao, Y. (2018). Acupoint therapy on diabetes mellitus and its common chronic complications: a review of its mechanisms. *Biomed. Res. Int.* 2018:3128378. doi: 10.1155/2018/3128378
- Ferreira, J. F., Ahmed Mohamed, A. A., and Emery, P. (2016). Glucocorticoids and rheumatoid arthritis. *Rheum. Dis. Clin. North Am.* 42, 33–46. doi: 10.1016/j.rdc.2015.08.006
- Guilfoyle, D. N., Gerum, S. V., Sanchez, J. L., Balla, A., Sershen, H., Javitt, D. C., et al. (2013). Functional connectivity fMRI in mouse brain at 7T using isoflurane. *J. Neurosci. Methods* 214, 144–148. doi: 10.1016/j.jneumeth.2013.01.019
- Hasona, N. A. (2018). Grape seed extract attenuates dexamethasone-induced testicular and thyroid dysfunction in male albino rats. *Andrologia* 50:e13002. doi: 10.1111/and.13002
- Hu, Y. X., He, J. R., Yang, B., Huang, X., Li, Y. P., Zhou, F. Q., et al. (2018). Abnormal resting-state functional network centrality in patients with high myopia: evidence from a voxel-wise degree centrality analysis. *Int. J. Ophthalmol.* 11, 1814–1820. doi: 10.18240/ijo.2018.11.13
- Huang, X., Zhou, F. Q., Hu, Y. X., Xu, X. X., Zhou, X., Zhong, Y. L., et al. (2016). Altered spontaneous brain activity pattern in patients with high myopia using amplitude of low-frequency fluctuation: a resting-state fMRI study. *Neuropsychiatr. Dis. Treat.* 12, 2949–2956. doi: 10.2147/NDT.S118326
- Iida, H., Ohata, H., Iida, M., Watanabe, Y., and Dohi, S. (1998). Isoflurane and sevoflurane induce vasodilation of cerebral vessels via ATP-sensitive K⁺ channel activation. *Anesthesiology* 89, 954–960. doi: 10.1097/00000542-199810000-00020
- Ji, Y. H., Ji, Y. H., and Sun, B. D. (2019). [Effect of acupuncture combined with repetitive transcranial magnetic stimulation on motor function and cerebral hemodynamics in children with spastic cerebral palsy with spleen-kidney deficiency]. *Zhen Ci Yan Jiu* 44, 757–761. doi: 10.13702/j.1000-0607.190154

ETHICS STATEMENT

The animal study was reviewed and approved by the Ethics Committee of Eye Institute of Shandong University of Traditional Chinese Medicine.

AUTHOR CONTRIBUTIONS

HB and WJ conceived and formulated the research. TZ, QJ, FX, and RZ raised animals and performed treatment. WJ, QJ, FX, DL, and DG conducted rsfMRI measurement. WJ and QJ analyzed the data. WJ, QJ, and TZ wrote the paper. All authors read and approved the final manuscript.

FUNDING

This work was supported by National Key Research and Development Program (Nos. 2019YFC1710200 and 2019YFC1710204) and Key Research and Development Program of Shandong Province (2017CXGC1211, 2018JHZ005, and 2019GSF108252).

ACKNOWLEDGMENTS

We would like to thank Alice Chen, Schulich School of Medicine and Dentistry, Western University, London, ON, Canada, for her assistance in editing the manuscript. We also acknowledge Drs. Xianglin Li and Zhenbo Sun for their technical support in MRI acquisition.

- Jing, Q., Ren, L., Deng, X., Zhang, N., Fu, M., Wang, G., et al. (2020). Electroacupuncture promotes neural proliferation in hippocampus of perimenopausal depression rats via wnt/ β catenin signaling pathway. *J. Acupunct. Meridian Stud.* 13, 94–103. doi: 10.1016/j.jams.2020.03.065
- Knepper, P. A., Collins, J. A., and Frederick, R. (1985). Effects of dexamethasone, progesterone, and testosterone on IOP and GAGs in the rabbit eye. *Invest. Ophthalmol. Vis. Sci.* 26, 1093–1100.
- Liu, H., Xu, J., Shan, B., Li, Y., Li, L., Xue, J., et al. (2012). Determining the precise cerebral response to acupuncture: an improved fMRI study. *PLoS ONE* 7:e49154. doi: 10.1371/journal.pone.0049154
- Lu, X., Xiong, Z., Li, J., Zheng, S., Huo, T., and Li, F. (2011). Metabonomic study on 'Kidney-yang deficiency syndrome' and intervention effects of rhizoma drynariae extracts in rats using ultra performance liquid chromatography coupled with mass spectrometry. *Talanta* 83, 700–708. doi: 10.1016/j.talanta.2010.09.026
- Ma, B., Yang, J., Yuan, A. H., Li, C. F., Gao, T., and Song, S. T. (2019). [Effect of acupuncture and moxibustion on brain functional connectivity network in patients with refractory facial paralysis]. *Zhongguo Zhen Jiu* 39, 1321–1326. doi: 10.13703/j.0255-2930.2019.12.017
- Marin-Castano, M. E., Elliot, S. J., Potier, M., Karl, M., Striker, L. J., Striker, G. E., et al. (2003). Regulation of estrogen receptors and MMP-2 expression by estrogens in human retinal pigment epithelium. *Invest. Ophthalmol. Vis. Sci.* 44, 50–59. doi: 10.1167/iovs.01-1276
- Mendola, J. D., Lam, J., Rosenstein, M., Lewis, L. B., and Shmuel, A. (2018). Partial correlation analysis reveals abnormal retinotopically organized functional connectivity of visual areas in amblyopia. *Neuroimage Clin.* 18, 192–201. doi: 10.1016/j.nicl.2018.01.022
- Mirzajani, A., Ghorbani, M., Rasuli, B., and Mahmoud-Pashazadeh, A. (2017). Effect of induced high myopia on functional MRI signal changes. *Phys. Med.* 37, 32–36. doi: 10.1016/j.ejpm.2017.04.004
- Morgan, I. G., French, A. N., Ashby, R. S., Guo, X., Ding, X., He, M., et al. (2018). The epidemics of myopia: aetiology and prevention. *Prog. Retin. Eye Res.* 62, 134–149. doi: 10.1016/j.preteyeres.2017.09.004
- O'Neill, J., Piacentini, J. C., and Peterson, B. S. (2019). Cingulate role in tourette syndrome. *Handb. Clin. Neurol.* 166, 165–221. doi: 10.1016/B978-0-444-64196-0.00011-X
- Oray, M., Abu Samra, K., Ebrahimiadib, N., Meese, H., and Foster, C. S. (2016). Long-term side effects of glucocorticoids. *Expert Opin. Drug Saf.* 15, 457–465. doi: 10.1517/14740338.2016.1140743
- Pace, T. W., Gaylord, R. L., Jarvis, E., Girotti, M., and Spencer, R. L. (2009). Differential glucocorticoid effects on stress-induced gene expression in the paraventricular nucleus of the hypothalamus and ACTH secretion in the rat. *Stress* 12, 400–411. doi: 10.1080/10253890802530730
- Panettieri, R. A., Schaafsma, D., Amrani, Y., Koziol-White, C., Ostrom, R., and Tliba, O. (2019). Non-genomic effects of glucocorticoids: an updated view. *Trends Pharmacol. Sci.* 40, 38–49. doi: 10.1016/j.tips.2018.11.002
- Papp, E. A., Leergaard, T. B., Calabrese, E., Johnson, G. A., and Bjaalie, J. G. (2014). Waxholm Space atlas of the Sprague Dawley rat brain. *Neuroimage* 97, 374–386. doi: 10.1016/j.neuroimage.2014.04.001.2014.04.001
- Paxinos, G., Watson, C. R., and Emson, P. C. (1980). AChE-stained horizontal sections of the rat brain in stereotaxic coordinates. *J. Neurosci. Methods* 3, 129–149. doi: 10.1016/0165-0270(80)90021-7
- Rudnicka, A. R., Kapetanakis, V. V., Wathern, A. K., Logan, N. S., Gilmartin, B., Whincup, P. H., et al. (2016). Global variations and time trends in the prevalence of childhood myopia, a systematic review and quantitative meta-analysis: implications for aetiology and early prevention. *Br. J. Ophthalmol.* 100, 882–890. doi: 10.1136/bjophthalmol-2015-307724
- Sha, F., Ye, X., Zhao, W., Xu, C. L., Wang, L., Ding, M. H., et al. (2015). Effects of electroacupuncture on the levels of retinal gamma-aminobutyric acid and its receptors in a guinea pig model of lens-induced myopia. *Neuroscience* 287, 164–174. doi: 10.1016/j.neuroscience.2014.12.022
- Shan, S. W., Tse, D. Y., Zuo, B., To, C. H., Liu, Q., McFadden, S. A., et al. (2018). Integrated SWATH-based and targeted-based proteomics provide insights into the retinal emmetropization process in guinea pig. *J. Proteomics* 181, 1–15. doi: 10.1016/j.jprot.2018.03.023
- Shen, Z. (1999). The location of deficiency syndrome of kidney Yang. *Chin. Med. J.* 112, 973–975.
- Song, X., Zhao, P., Wang, G., and Zhao, X. (2014). The effects of estrogen and androgen on tear secretion and matrix metalloproteinase-2 expression in lacrimal glands of ovariectomized rats. *Invest. Ophthalmol. Vis. Sci.* 55, 745–751. doi: 10.1167/iovs.12-10457
- Soravia, L. M., Schwab, S., Weber, N., Nakataki, M., Wiest, R., Strik, W., et al. (2018). Glucocorticoid administration restores salience network activity in patients with spider phobia. *Depress. Anxiety* 35, 925–934. doi: 10.1002/da.22806
- Stomby, A., Salami, A., Dahlqvist, P., Evang, J. A., Ryberg, M., Bollerslev, J., et al. (2019). Elevated resting-state connectivity in the medial temporal lobe and the prefrontal cortex among patients with Cushing's syndrome in remission. *Eur. J. Endocrinol.* 180, 329–338. doi: 10.1530/EJE-19-0028
- Suzuki, T., Kinoshita, Y., Tachibana, M., Matsushima, Y., Kobayashi, Y., Adachi, W., et al. (2001). Expression of sex steroid hormone receptors in human cornea. *Curr. Eye Res.* 22, 28–33. doi: 10.1076/ceyr.22.1.28.6980
- Symonds, C. S., McKie, S., Elliott, R., William Deakin, J. F., and Anderson, I. M. (2012). Detection of the acute effects of hydrocortisone in the hippocampus using pharmacological fMRI. *Eur. Neuropsychopharmacol.* 22, 867–874. doi: 10.1016/j.euroneuro.2012.03.008
- Valdes-Hernandez, P. A., Sumiyoshi, A., Nonaka, H., Haga, R., Aubert-Vasquez, E., Ogawa, T., et al. (2011). An *in vivo* MRI template set for morphometry, tissue segmentation, and fMRI localization in rats. *Front. Neuroinform.* 5:26. doi: 10.3389/fninf.2011.00026
- Vieira, J. S., Saraiva, K. L., Barbosa, M. C., Porto, R. C., Cresto, J. C., Peixoto, C. A., et al. (2011). Effect of dexamethasone and testosterone treatment on the regulation of insulin-degrading enzyme and cellular changes in ventral rat prostate after castration. *Int. J. Exp. Pathol.* 92, 272–280. doi: 10.1111/j.1365-2613.2011.00772.x
- Wang, C., Zhou, D. F., Shuai, X. W., Liu, J. X., and Xie, P. Y. (2007). Effects and mechanisms of electroacupuncture at PC6 on frequency of transient lower esophageal sphincter relaxation in cats. *World J. Gastroenterol.* 13, 4873–4880. doi: 10.3748/wjg.v13.i36.4873
- Wang, S. J., Zhang, J. J., Yang, H. Y., Wang, F., and Li, S. T. (2015). Acupoint specificity on acupuncture regulation of hypothalamic-pituitary-adrenal cortex axis function. *BMC Complement. Altern. Med.* 15:87. doi: 10.1186/s12906-015-0625-4
- Wang, X., Zhang, B., Zhang, L., and Liu, S. (2017). Electroacupuncture suppresses morphine reward-seeking behavior: lateral hypothalamic orexin neurons implicated. *Neurosci. Lett.* 661, 84–89. doi: 10.1016/j.neulet.2017.09.057
- Wang, Y. Y., Gao, M., Qiu, G. P., Xu, J., Wu, Y. J., Xu, Y., et al. (2020). [Effect of electroacupuncture on the P35/P25-cyclin-dependent kinase 5-Tau pathway in hippocampus of rats with Alzheimer's disease]. *Zhen Ci Yan Jiu* 45, 194–201. doi: 10.13702/j.1000-0607.190415
- Wen, Z., Zhou, F. Q., Huang, X., Dan, H. D., Xie, B. J., and Shen, Y. (2018). Altered functional connectivity of primary visual cortex in late blindness. *Neuropsychiatr. Dis. Treat.* 14, 3317–3327. doi: 10.2147/NDT.S183751
- Wickham, L. A., Gao, J., Toda, I., Rocha, E. M., Ono, M., and Sullivan, D. A. (2000). Identification of androgen, estrogen and progesterone receptor mRNAs in the eye. *Acta Ophthalmol. Scand.* 78, 146–153. doi: 10.1034/j.1600-0420.2000.078002146.x
- Wickham, L. A., Rocha, E. M., Gao, J., Krenzer, K. L., da Silveira, L. A., Toda, I., et al. (1998). Identification and hormonal control of sex steroid receptors in the eye. *Adv. Exp. Med. Biol.* 438, 95–100. doi: 10.1007/978-1-4615-5359-5_12
- Wu, S., Guo, D., Wei, H., Yin, X., Zhang, L., Guo, B., et al. (2020). Disrupted potassium ion homeostasis in ciliary muscle in negative lens-induced myopia in Guinea pigs. *Arch. Biochem. Biophys.* 688:108403. doi: 10.1016/j.abb.2020.108403
- Xia, D., Chen, P., Du, P., Ding, L., and Liu, A. (2017). [Efficacy of acupoint catgut embedding combined with ginger-partitioned moxibustion on chronic fatigue syndrome of spleen-kidney yang deficiency syndrome and its effects on T lymphocyte subsets and activity of NK cell]. *Zhongguo Zhen Jiu* 37, 814–818. doi: 10.13703/j.0255-2930.2017.08.004
- Xiang, S. J., Li, M. H., Chan, C. O., Shen, Q., Chen, S. B., An, B. C., et al. (2019). Altered metabolites in guinea pigs with allergic asthma after acupoint sticking therapy: new insights from a metabolomics approach. *Phytomedicine* 54, 182–194. doi: 10.1016/j.phymed.2018.09.021
- Yan, Y., Pan, C., Wu, J., and Yang, L. (2017). [Efficacy of acupuncture-moxibustion periodic therapy on follicular maldevelopment differentiated

- as spleen and kidney yang deficiency]. *Zhongguo Zhen Jiu* 37, 39–44. doi: 10.13703/j.0255-2930.2017.01.009
- Yang, J., Wang, Y., Bao, Y., and Guo, J. (2008). The total flavones from Semen cuscute reverse the reduction of testosterone level and the expression of androgen receptor gene in kidney-yang deficient mice. *J. Ethnopharmacol.* 119, 166–171. doi: 10.1016/j.jep.2008.06.027
- Zerbi, V., Ielacqua, G. D., Markicevic, M., Haberl, M. G., Ellisman, M. H., A, A.B., et al. (2018). Dysfunctional autism risk genes cause circuit-specific connectivity deficits with distinct developmental trajectories. *Cereb. Cortex* 28, 2495–2506. doi: 10.1093/cercor/bhy046
- Zerbi, V., Wiesmann, M., Emmerzaal, T. L., Jansen, D., Van Beek, M., Mutsaers, M. P., et al. (2014). Resting-state functional connectivity changes in aging apoE4 and apoE-KO mice. *J. Neurosci.* 34, 13963–13975. doi: 10.1523/JNEUROSCI.0684-14.2014
- Zhai, L., Li, Q., Wang, T., Dong, H., Peng, Y., Guo, M., et al. (2016). Altered functional connectivity density in high myopia. *Behav. Brain Res.* 303, 85–92. doi: 10.1016/j.bbr.2016.01.046
- Zhang, M., Xv, G. H., Wang, W. X., Meng, D. J., and Ji, Y. (2017). Electroacupuncture improves cognitive deficits and activates PPAR-gamma in a rat model of Alzheimer's disease. *Acupunct. Med.* 35, 44–51. doi: 10.1136/acupmed-2015-010972
- Zhang, X., Peng, Y., Yu, J., Liu, C., Cheng, H., Liu, L., et al. (2009). Changes in histomorphometric and mechanical properties of femurs induced by acupuncture at the Shenshu point in the SAMP6 mouse model of senile osteoporosis. *Gerontology* 55, 322–332. doi: 10.1159/000214845
- Zhao, L., Wu, H., Qiu, M., Sun, W., Wei, R., Zheng, X., et al. (2013). Metabolic signatures of kidney yang deficiency syndrome and protective effects of two herbal extracts in rats using GC/TOF MS. *Evid. Based Complement. Alternat. Med.* 2013:540957. doi: 10.1155/2013/540957
- Zhao, L., Zhao, A., Chen, T., Chen, W., Liu, J., Wei, R., et al. (2016). Global and targeted metabolomics evidence of the protective effect of chinese patent medicine jinkui shenqi pill on adrenal insufficiency after acute glucocorticoid withdrawal in rats. *J. Proteome Res.* 15, 2327–2336. doi: 10.1021/acs.jproteome.6b00409
- Zhao, W., Bi, A. L., Xu, C. L., Ye, X., Chen, M. Q., Wang, X. T., et al. (2017). GABA and GABA receptors alterations in the primary visual cortex of concave lens-induced myopic model. *Brain Res. Bull.* 130, 173–179. doi: 10.1016/j.brainresbull.2017.01.017
- Zheng, W., Su, Z., Liu, X., Zhang, H., Han, Y., Song, H., et al. (2018). Modulation of functional activity and connectivity by acupuncture in patients with Alzheimer disease as measured by resting-state fMRI. *PLoS ONE* 13:e0196933. doi: 10.1371/journal.pone.0196933
- Zhou, I. Y., Liang, Y. X., Chan, R. W., Gao, P. P., Cheng, J. S., Hu, Y., et al. (2014). Brain resting-state functional MRI connectivity: morphological foundation and plasticity. *Neuroimage* 84, 1–10. doi: 10.1016/j.neuroimage.2013.08.037

Conflict of Interest: The authors declare that the research was conducted in the absence of any commercial or financial relationships that could be construed as a potential conflict of interest.

Copyright © 2021 Zhang, Jiang, Xu, Zhang, Liu, Guo, Wu, Wen, Wang, Jiang and Bi. This is an open-access article distributed under the terms of the Creative Commons Attribution License (CC BY). The use, distribution or reproduction in other forums is permitted, provided the original author(s) and the copyright owner(s) are credited and that the original publication in this journal is cited, in accordance with accepted academic practice. No use, distribution or reproduction is permitted which does not comply with these terms.



Stimulus Intervals Modulate the Balance of Brain Activity in the Human Primary Somatosensory Cortex: An ERP Study

Yang Liu^{1†}, Bo Dong^{1†}, Jiajia Yang², Yoshimichi Ejima², Jinglong Wu^{2,3}, Qiong Wu^{1,2*} and Ming Zhang^{1,2,4*}

¹ Department of Psychology, Suzhou University of Science and Technology, Suzhou, China, ² Cognitive Neuroscience Laboratory, Graduate School of Natural Science and Technology, Okayama University, Okayama, Japan, ³ Beijing Institute of Technology, Beijing, China, ⁴ Department of Psychology, Soochow University, Suzhou, China

OPEN ACCESS

Edited by:

Rong Chen,
University of Maryland, Baltimore,
United States

Reviewed by:

Qi Li,
Changchun University of Science and
Technology, China
Shuo Zhao,
Shenzhen University, China

*Correspondence:

Qiong Wu
wuqiong@usts.edu.cn
Ming Zhang
psychzm@mail.usts.edu.cn

[†]These authors have contributed
equally to this work and share first
authorship

Received: 10 June 2020

Accepted: 22 December 2020

Published: 27 January 2021

Citation:

Liu Y, Dong B, Yang J, Ejima Y, Wu J,
Wu Q and Zhang M (2021) Stimulus
Intervals Modulate the Balance of
Brain Activity in the Human Primary
Somatosensory Cortex: An ERP
Study.
Front. Neuroinform. 14:571369.
doi: 10.3389/fninf.2020.571369

Neuronal excitation and inhibition occur in the brain at the same time, and brain activation reflects changes in the sum of excitation and inhibition. This principle has been well-established in lower-level sensory systems, including vision and touch, based on animal studies. However, it is unclear how the somatosensory system processes the balance between excitation and inhibition. In the present ERP study, we modified the traditional spatial attention paradigm by adding double stimuli presentations at short intervals (i.e., 10, 30, and 100 ms). Seventeen subjects participated in the experiment. Five types of stimulation were used in the experiment: a single stimulus (one raised pin for 40 ms), standard stimulus (eight pins for 40 ms), and double stimuli presented at intervals of 10, 30, and 100 ms. The subjects were asked to attend to a particular finger and detect whether the standard stimulus was presented to that finger. The results showed a clear attention-related ERP component in the single stimulus condition, but the suppression components associated with the three interval conditions seemed to be dominant in somatosensory areas. In particular, we found the strongest suppression effect in the ISI-30 condition (interval of 30 ms) and that the suppression and enhancement effects seemed to be counterbalanced in both the ISI-10 and ISI-100 conditions (intervals of 10 and 100 ms, respectively). This type of processing may allow humans to easily discriminate between multiple stimuli on the same body part.

Keywords: traditional spatial attention paradigm, ERP, interstimulus interval, enhancement and suppression, primary somatosensory cortex

INTRODUCTION

When spatial attention to auditory (Alho et al., 1999; Karns and Knight, 2009) or visual stimuli (Noesselt et al., 2002; Macaluso et al., 2005) was modulated, evoked potentials were generated in the primary auditory or visual cortices. Regarding the somatosensory system, studies have been conducted using fMRI and event-related potentials (ERPs) in humans (Meador et al., 2002; Forster and Eimer, 2004; Schubert et al., 2008), and they found that attention enhances activity in the primary somatosensory cortex (SI) when using a single stimulus. Animal studies (Pilz et al., 2004; Braun et al., 2005; Reed et al., 2010) used double stimuli to show that the second stimulus suppresses the response to the first stimulus. This suggested that spatiotemporal interactions modulate the

response magnitude in human SI. However, it remains unclear how the balance between attentional enhancement and double asynchronous stimulation-induced suppression is maintained.

Many previous studies examining the effects of spatial-selective attention have found that attentional effects occur in the early stage, but they did not find modulation of somatosensory evoked potential (SEP) components generated in SI. Some ERP studies used a mechanical tactile stimulus and found a contralateral N80 component with sustained attention and a bilateral P100 component with spatial attention in the early stages (Eimer and Driver, 2000; Eimer and Forster, 2003b; Zopf et al., 2004). Other electroencephalography (EEG) studies using tactile spatial sustained attention to mechanical stimuli found that the earliest somatosensory component (P50) was significantly increased for attended stimuli (Zopf et al., 2004). In a simultaneous EEG-fMRI study, Schubert et al. (2008) used Braille stimulation and found significant effects of spatial-selective attention on P50 and P100 with left tactile stimuli and on N80 with right tactile stimuli in SI. Other ERP and SEP studies of mechanical tactile stimuli (Eimer and Forster, 2003a; Eimer et al., 2004; Forster and Gillmeister, 2011; Katus et al., 2012) showed that amplitudes of mid-latency components such as N140 and P200 were enhanced in response to tactile stimuli presented to the attended hand.

In addition, an electrophysiological study in owl monkeys (Reed et al., 2010) selected paired skin sites and delivered pulses simultaneously (0 ms delay) or with onset asynchronies of 10, 30, 50, 100, and 500 ms to investigate the effects of varying the temporal proximity of stimuli. This study indicated that maximal suppression of firing rates occurred when the stimulus onset times were 30–50 ms. The owl monkeys were sedated in this study, so a suppressed effect was observed under unattended conditions.

The underlying attention and temporal processes in the human somatosensory cortex remain unclear when paired mechanical stimuli are presented. Thus, we hypothesized that enhancement and suppression occur as follows in human somatosensory areas: (1) The enhancement effect of sustained spatial attention will be stronger than the suppression effect of paired stimulation. (2) The suppression effect of paired stimulation will be stronger than the enhancement effect of sustained spatial attention. (3) The enhancement effect of sustained spatial attention and the suppression effect of paired stimulation will exist at the same time.

The present experiment was designed to determine whether the enhancement from sustained spatial attention or suppression from paired stimulation affects neurophysiological responses in human SI. We extended the work of previous studies to investigate the temporal dynamics of neural responses when mechanical tactile stimulation is delivered to the left or right index finger at different interstimulus intervals with attention focused on one hand. Participants were asked to focus their spatial attention on tactile stimulation of one hand (on a finger), and we instructed them to detect rare tactile target stimuli on the index finger of the attended hand. To achieve this aim, ERPs were computed in response to tactile stimulation.

MATERIALS AND METHODS

Participants

Nineteen undergraduate students were recruited as volunteers. With further analysis, two participants were excluded from the statistical analysis because of low performance. Seventeen participants (age range: 21–25; mean age: 22.5) remained in the sample. All participants had normal or corrected-to-normal vision and were right-handed. They had no neurological/psychiatric disorders and no hearing problems. The experimental protocol was approved by the ethics committee of Okayama University.

Material and Procedure



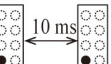
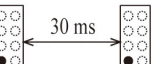
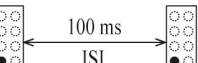
The experiment was conducted in a dimly lit, sound-attenuated room, with participants facing a computer screen (17 inch, LG, FLATRON) at a viewing distance of 60 cm. Tactile stimuli were applied to the distal phalanx of the left or right index finger using a piezoelectric Braille stimulator (KGS, Saitama, Japan). Each stimulator had eight individually controllable plastic pins grouped in a 2×4 array. The diameter of each pin was 1.3 mm. The distance between pins was 2.4 mm. Using a custom-built electrical drive, pins could be elevated from the resting position by 0.7 mm with a tactile force of 0.177 N/pin. The mechanical onset from the trigger to the highest position was ~ 38 ms, as measured by a high-speed camera, so we set the tactile stimuli presentation time to 40 ms.

Tactile stimuli were included for the standard and target. The target was 8 pins and was presented only on the side indicated by the visual instructions. The standard was one pin in the lower left (or right) when stimuli were presented on the left (or right) index finger. The stimulus presentations were composed of single and double conditions. The temporal proximity of stimulus presentations in the double condition consisted of three different interstimulus intervals (10, 30, and 100 ms). The interstimulus interval (ISI) is the time interval between the first tactile stimulus offset and second tactile stimulus onset (**Figure 1A**).

Visual and tactile stimuli were presented by using Presentation software (Neurobehavioral Systems Inc., Albany, California, USA) housed outside of the dimly lit room. A block design was used for this experiment in which the standard and target stimuli were randomized in blocks of 10 trials, with 15 blocks in one session (for a total of 150 trials). In summary, the experiment comprised 16 separate sessions, consisting of 240 blocks for a total of 2,400 trials. Visual instructions indicating the left or right index fingers (each instruction angle was $5 \times 7^\circ$ flat at 3.5° left or right from the fixation) changed to red and were presented for 300 ms at the beginning of each block. The instructions asked the participants to keep their attention on the left or right index finger for that block. A fixation (a white cross of $1.7 \times 1.7^\circ$ of visual angle) was located between both instructions (**Figure 1B**). Each session contained four experimental conditions: a single condition and three types of double conditions (ISI-10 condition, ISI-30 condition and ISI-100 condition).

Figure 1B illustrates the experimental stimulation procedure for the attended left hand. Each block began with the visual instruction, which was presented for 300 ms. Within the 300 ms,

A Tactile stimulation conditions

Name		Stimuli	Rate
Target			20%
Standard	Single condition		80%
	Double condition		
			
			

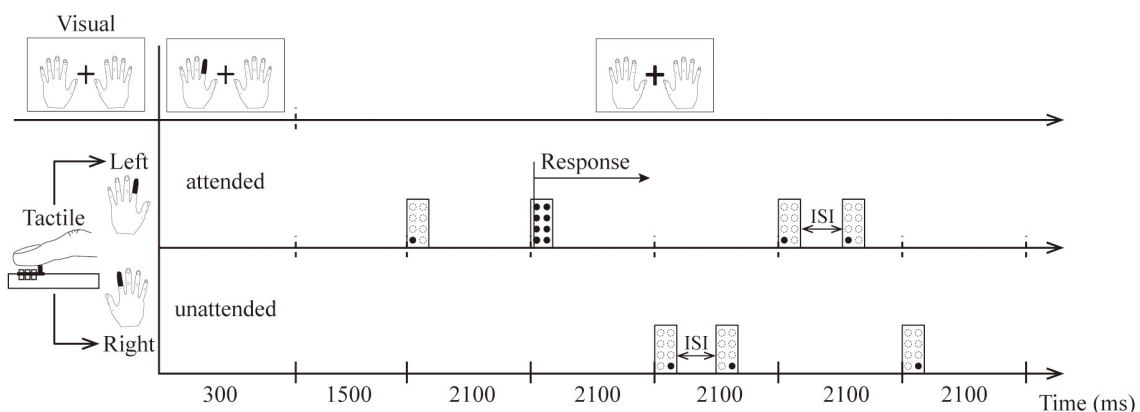
B Illustration of the experimental procedure with an attended left hand.

FIGURE 1 | (A) The types of tactile stimulation: standard (1 pin) and target (8 pins). **(B)** Illustration of attended left hand. The visual instruction was presented for 300 ms, and participants were instructed to direct their attention to the left index finger until the next instruction appeared. Standard stimuli presented on the left hand as attended stimuli. Stimuli delivered to the other hand were unattended stimuli. After the 1,500 ms interval, tactile stimuli (including two target stimuli and eight standard stimuli per block) were presented unilaterally to the left or right hand within 600 ms (total 2,100 ms). The target was presented only on the left side, and the participant responded vocally when it was detected.

the index finger of the left hand turned red in the visual instructions, and the subjects kept their attention on the finger position indicated by red (i.e., left index finger) until the next block. They were required to respond vocally when the target stimulus was detected on the left index finger. Thus, the participants had to direct their attention to the attended hand. A standard stimulus presented to this hand was named the attended stimulus. In contrast, stimuli delivered to the other hand were named unattended stimuli. After a 1,500-ms interval, tactile stimuli (including two target stimuli and eight standard stimuli per block) were presented unilaterally to the left or right hand within 600 ms (for a total of 2,100 ms as indicated in **Figure 1B**). Visual instructions and tactile stimulation were presented in pseudorandom order. During the entire experiment, the participants were also instructed to avoid movements of the body, in particular, the eyes and fingers.

EEG Recording and Data Analysis

An EEG system (Brain Amp MR plus, Germany) was used to record signals through 28 electrodes mounted on an electrode cap (Easy cap, Herrsching Breitbrunn, Germany) as specified by the International 10–20 System. All electrodes were referenced to the combined signals from the bilateral earlobes. A horizontal electrooculogram (HEOG) was recorded from the outer canthus of the left eye. Eye blinks and vertical eye movements were recorded from an electrode placed 1.5 cm below the left eye. The impedance of all electrodes was below 5 k Ω . The raw signals were digitized with a sample frequency of 500 Hz with a 60-Hz notch filter. The bandpass of the amplifiers was DC to 250 Hz.

Brain Vision Analyzer software (version 1.05, Germany) was used to analyze the ERPs, which were averaged separately for each stimulus type offline. To remove the target stimulus, we analyzed only ERPs elicited by standard stimuli. The continuous EEG

signals were segmented offline from 100 ms before to 500 ms after tactile stimulus onset. Baseline corrections were made against the data from -100 to 0 ms. We rejected artifact trials in which the amplitude reached $\pm 80 \mu\text{V}$ from -100 to 500 ms, and we filtered the data with a bandpass filter retaining frequencies between 0.01 and 30 Hz. The data from each electrode were then averaged, and a grand average ERP was computed across all participants for each stimulus type.

For further analysis, the mean amplitude data were computed within the following time windows relative to stimulus onset: P50 ($34\text{--}62$ ms), N80 ($64\text{--}92$ ms), P100 ($94\text{--}122$ ms), N140 ($124\text{--}172$ ms), P200 ($174\text{--}242$ ms), and P300 ($244\text{--}342$ ms). In each time window, the mean amplitude data were analyzed using repeated measures analyses of variance (ANOVAs) with two factors (attended vs. unattended) \times 4 conditions (single, ISI-10, ISI-30 and ISI-100 conditions), and data from electrodes C3 and C4 were analyzed separately. RStudio (Version 1.1.383) was used for all statistical analyses.

RESULTS

Figure 2 shows the grand averaged waveforms for the single condition and double conditions (ISI-10 condition, ISI-30 condition and ISI-100 condition). The electrode sites were C3/4, approximately overlying the contralateral SI. The black solid line represents the attended state, and the black dotted line represents the unattended state. In the single condition, attended stimuli elicited more positive responses than the unattended state. The double conditions resulted in the following: in the ISI-10 condition, the attended stimuli elicited activity similar to the unattended state; in the ISI-30 condition, the unattended stimuli elicited more positive activity than the attended state; and in the ISI-100 condition, the attended stimuli elicited activity levels close to the unattended state once again.

The left column in **Figure 2** shows the ERPs elicited in the four conditions by tactile stimuli presented on the right index finger at contralateral electrodes (C3, right hand). All subjects demonstrated a clear P45 component in their responses to tactile stimuli presented to the right index fingers. ANOVA of the mean amplitudes of P45 revealed a main effect [$F_{(1,16)} = 4.740$; $p < 0.05$] of attention at C3, which was not accompanied by an attention \times condition interaction; ANOVA of mean amplitudes of P100 revealed a main effect [$F_{(1,16)} = 6.175$; $p < 0.05$] of attention at C3, which was not accompanied by an attention \times condition interaction. There was a main effect of conditions [$F_{(3,16)} = 3.230$; $p < 0.05$] at C3 for the P300 component.

The right column of **Figure 2** shows the ERPs elicited in the four conditions by a tactile stimulus presented to the left index finger at contralateral electrodes (C4, left hand). The analysis of the left side for P45 and N80 revealed no main effect or interaction between attention and conditions, and only a weak significant difference in the t -test was found between the attention states in the ISI-30 condition ($p < 0.05$). There was a significant interaction between attention and conditions [$F_{(3,16)} = 6.589$; $p < 0.001$] for P100; paired t -tests found the most significant difference between the unattended and

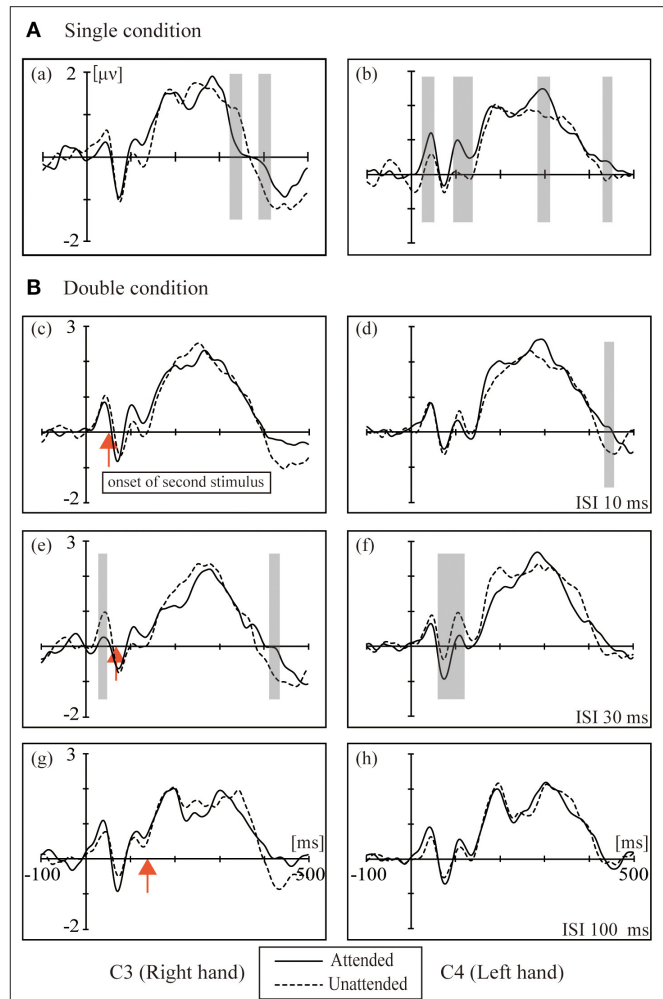


FIGURE 2 | The grand averaged waveforms for the (A) single condition (a, b) and (B) double conditions: (c,d) ISI 10 ms; (e,f) ISI 30 ms; (g–i) ISI 100 ms. The electrode sites were C3/4 approximately overlying the contralateral SI. Black solid line: attended. Black dotted line: unattended. The red arrow marks the onset of the second stimulus. The shaded areas indicate the periods used for the pointwise running t -tests comparing attended to unattended for all participants ($p < 0.05$).

ISI-30 conditions ($p < 0.001$). No main effects of attention and conditions were found for N140, P200 and P300.

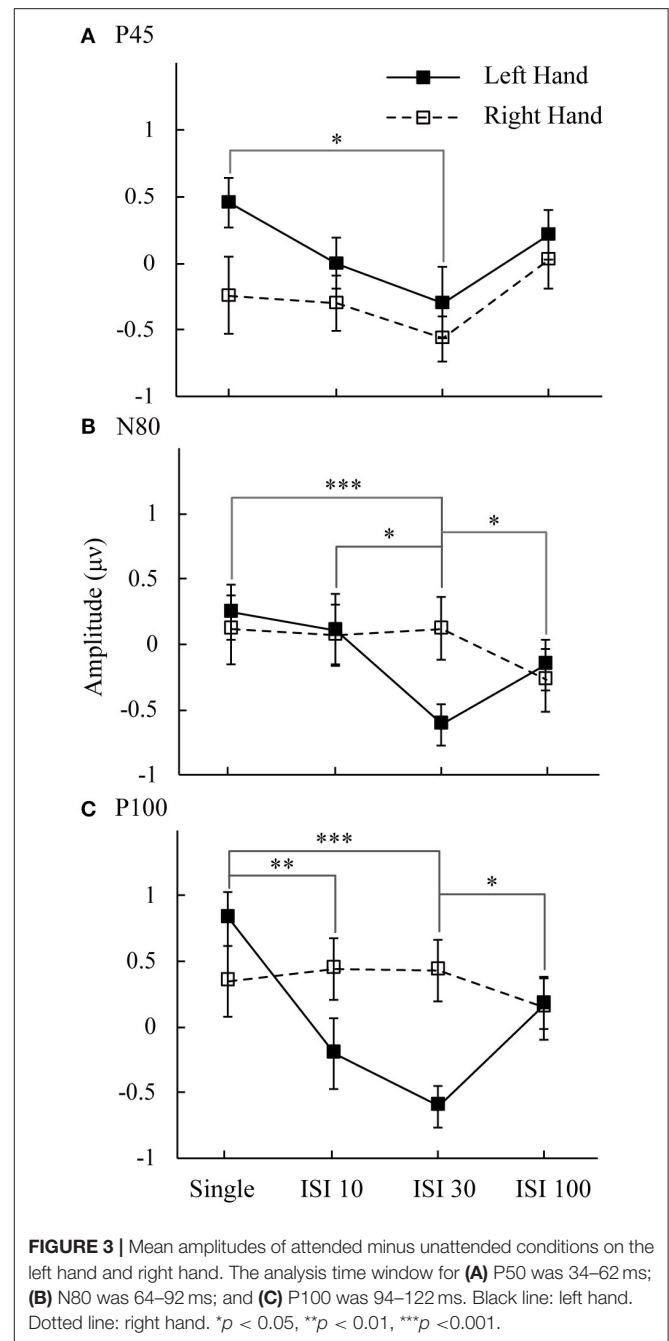
Figure 3 shows the mean amplitudes for the P45, N80, and P100 components. This result represents the attended minus unattended conditions on the left hand and right hand. Three components showed the lowest amplitude in the ISI-30 condition with the left-hand stimulus. The main effect of attention on the mean amplitudes of the P45 component was significant [$F_{(1,16)} = 6.14$, $p < 0.05$]. *Post hoc* comparisons between the single and ISI-30 conditions showed that most activation occurred at the C4 electrode ($p < 0.05$). Regarding the N80 component, the interaction between attention and ISI was clear [$F_{(3,48)} = 5.88$, $p < 0.05$], and the mean amplitudes in the single and ISI-10 conditions were significantly higher than that in the ISI-30

condition ($p < 0.05$). ISI-30 and ISI-100 were also significantly different ($p < 0.05$). These results were also limited to the C4 electrode (left hand). In the last component, P100, there was no main effect or interaction at the C3 electrode, although an effect similar to the attention main effect was found [$F_{(1,16)} = 3.77$, $p = 0.07$], but at the C4 electrode, an interaction effect between attention and ISI was clearly found [$F_{(3,48)} = 6.6$, $p < 0.05$]. The mean amplitude in the single condition was higher than that in the ISI-10 and ISI-30 conditions ($p < 0.01$). Additionally, there was a significant difference between ISI-30 and ISI-100 conditions ($p < 0.05$). For the right hand, there were no significant differences between conditions for P45, N80, and P100.

DISCUSSION

This study used double asynchronous stimulation to investigate the relationship between spatial attention enhancement and double asynchronous stimulation-induced suppression of brain activity in human SI. The participants were asked to focus their spatial attention on tactile stimulation of one hand (on a finger), and we instructed them to detect rare tactile target stimuli at the index finger of the attended hand. In double stimulation conditions, as the interstimulus intervals increased, a V-shaped effect was observed. We suggest that this occurs through an attention enhancement and a double stimulation-suppression effect.

We found a suppression effect in the ISI-30 condition, supporting a hypothesis from previous studies that multisensory stimulation shortens the response latencies of neurons and that post-activation inhibition of neurons is stronger than single stimulation. Research in monkeys found that the suppressive effect of paired stimulation activation on the interphalangeal nerve was stronger than that on the adjacent phalanges. The inhibition of interphalangeal nerve activity was caused by the proximity of receptor-related nerve cells in area 3b, which leads to nerve post-activation inhibition. As was observed in monkeys, neural response intensity was generally suppressed by a preceding conditioning stimulus when the test stimulus occurred after a 30- or 50-ms delay (Reed et al., 2010). Other similar studies (Fanselow and Nicolelis, 1999) examining rat whisker nerve reflexes found nerve post-activation inhibition following paired stimulation in quiet and movement states. In addition, Christian 2017 used double visual stimuli to investigate repetition suppression and suggested that stimulus-specific expectations about objects modulated the LOC and propagated back to the earliest cortical station processing visual input (Grill-Spector and Malach, 2001; Utzerath et al., 2017). In the present study, the visual input was equivalent to cues to improve sensitivity to the tactile input, and the stimulus was repeatedly presented in the same location of the fingers. It was more intuitive to find nerve post-activation inhibition in area 3b. This experiment extended previous studies in monkeys and verified that the paired stimulation suppression effect in human primary somatosensory cortex 3b is similar to that in monkeys. The time of nerve post-activation inhibition may be ~ 30 –50 ms.



In the single condition, we found some significant ERP components in the contralateral hemisphere by comparisons with the unattended side. The P50 and P100 components at the C4 electrode were significantly stronger on the attended side than on the unattended side (Figure 2). An fMRI-EEG study used braille stimulation to investigate attentional effects on S1, and it found that left tactile stimulation (P50) was significantly enhanced by spatial-selective attention, suggesting that attention enhances the sensory signal during its early passage in S1 (Schubert et al., 2008). This study also showed that P50 was the earliest component to be modulated by spatial-selective

attention using stimuli similar to braille stimulation. Thus, the asymmetric effects of spatial selective attention on the two sides could also be found in the early and middle processing stages. For stimuli on the left hand, P50, P100, and P300 were found when comparing the attended vs. unattended hand, but on the other side, only the P300 attentional effect was found in the attended vs. unattended hand comparison. These asymmetric hemispheric activations may be explained by Mesulam's modality-non-specific model of spatial attention (Mesulam, 1999). That is, higher-order areas in the left hemisphere control attention for events only on the right side, whereas the right hemisphere controls attention for both the left and right sides. Both theories may explain the asymmetric attentional effects on the SEPs, leading to earlier attentional modulation for left stimuli (i.e., P50 and P100 only for left and not for right stimuli).

We found some attentional enhancement in the single condition only. In the double stimuli conditions, the attentional effect was partially decreased as the interstimulus interval increased. A previous study suggested that when two or more stimuli were presented, the inhibition effects in based on the preferred stimulus (Reed et al., 2010). In the ISI-10 condition, we did not observe any enhancement or suppression effect. There are two possibilities that explain these results: the interval may be too short, such that the subject cannot recognize the double stimuli, and when the stimulus is changed to double, the suppression effect is activated much more strongly than the attentional enhancement effect. According to the interaction of spatial attention enhancement and double asynchronous stimulation-induced suppression, when the enhancement and suppression effects are equal, there was no difference between attended and unattended states in terms of the neurophysiological responses to double asynchronous stimulation (Figures 2, 3). We suggest a tentative explanation that may account for this finding: the attention enhancement and double asynchronous stimulation-induced suppression

effects decreased as the interstimulus interval increased. The stimulatory effect of attention is mutually competitive with the inhibitory effect of double stimulation. Moreover, the enhancement of spatial attention may be modulated by double stimulation suppression.

DATA AVAILABILITY STATEMENT

The raw data supporting the conclusions of this article will be made available by the authors, without undue reservation.

ETHICS STATEMENT

The studies involving human participants were reviewed and approved by the Ethics Committee of Okayama University. The patients/participants provided their written informed consent to participate in this study.

AUTHOR CONTRIBUTIONS

YL, BD, JY, JW, QW, and MZ designed experiments. YL, BD, JY, YE, JW, and QW conducted experiments. YL and BD analyzed data. YL, BD, QW, and MZ wrote manuscript. All authors approved the manuscript.

FUNDING

This research was supported by the Japan Society for the Promotion of Science KAKENHI (Grant nos. 17K18855, 18H05009, 18K12149, 18K8835, 18H01411, 19KK0099, and 20K04381), National Natural Science Foundation of China (Grant no. 31700939), and a Grant-in-Aid for Strategic Research Promotion from Okayama University. In addition, this research was supported by the Social Science project of Suzhou University of Science and Technology (Grant nos. 332012902, 341922905).

REFERENCES

- Alho, K., Medvedev, S. V., Pakhomov, S. V., Roudas, M. S., Tervaniemi, M., Reinikainen, K., et al. (1999). Selective tuning of the left and right auditory cortices during spatially directed attention. *Brain Res. Cogn. Brain Res.* 7, 335–341. doi: 10.1016/S0926-6410(98)00036-6
- Braun, C., Hess, H., Burkhardt, M., Wühle, A., and Preissl, H. (2005). The right hand knows what the left hand is feeling. *Exp. Brain Res.* 162, 366–373. doi: 10.1007/s00221-004-2187-4
- Eimer, M., and Driver, J. (2000). An event-related brain potential study of cross-modal links in spatial attention between vision and touch. *Psychophysiology* 37, 697–705. doi: 10.1111/1469-8986.3750697
- Eimer, M., and Forster, B. (2003a). Modulations of early somatosensory ERP components by transient and sustained spatial attention. *Exp. Brain Res.* 151, 24–31. doi: 10.1007/s00221-003-1437-1
- Eimer, M., and Forster, B. (2003b). The spatial distribution of attentional selectivity in touch: evidence from somatosensory ERP components. *Clin. Neurophysiol.* 114, 1298–1306. doi: 10.1016/S1388-2457(03)00107-X
- Eimer, M., Forster, B., Fieger, A., and Harbich, S. (2004). Effects of hand posture on preparatory control processes and sensory modulations in tactile-spatial attention. *Clin. Neurophysiol.* 115, 596–608. doi: 10.1016/j.clinph.2003.10.015
- Fanselow, E. E., and Nicolelis, M. A. (1999). Behavioral modulation of tactile responses in the rat somatosensory system. *J. Neurosci.* 19:7603. doi: 10.1523/JNEUROSCI.19-17-07603.1999
- Forster, B., and Eimer, M. (2004). The attentional selection of spatial and non-spatial attributes in touch: ERP evidence for parallel and independent processes. *Biol. Psychol.* 66, 1–20. doi: 10.1016/j.biopsycho.2003.08.001
- Forster, B., and Gillmeister, H. (2011). ERP investigation of transient attentional selection of single and multiple locations within touch. *Psychophysiology* 48, 788–796. doi: 10.1111/j.1469-8986.2010.01147.x
- Grill-Spector, K., and Malach, R. (2001). fMR-adaptation: a tool for studying the functional properties of human cortical neurons. *Acta Psychol.* 107, 293–321. doi: 10.1016/S0001-6918(01)00019-1
- Karns, C. M., and Knight, R. T. (2009). Intermodal auditory, visual, and tactile attention modulates early stages of neural processing. *J. Cogn. Neurosci.* 21, 669–683. doi: 10.1162/jocn.2009.21037
- Katus, T., Andersen, S. K., and Müller, M. M. (2012). Maintenance of tactile short-term memory for locations is mediated by spatial attention. *Biol. Psychol.* 89, 39–46. doi: 10.1016/j.biopsycho.2011.09.001

- Macaluso, E., Driver, J., van Velzen, J., and Eimer, M. (2005). Influence of gaze direction on crossmodal modulation of visual ERPS by endogenous tactile spatial attention. *Brain Res. Cogn. Brain Res.* 23, 406–417. doi: 10.1016/j.cogbrainres.2004.11.003
- Meador, K. J., Allison, J. D., Loring, D. W., Lavin, T. B., and Pillai, J. J. (2002). Topography of somatosensory processing: cerebral lateralization and focused attention. *J. Int. Neuropsychol. Soc.* 8, 349–359. doi: 10.1017/S.1355617702813169
- Mesulam, M. M. (1999). Spatial attention and neglect: parietal, frontal and cingulate contributions to the mental representation and attentional targeting of salient extrapersonal events. *Philos. Transact. R. Soc. B Biol. Sci.* 354, 1325–1346. doi: 10.1098/rstb.1999.0482
- Noesselt, T., Hillyard, S. A., Woldorff, M. G., Schoenfeld, A., Hagner, T., Jancke, L., et al. (2002). Delayed striate cortical activation during spatial attention. *Neuron* 35, 575–587. doi: 10.1016/S0896-6273(02)00781-X
- Pilz, K., Veit, R., Braun, C., and Godde, B. (2004). Effects of co-activation on cortical organization and discrimination performance. *Neuroreport* 15, 2669–2672. doi: 10.1097/00001756-200412030-00023
- Reed, J. L., Qi, H. X., Zhou, Z., Bernard, M. R., Burish, M. J., Bonds, A. B., et al. (2010). Response properties of neurons in primary somatosensory cortex of owl monkeys reflect widespread spatiotemporal integration. *J. Neurophysiol.* 103, 2139–2157. doi: 10.1152/jn.00709.2009
- Schubert, R., Ritter, P., Wustenberg, T., Preuschhof, C., Curio, G., Sommer, W., et al. (2008). Spatial attention related SEP amplitude modulations covary with BOLD signal in S1—a simultaneous EEG–fMRI study. *Cereb. Cortex* 18, 2686–2700. doi: 10.1093/cercor/bhn029
- Utzerath, C., John-Saaltink, E., Buitelaar, J., and Lange, F. P. (2017). Repetition suppression to objects is modulated by stimulus-specific expectations. *Sci. Rep.* 7:8781. doi: 10.1038/s41598-017-09374-z
- Zopf, R., Giabbiconi, C. M., Gruber, T., and Müller, M. M. (2004). Attentional modulation of the human somatosensory evoked potential in a trial-by-trial spatial cueing and sustained spatial attention task measured with high density 128 channels EEG. *Cogn. Brain Res.* 20, 491–509. doi: 10.1016/j.cogbrainres.2004.02.014

Conflict of Interest: The authors declare that the research was conducted in the absence of any commercial or financial relationships that could be construed as a potential conflict of interest.

Copyright © 2021 Liu, Dong, Yang, Ejima, Wu, Wu and Zhang. This is an open-access article distributed under the terms of the Creative Commons Attribution License (CC BY). The use, distribution or reproduction in other forums is permitted, provided the original author(s) and the copyright owner(s) are credited and that the original publication in this journal is cited, in accordance with accepted academic practice. No use, distribution or reproduction is permitted which does not comply with these terms.



Evaluation of Task fMRI Decoding With Deep Learning on a Small Sample Dataset

Sunao Yotsutsuji^{1*}, Miaomei Lei² and Hiroyuki Akama^{1,3}

¹ School of Life Science and Technology, Tokyo Institute of Technology, Tokyo, Japan, ² Ex-Graduate School of Science and Technology, Tokyo Institute of Technology, Tokyo, Japan, ³ Institute of Liberal Arts, Tokyo Institute of Technology, Tokyo, Japan

OPEN ACCESS

Edited by:

Rong Chen,
University of Maryland, Baltimore,
United States

Reviewed by:

Qinglin Dong,
Harvard Medical School,
United States
Xiang Li,
National Supercomputer Center,
China

*Correspondence:

Sunao Yotsutsuji
yotsutsuji.s.aa@m.titech.ac.jp

Received: 29 June 2020

Accepted: 25 January 2021

Published: 12 February 2021

Citation:

Yotsutsuji S, Lei M and Akama H
(2021) Evaluation of Task fMRI
Decoding With Deep Learning on
a Small Sample Dataset.
Front. Neuroinform. 15:577451.
doi: 10.3389/fninf.2021.577451

Recently, several deep learning methods have been applied to decoding in task-related fMRI, and their advantages have been exploited in a variety of ways. However, this paradigm is sometimes problematic, due to the difficulty of applying deep learning to high-dimensional data and small sample size conditions. The difficulties in gathering a large amount of data to develop predictive machine learning models with multiple layers from fMRI experiments with complicated designs and tasks are well-recognized. Group-level, multi-voxel pattern analysis with small sample sizes results in low statistical power and large accuracy evaluation errors; failure in such instances is ascribed to the individual variability that risks information leakage, a particular issue when dealing with a limited number of subjects. In this study, using a small-size fMRI dataset evaluating bilingual language switch in a property generation task, we evaluated the relative fit of different deep learning models, incorporating moderate split methods to control the amount of information leakage. Our results indicated that using the session shuffle split as the data folding method, along with the multichannel 2D convolutional neural network (M2DCNN) classifier, recorded the best authentic classification accuracy, which outperformed the efficiency of 3D convolutional neural network (3DCNN). In this manuscript, we discuss the tolerability of within-subject or within-session information leakage, of which the impact is generally considered small but complex and essentially unknown; this requires clarification in future studies.

Keywords: brain decoding, cross-subject modeling, cross-validation, deep learning, fMRI, model selection, MVPA

INTRODUCTION

In cognitive neuroscience, the framework for predicting the stimuli given to subjects or the tasks they perform based on their neural activity is called “decoding.” From a modeling perspective, we can evaluate predictive power and identify the brain regions that are the most informative for specific stimuli or tasks. Decoding has also been studied extensively in the context of mind-reading.

Abbreviations: 3DCNN, three-dimensional convolutional neural network; ANOVA, analysis of variance; CV, cross-validation; FWHM, full width at half maximum; Leave One Subject Out, leave-one-subject-out cross-validation; M2DCNN, multichannel two-dimensional convolutional neural network; MNI, Montreal Neurological Institute; MVPA, multi voxel pattern analysis; Permutation, permutation test; PLR, penalized logistic regression; SVM, support vector machine; Test, test set; Train, training set; Valid, validation set.

The most widely used decoding strategy is a pattern classification method called Multi Voxel Pattern Analysis (MVPA; Cohen et al., 2017). Haxby et al. (2001) showed that visual categories of stimuli can be classified based on neural activity, distributed and not clustered in small areas of the ventral temporal lobe. Subsequently, the feasibility of decoding has been explored using a variety of machine learning methods. Typically, these include various types of classifiers such as the logistic regressions, the Support Vector Machine, and the Gaussian Naive Bayes.

More recently, with the increasing interest in deep learning, studies applying non-linear multi-layer network models to decoding have been reported (Koyamada et al., 2015; Gao et al., 2019b; Thomas et al., 2019). Deep learning has the advantage of being able to simultaneously learn end-to-end, overcoming the previous faults of multi-step learning processes; previously, the classifier was learned after extracting brain regions as features, but it has now become possible to perform feature extraction and classifier learning from the whole brain at once (Wang et al., 2020). However, there remain some problems, such as the difficulty in applying deep learning to high-dimensional data and small sample size conditions (Cho et al., 2016; Yang et al., 2017).

In cognitive neuroimaging research, there tends to be a paucity of data due to experimental costs in terms of participant selection or session length, due to the complex demands of such research. When using machine learning for data analysis in sporadic experiments of this type, low statistical power and large errors in the evaluation of predictive accuracy often result. There is no clear solution to this issue, since it is important to exclude any unavoidable information leakage from a within-subject analysis. This is a crucial issue, especially when applied to a clinical context (Varoquaux et al., 2017; Varoquaux, 2018; Cearns et al., 2019).

In this study, in using a small-sized neurocognitive dataset, several cross-validation methods with different split units were used to evaluate the relative fit of different models. The models were used to analyze the results of a neurolinguistic experiment, from which a multi-site large-scale dataset is unlikely to be produced. In detail, we adopted a complicated task design for the experiment (conceptual association involving language switch), with an idiosyncratic subject group (early bilinguals familiar with two heterogeneous orthographic systems). This problem setting is particularly problematic for deep learning models because of the high-dimensional and small sample size dataset. At this point, we also identified the best method to adjust for and minimize information leakage to obtain desirable performance in the presence of a small-sized neurocognitive dataset.

METHODS

This study was performed in accordance with the Declaration of Helsinki and was approved by the Ethics Committee of the Tokyo Institute of Technology (approval number: B13001). Written informed consent was obtained from all subjects before participation. The details of the experiment are described in the **Supplementary Material**.

Datasets

Five Korean-Chinese early bilinguals participated in the functional magnetic resonance imaging (fMRI) experiments, which involved six repeated runs of a total of 20 mammal or 20 tool object images with name captions given in either Korean or Chinese, depending on the run numbers. The dataset consisted of 1,200 trials (6 runs \times 40 items for each subject; 600 trials for each class) produced by a rapid event-related design with stimulus randomization. For each trial, response data were obtained by using boxcars for 5–8 s after the stimulus onset (Akama et al., 2012); hence, there were four boxcars for which the magnitudes were averaged to generate data in each trial (except for one classifier described below). The target of the group-level MVPA was focused on the discrimination of the conceptual categories (“mammal” versus “tool”), although the language difference could result in a small degree of interference.

Using SPM8 (Friston et al., 1994), we performed a series of pre-processing steps including head movement correction, superimposing anatomical images, gray matter segmentation, conversion to Montreal Neurological Institute (MNI) coordinates, and resolution correction, after which a gray mask was applied using Nipy (Millman and Brett, 2007). Furthermore, each volume was cropped to exclude areas that were not part of the brain before z-scoring the entire image.

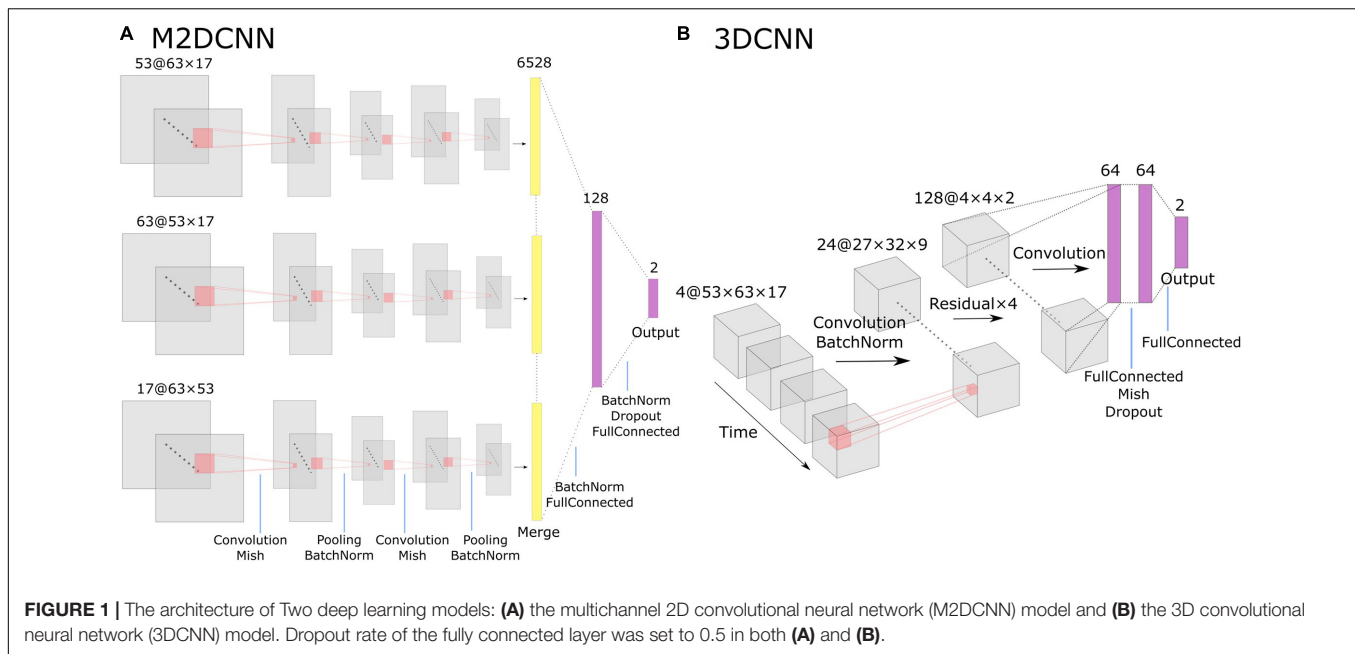
Classifiers

Based on previous studies, we used four classifiers: penalized logistic regression (PLR), support vector machine (SVM), multichannel 2D convolutional neural network (M2DCNN), and 3D convolutional neural network (3DCNN). The codes for PLR and SVM were implemented using the Python package scikit-learn (Pedregosa et al., 2011), while those for M2DCNN and 3DCNN employed Pytorch (Paszke et al., 2019; both available at: https://github.com/sn0422j/mt_deep).

The PLR (L2 norm) and SVM (Linear SVM) were used, respectively, as the most popular classifiers. Regularization parameters were optimized with nested cross-validation (Nested-CV); for the activity vector, the boxcars were averaged, and 500 voxels were selected by analysis of variance (ANOVA).

For the M2DCNN model, we referred to the work of Hu et al. (2019), which meant that the model consisted of three two-dimensional convolutional layers corresponding to the axes of three orthogonal planes, a merge layer that concatenates features, and a fully connected layer for classification. **Figure 1A** shows the architecture of this model. A Mish function (Misra, 2019) was used for the activation function to prevent overfitting. To train our model, we used cross-entropy as a loss function and Adam [learning rate = 0.001, beta = (0.9, 0.999)] for optimization; 300 epochs were performed with exponential learning rate decay. The average images of the boxcars were used as the input to the model.

The 3DCNN model was based on the report of Wang et al. (2020; **Figure 1B**) to capture local spatiotemporal changes by applying three-dimensional convolutional filters over a time series. This training configuration was the same as the M2DCNN model, and the boxcars were used as the input to the model. It should be noted that the 3DCNN model allowed us to input



without averaging the magnitudes of the critical boxcars as a single 4D data.

Evaluation of Accuracy

With a view to comparing the effectiveness of the following three cross-validation (CV) methods, we performed a five-fold CV for each method to calculate the classification accuracy of the test set split out from the small boxcar data: leave-one-subject-out CV, session shuffle split, and sample shuffle split. Note that for these CV methods, the data for the folds were subtracted from the six runs in each experiment, since we did not leave out any run(s) as a unit in this modeling.

When using the leave-one-subject-out CV as a splitting strategy, each subject was assigned a particular fold pattern so that only one individual's data was included in each test set (abbreviated hereafter as Test) and another one in the validation set (abbreviated as Valid) at every CV step (**Figure 2A**). Hence, each fold contained three subjects as providers of a training set (Train for short), one subject for the Valid, and another one for the Test.

In the session shuffle split, a fold was created in a run-by-run manner, regardless of subject identification, and by selecting 20% of the trials (taken as blocks) included in each run as Test or Valid at random (**Figure 2B**). The proportion of the numbers of data randomly assigned to the Train, Valid, and Test sets was identical throughout all folds (3:1:1). In other words, in each fold we had 18 runs for Train, 6 runs for Valid, and 6 runs for Test.

In the sample shuffle split method, a fold was set in a trial-by-trial manner, without considering data attribution to subject and runs, and by randomly selecting 144 trials for Train, 48 trials for Valid, and the remaining 48 trials for Test (**Figure 2C**). The proportion of the three subsets was kept at 3:1:1 as was the case with the session shuffle split method.

Additionally, we performed a permutation test in which labels were randomly re-labeled 100 times, to calculate the chance level for each cross-validation method. With regards to the classifier, the PLR with the above settings was used as the baseline. We calculated the p value for each combination of classifiers and CV methods using the Wilcoxon rank-sum test. The statistical analyses were conducted using Scipy.stats Version 1.4.1. A p value of less than 0.005 was the threshold for statistical significance.

RESULTS

The accuracy and p values for the three cross-validations and the four classifiers are shown in **Figure 3** and **Table 1**. PLR, SVM, and M2DCNN elicited significantly higher accuracy (p value < 0.0005) than the chance level for the session shuffle split and sample shuffle split. 3DCNN recorded almost the same accuracy as the chance level.

In general, the accuracy of the classifier was improved with, in ascending order, leave-one-subject-out CV, session shuffle split, and sample shuffle split. In the leave-one-subject-out CV, the best precision rate (0.511) was obtained with the PLR classifier, but this was not significant (p value > 0.005). In the session shuffle split and sample shuffle split, the best precision rate (0.640, 0.751, respectively) was obtained with the M2DCNN classifier. We regarded the value of 0.640 using session shuffle split as the authentic accuracy, which is discussed below.

DISCUSSION

Comparison of Methods

In this section, we review the properties of all of the split methods, respectively, and then assess the performance and structure of

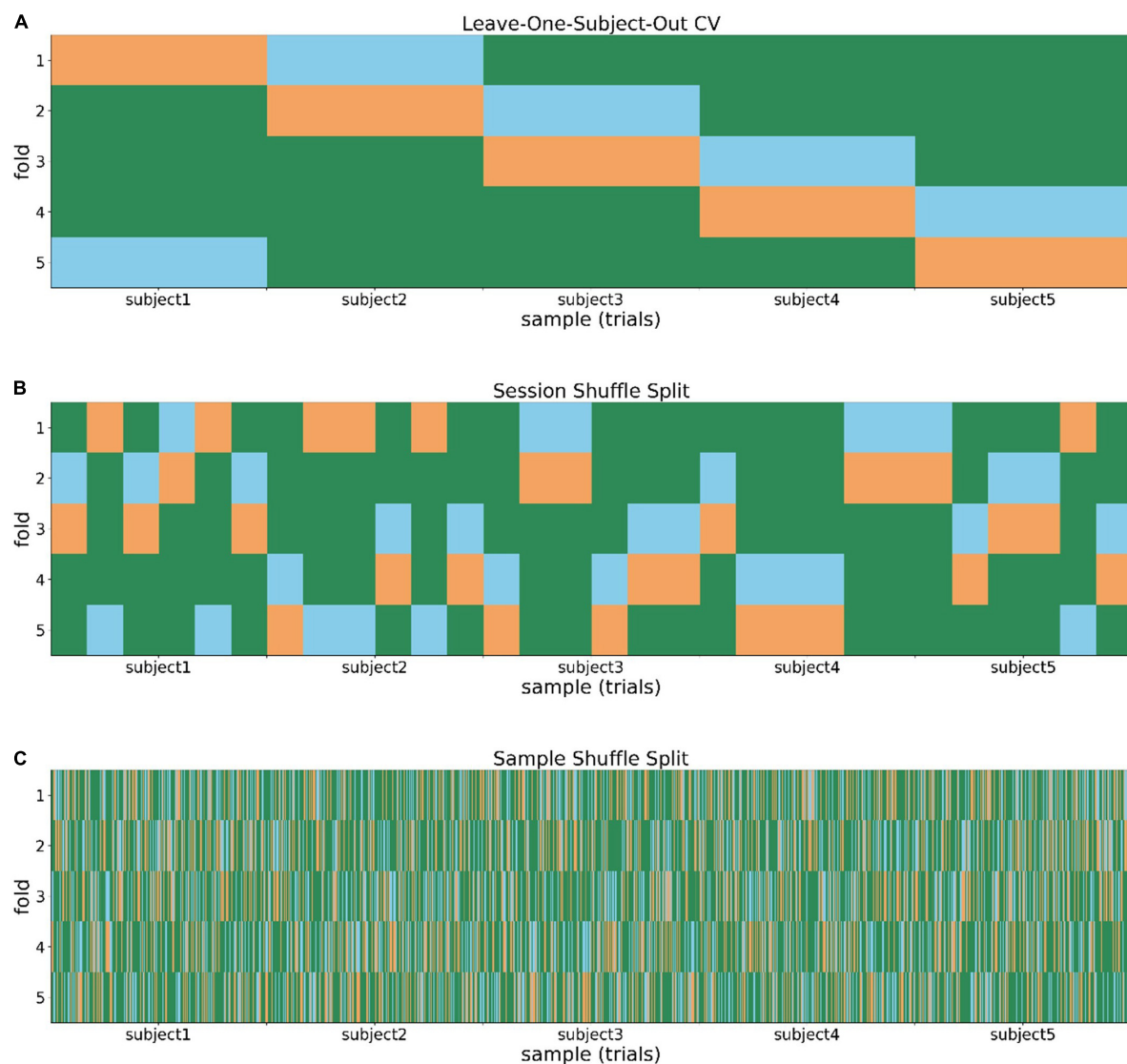


FIGURE 2 | Three splitting methods for the evaluation of accuracy: **(A)** Leave-one-subject-out cross-validation; **(B)** session shuffle split; and **(C)** sample shuffle split. The training set (green), validation set (blue), and test set (orange) are colored differently.

several deep learning models. Each CV method has a different data distribution within each of the splits. For the leave-one-subject-out CV, the breakdown of a fold composed of Train, Valid, and Test was limited to 3, 1, and 1 subject(s), respectively. Thus, we assume that the classifiers would be insufficient to achieve good generalization performance in the classification of further unknown subjects. The data were under-sampled from a large population of subjects, since the individual variability between subjects should be significantly larger than within-subject fluctuations in terms of functional activity (Miller et al., 2009). As a result, statistical machine learning methods were far from a good fit.

When it comes to the session shuffle split and sample shuffle split methods, for which within-subject leakage was unpreventable, statistical machine learning was likely to be

successful by reducing the effect of individual functional differences. Further improvement in the accuracy of the sample shuffle split may be dependent on the leakage caused in a time series due to the higher similarity of functional activity within runs than between runs (Varoquaux et al., 2017; Varoquaux, 2018). Moreover, it should be considered that two types of session-wise stimuli were provided to each subject with orthographic variability by language switch, which might have had a significant impact on his/her task performance.

Individual functional differences have traditionally limited the application of classifiers; solutions addressing this include functional alignment (hyperlalignment; Haxby et al., 2011), the use of large datasets (Varoquaux et al., 2017; Varoquaux, 2018), and some few-shot learning techniques like transfer learning in deep learning (Gao et al., 2019a,b; Wang et al., 2020),

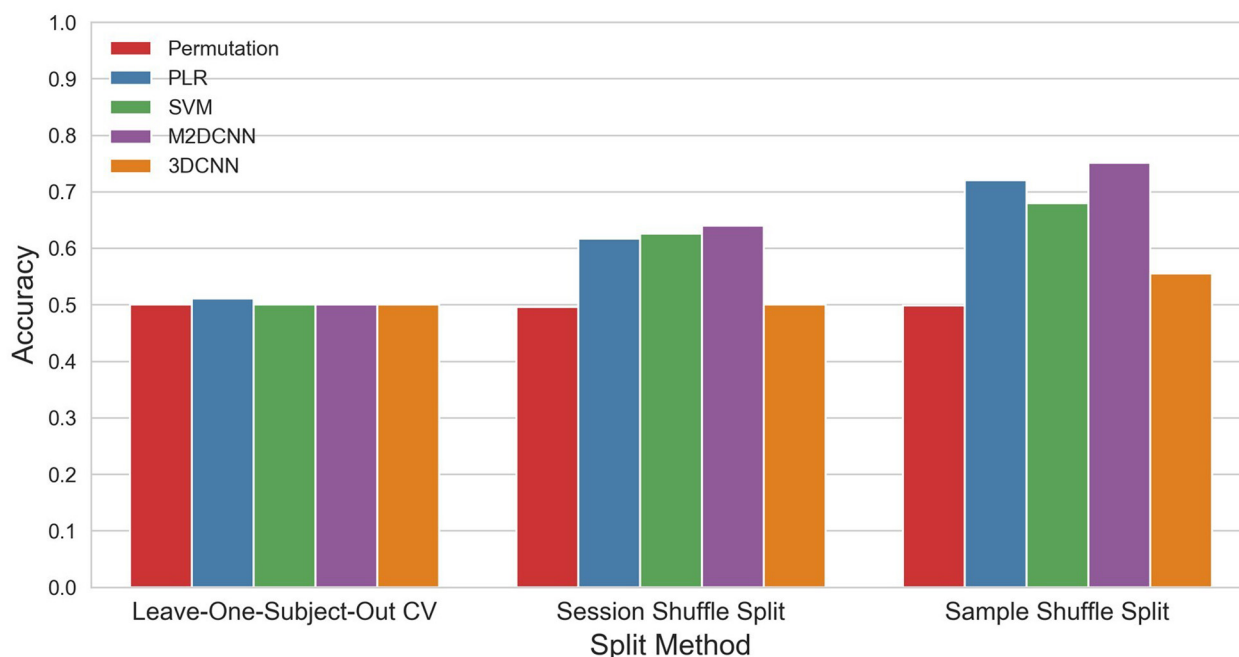


FIGURE 3 | The mean accuracy for each split method and classifier. The permutation accuracy represents the chance level for each split method. 3DCNN, three-dimensional convolutional neural network; M2DCNN, multichannel two-dimensional convolutional neural network; PLR, penalized logistic regression; SVM, support vector machine.

TABLE 1 | The mean accuracy and the associated p value for each split method and classifier.

Split method	Training method	Accuracy	p value
Leave-One-Subject-Out CV	PLR	0.511	0.1529
	SVM	0.500	0.9760
	M2DCNN	0.500	0.9700
	3DCNN	0.500	0.9700
Session Shuffle Split	PLR	0.617	0.0002**
	SVM	0.626	0.0002**
	M2DCNN	0.640	0.0002**
	3DCNN	0.500	0.9101
Sample Shuffle Split	PLR	0.720	0.0002**
	SVM	0.680	0.0002**
	M2DCNN	0.751	0.0002**
	3DCNN	0.555	0.0017*

A single asterisk (*) indicates $p < 0.005$; double asterisks (**) indicate $p < 0.0005$. CV, cross-validation. The highest accuracy in each split method is highlighted in bold.

transfer learning in shared response modeling (Zhang et al., 2018; Yousefnezhad et al., 2020), and meta-learning. It is difficult, however, to use these methods for deep learning with a limited sample size and a unique experimental condition. Therefore, leaking information to some extent as referenceable prior knowledge and discussing end-to-end models appears to be one of the better solutions to address this issue. The session shuffle split model appears to be the best way to evaluate the accuracy of the models in this case, since the individual functional

differences are referenceable without being affected by the time-series correlation.

The M2DCNN model, which achieved the highest accuracy with little information leakage, was evaluated using gradients to locate what the model learned for classification. This analysis resulted in consistency with prior research describing similar experimental tasks (see **Supplementary Material** for analytical details). In this regard, a deep learning end-to-end model could detect category-specific responses that are common to the subjects.

The unexpectedly poor efficiency of the 3DCNN model for the present analysis is worthy of discussion. Prior studies that applied the 3DCNN model to task fMRI (Hu et al., 2019; Wang et al., 2020) showed high accuracy in block designs, with sustained and homogeneous task characteristics. The rapid event-related design that we employed in our experiment might promote greater variability within the time series. Given this, a model that explicitly incorporates time series information, such as long short-term memory (LSTM), may fit better (Thomas et al., 2019) for a checkered experiment session.

Limitations and Future Directions

In this section, we provide some limitations of this study and discuss the best method to adjust the information leakage level. There are some limitations to this study. The accuracy reported in this study is not an indicator of the generalizable performance of the entire subject population, due to the leakage of information. Here, we define information leakage as the phenomenon where the i.i.d. split units for each split strategy have dependence as

a consequence of the structured property of data distribution. There are several levels of information leakage, which should be separated out in terms of legitimacy (Kaufman et al., 2012). Based on this idea, we propose readily attributing levels as “heavy” or “light” for those actions.

In the fMRI decoding framework, heavy leakage has been considered to be so serious that it affects the authenticity of accuracy indicators, such as that seen in supervised feature selection prior to splitting or hyperparameter optimization with Test data (Kaufman et al., 2012). In contrast, light leakage is likely to occur when the Train and Test data are not completely independent, with their indirect and hidden relationship being difficult to scrutinize; its impact is generally taken as small but complex and essentially unknown.

In this study, we presented an example of training a complex model by allowing light information leakage. For group analysis, the sample shuffle split method ignored the leakage likely to be caused in a time series and hypothesized the independence of trials within runs. We believe that under this condition, the rate of 0.651 obtained by the session shuffle split and the M2DCNN classifier was the authentic limit of classification accuracy in this study. Beyond this scope, some results of multivariate analysis based on heavy leakage might be considered to work entirely outside the context of machine learning; for example, an adaptive reuse of them is possible, such as that seen with a brain semantic map reflecting the representational similarity of concepts. However, open questions remain unanswered in relation to the utility of such rich information handling.

In regards to the underestimation of cross-validation loss, our research indicated a need to demonstrate how we could control the data independence and support the significance of the indicator in a non-parametric way; for example, by using a permutation test (Varoquaux et al., 2017; Varoquaux, 2018). However, when investigating cognitive processes specific to a narrow population as in the case of this study, it is important to model within-subject variability by taking more data, even with fewer subjects, and reducing within-subject errors (Smith and Little, 2018). Future studies are required to develop and train a more reliable classifier for each subject and to stably as well as precisely detect consistent shared effects across subjects with higher statistical power.

CONCLUSION

In this study, we examined the application of complex models for the decoding of fMRI under the constrained condition of a small

sample size in a unique cognitive experiment. It was shown that even when data bias was caused by functional variability across subjects, in spite of greatly limited performance of the classifiers, the complex model could be successfully applied by taking a moderate split to control information leakage. This might be a key to success in deep learning for overcoming a paucity of fMRI data. In this study, we have discussed the tolerability of within-subject or within-session information leakage, of which the impact was generally considered to be small but complex and essentially unknown; this requires clarification in future studies.

DATA AVAILABILITY STATEMENT

The raw data supporting the conclusions of this article will be made available by the authors, without undue reservation.

ETHICS STATEMENT

The studies involving human participants were reviewed and approved by the Ethics Committee of the Tokyo Institute of Technology (approval number: B13001). The patients/participants provided their written informed consent to participate in this study.

AUTHOR CONTRIBUTIONS

SY and HA: conceptualization, investigation, methodology, and writing. SY, ML, and HA: data curation and analysis. HA: supervision. All authors contributed to the article and approved the submitted version.

ACKNOWLEDGMENTS

We would like to thank Y. Minowa for useful discussions. We would also like to thank Editage (www.editage.com) for English language editing. Finally, we are grateful to the subjects for participating in the experiment.

SUPPLEMENTARY MATERIAL

The Supplementary Material for this article can be found online at: <https://www.frontiersin.org/articles/10.3389/fninf.2021.577451/full#supplementary-material>

REFERENCES

- Akama, H., Murphy, B., Na, L., Shimizu, Y., and Poesio, M. (2012). Decoding semantics across fMRI sessions with different stimulus modalities: a practical MVPA study. *Front. Neuroinform.* 6:24. doi: 10.3389/fninf.2012.00024
- Cearns, M., Hahn, T., and Baune, B. T. (2019). Recommendations and future directions for supervised machine learning in psychiatry. *Transl. Psychiatry* 9:271. doi: 10.1038/s41398-019-0607-2
- Cho, J., Lee, K., Shin, E., Choy, G., and Do, S. (2016). How much data is needed to train a medical image deep learning system to achieve necessary high accuracy? *arXiv [Preprint]*. Available online at: <https://arxiv.org/abs/1511.06348> (accessed April 25, 2020).
- Cohen, J. D., Daw, N., Engelhardt, B., Hasson, U., Li, K., Niv, Y., et al. (2017). Computational approaches to fMRI analysis. *Nat. Neurosci.* 20, 304–313. doi: 10.1038/nn.4499
- Friston, K. J., Holmes, A. P., Worsley, K. J., Poline, J. P., Frith, C. D., and Frackowiak, R. S. J. (1994). Statistical parametric maps in functional imaging:

- a general linear approach. *Hum. Brain Mapp.* 2, 189–210. doi: 10.1002/hbm.460020402
- Gao, Y., Zhang, Y., Cao, Z., Guo, X., and Zhang, J. (2019a). Decoding brain states from fMRI signals by using unsupervised domain adaptation. *IEEE J. Biomed. Health Inform.* 24, 1677–1685. doi: 10.1109/JBHI.2019.2940695
- Gao, Y., Zhang, Y., Wang, H., Guo, X., and Zhang, J. (2019b). Decoding behavior tasks from brain activity using deep transfer learning. *IEEE Access* 7, 43222–43232. doi: 10.1109/ACCESS.2019.2907040
- Haxby, J. V., Gobbini, M. I., Furey, M. L., Ishai, A., Schouten, J. L., and Pietrini, P. (2001). Distributed and overlapping representations of faces and objects in ventral temporal cortex. *Science* 293, 2425–2430. doi: 10.1126/science.1063736
- Haxby, J. V., Guntupalli, J. S., Connolly, A. C., Halchenko, Y. O., Conroy, B. R., Gobbini, M. I., et al. (2011). A common, high-dimensional model of the representational space in human ventral temporal cortex. *Neuron* 72, 404–416. doi: 10.1016/j.neuron.2011.08.026
- Hu, J., Kuang, Y., Liao, B., Cao, L., Dong, S., and Li, P. (2019). A multichannel 2D convolutional neural network model for task-evoked fMRI data classification. *Comput. Intell. Neurosci.* 2019:5065214. doi: 10.1155/2019/5065214
- Kaufman, S., Rosset, S., Perlich, C., and Stitelman, O. (2012). Leakage in data mining: formulation, detection, and avoidance. *ACM Trans. Knowl. Discov. Data* 6:15. doi: 10.1145/2382577.2382579
- Koyamada, S., Shikauchi, Y., Nakae, K., Koyama, M., and Ishii, S. (2015). Deep learning of fMRI big data: a novel approach to subject-transfer decoding. *arXiv* [Preprint]. Available online at: <https://arxiv.org/abs/1502.00093> (accessed April 25, 2020).
- Miller, M. B., Donovan, C. L., Van Horn, J. D., German, E., Sokol-Hessner, P., and Wolford, G. L. (2009). Unique and persistent individual patterns of brain activity across different memory retrieval tasks. *Neuroimage* 48, 625–635. doi: 10.1016/j.neuroimage.2009.06.033
- Millman, K. J., and Brett, M. (2007). Analysis of functional magnetic resonance imaging in Python. *Comput. Sci. Eng.* 9, 52–55. doi: 10.1109/MCSE.2007.46
- Misra, D. (2019). Mish: a self regularized non-monotonic neural activation function. *arXiv* [Preprint]. Available online at: <https://arxiv.org/abs/1908.08681> (accessed April 26, 2020).
- Paszke, A., Gross, S., Massa, F., Lerer, A., Bradbury, J., Chanan, G., et al. (2019). “PyTorch: an imperative style, high-performance deep learning library,” in *Advances in Neural Information Processing Systems*, eds H. Wallach, H. Larochelle, A. Beygelzimer, F. Alché-Buc, E. Fox, and R. Garnett (Red Hook, NY: Curran Associates, Inc), 8024–8035.
- Pedregosa, F., Varoquaux, G., Gramfort, A., Michel, V., Thirion, B., Grisel, O., et al. (2011). Scikit-learn: machine learning in Python. *J. Mach. Learn. Res.* 12, 2825–2830.
- Smith, P. L., and Little, D. R. (2018). Small is beautiful: in defense of the small-N design. *Psychon. Bull. Rev.* 25, 2083–2101. doi: 10.3758/s13423-018-1451-8
- Thomas, A. W., Heekeren, H. R., Müller, K. R., and Samek, W. (2019). Analyzing neuroimaging data through recurrent deep learning models. *arXiv* [Preprint]. Available online at: <https://arxiv.org/abs/1810.09945> (accessed April 25, 2020).
- Varoquaux, G. (2018). Cross-validation failure: small sample sizes lead to large error bars. *Neuroimage* 180, 68–77. doi: 10.1016/j.neuroimage.2017.06.061
- Varoquaux, G., Raamana, P. R., Engemann, D. A., Hoyos-Idrobo, A., Schwartz, Y., and Thirion, B. (2017). Assessing and tuning brain decoders: cross-validation, caveats, and guidelines. *Neuroimage* 145, 166–179. doi: 10.1016/j.neuroimage.2016.10.038
- Wang, X., Liang, X., Jiang, Z., Nguchu, B. A., Zhou, Y., Wang, Y., et al. (2020). Decoding and mapping task states of the human brain via deep learning. *Hum. Brain Mapp.* 41, 1505–1519. doi: 10.1002/hbm.24891
- Yang, Q., Liu, B., Wei, Y., and Zhang, Y. (2017). “Deep neural networks for high dimension, low sample size data,” in *Proceedings of the 26th International Joint Conference on Artificial Intelligence (IJCAI’17)* (Palo Alto, CA: AAAI Press), 2287–2293.
- Yousefnezhad, M., Selvitella, A., Zhang, D., Greenshaw, A. J., and Greiner, R. (2020). Shared space transfer learning for analyzing multi-site fMRI data. *arXiv* [Preprint]. Available online at: <http://arxiv.org/abs/2010.15594> (accessed January 20, 2021).
- Zhang, H., Chen, P.-H., and Ramadge, P. (2018). “Transfer Learning on fMRI Datasets,” in *Proceedings of the Twenty-First International Conference on Artificial Intelligence and Statistics*, Playa Blanca, 595–603.

Conflict of Interest: The authors declare that the research was conducted in the absence of any commercial or financial relationships that could be construed as a potential conflict of interest.

Copyright © 2021 Yotsutsuji, Lei and Akama. This is an open-access article distributed under the terms of the Creative Commons Attribution License (CC BY). The use, distribution or reproduction in other forums is permitted, provided the original author(s) and the copyright owner(s) are credited and that the original publication in this journal is cited, in accordance with accepted academic practice. No use, distribution or reproduction is permitted which does not comply with these terms.

Advantages of publishing in Frontiers



OPEN ACCESS

Articles are free to read
for greatest visibility
and readership



FAST PUBLICATION

Around 90 days
from submission
to decision



HIGH QUALITY PEER-REVIEW

Rigorous, collaborative,
and constructive
peer-review



TRANSPARENT PEER-REVIEW

Editors and reviewers
acknowledged by name
on published articles

Frontiers

Avenue du Tribunal-Fédéral 34
1005 Lausanne | Switzerland

Visit us: www.frontiersin.org

Contact us: frontiersin.org/about/contact



REPRODUCIBILITY OF RESEARCH

Support open data
and methods to enhance
research reproducibility



DIGITAL PUBLISHING

Articles designed
for optimal readership
across devices



FOLLOW US

@frontiersin



IMPACT METRICS

Advanced article metrics
track visibility across
digital media



EXTENSIVE PROMOTION

Marketing
and promotion
of impactful research



LOOP RESEARCH NETWORK

Our network
increases your
article's readership